

CRANFIELD UNIVERSITY

ALEXANDER M. TOTHILL

Developing a Proof of Principle 3D-Printed
Lab-On-A-Disc Assay Platform.

SCHOOL OF AEROSPACE, TRANSPORT AND
MANUFACTURING

PhD Thesis

Academic Year: 2013 - 2017

Supervisor: Professor S. W. James
Dr M. Partridge
Professor R. P. Tatam

May 2017

CRANFIELD UNIVERSITY

SCHOOL OF AEROSPACE, TRANSPORT AND MANUFACTURING

PhD Thesis

Academic Year 2013 - 2017

ALEXANDER M. TOTHILL

Developing a Proof of Principle 3D-Printed
Lab-On-A-Disc Assay Platform.

Supervisor: Professor S. W. James

Dr M. Partridge

Professor R. P. Tatam

May 2017

This thesis is submitted in partial fulfilment of the requirements for the
degree of Doctor of Philosophy.

© Cranfield University 2017. All rights reserved. No part of this publication may be
reproduced without the written permission of the copyright owner.

ABSTRACT

A 3D-printed microfluidic lab-on-a-disc (LOAD) device was designed and manufactured using a low cost (~£1600) consumer grade fused deposition modelling (FDM) Ultimaker 2+ 3D printer with imbedded microfluidic channels 1 mm wide, 400 μm depth and with a volumetric capacity of approximate 23 μl . FDM printers are not typically used, or are capable, of producing the fine detailed structures required for microfluidic fabrication; in addition 3D-printed objects can suffer from poor optical transparency. However, in this work, imbedded microfluidic channels were produced and the optical transparency of the device was improved through manufacture optimisation to such a point that optical colourimetric assays can be performed in a microfluidic cuvette device with sample path length of 500 μm and volumetric capacity of 190 μl . When acetone vapour treatment was used, it was possible to improve transparency of plastic samples by up to a further 30%. The LOAD device is capable of being spun using an unmodified optical disc drive (ODD), demonstrating the centrifugation based separation of plasma from whole blood in a low-cost FDM 3D-printed microfluidic LOAD device.

A cholesterol assay and glucose assay was developed and optimised using cholesterol oxidase (ChOx) or glucose oxidase (GLOx) respectively and horseradish peroxidase (HRP) for the oxidative coupling of chromotropic acid (CTA) and 4-aminoantipyrine (AAP). This produced a blue quinoneimine dye with a broad absorbance peaking at 590 nm for the quantification of cholesterol/glucose in solution. The colourimetric enzymatic cascade assays were developed for use within low-cost FDM 3D-printed microfluidic devices to demonstrate the capabilities and functionality of the devices. For comparison, the assay was run in standard 96 well plates with a commercial plate reader. The results demonstrated that the quantification of 0-10 mM glucose solution using a 3D-printed microfluidic optical device had a performance comparable to a plate reader assay; glucose assay in whole blood samples $R^2 = 0.96$.

KEYWORDS: 3D-Printing; Microfluidics; Devices; Glucose; Enzymatic; Low cost; whole blood.

ACKNOWLEDGEMENTS

I would like to offer my sincere gratitude to my supervisors Dr Matthew Partridge, Professor Stephen James and Professor Ralph Tatam for allowing me to join the Engineering Photonics group when Cranfield Health closed. Their invaluable support, guidance and optimism over the past two years made the completion of this work possible. In addition I would like to thank all the members of the Engineering Photonics group, especially my friends James Barrington, Antonio Rendon Romero, Evangelos Rigas and Nickolas Davis who went out of their way to welcome me to the group and offer any help they could. I will treasure the laughs and fun we had in the dungeon we called an office. I would also like to thank Professor Seamus Higson and Dr Frank Davis for their supervision at the beginning of the project and Professor David Cullen his constructive criticism and insight during project reviews.

I would like to offer special thanks to my family and friends for their inspiration and understanding. I would like to thank Dr Jake Chandler for his friendship, advice and our long lunch break discussions that led to several breakthroughs during the project. I especially would like to thank my mother Professor Ibtisam Tothill for her encouragement, support and the delightfully unachievable standard levels to which she held me during this project.

Finally I would like to show my eternal love and gratitude to my fiancée Dr Sinéad Carr. Without her help, love and support throughout this project I would not have been able to complete this work.

TABLE OF CONTENTS

ABSTRACT	i
ACKNOWLEDGEMENTS.....	ii
TABLE OF CONTENTS	iii
LIST OF FIGURES	vi
LIST OF TABLES	xiv
LIST OF EQUATIONS.....	xv
LIST OF ABBREVIATIONS.....	xvi
1 Chapter 1: Introduction	1
1.1 Rationale for the Research	2
1.2 Aims and Objectives	4
2 Chapter 2: Literature Review.....	6
2.1 An Overview of Cardiovascular Disease and Diabetes Mellitus.....	7
2.1.1 Cholesterol.....	11
2.1.2 Glucose	13
2.2 Point-of-Care (POC) Testing.....	15
2.2.1 Advantages of Point-of-Care Diagnostics.....	17
2.2.2 Disadvantages of Point-of-Care Diagnostics	18
2.2.3 Point-of-Care Glucose Monitor	20
2.2.4 Lateral Flow Assays.....	22
2.3 Lab-On-A-Disc (LOAD).....	24
2.3.1 Optical Disc Drives (ODD) and Discs.....	31
2.3.2 Particle Separation on a Centrifugal Microfluidic Platform	36
2.4 3D-Printing Technology	40
2.4.1 Manufacturing Materials.....	48
2.5 This Project	50
3 Chapter 3: Development of a Quantitative Optical Assay for Cholesterol and Glucose	53
3.1 Introduction.....	54
3.2 Materials and Methods	56
3.2.1 Buffers and Solutions.....	57
3.2.2 Enzyme Specifications	58
3.2.3 Preliminary Investigation into Chromotropic Acid (CTA) and 4-Aminoantipyrine (AAP) Concentration.	60
3.2.4 Investigation of CTA:AAP molar ratio.....	60
3.2.5 Optimisation of Horseradish Peroxidase (HRP) Concentration.	61
3.2.6 Optimisation of Cholesterol Oxidase (ChOx) Concentration.	61
3.2.7 Development of the Cholesterol Assay in Buffer.	61
3.2.8 Development of the Cholesterol Assay in Plasma.....	62

3.2.9 Development of the Cholesterol Assay in Whole Blood.....	62
3.2.10 Optimisation of Glucose Oxidase (GLOx) Concentration.....	62
3.2.11 Development of the Glucose Assay in Buffer.....	63
3.3 Results and Discussion.....	63
3.3.1 Preliminary Investigation into Chromotropic Acid (CTA) and 4-Aminoantipyrine (AAP) Concentration.	64
3.3.2 Investigation of CTA:AAP molar ratio.....	70
3.3.3 Optimisation of Horseradish Peroxidase (HRP) Concentration	76
3.3.4 Optimisation of Cholesterol Oxidase (ChOx) Concentration	78
3.3.5 Development of the Cholesterol Assay in Buffer	84
3.3.6 Development of the Cholesterol Assay in Plasma.....	86
3.3.7 Development of the Cholesterol Assay in Whole Blood	91
3.3.8 Optimisation of Glucose Oxidase (GLOx) Concentration	94
3.3.9 Development of the Glucose Assay in Buffer	96
3.4 Conclusions	99
4 Chapter 4: Lab-On-A-Disc Platform Design and Manufacture	102
4.1 Introduction	103
4.2 Materials and Methods	104
4.2.1 3D-Printer	104
4.2.2 Software	106
4.2.3 3D-Printing Process	106
4.2.4 Print Material.....	106
4.2.5 Other Materials	109
4.2.6 Instrumentation Used to Measure Attenuation	109
4.2.7 Optical Coherence Tomography Instrumentation	110
4.2.8 Plastic Samples	111
4.2.9 Open Face Plastic Channel Samples	112
4.2.10 Effect of Layer Height and Print Speed on Optical Transparency	113
4.2.11 Effect of 3D-Printer Print Head Position in Relation to Printer Build Table on Optical Transparency.....	113
4.2.12 Effect of Acetone Vapour Treatment on Optical Transparency.....	114
4.2.13 Effect of Acetone Liquid Treatment on Optical Transparency.....	114
4.2.14 Effect of Acetone Liquid on Channel Surface Roughness	114
4.3 Results and Discussion.....	115
4.3.1 Effect of Layer Height and Print Speed on Optical Transparency	115
4.3.2 Effect of 3D-Printer Print Head Position in Relation to Printer Build Table on Optical Transparency.....	119
4.3.3 Effect of Acetone Vapour Treatment on Optical Transparency.....	123
4.3.4 Effect of Acetone Liquid Treatment on Optical Transparency.....	127
4.3.5 Development of a FDM 3D-Printed LOAD Platform.....	129

4.3.6 Effect of Acetone Liquid on Channel Surface Roughness	143
4.3.7 Problems.....	154
4.4 Conclusions.....	155
5 Chapter 5: The Performance of a Whole Blood Colourimetric Assay in a 3D- Printed LOAD Device	157
5.1 Introduction.....	158
5.2 Materials and Methods	159
5.2.1 Buffers and Solutions.....	159
5.2.2 Microfluidic Cuvette Devices.....	160
5.2.3 Spectral Analysis Instrumentation	161
5.2.4 Centrifuge Pellet Device	161
5.2.5 Glucose Assay in 3D-Printed Microfluidic Cuvette Device	162
5.2.6 Blood Separation in a 3D-Printed Pellet Device	163
5.2.7 Glucose assay in LOAD Platform.....	163
5.3 Results and Discussion.....	164
5.3.1 Glucose Assay Performed in a 3D-Printed Microfluidic Device.	165
5.3.2 Device Variability	173
5.3.3 Blood separation in 3D-Printed Device	175
5.3.4 Blood separation in a Low-Cost 3D-Printed FDM Microfluidic LOAD Device.	181
5.3.5 Performing the Glucose Assay in Whole Blood and Centrifugation in a Low-Cost FDM 3D-Printed Microfluidic LOAD Device.	197
5.4 Conclusions.....	203
6 Chapter 6: General Conclusions and Future Work.....	206
6.1 General Conclusions	207
6.2 Development of an Optical Cholesterol and Glucose Assay	209
6.3 LOAD Device Design, Manufacture and Optimisation	209
6.4 The Performance of a Whole Blood Colourimetric Assay in a Low-Cost FDM 3D-Printed LOAD Microfluidic Device.....	210
6.5 Limitations	212
6.6 Proposed Future Work	213
6.7 Final Conclusions	216
LIST OF PUBLICATIONS	217
REFERENCES.....	218
PEER-REVIEWED JOURNAL PAPER.....	240
CONFERENCE PAPER/AWARD	248

LIST OF FIGURES

Figure 1.1: Schematic of the work carried out in this project and the layout of this thesis. (CTA: chromotropic acid; AAP: 4-aminoantipyrine; HRP: horseradish peroxidase; ChOx: cholesterol oxidase; GLOx: glucose oxidase).....	5
Figure 2.1: Global distribution of CVD mortality rates in (A) males and (B) females (age standardised, per 100,000) (Mendis <i>et al.</i> 2011).....	7
Figure 2.2: Proportion of all deaths caused by principal disease groups in England, 2004-11 (Mellon <i>et al.</i> , 2013).....	8
Figure 2.3: Deaths by cause in the UK. Red= deaths due to CVD, Pink= other deaths (Figure taken from: Townsend <i>et al.</i> , 2012).....	9
Figure 2.4: Chemical structure of cholesterol.	11
Figure 2.5: Chemical structure of glucose (Sigma-Aldrich, 2017).	13
Figure 2.6: (A) personal glucose monitor (Abbott Laboratories, USA); (B) personal cholesterol monitor (Bioptik Technology Inc., Taiwan).	21
Figure 2.7: Lateral flow pregnancy test.....	22
Figure 2.8: (A) Typical lateral flow immunoassay format. (B) Sample is applied to the sample pad. Analyte present in the sample binds to the antibody-conjugated label, and then binds to the control line and test line to return a positive result. If the analyte is absent, the label binds only to the control line, generating a negative control result (Gubala <i>et al.</i> , 2012).....	23
Figure 2.9: (A) LOAD blood analyser; (B) Dual layer LOAD platform (Lee <i>et al.</i> , 2009)..	27
Figure 2.10: Separation of plasma from whole blood on centrifugal microfluidic LOAD platform after 30 seconds (d: depth). (Kim <i>et al.</i> , 2013).....	28
Figure 2.11: Abaxis Piccolo Xpress LOAD instrument (Abaxis.com, 2014).....	29
Figure 2.12: Paper based glucose sensor for use in a standard off-the-shelf glucose meter (Nie <i>et al.</i> , 2010).	31
Figure 2.13: A common mass produced optical disc drive (Newegg.com, 2014).	32
Figure 2.14: Optical disc drive without top casing showing internal components. (A) Disc rotation array; (B) Laser array (Ebay.com, 2014).	33
Figure 2.15: Blu-Ray drive containing two laser systems, one for Blu-Ray discs and one for CD/DVD discs (Study.com, 2014).....	34
Figure 2.16: Forces experienced by a fluid plug on a rotating disc.....	37
Figure 2.17: Illustration of centrifugal force (Calctool.org, 2008).....	37

Figure 2.18: Blood separation in a tilted channel and a straight channel. The blue arrows show how the particle sedimentation distance is shorter in a slanted than a straight channel (Kim <i>et al.</i> , 2013).....	40
Figure 2.19: Overview of solid freeform fabrication technologies used for biomedical applications. For each technique, the symbols indicate whether polymers and/ or ceramics, hydrogels and living cells have been employed (Melchels <i>et al.</i> , 2010).43	43
Figure 2.20: Basic Fused Deposition Modelling (FDM) setup (RepRap.org, 2014).	44
Figure 2.21: Stereolithography principle set up (Custompart.net, 2008).....	45
Figure 3.1: Proposed mechanism for peroxidase-catalysed formation of a quinoneimine dye (Wong <i>et al.</i> , 1981).	65
Figure 3.2: The image shows the increasing quinoneimine dye concentration observed as CTA+AAP concentration increases. Each well contains 100 μ l taken from each 1 ml sample. Each sample contains HRP (5 U/ml), H ₂ O ₂ (12 mM) and varying concentrations of CTA and AAP as follows: Line (A) CTA (0 mM), AAP (0 mM); (B) CTA (1 mM), AAP (1 mM); (C) CTA (3 mM), AAP (3 mM); (D) CTA (5 mM), AAP (5 mM); (E) CTA (6 mM), AAP (6 mM); (F) CTA (8 mM), AAP (8 mM).	67
Figure 3.3: Preliminary absorbance spectrum produced from a 1 ml sample containing HRP (5 U/ml), CTA (2 mM), AAP (2 mM) and H ₂ O ₂ (4 mM). The absorbance was measured in 100 μ l after 10 minute incubation.	68
Figure 3.4: Absorbance detected in 10 control/blank solutions containing HRP (5 U/ml), CTA (6m M) and AAP (6 mM).	69
Figure 3.5: Change in absorbance recorded at a range (0-80 mM) of CTA concentrations with H ₂ O ₂ (5 mM), HRP (6 U/ml) and AAP (10 mM) in PBS (n=3).	71
Figure 3.6: The image shows the quinoneimine dye concentration observed as CTA concentration increases. Group 1 is undiluted sample; group 2 is a 1 in 10 dilution. Each well contains 100 μ l taken from each 1 ml sample. Each sample contains HRP (6 U/ml), H ₂ O ₂ (5 mM), AAP (10 mM) and varying concentrations of CTA as follows: Line (A) 0 mM; (B) 10 mM; (C) 20 mM; (D) 30 mM; (E) 40 mM; (F) 50 mM; (G) 60 mM; (H) 70 mM; (I) 80 mM.	71
Figure 3.7: Change in absorbance recorded at a range (0-80 mM) of AAP concentrations with H ₂ O ₂ (5 mM), HRP (6 U/ml) and CTA (10 mM) in PBS (n=3). 72	72
Figure 3.8: The image shows the quinoneimine dye concentration observed as AAP concentration increases. Group 1 is undiluted sample; group 2 is a 1 in 10 dilution. Each well contains 100 μ l taken from each 1 ml sample. Each sample contains HRP (6 U/ml), H ₂ O ₂ (5 mM), CTA (10 mM) and varying concentrations of AAP as follows: Line (A) 0 mM; (B) 10 mM; (C) 20 mM; (D) 30 mM; (E) 40 mM; (F) 50 mM; (G) 60 mM; (H) 70 mM; (I) 80 mM.	73

Figure 3.9: 1 ml samples containing HRP (6 U/ml) and AAP (40 mM) in PBS after 5 minutes incubation. (A) Contains no H ₂ O ₂ ; (B) contains H ₂ O ₂ (5 mM).	74
Figure 3.10: Change in absorbance recorded at a range (0-40 mM) of CTA concentrations with H ₂ O ₂ (0-10 mM), HRP (6 U/ml) and AAP (10 mM) in PBS (n=3).	75
Figure 3.11: Change in absorbance recorded at a range (0-6 U/ml) of HRP concentrations with H ₂ O ₂ (8 mM), CTA (6 mM) and APP (6 mM) in PBS (n=3).	77
Figure 3.12: Change in absorbance recorded at a range (0-1 U/ml) of ChOx concentrations with cholesterol (2.75 mM), HRP (6 U/ml), CTA (6 mM) and AAP (6 mM) in PBS (n=3).	81
Figure 3.13: Change in absorbance recorded at a range (0-1 U/ml) of ChOx concentrations with cholesterol (5.5 mM), HRP (6 U/ml), CTA (6 mM) and AAP (6 mM) in PBS (n=3).	82
Figure 3.14: Change in absorbance recorded at a range (0-1 U/ml) of ChOx concentrations with cholesterol (7.6 mM), HRP (6 U/ml), CTA (6 mM) and AAP (6 mM) in PBS (n=3).	82
Figure 3.15: Change in absorbance recorded at a range (0-1 U/ml) of ChOx concentrations with cholesterol (8.9 mM), HRP (6 U/ml), CTA (6 mM) and AAP (6 mM) in PBS (n=3).	83
Figure 3.16: Change in absorbance recorded at a range (0-8.9 mM) of cholesterol concentrations with ChOx (1 U/ml), HRP (6 U/ml), CTA (6 mM) and AAP (6 mM) in PBS (n=3).	84
Figure 3.17: The image shows the quinoneimine dye concentration observed as cholesterol concentration increases after 5 minutes incubation. The assay contains cholesterol (0-9.3 mM), ChOx (1 U/ml), HRP (6 U/ml), CTA (6 mM) and AAP (6 mM).	85
Figure 3.18: Change in absorbance recorded at a range (0-9.3 mM) of cholesterol concentrations with ChOx (1 U/ml), HRP (6 U/ml), CTA (6 mM) and AAP (6 mM) in PBS (n=7).	86
Figure 3.19: Transparent red plasma after defibrinated whole horse blood was centrifuged at 5,000 RPM for 15 minutes.	88
Figure 3.20: Defibrinated whole horse blood after centrifugation, (A) wash 0; (B) wash 1; (C) wash 2; (D) suspended whole horse blood before (left) and after (right) washing.	89
Figure 3.21: The image shows the quinoneimine dye concentration observed as cholesterol concentration increases. (A) Colour immediately after sample application (0 minutes incubation); (B) colour after 5 minutes incubation.	90

Figure 3.22: Change in absorbance recorded at a range (0-9.3 mM) of cholesterol concentrations with ChOx (1 U/ml), HRP (6 U/ml), CTA (6 mM) and AAP (6 mM) in horse plasma (n=9).....	91
Figure 3.23: The image shows the quinoneimine dye concentration observed in whole horse blood as cholesterol concentration increases. (A) Before addition of ChOx; (B) after addition of ChOx (2 U/ml) and 5 minutes incubation.....	92
Figure 3.24: The image shows the quinoneimine dye concentration observed as cholesterol concentration increases in plasma extracted from whole horse blood.	93
Figure 3.25: Change in absorbance recorded at a range (0-12 mM) of cholesterol concentrations with ChOx (2 U/ml), HRP (12 U/ml), CTA (12 mM) and AAP (12 mM) in whole horse blood (n=6).....	93
Figure 3.26: Change in absorbance recorded at a range (0-50 U/ml) of GIOx concentrations with glucose (10 mM), HRP (6 U/ml), CTA (20 mM) and AAP (10 mM) in PBS (n=3).....	95
Figure 3.27: Glucose assay in buffer. The image shows the quinoneimine dye concentration observed as glucose concentration increases. Group 1 is undiluted sample; group 2 is a 1 in 10 dilution. Each well contains 100 µl taken from each 1 ml sample. Each sample contains GIOx (20 U/ml), HRP (6 U/ml), CTA (20 mM), AAP (10 mM) and varying concentrations of glucose as follows: Line (A) 0 mM; (B) 1 mM; (C) 2 mM; (D) 3 mM; (E) 4 mM; (F) 5 mM; (G) 6 mM; (H) 7 mM; (I) 8 mM; (J) 9 mM; (K) 10 mM.....	97
Figure 3.28: Change in absorbance recorded at a range (0-10 mM) of glucose concentrations with GIOx (20 U/ml), HRP (6 U/ml), CTA (20 mM) and AAP (10 mM) in PBS (n=3).....	97
Figure 3.29: Change in absorbance recorded at a range (0-10 mM) of glucose concentrations with GIOx (20 U/ml), HRP (6 U/ml), CTA (20 mM) and AAP (10 mM) in PBS (n=3).....	98
Figure 4.1: Ultimaker 2+, (A) 3D-printer; (B) print head/extruder (Ultimaker Ltd., 2014).	104
Figure 4.2: 3D-printing protocol followed in this thesis.....	106
Figure 4.3: Instrumentation used to measure attenuation.	110
Figure 4.4: Schematic of instrumentation used for optical coherence tomography (Thorlabs Inc., 2007).....	111
Figure 4.5: Schematic of plastic sample.	112
Figure 4.6: Schematic of the microfluidic channel. (A) Channel specifications; (B) cross-sectional specifications.....	113

Figure 4.7: Attenuation measured at a wavelength of 633 nm in 400 μ m thick plastic samples made from Ultimaker PLA Translucent using 6 different layer-heights (n=3).....	116
Figure 4.8: Attenuation in Ultimaker PLA Translucent plastic samples made with 3 different layer heights at 3 different speeds (n=3).	118
Figure 4.9: Illustration of squashed filament strand (bead) compared to traditional circular strand (bead) (Dolomite, 2016).....	120
Figure 4.10: Attenuation in Ultimaker PLA Translucent plastic samples made with two different print head to build table distances (n=3).	121
Figure 4.11: Plastic samples printed on a machine with calibrated and uncalibrated print head to build table distance. (A) Calibrated (< 0.05 mm); (B) Uncalibrated (0.25 mm).	122
Figure 4.12: Microscope pictures taken of plastic samples printed on a machine with calibrated (< 0.05 mm) and uncalibrated (0.25 mm) print head to build table distance. (A) calibrated 5x magnification; (B) calibrated 10x magnification; (C) calibrated 20x magnification; (D) uncalibrated 5x magnification; (E) uncalibrated 10x magnification; (F) uncalibrated 20x magnification.....	123
Figure 4.13: Changes in the attenuation of Ultimaker PLA Translucent plastic samples exposed to acetone vapour for a range of durations (n=3).	124
Figure 4.14: Images of plastic samples after acetone vapour treatment. As exposure time increases, warping and clouding increase. Exposure time: (A) 5 seconds; (B) 10 seconds; (C) 20 seconds; (D) 30 seconds; (E) 40 seconds; (F) 50 seconds; (G) 60 seconds.	126
Figure 4.15: Microscope pictures taken of plastic samples after acetone vapour treatment (5 x magnification). Exposure time: (REF) 0 seconds; (A) 5 seconds; (B) 10 seconds; (C) 20 seconds; (D) 30 seconds; (E) 40 seconds; (F) 50 seconds; (G) 60 seconds.	126
Figure 4.16: Change in attenuation in Ultimaker PLA Translucent plastic samples exposed to acetone solution of increasing concentration (n=3).	127
Figure 4.17: Images of plastic samples after acetone liquid treatment and microscope pictures (5 x magnification). As acetone concentration increases clouding increases. Concentration: (A) 0%; (B) 20%; (C) 40%; (D) 60%; (E) 80%; (F) 100%.128	
Figure 4.18: Optical disc drive spindles. (A) with disc locking clips (Study.com, 2014); (B) without disc locking clips (Ausgamestore.com, 2008).	130
Figure 4.19: Schematic of first LOAD device. (A) Disc specifications and channel layout; (B) channel specifications; (C) pore schematic; (D) cross-sectional specifications.	132

Figure 4.20: Angled view of printed disc faces to show different surface quality. (A) The surface of plate 1; (B) The surface of plate 3.	133
Figure 4.21: (A) Schematic of circular channel. (B) Illustration of how strands are deposited to form the channel. (C) Microscope pictures taken of circular channel samples (5 x magnification).....	135
Figure 4.22: (A) Schematic of triangular channel; (B) Illustration of how strands are deposited to form the channel. (C) Microscope picture taken of triangular channel sample (5 x magnification).	136
Figure 4.23: Microscope pictures taken of square channel samples printed with extrusion temperature at 200 °C (5 x magnification). (A) 2 mm ² ; (B) 1 mm ² ; (C) 0.5 mm ²	138
Figure 4.24: Schematic of second LOAD device, channel capacity ~23 µl. (A) Device specifications and channel layout; (B) channel specifications; (C) cross-sectional specifications.	139
Figure 4.25: (A) 3D-printed LOAD device printed using PLA Translucent; (B) LOAD channels filled with red dye solution to illustrate improved optical transparency and successful formation of imbedded microfluidic channels.	140
Figure 4.26: Time lapse series to quantify fluid loss from disc channels; (A) 0 hours; (B) 12 hours; (C) 24 hours.	142
Figure 4.27: OCT image of 3D-printed channel sample (schematic: section 4.3.5).	145
Figure 4.28 : (A) Schematic of channel sample. (B) OCT images of channel samples printed using schematic (A).	146
Figure 4.29: OCT image of channel surface with surface roughness features highlighted.	147
Figure 4.30: OCT images focused on channel surface, pre and post acetone treatment.	150
Figure 5.1: Schematic of the microfluidic device.	160
Figure 5.2: Instrumentation used for spectral analysis.	161
Figure 5.3: Schematic of the 3D-printed centrifuge pellet.....	162
Figure 5.3: Generic optical disc drive with 3D-printed LOAD device placed on top of a data disc.....	164
Figure 5.5: Microfluidic cuvette, (A) before glucose assay; (B) after glucose assay. Also shown are microfluidic cuvettes prepared with, (C) 100 µm thick chamber; (D) S shaped channel.....	166
Figure 5.5: Change in the quinoneimine dye absorbance spectra with glucose concentration. Glucose (0-10 mM), CTA (20 mM), AAP (10 mM), GLOx (20 U/ml)	

and HRP (6 U/ml) in PBS solution. The assay was read after 2 minute incubation. Assay performed in 500 μ m pathlength cuvette.	167
Figure 5.7: Difference in the absorbance of glucose concentration at 590 nm and 650 nm, n=3. Glucose (0-10 mM), CTA (20 mM), AAP (10 mM), GLOx (20 U/ml) and HRP (6 U/ml) in PBS solution. The assay was read after 2 minute incubation. ...	168
Figure 5.8: Absorbance comparison between 3D printed microfluidic device and well plate reader, n=3. Glucose (0-10 mM), CTA (20 mM), AAP (10 mM), GLOx (20 U/ml) and HRP (6 U/ml) in PBS solution. The assay was read after 2 minute incubation.....	169
Figure 5.9: Glucose assay in whole blood samples, red cell mass is visible in the base of the tube. Glucose concentrations: (A) 0 mM; (B) 2 mM; (C) 4 mM; (D) 6 mM; (E) 8 mM; (F) 10 mM.....	171
Figure 5.10: The glucose assay in whole blood read in a 500 μ m path length microfluidic cuvette device, n=3. Glucose (0-10 mM), CTA (20 mM), AAP (10 mM), GLOx (20 U/ml) and HRP (6 U/ml) in defibrinated whole horse blood. The assay was read after 2 minute incubation.	171
Figure 5.11: Difference as a percentage of intensity in the spectra of 3D printed cuvette devices compared to a PMMA cuvette.	173
Figure 5.12: Batch 1 Pellet containing whole horse blood, (A) before centrifugation; (B) after centrifugation, (left) partial success with 25% of the blood sample remaining and separated, (right) 100% of blood sample leaked out of the pellet.	176
Figure 5.13: Batch 2 Pellet containing whole horse blood, (A) before centrifugation; (B) after centrifugation.	177
Figure 5.14: Heat-treated pellets containing whole horse blood after centrifugation. Warping to structure and clouding of the plastic is visible.....	179
Figure 5.15: PLA LOAD microfluidic device with channels filled with whole horse blood, (A) before centrifugation; (B) after centrifugation for ~ 5 seconds.	182
Figure 5.16: (A) PLA LOAD microfluidic device before heat-treatment; (B) PLA LOAD device after heat-treatment at 60 $^{\circ}$ C for 2 hours.....	183
Figure 5.17: PLA LOAD microfluidic device containing whole blood following heat-treatment at 60 $^{\circ}$ C for 2 hours. (A) before centrifugation; (B) after ~ 5 seconds centrifugation.	184
Figure 5.18: PLA LOAD microfluidic device after excess duration (>24 hours) heat-treatment at 60 $^{\circ}$ C, (A) without red dye; (B) with red dye.	185
Figure 5.19: Illustration of channels printed (A) orthogonal to the build table; (B) parallel to the build table. The arrow indicates motion of fluid when centrifugal force is applied.	188

Figure 5.20: LOAD device as seen in Cura software. (A) 0.41 mm shell thickness; (B) 2 mm shell thickness.	189
Figure 5.21: PLA LOAD device containing whole blood. (A) before centrifugation; (B) after ~ 5 second centrifugation; (C) after excess duration (> 24 hours) heat-treatment at 60 °C before centrifugation; (D) after excess duration (> 24 hours) heat-treatment at 60 °C after ~ 5 second centrifugation.	191
Figure 5.22: 2 mm shell thickness PLA LOAD device containing whole blood after excess duration (> 24 hours) heat-treatment at 60 °C, (A) before centrifugation; (B) after ~ 5 seconds centrifugation; (C) successful blood separation in microfluidic LOAD channel; (D) unsuccessful channel.	193
Figure 5.23: Illustration of channels printed with varying layer heights: (A) 0.06 mm; (B) 0.1 mm; (C) 0.2 mm.	194
Figure 5.24: 0.1 mm layer height PLA LOAD device containing whole blood, (A) before centrifugation; (B) after ~ 5 seconds centrifugation; (C) blood separation in microfluidic LOAD channel.	195
Figure 5.25: 0.1 mm layer height PLA LOAD device containing whole blood after 60 °C heat-treatment for 2 hours, (A) before centrifugation; (B) after ~ 5 seconds centrifugation; (C) blood separation in microfluidic LOAD channel.	196
Figure 5.26: 0.1 mm layer height PLA LOAD device containing whole blood, (A) before centrifugation; (B) after ~ 10 seconds centrifugation; (C) blood separation and colour generation in microfluidic LOAD channel.	198
Figure 5.27: 0.1 mm layer height PLA LOAD device containing whole blood after 60 °C heat-treatment for 2 hours, (A) before centrifugation; (B) after ~ 5 seconds centrifugation; (C) blood separation and colour generation in microfluidic LOAD channel.	199
Figure 5.28: 0.06 mm layer height PLA LOAD device containing whole blood after excess duration (>24 hours) heat-treatment at 60 °C, (A) before centrifugation; (B) after ~ 5 seconds centrifugation; (C) blood separation and colour generation in microfluidic LOAD channel; (D) comparison of whole blood separation without assay reagents (left) and with assay reagents (right).....	200
Figure 5.29: Schematics of final LOAD design, channel capacity ~23 µl. (A) Device specifications and channel layout; (B) channel specifications; (C) pore specifications; (E) cross-sectional specifications.....	202

LIST OF TABLES

Table 3.1: Cholesterol solution concentration as prepared and the concentration stated using an Easy Touch GC monitor (Bioptik Technology, Taiwan) approx. 10 minutes after preparation (n=6).....	80
Table 4.1: Quick reference of differences between ABS and PLA (English, 2012).....	107
Table 4.2: Reference of thermal properties of ABS and PLA (Grieser, 2016).	108
Table 4.3: Reference of material properties of ABS and PLA (Makeitfrom.com, 2017).	108
Table 4.4: Mean deviation (R_a) of channel surface trace from the ideal surface (μm).148	
Table 4.5: Root mean squared deviation (R_q) of channel surface trace from the ideal surface (μm).....	149
Table 4.6: Peak to valley distance (PV) (μm).	151
Table 4.7: Root mean squared deviation (R_q) of channel surface trace from the average surface (R_a) (μm).....	152
Table 5.1: Intra-filament (%) CV	174
Table 5.2: Blood sample (%) remaining in 3D-printed PLA microfluidic pellet after centrifugation for 2 minutes at 6000 RPM.....	178
Table 5.3: Blood sample (%) remaining in 3D-printed PLA microfluidic pellet after centrifugation for 2 minutes at 6000 RPM following heat-treatment at 60 °C for 2 hours.....	180
Table 5.4: Summary of passive fluid loss over time following heat-at 60 °C.	186

LIST OF EQUATIONS

Equation 1: $F_c = r\omega^2m$	37
Equation 2: $FC = r\omega^2VP(PP - Pl)$	38
Equation 3: $Fr = -6\pi\eta lrP\mu$	38
Equation 4: $u = sPr\omega^2$	38
Equation 5: $SP = mP6\pi\eta lrP(1 - plpP)$	38
Equation 6: $v = -v_01 + hwsin\theta$	39
Equation 7: <i>cholesterol + O₂ChOxcholest - 4 - en - 3 - one + H₂O₂</i>	55
Equation 8: <i>CTA + AAP + 2H₂O₂HRP quinoneimine dye + 4H₂O</i>	55
Equation 9: <i>glucose + H₂O + O₂GlOx gluconic acid + H₂O₂</i>	55
Equation 10: $A = \log oI $	66
Equation 11: $100VT - i = 1NVxiVT$	141
Equation 12: $Ra = 1Ni - 1Nyi$	144
Equation 13: $Rq = 1Ni = 1Nyi^2$	144
Equation 14: $LoD = 3.3SyS$	170

LIST OF ABBREVIATIONS

AAP	4-Aminoantipyrine
ABS	Acrylonitrile butadiene styrene
ATP	Adenosine triphosphate
CAD	Computer-aided design
CHD	Coronary heart disease
ChOx	Cholesterol oxidase
CTA	Chromotropic acid
CVD	Cardiovascular disease
%CV	Coefficient of Variation (%)
DM	Diabetes mellitus
DM-2	Type-2 diabetes mellitus
FDM	Fused deposition modelling
GLOx	Glucose oxidase
HDL	High-density lipoprotein
HRP	Horseradish Peroxidase
LDL	Low-density lipoprotein
LFA	Lateral Flow Assay
LOAD	Lab-on-a-disc
M	Molar concentration
OCT	Optical coherence tomography
ODD	optical disc drive
PLA	Poly[lactic acid]
PMMA	Poly[methylmethacrylate]
PV	Peak to valley distance
Ra	Arithmetic average deviation
Rq	Root mean squared deviation

Chapter 1: Introduction

1.1 Rationale for the Research

The increasing burden being placed on health care services by an aging population, obesity epidemic and diabetes epidemic (NICE, 2012) is creating the necessity for point-of-care (POC) testing for serious pathologies like cardiovascular disease and diabetes (Tang *et al.*, 2007). However, the inaccuracy of presently available POC diagnostic devices relative to lab based assays, and their frequent limitation to a single analyte means that disease diagnosis continues to rely on the quantification of a panel of blood-based biomarkers utilising laboratory assays and equipment. Whilst lab-on-a-disc (LOAD) devices seek to solve this problem, the current commercial devices available are expensive, often in excess of £10,000, rendering them outside the budget of many institutions.

The advance of solid freeform fabrication techniques, such as 3D-printing, has significantly improved the ability to prepare solid structures with precise geometries (Hutmacher *et al.*, 2004), including internal cavities, facilitating the rapid production of analytical platforms and the ability to alter or redesign any aspect without significantly inflating costs. While the use of 3D-printing to produce cost-effective tools for biomedical applications has significant potential (Cohen *et al.*, 2006; Ballyns *et al.*, 2009), to-date its use in the optical and biosensors field has been limited. The 3D-printing instruments utilised in the manufacture of devices for biomedical applications can cost in excess of £150,000 and the materials are not readily available for public use, causing the technology to be inaccessible for the majority of establishments. In addition, the devices require post-print finishing including cleaning and polishing using sand paper and water to achieve the correct finish and acceptable levels of optical transparency for use (Chen *et al.*, 2014). The necessity of post-print finishing techniques such as physical removal of material and polishing to improve 3D-printed devices greatly limits the potential for use in optical microfluidic devices, especially those with inaccessible microfluidic channels, regardless of the 3D-printer quality. This emphasises the need for the development of accessible and affordable

prototyping technology and post-print finishing techniques suitable for biomedical microfluidics.

Low-cost (< £2000) fused deposition modelling (FDM) 3D-printing technology is widely accessible, with a range of printing materials readily available from multiple sources. However, low-cost FDM 3D-printed optical assay platforms can suffer from the poor optical properties and performance of polymers available (Ho *et al.*, 2015). Poor optical transparency is a fundamental obstacle that must be overcome for the technology to progress because of its impact on sensing performance. In addition, the low quality of objects manufactured by low-cost FDM 3D-printers render them unsuitable for use in a medical or diagnostic setting; POC devices rely heavily on microfluidic channels to control sample volume, reagent mixing and flow rate (Heller and Feldman, 2010; Gubala *et al.*, 2012), and so far low-cost FDM 3D-printers have been incapable of constructing imbedded microfluidic channels suitable for use in a diagnostic setting (Au *et al.*, 2014).

The primary aim of this research is to investigate the feasibility of the use of low-cost FDM 3D-printing technology to develop a microfluidic LOAD device based on a digital versatile disc (DVD) for the rapid quantification of blood based analytes. The device should be capable of centrifuging whole blood to give clear plasma that can then be used for colourimetric quantitative assays and for the detection of biomarkers. The intention is that the device should be capable of using an unmodified optical disc drive (ODD) to operate as a low-cost reader. This would aid in the diagnosis and prognosis of disease states without the need for samples to be sent to a dedicated laboratory as well as being able to perform multiple assays on a single platform, something which few existing POC devices are capable of. Elevated cholesterol and glucose concentrations are linked to the progression of serious diseases such as cardiovascular disease (CVD) and diabetes mellitus (DM); consequently, they are widely screened for and quantified across the world. Cholesterol and glucose will be used as model markers to demonstrate the functionality of the LOAD device developed in this work.

1.2 Aims and Objectives

The aim of this project is to design, develop and produce multiple imbedded microfluidic channels in a LOAD assay device with sufficient optical transparency that optical assays can be performed within. The device is intended to be capable of separating plasma from whole blood via centrifugation in ≤ 2 minutes to be competitive with existing centrifugal blood separation systems (Moen *et al.*, 2016), and to be used with an unmodified ODD. It is hoped, that if successful, the combination of low-cost ($< \pounds 2000$) FDM 3D-printing technology with a microfluidic LOAD device could provide POC functionality, portability and affordability. In addition, quantitative colourimetric assays for glucose and cholesterol will be developed and optimised for use within the low-cost FDM 3D-printed microfluidic devices, to demonstrate the functionality and capability of such devices. In line with being able to use an unmodified ODD as a reader device, the assays should have absorbance (A) in the 650 nm region, the wavelength of a DVD laser.

Three fundamental principles must be demonstrated and proven to establish the feasibility of using low-cost FDM 3D-printing technology as a means of developing and manufacturing microfluidic LOAD assay devices for use with whole blood samples.

1. Imbedded microfluidic channels can be formed.
2. Quantitative whole blood optical assays can be performed in the 3D-printed microfluidic device.
3. Separation of plasma from whole blood via centrifugation can be performed in the 3D-printed microfluidic device.

If these three principles can be established, there is the potential for developing a LOAD device using low-cost FDM 3D-printing technology that is capable of performing centrifugation based whole blood separation and optical assays in microlitre blood volumes. The LOAD device will then be demonstrated for glucose detection.

A systematic outline of the project and the thesis structure can be seen in Figure 1.1.

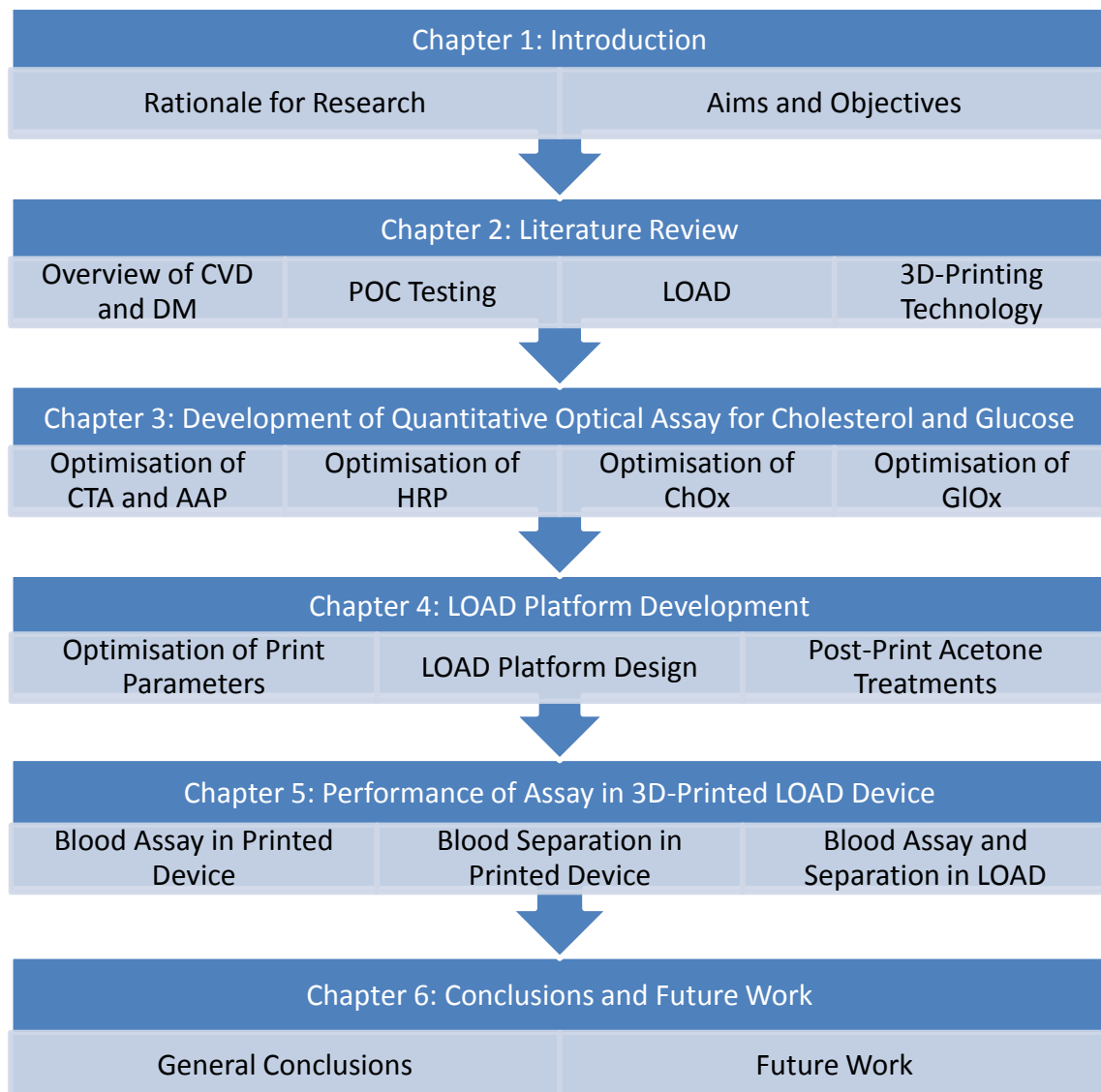


Figure 1.1: Schematic of the work carried out in this project and the layout of this thesis. (CTA: chromotropic acid; AAP: 4-aminoantipyrine; HRP: horseradish peroxidase; ChOx: cholesterol oxidase; GLOx: glucose oxidase).

Chapter 2: Literature Review

2.1 An Overview of Cardiovascular Disease and Diabetes Mellitus

Cardiovascular disease (CVD) is listed as the primary cause of death world-wide by The World Health Organisation (World Health Organisation, 2013). In 2008 an estimated 17.3 million deaths were related to CVDs equating to 30% of all deaths globally, with 7.3 million and 6.2 million deaths being due to coronary heart disease (CHD) and stroke respectively. It is estimated that deaths due to CHD and stroke alone will increase to 23.3 million by 2030 and that CVD will remain the leading cause of death in the world. Figure 2.1, shows the global distribution of reported CVD mortality rates in males and females.

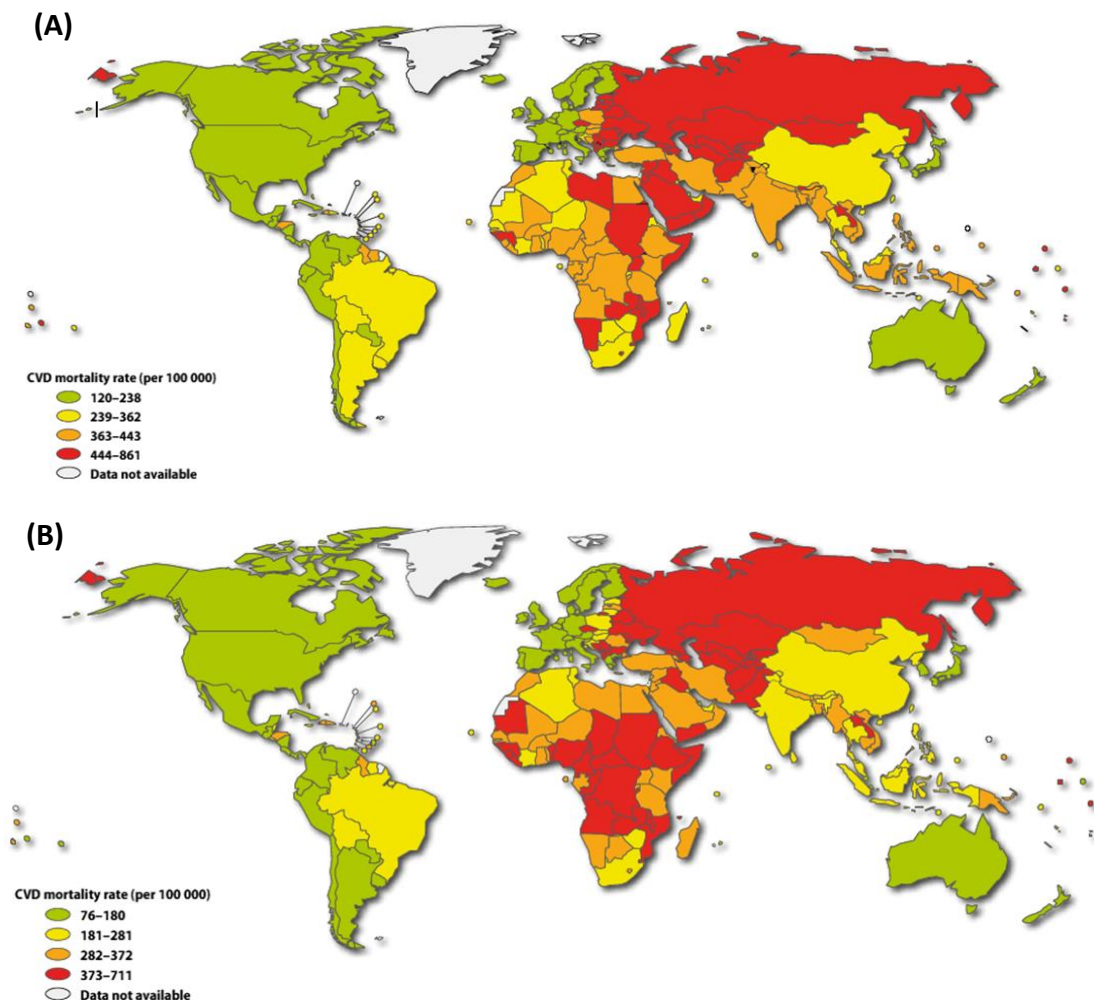


Figure 2.1: Global distribution of CVD mortality rates in (A) males and (B) females (age standardised, per 100,000) (Mendis *et al.* 2011).

The majority of CVDs are easily preventable with appropriate and early intervention by addressing the major risk factors such as type-2 diabetes mellitus (DM-2), hypercholesterolemia, smoking and other tobacco use, poor diet and obesity, physical inactivity and hypertension (World Health Organisation, 2013). Although the number of deaths due to CVD has been declining steadily in England as shown by Figure 2.2, the prevalence of CVD related ailments is increasing (Scarborough *et al.*, 2011) with over three million people currently suffering from CVD and over 25% of deaths caused by some form of CVD as shown in Figure 2.3. This costs the UK over £30 billion annually, however, 80%-90% of premature CVD is preventable and easily treatable if intervention is implemented early enough (Capewell *et al.*, 2008).

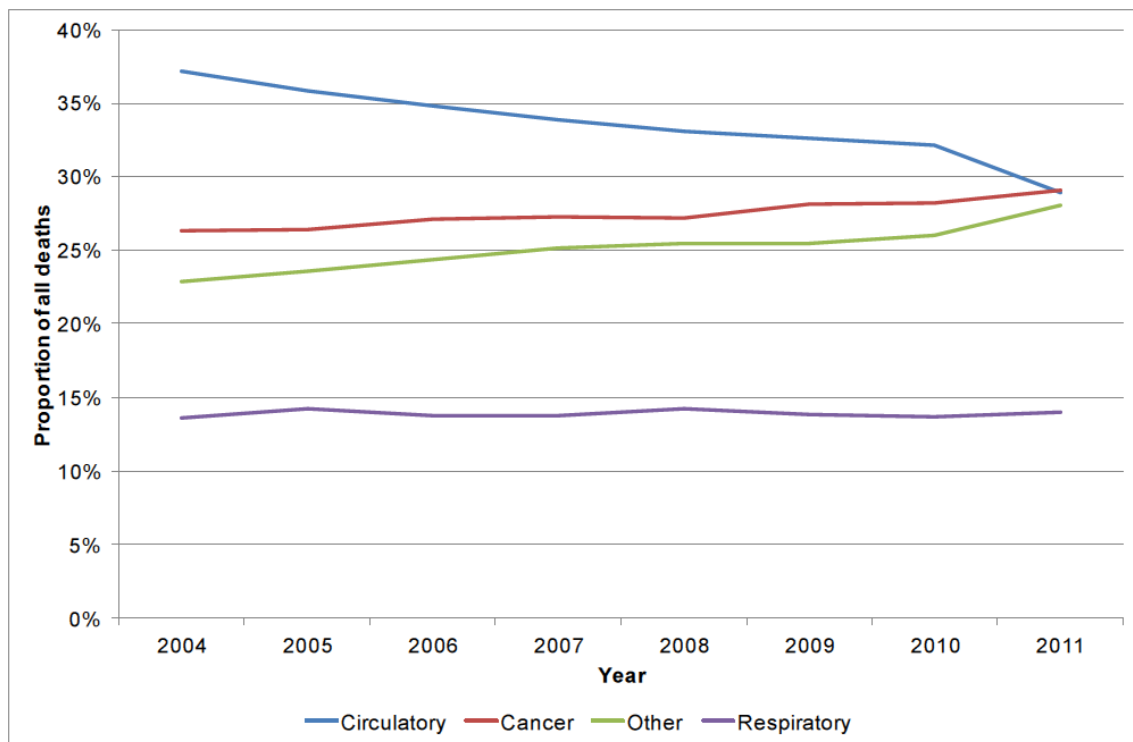
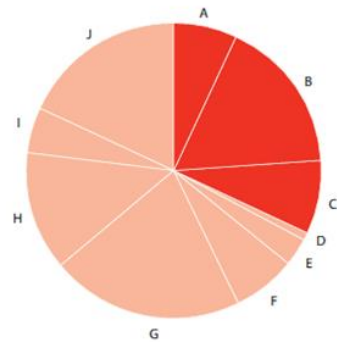


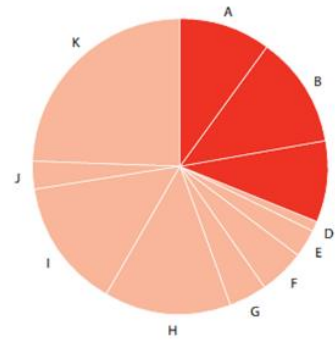
Figure 2.2: Proportion of all deaths caused by principal disease groups in England, 2004-11 (Mellon *et al.*, 2013).

Deaths by cause in men, United Kingdom 2010



- A. Stroke (7%)
- B. Coronary heart disease (17%)
- C. Other cardiovascular disease (8%)
- D. Diabetes (1%)
- E. Colo-rectal cancer (3%)
- F. Lung cancer (7%)
- G. Other cancers (21%)
- H. Respiratory disease (13%)
- I. Injuries and poisoning (5%)
- J. All other causes (18%)

Deaths by cause in women, United Kingdom 2010



- A. Stroke (10%)
- B. Coronary heart disease (12%)
- C. Other cardiovascular disease (9%)
- D. Diabetes (1%)
- E. Colo-rectal cancer (3%)
- F. Lung cancer (5%)
- G. Breast cancer (4%)
- H. Other cancers (14%)
- I. Respiratory disease (14%)
- J. Injuries and poisoning (3%)
- K. All other causes (24%)

Figure 2.3: Deaths by cause in the UK. Red= deaths due to CVD, Pink= other deaths (Figure taken from: Townsend *et al.*, 2012).

Diabetes mellitus (DM) is the most common endocrine disorder of carbohydrate metabolism. It is a lifelong condition where a person's body is unable to regulate blood glucose levels due to either lack of insulin production (type-1 diabetes) or resistance to insulin (type-2 diabetes). Worldwide, it is a leading cause of morbidity and mortality and a major health problem for most developed societies. The prevalence of diabetes continues to increase; the World Health Organization (WHO) estimated that 71 million people worldwide were living with diabetes in 2000, and predicted the number to rise to 366 million by 2030 (Wild *et al.*, 2004). A more recent WHO study states that the number of people with diabetes has already surpassed these predictions and that it had risen to 422 million in 2014. The study also shows that the global prevalence of diabetes in people over 18 years of age was 8.5% in 2014. A sedentary lifestyle combined with changes in eating habits and the increasing

frequency of obesity is thought to be the major causes of such increased rates (World Health Organisation, 2016).

While treatment for diabetes varies according to type and severity, all patients are recommended to check regularly their blood glucose levels. Frequency of testing varies according to the patient but a type-1 diabetic would be expected to test at least 4 times a day. The primary diagnostic tool for patients living with diabetes is the personal blood glucose monitor (Skeie *et al.*, 2009; Tunis and Minshall, 2010). The aim of regular blood glucose testing is to provide real-time information for patients to modify medications, change dietary intake, and adjust physical activity in order to achieve glycaemic goals (Boutati and Raptis, 2009; American Diabetes Association, 2010) and to help the patient maintain normal blood glucose levels. Failure to maintain normal blood glucose levels can lead to nephropathy, neuropathy, and retinopathy, and is a large risk factor for CVD (Matthews and Neil, 2008).

Due to the increasing effectiveness of the pharmacological treatment that is used as an intervention for type-2 diabetes, the survival rate has improved. However this has led to increased prevalence of type-2 diabetes especially in developed countries (Støvring *et al.*, 2003). Without proper implementation of dietary changes and increased physical activity to reduce obesity in type-2 diabetics this will inevitably result in increasing proportions of deaths from cardiovascular disease in these countries, as well as increased prevalence and associated consequences of other complications of diabetes (Wild *et al.*, 2004).

Cholesterol and glucose quantification have become routine in healthcare examinations (Plessis *et al.*, 2000); they are well documented molecules with quantitative assays for both laboratory and POC use. Cholesterol and glucose are ideal example markers and therefore will be used to demonstrate the functionality of the LOAD test system that is to be developed in this project.

2.1.1 Cholesterol

Cholesterol, cholest-5-en-3 β -ol, is a steroid lipid, Figure 2.4, that is found naturally in blood and body tissues, especially liver, spinal cord, and brain. The majority of the cellular cholesterol is found in the cell membrane as an important structural molecule where it comprises approximately 45% of the total lipid (Girotti, 2002) and is involved in many biochemical processes (Hanukoglu, 1992). It is used in the synthesis of vitamin D, steroid hormones including cortisol, cortisone and aldosterone, and sex hormones including progesterone, oestrogen, and testosterone and used in the formation of nerve myelin (Pawlina and Ross, 2007). However due to increasingly unhealthy diet and passive lifestyle, sustained elevated levels have become synonymous with cardiovascular disease (Wilson, 2016).

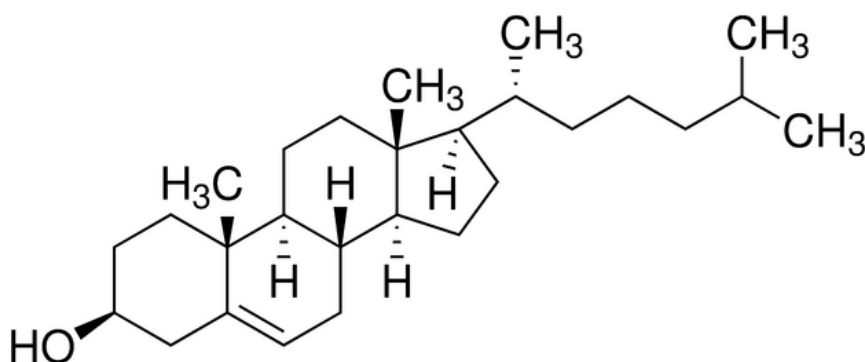


Figure 2.4: Chemical structure of cholesterol.

Cholesterol is insoluble in water and blood, therefore, it circulates within the lipoproteins low-density lipoprotein (LDL) and high-density lipoprotein (HDL). Lipoprotein particles, known as chylomicrons, transport a mix of dietary lipids including triglycerides (85–92 %), phospholipids (6–12 %), cholesterol (1–3 %) and proteins (1–2 %) from the gastrointestinal tract to the liver and other body sites (Hussain, 2000). Cholesterol is produced mainly in the liver from acetyl coenzyme A (CoA) via the HMG-CoA reductase pathway (Mehta, 2013), at approximately 1 g a day (Freeman and Junge, 2005); other locations include adrenal glands, reductive organs and the

intestines. In the liver cholesterol is converted into LDL, which carries cholesterol to the body cells, HDL carries it back to the liver for excretion (American Heart Association, 2014).

Animal fats are a mix of triglycerides, phospholipids and cholesterol (Berry, 2004), and major dietary sources of cholesterol include cheese, egg yolk, and meat high in fat. Cholesterol is not found in plant sources in significant quantities as far as diet goes (Behrman and Gopalan, 2005). Fat intake via diet affects blood cholesterol levels. Diets high in unsaturated fat have been shown to have lower serum LDL and total cholesterol levels and higher HDL serum levels; diets high in saturated fat displayed higher LDL, HDL and total cholesterol levels (Mensink and Katan, 1992). Due to the link that has been established between low HDL and high LDL in cardiovascular disease prevalence, many public health bodies recommend reduction of LDL cholesterol via dietary and lifestyle changes (NHS UK, 2013). The production of cholesterol in the body is directly regulated by current cholesterol levels, increased cholesterol intake via food leads to decreased endogenous production. The primary mechanism for cholesterol regulation is detection of intracellular cholesterol in the endoplasmic reticulum by sterol regulatory element binding protein 1 and 2. In the 1970s the work performed by Dr Michael S. Brown and Dr Joseph L. Goldstein shed light on large sections of the signalling pathway for which they won the 1985 Nobel Prize in Physiology or Medicine (Nobelprize.org, 2014). Cholesterol is removed from the body through oxidation in the liver into bile acids which are then excreted in bile (Javitt, 1994). As a monounsaturated lipid cholesterol is vulnerable to oxidation, one of the products is hydrogen peroxide which is usually the molecule being detected by existing cholesterol assays (Temani *et al.*, 2014).

Numerous methodologies exist for the quantification of cholesterol, often involving chemical and enzyme based assays (Brahim *et al.*, 2001; Singh *et al.*, 2004). It has been stated by Singh *et al.* (2004) that chemical reaction based cholesterol assays have commonly suffered interference from lack of specificity and selectivity and required the use of corrosive agents (Singh *et al.*, 2006), in comparison, enzymatic

methods utilising cholesterol oxidase (ChOx) provide advantages to both selectivity and specificity.

The following cholesterol blood levels are generally regarded as desirable (NHS UK, 2013a):

- Total cholesterol (TC): ≤ 5.0 mM (2 mg/ml) for health adult.
- Low-density lipoprotein (LDL) cholesterol after an overnight fast: ≤ 3.0 mM
- High-density lipoprotein (HDL) cholesterol: ≥ 1.2 mM
- TC/HDL ratio: ≤ 4.5 .

2.1.2 Glucose

Glucose, also known as D-(+)-glucose, Figure 2.5, is an important carbohydrate in human metabolism (hyperphysics, 2016) and fuel source in biological systems; it is utilised through aerobic respiration, anaerobic respiration or fermentation. Glucose has 6 carbon atoms so is classed as a hexose monosaccharide.

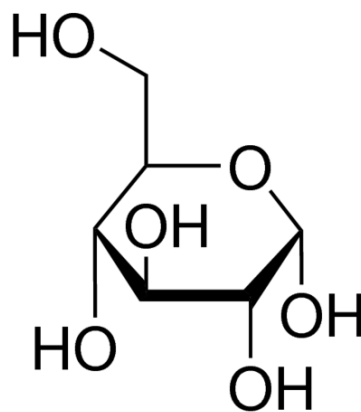


Figure 2.5: Chemical structure of glucose (Sigma-Aldrich, 2017).

The human body utilizes glucose through aerobic respiration; glucose is metabolised and oxidised in the body via glycolysis, the Krebs cycle/citric acid cycle and oxidative phosphorylation to form CO_2 , water and energy primarily in the form of

adenosine triphosphate (ATP). Approximately 3.75 kilocalories (16 kilojoules) of food energy is produced per gram of glucose (Food and Agriculture Organization, 2003). Glucose requires no digestion and therefore can be provided intravenously as a nutrient if required, for example in hospitals. Glucose is on the WHO list of essential medicines, the most important medications required in a basic health system (World Health Organisation, 2015). It is made during photosynthesis from water and carbon dioxide, using energy from sunlight.

The majority of dietary carbohydrate often contains glucose, either as the only constituent (such as the polysaccharides starch and glycogen), or bonded with another monosaccharide (such as sucrose, which is a disaccharide of glucose with fructose, or lactose, which is a disaccharide of glucose with galactose) (Harvard School of Public Health, 2016). Glucose polysaccharides are broken down to monosaccharides in the duodenum and small intestine by pancreatic and intestinal glucosidases (Ferraris, 2001); glucose is then transported into the blood stream.

Following absorption, most glucose is absorbed and stored by the liver, adipose tissue and muscle cells under the influence of insulin. Insulin and glucagon are the most well-known of the glucoregulatory hormones (Aronoff *et al.*, 2004). Insulin allows the body's cells to absorb and use glucose, decreasing blood glucose levels. Without it, glucose cannot enter the cell and therefore cannot be used as fuel for the body's functions (Hormone.org, 2017). Glucagon causes the liver cells to increase blood glucose levels by promoting the conversion of glycogen to glucose which is released into the blood stream. Typical blood glucose concentration is approximately 4-7 mM however it can become raised in people with diabetes (Diabetes.co.uk, 2017). As a result of its importance in human health, glucose is an analyte in common medical blood tests (Clarke and Foster, 2012).

The following glucose blood levels are generally regarded as desirable for adults with type 1 diabetes (Diabetes UK, 2015):

- On waking: 5-7 mM
- Before meals: 4-7 mM

- 90 minutes after meals: 5-9 mM

The ever increasing population of diabetic patients in combination with the essential requirement to maintain normal blood glucose levels has resulted in glucose sensors leading the biosensor market (Yoo and Lee, 2010). The glucose biosensor market is predicted to reach £24 billion by 2022 (Grand View Research, 2016). The glucose level meters are most commonly calibrated for blood-plasma, have a small sample requirement of 0.3-1.5 μl and have quick time to result, <10 seconds. Despite being the most accurate blood glucose assay methodology, laboratory analysis is unsuited for regular patient testing due to the time, cost and facility requirements. Therefore POC testing is usually used in both inpatient and outpatient environments. Enzyme based screen-printed electrodes are the most common form of disposable POC glucose biosensors (Yoo and Lee, 2010). They are cheap (£20-£30 per box of 50 strips) and are used in conjunction with a digital meter, often no bigger than a mobile phone.

2.2 Point-of-Care (POC) Testing

With healthcare education improving and the public becoming more aware of their health and the long term effects of poor lifestyle and diet, the use of POC testing and home testing devices has become popular for risk monitoring and management (Ryan *et al.*, 2010). The ability to give a patient an accurate measurement of their glucose or cholesterol in their homes or in a doctor's surgery without the need for time consuming laboratory testing can help identify disease states such as hypercholesterolemia or diabetes earlier before permanent damage has occurred (Von Lode, 2005).

The importance of early identification of elevated cholesterol or glucose levels can be the difference between life and death. CVD has no early warning signs, therefore minimising modifiable risk factors and tracking those which can be quantified, such as blood cholesterol levels, is vital for improving prognosis and

reducing disease prevalence. The difficulty in diagnosing CVD puts additional pressure on the ability to monitor early risk-factors, such as elevated blood cholesterol levels and monitoring the development of diabetic states through blood glucose levels. Diabetic patients have much more immediate requirements for disease monitoring. Hyperglycaemia if left untreated can lead to coma and death within days and hypoglycaemia if left untreated will lead to coma and death within hours (Diabetes.co.uk, 2017).

When developing assays for the detection of biomarkers, sensitivity, specificity and short turn-around time is important, to allow results to be available within a clinically useful timeframe (Qureshi *et al.*, 2012). These assays should be readily available on a wide range of analytical platforms and should be relatively inexpensive. Target turnaround times should be less than 1 hour from blood collection to the reporting of results (Weber *et al.*, 2005).

Point-of-care (POC) diagnostic tests are described as in-vitro tests at or near the site of patient care that do not require trained laboratory staff or equipment to generate diagnostic data (Leedsth.nhs.uk, 2014). POC testing can be used for quantification or identification of proteins, nucleic acids, metabolites, drugs, dissolved ions and gases, human cells and microbes in samples of blood, saliva, urine, or other bodily fluids or (semi)solids (Gubala *et al.*, 2012). Capable of being used in a healthcare setting, patient home or in field conditions, POC tests are rapidly becoming the first choice for patient diagnostics as these tests are simple to use, sometimes capable of detecting multiple analytes (Birtwell and Morgan, 2009; Schudel *et al.*, 2011), accept a sample with little or no pre-preparation and provide a result in seconds to hours (Meagher *et al.*, 2008).

Result interpretation is shifting away from simple colour change and towards quantitative read-outs from hand-held devices to benchtop instruments. These devices are often capable of providing a digital result and controlling the assay process if necessary (Gubala *et al.*, 2012). Common requirements of POC devices include small sample size (<1 µl up to 1 ml depending on the biological media), low reagent

consumption (Wang *et al.*, 2010), and utilisation of low-cost disposable consumables that control sample size, flowrate, preparation, reagent mixing and assay reaction time (Jonsson *et al.*, 2008). These requirements are the key challenges that device developers must consider when designing a POC device.

There are a number of detailed reviews of POC diagnostic devices in the academic literature, including micro-total-analysis-systems (Rivet *et al.*, 2011), miniaturized isothermal nucleic acid amplification (Asiello and Baeumner, 2011) and molecular biological techniques for gene assay (Lien and Lee, 2010), and current and anticipated technology for POC infection diagnosis (Bissonnette and Bergeron, 2010). These reviews articulate the growing trend towards the use of POC devices as replacements for laboratory based equipment.

2.2.1 Advantages of Point-of-Care Diagnostics

Methods used currently for disease diagnosis and chemical analysis are both time-consuming and labour-intensive, and many tests are restricted to biomedical laboratories as they require specialised instrumentation and trained staff (Gubala *et al.*, 2012). Due to patients having to wait days or even weeks for test results, the delay initiating treatment has the potential for fatal consequences. To address these limitations, POC devices have been developed that offer rapid analytical testing and that allow medical diagnosis to be performed on-site by non-professionals, for example, as patients checking their own health conditions (Ryan *et al.*, 2010). This allows treatment to be initiated promptly and subsequent monitoring can be implemented, resulting in improved patient outcome (Soper *et al.*, 2006).

POC devices are designed and intended specifically to provide quick test-to-result times in comparison to laboratory assay procedures and be performed by the patients themselves, or by a healthcare professional in a POC setting. While the samples do not require a dedicated laboratory and trained staff, resulting in reductions

in travel time and the provision of results, accuracy and reliability must not be sacrificed for speed (Gubala *et al.*, 2012).

In the past decade there has been a fundamental shift in healthcare, centred on patient self-care, whereby patients are actively encouraged to be directly involved in their personal health and treatment of chronic illness. This results in the patient taking an active interest in managing their condition and improves patient compliance (Price, 2001; Laurence *et al.*, 2010) resulting in better clinical outcomes (Douketis, 2001). The development of POC devices enables and encourages patients to self-test. This has a large impact on reducing doctor and healthcare professional work load, reduces hospital admissions and increases public awareness and education of healthcare and disease.

POC readers can cost significantly less than laboratory instruments as they are smaller, less complex and often specialised in performing a single diagnostic test. For example, a Varioskan Flash spectral scanning multimode reader (ThermoScientific Ltd., UK) can cost approximately £38,500 (VWR.com, 2017) whereas a POC glucose meter often costs <£30. As POC readers are often intended for use with disposable sample devices, there is no need for cleaning or calibration of the reader. However, the relative complexity of the consumables compared to a blood-tube, results in greater consumable costs which are often passed onto patients (Gubala *et al.*, 2012). The fact that patients are able to perform the testing themselves also reduces staff costs for the healthcare institution.

2.2.2 Disadvantages of Point-of-Care Diagnostics

Some of the advantages of POC diagnostics can also be viewed as disadvantages. As mentioned in section 2.2.1, the reduced complexity of low-cost POC readers results in increased complexity of the consumables required for operation. Whereas a dedicated pathology laboratory has a reduced cost per test, when spread over the thousands of samples processed, the POC consumables are often the financial

responsibility of the patient, which can become expensive. Readers and devices are often capable of performing only a single type of assay and only one assay per run. Therefore, multiple readers and different consumable devices are necessary for the detection and quantification of multiple analytes, which further increases cost.

The POC setting is often heavily reliant on the person performing the test to be able to understand and perform the correct protocol, which is not always possible, and which can lead to incorrect interpretation of results and may lead to patient harm if, for example, incorrect dosing of medication is given as a consequence. In addition there is less chance of a healthcare professional being able to identify warning signs should a patient misinterpret diagnostic data.

Issues have been raised about the accuracy of results obtained from POC devices, specifically those with single-use test cartridges, and about how errors in POC device design can contribute to possible inaccuracy (Gubala *et al.*, 2012). A report was published by Venge *et al.* comparing POC results for the cardiac biomarker cardiac troponin I with those from laboratory analysers and the subsequent effect on patient diagnosis (Venge *et al.*, 2010). Venge *et al.* discuss how laboratory based assays identified elevated cardiac troponin I levels in more patients than did the POC assays. The consequence was that laboratory testing was able to identify a higher proportion of people in the study (80.9%) who died of CVD than were identified by the POC assays (50.6%). The conclusion was that “the clinical judgment of the patient with suspected myocardial ischemia should not solely rely on results from POC assays.” (Venge *et al.*, 2010).

This demonstrates the challenges of quantification in POC devices, as diagnostic and therapeutic information is gathered from a single test and calibration is performed across batch sampling. In addition, vital processes such as mixing, incubation timing, sample normalization, and rinsing may not be performed or controlled as well as in laboratory tests (Gubala *et al.*, 2012). For example, where reagents are contained within the POC device, the key process of reagent-sample mixing is dependent on and affected by the efficacy with which the reagent distribution occurs within the sample,

which is beyond the control of the user. Should variances in reagent uniformity within the sample occur, variances in the result will also occur. Gubala *et al.* specifies that “critical issues arise in the dispersion of dried reagents into the sample, in the mixing of reagents and sample, and in the control of incubation time” (Gubala *et al.*, 2012). In addition, the use of whole blood samples in POC devices often requires filtration features, which increases the risk of unforeseen reactivity between filter materials and blood components that may influence results.

2.2.3 Point-of-Care Glucose Monitor

A biosensor can be defined as a “compact analytical device or unit incorporating a biological or biologically derived sensitive recognition element integrated or associated with a physio-chemical transducer” (Turner, 2000). As mentioned in section 2.1.2, glucose quantification biosensors are the leader in commercial POC testing, and the technology is expansively described (Wang, 2008; Heller and Feldman, 2010).

The majority of the current commercial self-test glucose quantification systems are enzymatic electrochemical biosensors, and the development of the technology has led to a reduction in the time-to-result to < 5 seconds and to a reduction in the required blood sample volume to as little as 0.06 µl. Examples of electrochemical POC devices can be seen in Figure 2.6.

The three main components of a biosensor are:

1. A biological detection part, usually enzymes or antibodies, which identifies the target analyte from other chemicals (Chambers *et al.*, 2008; Goode *et al.*, 2016).
2. A transducer, for example an electrochemical or optical device, that converts the biorecognition event into a quantifiable signal (Newman and Setford, 2006).

3. A signal processing system that converts the signal into a readable form (Hiratsuka *et al.*, 2008).

The glucose biosensor operates by the oxidation of glucose into gluconic acid and hydrogen peroxide by immobilised glucose oxidase (GLOx) (Weibel and Brights, 1971). GLOx is the standard enzyme for glucose biosensors due to its specificity and selectivity. It is also cheap, readily available and resistant to a wide range of pH and temperature (Heller and Feldman, 2008; Bankar *et al.*, 2009). The hydrogen peroxide undergoes oxidation at a catalytic anode that measures the number of electron transfers, which is proportional to the concentration of glucose in the sample (Guilbault and Lubrano, 1973). As blood oxygenation levels can vary, modern glucose assays bypass oxygen and instead rely on the use of mediators such as ferrocene-derivatives which undergo redox reactions and are quantified (Heller and Feldman, 2008). Electrochemical transducers are used because of their better sensitivity, reproducibility, easy maintenance and low cost compared to other transducers such as optical, thermometric, piezoelectric, and magnetic (Yoo and Lee, 2010).



Figure 2.6: (A) personal glucose monitor (Abbott Laboratories, USA); (B) personal cholesterol monitor (Biotek Technology Inc., Taiwan).

The personal glucose meter is a compact system (smaller than a mobile phone), cheap (<£30) and is simple to use as results are displayed digitally and are able to determine the blood sugar level within seconds (<10 seconds). Glucose meters use cheap (<£30 for a pack of 50) disposable microfluidic electrochemical sensor chips that require small sample size (<10ul) using whole blood. The personal glucose meter device embodies the ideal parameters of a POC testing system (Chin *et al.*, 2012). Other such devices include electrochemical cholesterol meters and lateral flow pregnancy tests (Koczula and Gallotta, 2016).

2.2.4 Lateral Flow Assays

The lateral-flow assay (LFA), presented in 1988 by Unipath, is widely used for pregnancy confirmation (Figure 2.7) and ovulation tracking and is the most commonly available commercial POC diagnostic method (Lee, 2008). Other uses include screening for infectious disease, drugs and blood based protein markers (Gubala *et al.*, 2012). LFA devices utilise fluid flow to operate and incorporate porous membranes, antibodies and an optical transducer system (Lee, 2008).



Figure 2.7: Lateral flow pregnancy test.

In an LFA, sample fluid containing the analyte disperses particulate labels with adsorbed antibodies or nucleic acids, which bind specifically to the analyte during an incubation phase; labels are often colloidal gold, latex spheres or dyed polystyrene (Lee, 2008; Assadollahi *et al.*, 2009). The labelled analyte is then immobilised and detected optically in the read-out zone. The concentration of label in the read-out

zone is influenced by sample flow rate and by the quantity of analyte in the sample (Gubala *et al.*, 2011). An illustration of the principle of an LFA can be seen in Figure 2.8.

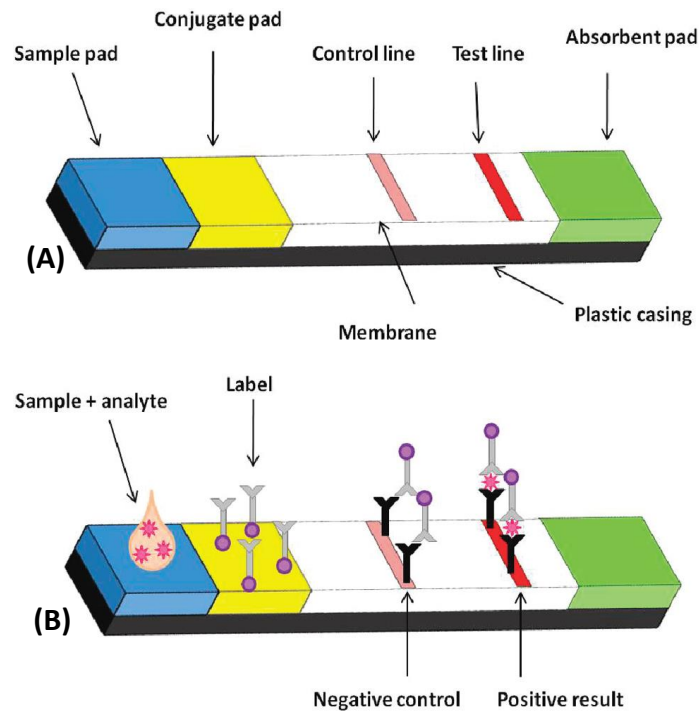


Figure 2.8: (A) Typical lateral flow immunoassay format. (B) Sample is applied to the sample pad. Analyte present in the sample binds to the antibody-conjugated label, and then binds to the control line and test line to return a positive result. If the analyte is absent, the label binds only to the control line, generating a negative control result (Gubala *et al.*, 2012).

Gubala *et al.* discuss the primary limitations of LFA, specifically accuracy. This is due to lack of control of the sample volume into which the label is dispersed, uniformity of dispersion and flow rate, which is the main determinant of contact and incubation times (Gubala *et al.*, 2012). Materials used in LFA development are another area of concern, as standard LFA materials—nitrocellulose, polyester, rayon—suffer from varying degrees of nonspecific binding, brittleness, and sensitivity to humidity (Assadollahi *et al.*, 2009).

As with the majority of POC devices, LFA and hand-held electrochemical devices can generally perform quantification of only one specific analyte and perform one assay run at a time per device. This limits their application in performing a bank of diagnostic tests on one device at the same time. As discussed in section 2.2.2, a key

criticism of POC devices is their lack of accuracy when compared to laboratory based tests. The ability to provide a suite of diagnostic data from a single operation on one device would not only mitigate the inaccuracy as multiple analytes can be compared, but would also provide far greater quantitative diagnostic data for the user to utilize when considering therapeutic and prognostic outcomes for the patient.

Multi-marker POC devices would also provide healthcare professionals with the ability to look for other indicators or markers of disease states. If ambulance staff were able to quantify multiple biomarkers associated with a heart attack, then they could start lifesaving procedures on route to the hospital rather than delaying treatment, therefore greatly increasing heart attack survival rates. Multi-marker devices such as the Abbott i-STAT (Abbott Laboratories, USA) have been produced, however, these devices are still prohibitively expensive for most POC settings (> £6000 for a refurbished model (Blockscientificstore.com, 2017)). The use of inexpensive readily available multi-marker testing devices for home or POC use may reduce workload on hospital pathology labs and doctor's surgeries, and may reduce hospital admissions through the screening and testing of common biomarker molecules and early identification of disease states.

2.3 Lab-On-A-Disc (LOAD)

The requirement for new developments of economical analytical screening tools has prompted miniaturisation as a potential method to improve performance, speed, and portability (Arnandis-Chover *et al.*, 2014). Lab-on-a-chip, LOAD and microfluidic analysis systems are some of the most recent developments in miniaturisation of chemical and biological analysis (Mirasoli *et al.*, 2014). Ideally these analytical tools should be designed to be capable of performing all the steps of the analysis (sample pre-treatment, reagents delivery, mixing, separation and detection) with the advantages of low sample and reagent consumption, fast analysis, reduced costs (Mirasoli *et al.*, 2014). Miniaturisation has practical advantages when it comes to application. The ability to scale down traditional bench-top analytical processes and to

transfer them to a portable self-operating system is leading the way for extra-laboratory analyses in clinical chemistry, food analysis, environmental monitoring and bio-warfare protection (Mark *et al.*, 2010). There is also the potential to automate standard time-consuming laboratory practices (Chen *et al.*, 2012).

A range of detection technologies have been employed in miniaturised analytical systems, with most applications relying on fluorescence and electrochemical detection (Nwankire *et al.*, 2013; Mirasoli *et al.*, 2014). However, the lack of simple and portable analytical sensing systems combining high resolution detection and quantification at competitive costs restricts the spread of molecular detection and quantification in POC settings outside the lab (Arnandis-Chover *et al.*, 2014).

LOAD platforms, particularly microfluidic centrifugal systems, are a source of interest in both academia and industry, as they have a potential to integrate labour intensive biochemical assay procedures onto a single, portable automated device with low cost (Nwankire *et al.*, 2013). LOAD systems integrate a number of microfluidic components for liquid operations on a platform similar to a compact disc (CD) through the use of the capillary-effect and centrifugal and Coriolis force on a rotating reference frame, with no requirement for connection to external pumps or power supplies (Chen *et al.*, 2012). A LOAD system requires only a single motor to control complex fluid transportation and sample loading at different rotation speeds, which simplifies complex assay procedures (Bruchet *et al.*, 2013). Furthermore, the materials themselves and the methods used for the fabrication of LOAD systems are relatively inexpensive and facilitate large volume and low cost manufacture. Due to the low cost, these platforms could be considered disposable, which helps eliminate cross-contamination of biological samples (Rivet *et al.*, 2011). In addition, because they are single-use, they do not require recalibration or maintenance. Plastics are lightweight and easy to transport and store, offering the potential for the use of the devices to improve health care in developing countries, where expensive equipment is not available (Mark *et al.*, 2010).

The LOAD has been considered an ideal solution for POC applications not only because of the reduced amount of reagents and analysis time but also because it reduces errors related to human intervention (Kim *et al.*, 2013). Furthermore, it can handle relatively large numbers of blood samples which could be an additional advantage for large scale screening for pathology. Having a rapid, accurate, and easy-to-use test available in a POC setting would provide great benefits to the health care system and the patients. Thus, the development of an ‘at-line’, ‘sample-to-answer’ microfluidic-based assay system for biomarker monitoring is an important development for the diagnostic industry (Nwankire *et al.*, 2013).

Blood is the most commonly tested biological sample; plasma separation from whole blood is a key step for sample preparation in POC diagnostics (Toner and Irimia, 2005) and is often the first step in biomedical diagnostics (Kinahan *et al.*, 2014). Various methods of plasma separation from whole blood have been investigated in order to reduce the volume of whole blood required and to develop diagnostic devices for use in a POC setting. Systems utilizing hydrodynamic focusing (Di Carlo *et al.*, 2008), filtration (VanDelinder and Groisman, 2006), acoustic standing waves (Petersson *et al.*, 2005), electrophoresis (Nakashima *et al.*, 2010) and magnetic forces (Takayasu *et al.*, 2000) have been investigated for use in microfluidic devices. However, density based cell separation by centrifugation remains the gold standard method for plasma separation in whole blood in both microfluidic devices and conventional clinical settings (Kim *et al.*, 2013). Centrifuge based blood separation can be implemented and performed in LOAD platforms with relative ease (Burger *et al.*, 2012) compared to the previously stated separation methods. LOAD platforms are also able to perform biochemical analysis on the samples, in addition to plasma separation within the same platform. Therefore, LOAD has been considered as an ideal solution for POC applications.

Centrifugation is simple and efficient but requires a relatively large volume of the sample (typically larger than 1 mL), which requires staff with medical training to obtain the sample which can be painful or uncomfortable for the patient. Efforts to incorporate LOAD platforms for biomedical applications include blood-based

processing (Lee *et al.*, 2009; Schaff and Sommer, 2011) shown in Figure 2.9, nucleic acid analysis (Focke *et al.*, 2010; Lutz *et al.*, 2010) and immunoassays (Chen *et al.*, 2011).

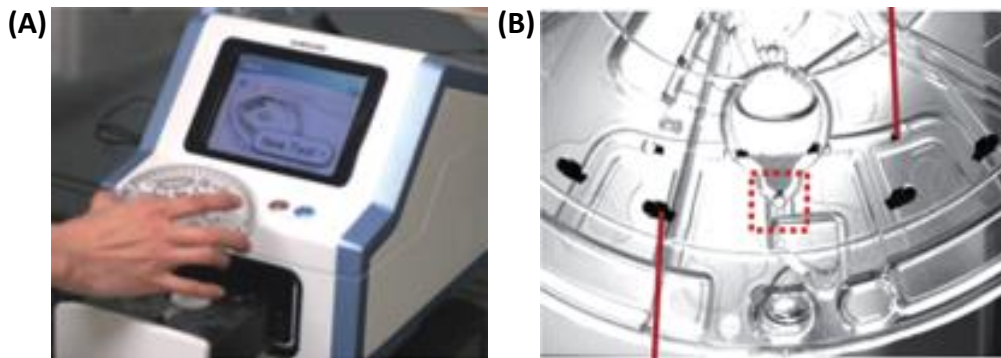


Figure 2.9: (A) LOAD blood analyser; (B) Dual layer LOAD platform (Lee *et al.*, 2009).

Centrifugal microfluidic LOAD platforms are particularly suited to POC blood separation as they can perform not only plasma separation using reduced sample volume, Figure 2.10 (Kim *et al.*, 2013), but also allow a variety of follow-up biochemical analysis to be undertaken on the same platform. For example, fully integrated colourimetric analysis of clinical chemistry (Lee *et al.*, 2011) and pathogenic virus DNA extraction have been demonstrated using plasma samples separated from whole blood on spinning discs in an automated and parallel fashion (Cho *et al.*, 2007; Madou *et al.*, 2006).

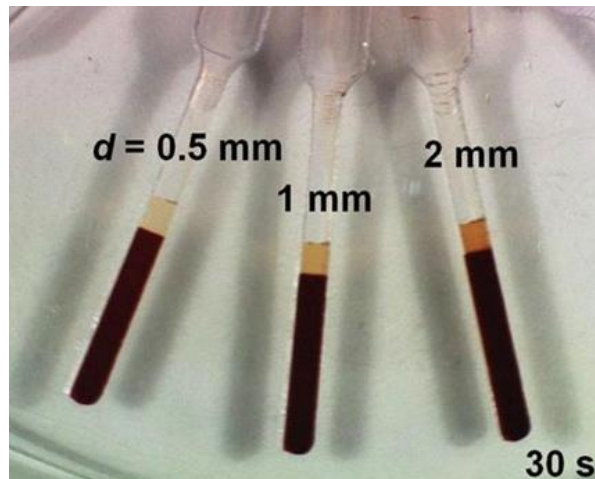


Figure 2.10: Separation of plasma from whole blood on centrifugal microfluidic LOAD platform after 30 seconds (d: depth). (Kim *et al.*, 2013)

Research into microfluidics has been increasing during the past decade (Mark *et al.*, 2012). However, despite several devices going to market successfully and the market expected to reach £6 Billion by 2020 from £2.4 Billion in 2015 (Markets and Markets, 2015), the availability of microfluidic products is limited and they are not sold in large numbers in mass markets (Mark *et al.*, 2012).

Market penetration is restricted by several factors. The development of microfluidic POC devices is often time consuming and expensive, not only for the microfluidic devices but also for the processing instrument. The primary and fundamental hurdle is the technical development of an acceptable device; aspects such as accuracy, reproducibility, long-term stability, acceptable sample size, portability and ease of use must be overcome and then an instrument capable of reading the device/interpreting the results with the same standards must be developed (Gubala *et al.*, 2012). These factors result in extremely high development costs, which limits the potential applications to those which will provide a return on such high investments (Whitesides, 2006). Once the technical aspects have been overcome, the customer is then presented with a substantial upfront investment for a processing instrument, commonly in the range of £10,000–£100,000 or more, which is severely limiting, especially in resource deprived areas (Mark *et al.*, 2012). Devices such as the glucose meter have had success because these hurdles have been

overcome, such that the costs to the customer make it readily available to the general public and not just highly funded laboratories.

With the development of LOAD platforms progressing, the main obstacle faced is the analysis and interpretation of the results produced within the platform. The readers produced are designed from the ground up for a specific LOAD platform with specialised custom components (Lee *et al.*, 2011) resulting in expensive units such as the Abaxis Piccolo Xpress, with the reader unit costing in excess of £14,000 and the LOAD panels costing £104 for 10 (Figure 2.11). Units such as these are only suitable for clinical settings and not for general POC testing.



Figure 2.11: Abaxis Piccolo Xpress LOAD instrument (Abaxis.com, 2014).

An approach being adopted by device developers to mitigate the high development costs, and the subsequently inflated retail costs, is to produce disposable devices for use with existing off-the-shelf instruments (Li *et al.*, 2008). This removes

the requirement for the development of expensive custom instrumentation that inflates development and purchase costs. This approach has several advantages for both developers and customers and the combination of microfluidic liquid handling and off-the-shelf processing instruments could open new potential markets and facilitate commercial distribution of useful microfluidic products (Mark *et al.*, 2012). Device companies would not have to invest time and resources developing instrumentation from the ground up and instead inexpensive, disposable microfluidic devices can be designed to be operated on existing, mass-produced instruments that are already common in labs or at home. The instruments could be utilised either as they are or with modification. However, the instruments would likely require a minimum of a firmware update to be used with the devices. As the level of modification required increases, so does cost, but the use of mass-produced components from instruments greatly mitigates these costs and the required resources are substantially less than developing an instrument from concept (Li *et al.*, 2008). Reduced development costs for device companies would decrease investment costs and render more research applications financially viable. In addition, the customer would not be discouraged by high investments for an instrument and benefits from miniaturization, integration and automation of liquid handling operations (Mark *et al.*, 2012).

There has been progress towards this goal, with Nie *et al.* developing a paper based device for the quantification of glucose, cholesterol and L-lactate in human plasma that can be used with a standard electrochemical glucose meter, Figure 2.12 (Nie *et al.*, 2010). This device highlights the cost advantages; a low-cost disposable chip using an off-the-shelf electrochemical glucose reader available for less than £20 (Nie *et al.*, 2010). One must be aware that developing devices for use with unmodified instruments would require collaboration between instrument developers and device developers to define and share approval procedures, responsibilities and warranties, especially for significantly controlled markets such as diagnostics, however both parties would benefit since instrument applications and therefore its customer base

are expanded, while the device developers market the consumables (Mark *et al.*, 2012).



Figure 2.12: Paper based glucose sensor for use in a standard off-the-shelf glucose meter (Nie *et al.*, 2010).

A cheaper approach to develop LOAD players is to utilize and modify existing mass produced technology to achieve the same goal. Arnandis-Chover *et al.* used adapted Blu-Ray optical drive components to develop a screening device and platform using high density arrays (Arnandis-Chover *et al.*, 2014).

2.3.1 Optical Disc Drives (ODD) and Discs.

Mass produced electronic optical disc drives (ODD), as seen in Figure 2.13, are resources with high potential for inexpensive molecular screening developments. ODDs contain all the components necessary to act as both a centrifuge and a fixed wavelength spectrophotometer (depending on the wavelength of the laser diode) in a single small, compact unit whilst offering good sensitivity and accuracy with minimal technical expertise and maintenance (Arnandis-Chover *et al.*, 2014). As a result, optical drives and CDs have been used in chemical and biochemical assays by adapting standard drives as quantitative detectors (Morais *et al.*, 2008; Yu *et al.*, 2013).

ODDs are an integral part of many consumer appliances such as compact disc (CD) players, digital versatile disc (DVD) players and computers. They use lasers to read and write data to or from optical discs. Some drives can only read from discs, but most

are commonly both readers and writers. CDs, DVDs, and Blu-ray discs are common types of optical media which can be read and recorded by such drives.



Figure 2.13: A common mass produced optical disc drive (Newegg.com, 2014).

Optical drives and CDs have been used for chemical and biochemical assays by adapting standard drives as quantitative detectors (Morais *et al.*, 2008; Yu *et al.*, 2012). An audio–video optical storage system consists of an optical drive and corresponding optical media.

The main elements of an optical drive are:

- An optical path consisting of a semiconductor laser and a set of optical lenses to shape, focus and guide the laser beam,
- A motor mechanism to drive the disc,
- A signal detection system, usually using photodiodes, for the light reflected from the disc.

(Arnandis-Chover *et al.*, 2014)

ODDs are attractive instruments for microfluidic POC systems since they are inexpensive (£10–£50) and readily available, however, they have limited capabilities in terms of liquid processing, thermal control and optical readout (Mark *et al.*, 2012). By combining a microfluidic LOAD platform with an ODD, it is possible to circumvent ODD limitations and create a low-cost, easy to use, portable POC system for the

identification and accurate quantification of biomarkers. Figure 2.14 shows the internal components as seen inside an ODD.

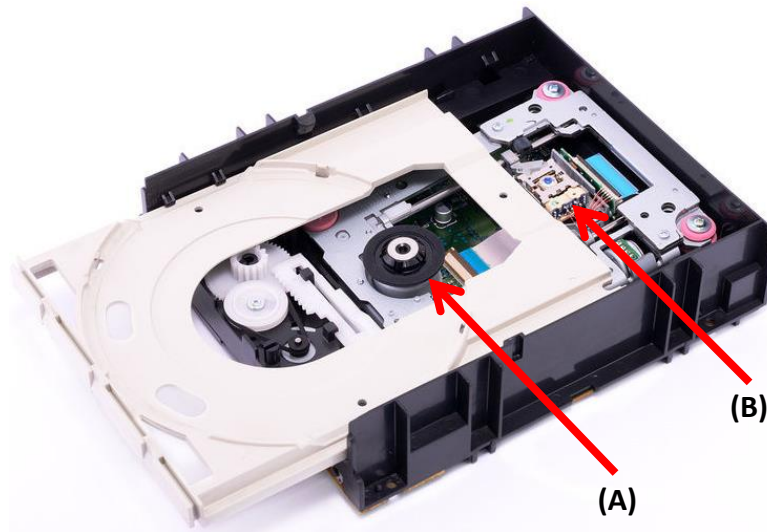


Figure 2.14: Optical disc drive without top casing showing internal components. (A) Disc rotation array; (B) Laser array (Ebay.com, 2014).

Different types of discs require different wavelengths. CDs use a wavelength of 780 nm, DVDs use a wavelength of 650 nm and Blu-ray discs use a wavelength of 405 nm. Due to the similarities between CD and DVD requirements, one laser set-up can be used for both. However, Blu-ray discs require a different laser set-up, such that optical drives that can accept both CD/DVD and Blu-ray discs will contain multiple lasers, as seen in Figure 2.15.

Optical drives intended for computer use are internal, connected via an ATA or SATA interface, or external which usually have USB or FireWire interfaces.

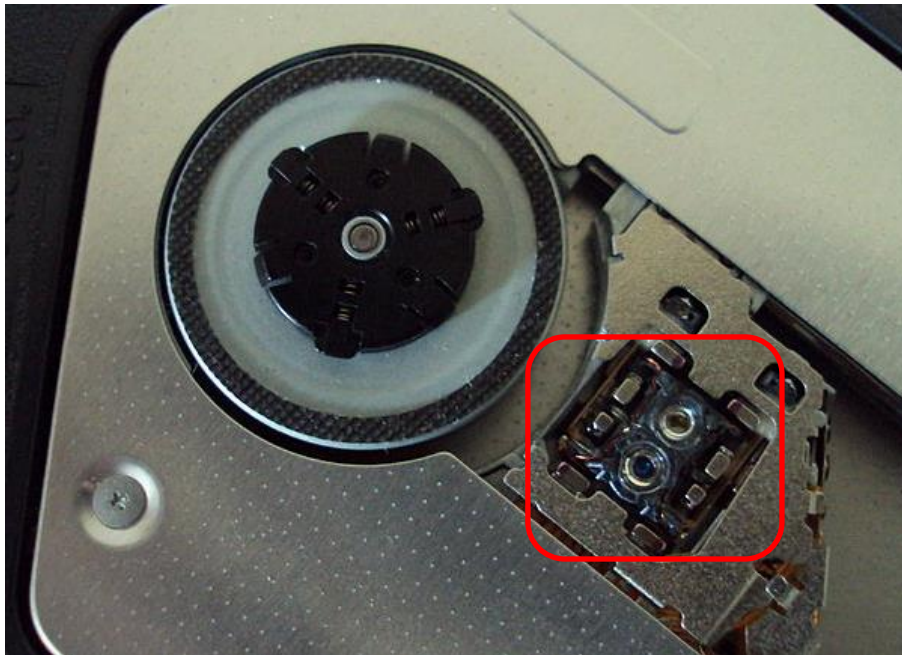


Figure 2.15: Blu-Ray drive containing two laser systems, one for Blu-Ray discs and one for CD/DVD discs (Study.com, 2014).

The data on optical discs is encoded in binary in the form of a single continuous spiral track of microscopic bumps (known as pits) or dye of differing reflectivity. Pits represent a zero, and flat surface/lack of pit (known as lands) represent a one. An optical drive reads data from a disc by shining the laser at the disc; pits scatter the light whereas lands reflect the light back which is detected by photodiodes that output electrical signals (Woodford, 2016).

In addition to the laser set-up, an optical drive has a rotational mechanism to spin the disc. Originally designed to work at only constant linear velocity where the disc speed varies between 200 – 500 revolutions per minute (RPM) depending on where the laser is reading, modern optical drives are capable of spinning much faster with more variability, as the needs of data discs evolved away from pure audio which require a constant read speed. Recent optical drives are easily capable of exceeding speeds of 12,000 RPM. However, there are safety concerns regarding the disc integrity when spun at extremely high speeds for prolonged periods. The extremely high speed

drives, such as 52x CD/DVD-RW which can spin at 30,000 RPM, have been known to exceed the physical limitations and structural capability of the discs, shattering them inside the drives with a risk of causing serious injury (Cochrane, 2002). While discs have also been shown to shatter at 20,000 RPM, the discs in these cases most likely had prior damage and contain structural weaknesses. At 25,000 RPM, structurally sound discs with no prior damage have been shown to fail and shatter whilst being spun for prolonged periods. Despite cases being reported of discs exploding at high speeds, it is extremely rare when the total number of discs and optical drives being used each day are taken into account (Rees, 2003).

The surface material used for the manufacture of optical discs is polycarbonate. CD and DVD discs are up to 120 mm in diameter, 1.2 mm thick with a 15 mm diameter spindle hole at the centre. CDs are a single clear polycarbonate substrate disc containing the data covered by a reflective aluminium surface to reflect the laser light and allow the data to be read, which is protected by a lacquer on which a label is usually printed. DVDs comprise of two polycarbonate substrate discs each of which is covered by a metallic layer (not always aluminium) and bonded together (Sharpless, 2003).

Bosco *et al.* performed statistical detection of PDGF proteins through aptamer-based surface functionalization of micro-cantilever arrays using a plug-and-play CD-like platform and laser system components from a DVD optical drive (Bosco *et al.*, 2013). They used a DVD-ROM based optical readout system to scan the micro-cantilever surfaces. The deflection profiles were measured using the astigmatic detection method embedded in commercial optical drives (Hnilička *et al.*, 2005). This platform used a custom built pulley belt system in order to rotate the disc rather than the drive system used within optical drives. Bosco *et al.* noted that utilising a DVD based optical reading system offered numerous advantages compared to traditional optical readout systems, for example the large amount of data provided for implementation of statistical data analysis and sensing reliability evaluation. The DVD laser optical unit provided nanometre resolution readout for multiple measurements of individual cantilevers

profiles, enhancing the amount of statistical data acquired on each assay (Bosco *et al.*, 2013).

As discussed in section 2.3, a cheaper approach to developing POC instruments is to utilize and modify existing mass produced technology to achieve the same goal. While a number of microfluidic devices for use with optical disk drives have been developed, they often require extensive manual preparation steps, significant modification to the disc drive and are not plug-and play solutions. Examples include automated haematocrit measurements (Riegger *et al.*, 2007), Ca^{2+} concentration measurements (Potyrailo *et al.*, 2006), biotin/streptavidin binding, DNA hybridization and IgG/anti-IgG interactions (Li *et al.*, 2008) and an immunoassay for C-reactive protein (Lange *et al.*, 2006). Arnandis-Chover *et al.* used adapted Blu-Ray optical drive components to develop a screening device and platform using high density arrays (Arnandis-Chover *et al.*, 2014) and Yu *et al.* have developed a digital readout methodology for screening biomolecular binding reactions on a disc using a standard unmodified computer drive (Yu *et al.*, 2013).

2.3.2 Particle Separation on a Centrifugal Microfluidic Platform

Microfluidics in rotating systems uses centrifugal, Coriolis and Euler forces to transport and manipulate liquids through their interaction with microstructures. Figure 2.16 shows the forces experienced by a liquid plug on a rotating disc.

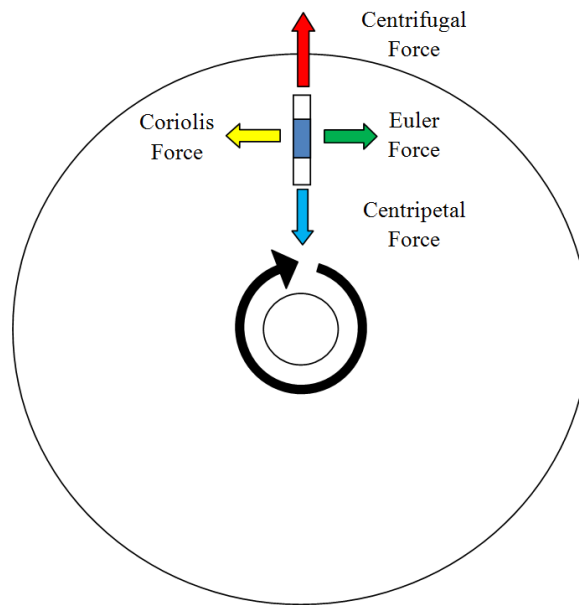


Figure 2.16: Forces experienced by a fluid plug on a rotating disc.

Centrifugal force (F_c), as illustrated in Figure 2.17, is given by:

$$F_c = r\omega^2 m \quad (1)$$

Where r is the radial position, ω is angular velocity (or linear velocity/ r) and m is mass.

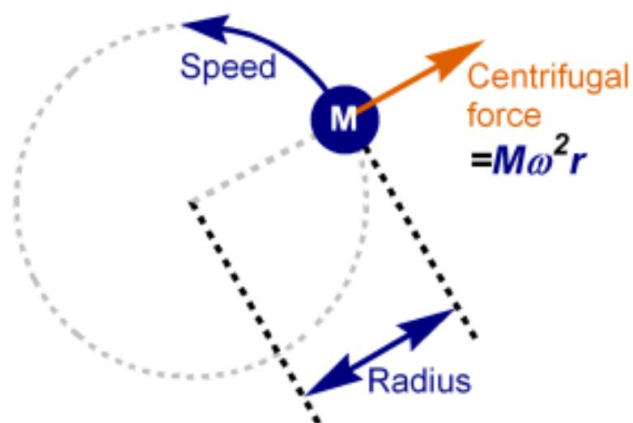


Figure 2.17: Illustration of centrifugal force (Calctool.org, 2008).

Sedimentation of particles in a centrifugal field is due to the density difference of the suspended particles and the media. The sedimentation of the particles can be accelerated by exposing them to a centrifugal force (F_C) given by:

$$F_C = r\omega^2 V_p (P_p - P_l) \quad (2)$$

Where V_p is the volume of the particle, P_p and P_l are the mass density of the particle and the liquid, respectively.

When the particle with radius r_p sediments in liquid with viscosity η_l at velocity μ , the friction force (F_r) caused by the Stokes drag is:

$$F_r = -6\pi\eta_l r_p \mu \quad (3)$$

Neglecting the interaction between the particles, the interplay of the centrifugal force and the friction force leads to the sedimentation velocity (u) given by:

$$u = S_p r \omega^2 \quad (4)$$

With the sedimentation coefficient (S_p):

$$S_p = \frac{m_p}{6\pi\eta_l r_p} \left(1 - \frac{\rho_l}{\rho_p}\right) \quad (5)$$

Where m_p is the mass of the particle. The empirical sedimentation coefficient of erythrocyte is 0.27×10^{-7} s (Van Wie and Hustvedt, 1988).

In 1920 it was seen that erythrocytes in whole blood would sediment at a faster rate when the container was inclined at an angle as opposed to being vertical, which is known as the Boycott effect. The proposed explanation for the enhanced sedimentation rate is that there is an increased surface area available for particle sedimentation. In a vertical container, particles can settle only on the bottom, whereas in an inclined container they can also settle on the upward facing wall. During the particle sedimentation process, the particles first approach the inclined wall and form concentrated slurry that is significantly heavier than the clear liquid, which rapidly slides down toward the bottom of the tube (Kim *et al.*, 2013).

Ponder and Nakamura and Kuroda proposed a kinematic model, PNK theory, to explain the Boycott effect and the increased settling rate observed in an inclined container (Kim *et al.*, 2013). According to PNK theory:

$$v = -v_0 \left(1 + \frac{h}{w} \sin \theta \right) \quad (6)$$

Where v is the sedimentation velocity in the slanted vessel, v_0 is the sedimentation velocity in the same vessel un-tilted, h is the height of blood cell suspension, w is the width of the vessel, θ and is the tilt angle from vertical. This equation suggests that the settling rate is increased by a factor of $(1 + h/w \sin\theta)$ over the non-tilted case. Thus, the sedimentation rate in a slanted container is equal to the vertical settling rate of particles multiplied by the horizontal projection of the channel area available for settling (Davis and Acrivos, 1985).

Kim *et al.* described the effects of sedimentation chamber geometry on blood separation times in rotating discs, particularly focusing on inducing the Boycott effect by inclining sedimentation chambers relative to the direction of centrifugal force (Kim *et al.*, 2013). Whole blood samples were spun at 2400 and 3600 RPM for three minutes and both speeds were able to separate plasma. These speeds are well within optical drive spin capabilities and the physical tolerance limit for polymer discs. As shown in Figure 2.18, the distance for particle sedimentation is shorter in a slanted channel than a straight channel.

Kim *et al.* showed that greater channel tilt angle, smaller channel width, lower sample cell fraction, and higher spin speed could enhance the blood separation rate and the channel depth or rotating direction did not. Significant enhancement of the blood separation rate, as high as 8 times for whole blood, was observed in the narrower separation channels on a spinning disc with larger tilt angles with respect to the radial direction (Kim *et al.*, 2013). These factors will need to be considered when optimisation of the assay platform design used in this project takes place.

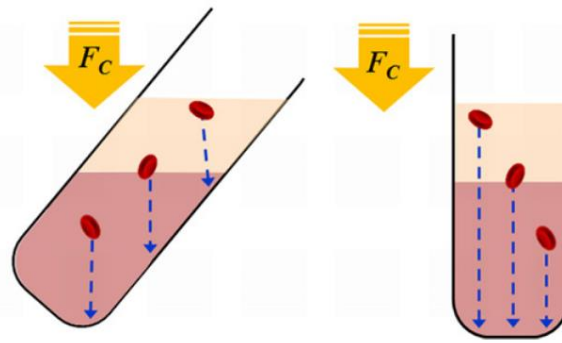


Figure 2.18: Blood separation in a tilted channel and a straight channel. The blue arrows show how the particle sedimentation distance is shorter in a slanted than a straight channel (Kim *et al.*, 2013).

2.4 3D-Printing Technology

The advance of solid freeform fabrication techniques, such as 3D-printing, has improved significantly the ability to prepare solid structures with precise geometries (Hutmacher *et al.*, 2004), including internal cavities, facilitating the rapid production of analytical platforms. The use of computer-aided designs (CAD) and data from imaging provides the ability to alter or redesign any aspect without significantly inflating costs. The rapid advancement of low-cost (<£2000 for the printer) 3D printing technology is partly due to the free and open source software and hardware development (Zhang *et al.*, 2013). In addition, there is a large library of CAD models available freely (Thingiverse.com, 2016) which provide shortcuts to product development.

The ability to manufacture detailed and complex prototypes in a fast and efficient way has caused rapid prototyping technology to become a useful tool for many areas of research and development. Fused deposition modelling (FDM) based 3D printers are readily available for purchase, either as self-assembly kits (Velleman.eu, 2016) or as pre-assembled units (MakerBot.com, 2016). While the use of 3D-printing to produce cost-effective tools for biomedical applications has significant potential (Ballyns *et al.*, 2009; Cohen *et al.*, 2006), its use in the optical and biosensors field is limited to-date. By developing a cheap, simple sensing platform capable of quantifying

a variety of different molecules in whole blood and other bodily fluids, the prevalence of disease states and the strain exerted on healthcare facilities may be lessened.

When investigating manufacturing procedures, the following core principles for all production processes must be considered:

- Performance requirements (i.e. tolerances, strength, weight, etc.)
- Production cost requirements
- Quality reproducible during mass production
- Uniform material properties throughout component.

(TheLibraryofManufacturing.com, 2014)

A large variety of methods have been used for the fabrication of microfluidic platforms, both standard chips and LOAD. Most techniques used for LOAD device channel formation (Moschou *et al.*, 2006; Nunes *et al.*, 2010), such as thermoforming, injection moulding, lamination (Miserere *et al.*, 2012), laser ablation, soft lithography, computer numerical control micro-milling (Kazarine *et al.*, 2012), xurography (Bartholomeusz *et al.*, 2005) and hot embossing, leave open faces that have to be closed by an additional layer. The device enclosing may be performed by adhesive, thermal and mechanical-based bonding techniques. This however introduces the potential for weakness and flaws in structural integrity which increases the risk of leaks, especially in centrifugal microfluidic platforms. It also adds additional design and manufacturing steps to the process, increasing production costs and time.

Most solid freeform fabrication techniques are an additive fabrication process that can rapidly recreate 3D CAD models with high accuracy by slicing them into layers and building the layers up progressively from a wide range of materials using deposition tools. These fabrication techniques include selective laser sintering, fused deposition modelling, and stereolithography. The designed external and internal (pore) geometry of the structure that is to be built can either be devised using 3D drawing computer software, be described using mathematical equations (Gabbrielli *et al.*, 2008), or be derived from scanning data of imaging technologies such as MRI or CT techniques

(Mankovich *et al.*, 1994). The possibility of using data from scans makes these manufacturing technologies particularly useful for applications in biomedical engineering, since it enables the fabrication of patient specific models or implants. The CAD-file describes the geometry and size of the parts to be built.

Solid freeform fabrication technology has the potential to fabricate LOAD platforms more rapidly with higher precision. Stereolithography techniques have been used to fabricate a silicone aortic valve replica based on X-ray computed tomography scans (Schaefermeier *et al.*, 2009; Sodian *et al.*, 2002). FDM has been employed to engineer hard tissue scaffolds such as knee menisci and intervertebral discs (Ballyns *et al.*, 2009) and encapsulated cells (Cohen *et al.*, 2006). These applications illustrate the benefits in the manufacturing of tailored parts on-site for use in clinical practice.

Originally, solid freeform fabrication techniques were developed to create prototypes when designing new products. Traditional prototyping methods involve laborious mould making and casting steps (Pham and Gault, 1998), whereas the ability to create an object within hours from a computer design by rapid prototyping significantly speeds up the development of products. Where traditional methods require the production of new moulds every time alterations are made to the design, which is time consuming and expensive, solid freeform fabrication requires only alteration of the CAD file, which affords the rapid production of analytical platforms, as well as the ability to alter or redesign any and all aspects without significantly inflating costs.

As solid freeform fabrication technologies are continuously evolving, fabrication costs are decreasing and the properties of the manufactured parts are improving. Therefore, these techniques are being used increasingly for the rapid manufacture of products in small batches. The time gain in product development, freedom of design and tool-free fabrication can outweigh the increased fabrication costs per item (Wendel *et al.*, 2008). The possibilities for using solid freeform fabrication methods for biomedical applications are numerous. But, despite the commercial availability of the technique for more than 20 years, it is still not extensively used in the medical and

diagnostic fields. Figure 2.19 shows an overview of solid freeform fabrication techniques.

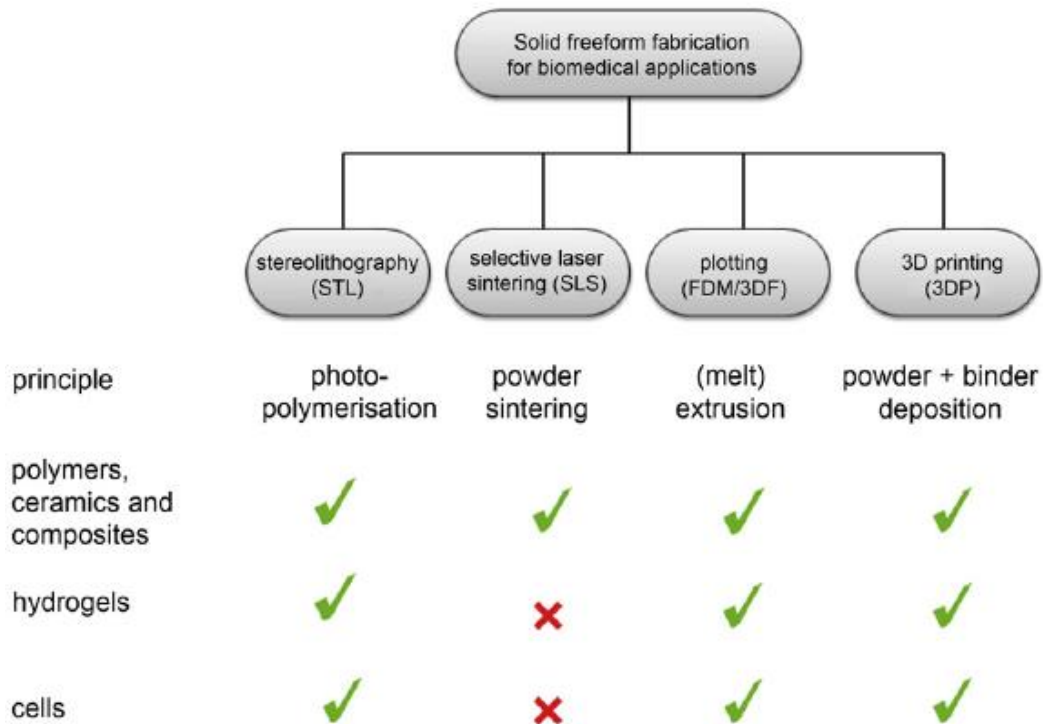


Figure 2.19: Overview of solid freeform fabrication technologies used for biomedical applications. For each technique, the symbols indicate whether polymers and/ or ceramics, hydrogels and living cells have been employed (Melchels *et al.*, 2010).

FDM is an extrusion based 3D printing method in which a pre-formed filament of a suitable material is fed and melted inside a heated liquefier before being extruded through a nozzle. The system operates in a temperature-controlled environment to maintain sufficient fusion energy between each layer.

Drawbacks of the FDM technique include the need for the input material to be of a specific diameter and to have material properties suitable to allow it to be fed through the rollers and nozzle. Any changes in the properties of the material require effort to recalibrate the setting of the feeding parameters. As a result, FDM has a narrow processing window. The resolution of FDM is relatively low, at 250 μm feature size.

As the process liquefies the materials used, the range of materials that can be used are limited to those with thermoplastic properties and the high temperatures used almost completely exclude natural polymers and prevent the incorporation of biomolecules into the platform structure, which can limit its versatility. Modifications of FDM to circumvent these limitations have encouraged the emergence of several new techniques. These include techniques that eliminate the requirement for precursor filaments or a system with reduced operating temperatures. A basic FDM setup is illustrated in Figure 2.20.

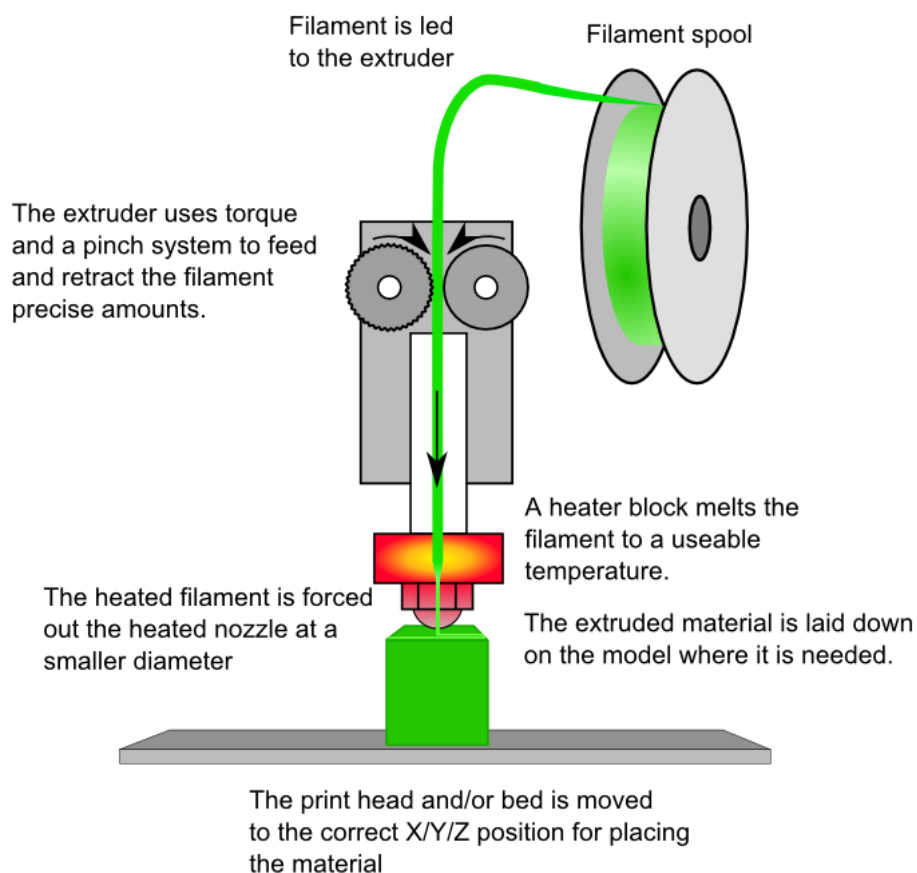


Figure 2.20: Basic Fused Deposition Modelling (FDM) setup (RepRap.org, 2014).

Stereolithography uses photo-polymerisation to solidify liquid resin under spatially controlled conditions; an illustration of the equipment set up is shown in Figure 2.21. A pattern is illuminated on the surface of the resin using a computer-controlled laser beam or a digital light projector with a computer-driven

building stage. The resin is solidified to a defined depth in the shape of the pattern, causing it to adhere to a support platform. After photo-polymerisation of the first layer, the platform is moved away from the surface and the built layer is recoated with liquid resin. A pattern is then cured in this second layer. As the depth of curing is slightly larger than the platform step height, good adherence to the first layer is ensured (unreacted functional groups on the solidified structure in the first layer polymerise with the illuminated resin in the second layer). This is repeated to form a solid 3D object. After draining and washing-off excess resin the structure requires post-curing with ultraviolet light to ensure that the conversion of reactive groups is complete and to improve the mechanical properties of the structure.

Stereolithography is particularly versatile with respect to the freedom of designing structures and the scales at which these can be built: submicron-sized structures as well as decimetre-sized objects have been fabricated. Regarding accuracy and resolution, stereolithography is superior to all other solid freeform fabrication techniques. While in most fabrication techniques the smallest details are 50-200 μm in size, many commercially available stereolithography setups can build objects that measure several cubic centimetres at a claimed accuracy of 20 μm .

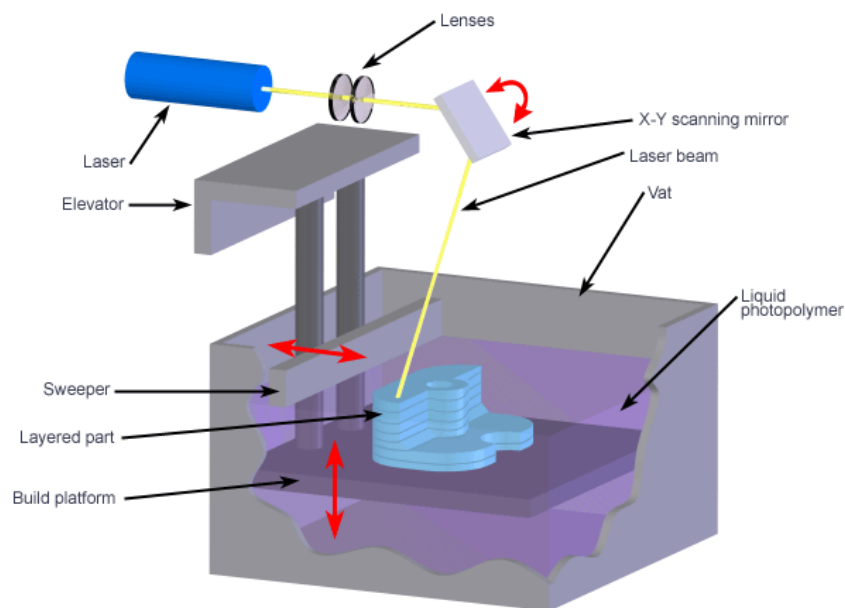


Figure 2.21: Stereolithography principle set up (Custompart.net, 2008).

While stereolithography has been in use for many years due to its high accuracy and quick turnaround time, it is used more for producing a physical representation of the final product rather than the final product itself, since the models produced are generally not as strong or durable as the final product needs to be. In addition, the increased cost (printer, supplies and materials) relative to other 3D-printing techniques, have resulted in stereolithography not being used as a product manufacturing technique. FDM printing is flexible in its applications and purposes due to the different materials available for use and it produces printed products that are sufficiently strong and durable to be considered final products. Overall it is less expensive than stereolithography, whilst maintaining many of the same characteristics. Therefore, this project will use FDM based 3D printing to produce the LOAD devices.

Chen *et al.* used polyjet based 3D-printing technology of a proprietary acrylate-based polymer material, Vero Clear, to produce plates for use with a standard plate reader for the quantitative analysis of red blood cells for transfusion medicine. Whilst capable of printing the plates, the Objet Connex 350 Multi-material 3D printer that was used to print the devices costs over £150,000 and the devices required post-print finishing including cleaning and polishing using sand paper and water to achieve acceptable physical properties and the levels of optical transparency required for use with a standard plate reader (Chen *et al.*, 2014); these finishing techniques would be unsuitable for use in sealed microfluidic channels. In addition, the material used is not readily available for public use.

Erkal *et al.* also used an Objet Connex 350 Multi-material 3D printer to produce 0.5 mm² microfluidic channels for use with electrodes for the detection of dopamine. Post-print techniques including sonication and scraping were required to properly form the channels of desired specification (Erkal *et al.*, 2014).

The recent introduction of the Fluidic Factory in March 2016 by Dolomite (Dolomite, Royston, UK) seeks to use FDM 3D-printing technology for the production of fluidically sealed microfluidic chips. However, the starting price of £14,000 for the printer and the £350 cost of each reel of cyclic olefin copolymer (Dolomite, 2016),

restricts access of affordable FDM 3D-printing technology for the production of microfluidic devices to consumers with relatively large financial resources.

Following the 3D-printing of objects, there are several post-print finishing methods that can be utilised to improve the quality/properties. These methods include:

- Cutting/trimming/grinding- the physical removal of polymer material to improve the form/structure of the object. As the process involves removing material from the structure, direct access to the area is required and errors can compromise the integrity of the object.
- Sanding/ polishing- the physical removal of polymer material to decrease the surface roughness and improve the surface finish. As the process involves removing material from the structure, direct access to the area is required and errors can compromise the integrity of the object.
- Chemical treatment- applying a chemical agent such as acetone to the object to decrease the surface roughness and improve the surface finish. Direct application requires direct access to the surface being treated; indirect application such as vapour treatment does not necessarily require direct access to the surface, however, control of the application process can be more difficult (Ultimaker.com, 2016a).
- Annealing/heat treatment- baking the object to increase the heat deflection temperature so parts retain more stiffness and form at higher temperatures. It can also improve object strength by improving strand and layer merging. Does not require direct access to all object surfaces, however, some shrinkage/warping may occur and object colour will change to opaque due to crystallisation of the polymer occurring (Proto-Pasta.com, 2017).

The requirement for post-print finishing techniques, such as physical removal of material and polishing, to improve 3D-printed objects greatly limits the potential for

3D printing of optical microfluidic devices, especially for the fabrication of inaccessible microfluidic channels. This emphasises the need for developing accessible and affordable prototyping technology.

2.4.1 Manufacturing Materials

Traditionally, glass and silicon have been used in the fabrication of microfluidic devices due to their well-established properties and compatibility with manufacturing techniques such as photolithography and micromachining (Ansari *et al.*, 2016). More recently, the use of relatively inexpensive large scale techniques such as injection moulding and hot embossing has led to an increase in the use of polymers for economical microfluidic device manufacture (Becker and Locascio, 2002). As well as being low-cost and disposable, polymers are highly adaptable for diagnostic purposes (Siegrist *et al.*, 2010). This has resulted in materials such as polymethylmethacrylate (PMMA) and polydimethylsiloxane (PDMS) becoming highly desirable for microfluidic device prototyping and manufacture (Ansari *et al.*, 2016) and for disposable lab equipment such as PMMA cuvettes (Sigma-Aldrich, 2016a). 3D-printed optical assay platforms can suffer from the poor optical characteristics (Willis *et al.*, 2012) of the available polymers, such as polylactic acid (PLA) and acrylonitrile butadiene styrene (ABS), particularly their poor optical transparency, which is a fundamental obstacle that must be overcome for the technology to progress.

Currently, the two most commonly used materials in low-cost FDM 3D printing are PLA and ABS. PLA is made from plants rich in starch like potato, corn and wheat. It is both commercially 100% compostable and 100% biodegradable. ABS is petroleum based plastic and is not safe to use for products which may come into contact with food. PLA and ABS are known as thermoplastics; they become soft and pliable with more liquid properties when heated and return to a solid state when cooled; this is a repeatable process.

While many thermoplastics exist, few are used in 3D printing due to the requirements imposed by the process; there are 3 different stages the material has to pass to be considered for use. The first stage is processing base plastic resin into a filament that the printer can accept for use. The plastic needs to form a consistent filament that is uniform in size, shape, density and be bubble free. The second stage is extrusion and trace-binding during the 3D printing process, which gives aesthetically pleasing and physically accurate parts. The final stage comprises the physical properties of the part; the material properties should match the proposed function, strength, durability, finish, transparency etc. (Chilson, 2013).

While ABS and PLA are both able to make physically accurate parts, there are differences between them that can influence the choice of the use of one over the other. With ABS, the major factor is its tendency to warp during printing, especially during the initial printing stages when the molten filament encounters a cold printing build table (MakerGeeks.com, 2014). This can render the parts unusable within the first few minutes of printing. The simplest method for reducing warping is the use of a heated build table (English, 2012). However, not all 3D printers have a heated build table and the ones that do tend to be significantly more expensive; the Ultimaker Original (Ultimaking Ltd., Netherlands) does not have a heated build table and starts at €995, whereas the Ultimaker 2 (Ultimaking Ltd., Netherlands) does have a heated build table included and starts at €1895. PLA does not suffer from warping to the same degree as ABS and therefore is often the material of choice when a heated build table is not available. For fine, sharp features, ABS is inferior to PLA as there commonly will be rounding of the points/corners (Chilson, 2013). A small amount of cooling at the nozzle can improve the points, but this runs the risk of reducing interlayer adhesion, which can lead to cracks in the part. The properties of PLA offer several advantages over ABS. At operating/printing temperature, PLA has increased fluidity than ABS and, if actively cooled, allows the production of sharper details without the risk of cracks. The greater flow can also result in better interlayer adhesion and increased strength (Chilson, 2013).

In general, ABS is strong, with a degree of flexibility that is greater than PLA, which makes it easier to work with and finish (Grieser, 2016). Its higher extrusion temperature, 235°C to 256°C, gives it higher resistance to heat (MakerGeeks.com, 2014). Also acetone can be used as a plasticiser which allows it to be welded, smoothed and finished using acetone. These properties make it a favoured material for mechanical/practical uses. PLA is as strong as ABS, but is far more brittle, which can make it harder to work with or finish. Its tendency to crack and shatter before bending limits practical applications and the lower extrusion temperature, approximately 210°C, makes it unsuitable for many conditions that involve raised temperatures due to it deforming and losing structural integrity and strength (MakerGeeks.com, 2014). However, due to its lower extrusion temperatures and increased fluidity when molten, this material has potential for great structural integrity and interlayer strength, higher maximum print speeds, increased printing resolution and finer details on prints, as well as far less tendency to warp. It also generally has a better finish after printing, reducing or removing entirely the need for finishing depending on personal preference. This makes it popular for display, hobby or household use (Chilson, 2013).

Due to its tendency to crack and splinter rather than bend, PLA is considered weaker than ABS; however similar force is required for them to fail (English, 2012). More commonly it is the calibration of the printer and the settings being used that result in a weaker or stronger object rather than the material used. Fill density, print speed, extrusion temperature, layer resolution and shell/wall thickness will all contribute to the structural strength of the item (English, 2012).

2.5 This Project

This project will investigate low-cost FDM 3D-printing as a potential development and production method for microfluidic LOAD devices. A LOAD device will be designed and optimised using 3D-printing for use with a mass-produced ODD. Mark *et al.* describes how most presented examples of microfluidic POC devices for use with ODDs still require extensive manual preparation steps and are not plug-and-

play solutions yet (Mark *et al.*, 2012). This project attempts to demonstrate the capability of 3D-printed LOAD devices as a one-step analytical platform that does not require such preparatory steps and has the potential for use in an ODD. Chin *et al.* lists central challenges to the commercialisation of microfluidic POC diagnostic devices, this includes methods of sample collection and working with complex sample specimens such as whole blood (Chin *et al.*, 2012). In this project, device development was aimed to progress towards the use of microfluidic quantities (<50 μ l) of whole blood such that samples ultimately can be taken using a finger prick device. This will ensure the device can use existing POC sample collection methods and is viable with complex sample specimens.

In order to be used as an assay platform, e.g. for the quantitative detection of cholesterol or glucose markers, the LOAD will be designed to integrate optical assays. Reagents will react with the target analytes in the sample solution and induce a colour change (Rivet *et al.*, 2011). For readout of the results of the assay, the intensities of the colours can be compared with those of calibration curves to quantify the concentration of analytes. With the use of this approach, colourimetric-assay-based paper-on-chip devices have been used to successfully quantify glucose, pH, and protein levels thus, colourimetric detection methods are ideal for simple POC diagnosis because of their visual readouts, low cost, and stability (Rivet *et al.*, 2011). Optical detection and quantification are widely employed in microfluidics and provide high sensitivity, rapidity and easy implementation for quantitative purposes (Rivet *et al.*, 2011).

As discussed in section 2.4, the equipment and running costs of 3D-printers primarily used for developing medicinal devices are prohibitively expensive (>£150,000), which, when combined with equally costly and commercially restricted consumables (which can be in excess of £750 per container of polymer) and monthly licensing fees to simply operate the machinery, is beyond the financial capabilities of many development and research laboratories.

This project will also explore the benefits of affordable and readily available FDM 3D-printing technology as a device development tool for POC devices whilst overcoming the limitations of FDM 3D-printing; firstly the poor product finish compared to traditional manufacturing methods and the poor optical transparency of FDM 3D-printed devices (Gross *et al.*, 2014) achievable when using readily available filament and affordable FDM 3D-printers. Secondly, the formation of imbedded microfluidic channels, which are a fundamental requirement for any POC diagnostic device. PLA will be the material used for device development and optimisation.

The LOAD device should be of the same dimensions of a CD (120 mm diameter and 1.2 mm thick), contain imbedded microfluidic channels (volume < 50 μ) and have optical transparency sufficient that colour can be visually observed within the channels.

The combination of microfluidic LOAD devices with low-cost FDM 3D-printing and mass-produced off-the-shelf optoelectric drives offers the potential for developing POC analytical tools at a fraction of the cost and time; the notion being that existing optical-disc drives could one day be repurposed with minimal modification as affordable diagnostic readers for use with the LOAD platform being developed in the project. The LOAD device would be a cheap, disposable platform, capable of testing multiple samples for multiple analytes simultaneously depending on platform design and colourimetric chemistries and suitable for both lab and POC due to relatively low upfront costs to the consumer.

Chapter 3: Development of a Quantitative Optical Assay for Cholesterol and Glucose

3.1 Introduction

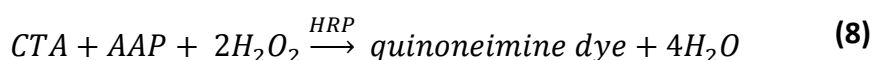
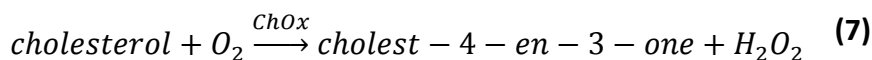
The quantification of metabolites such as cholesterol, glucose, urea and lactate in whole blood is highly important in clinical diagnostics. Cholesterol is abundant in humans and animals, being a structural component of cell membranes. Nerve, brain, skin and liver tissues contain particularly high volumes of cholesterol and it is the central component of nerve myelin (Saher *et al.*, 2005). Its role in the progression of disease states such as hypertension, arteriosclerosis, cerebral thrombosis, and coronary heart diseases makes its assay important for diagnosis and prevention of such conditions.

With the number of people living with diabetes increasing every day and expected to rise to 366 million by 2030, the quantification of glucose in solution remains of great importance. Diabetic patients are expected to self-monitor personal blood glucose levels through the use of home testing kits and healthcare professionals regularly perform blood glucose testing at health check-ups to screen for pre-diabetes or diabetes. For that reason, there is always a requirement for the development and progression of glucose assay methods. Hence, cholesterol and glucose were selected as the analytes of interest in this work.

Numerous analytical procedures involving chemical and enzymatic techniques have been used within cholesterol and glucose assays, (Brahim *et al.*, 2001; Singh *et al.*, 2006; Tsierkezos and Ritter, 2014; Yoo and Lee, 2010). However, enzymatic methods have been most popular due to their increased specificity and selectivity. Enzymatic methods use cholesterol oxidase (ChOx) or glucose oxidase (GLOx) to oxidize cholesterol or glucose respectively to produce hydrogen peroxide (H_2O_2); the H_2O_2 is then quantified.

Wong *et al.* discovered that horseradish peroxidase (HRP) catalyses the oxidative coupling of chromotropic acid (CTA) and aminoantipyrine (AAP) with hydrogen peroxide to produce a blue quinoneimine dye with high absorbance (A) at 650 nm region (Wong *et al.*, 1981). This reaction coincides with the output wavelength of the laser diodes used in DVD players (650 nm). The absorbance can then be measured and

compared against a calibration curve giving a concentration of cholesterol or glucose in blood samples. The method involves a single aqueous reagent, requires no sample pre-treatment, is reproducible, simple, specific, and uses no corrosive reagents. The enzyme catalysis reaction is shown below:



It is theoretically possible to quantify any chemical reaction that produces H_2O_2 using the enzymatic coupling of CTA and AAP via HRP. While this reaction has been used in the past to quantify glucose, it has not been used to quantify cholesterol. The quantification of cholesterol using this method will be investigated in this chapter.

The National Institute for Health and Care Excellence (NICE) recommends intervention, either lifestyle or pharmaceutical, by a healthcare professional if a person has total cholesterol levels >5.0 mM, (NICE, 2014). Therefore, the cholesterol range of the optical assay to be developed in this work needs to cover a cholesterol concentration range of 0-10 mM, as this is the region where the majority of patients' levels will lie. The reagents applied in the assay to be developed will be used at a concentration suitable for 0-12 mM cholesterol to ensure excess.

The following cholesterol blood levels are generally regarded as desirable (NHS UK, 2013a):

- Total cholesterol (TC): ≤ 5.0 mM (2 mg/ml) for health adult.
- Low-density lipoprotein (LDL) cholesterol after an overnight fast: ≤ 3.0 mM
- High-density lipoprotein (HDL) cholesterol: ≥ 1.2 mM
- TC/HDL ratio: ≤ 4.5 .

The following glucose blood levels are generally regarded as desirable for adults with type 1 diabetes (Diabetes UK, 2015):

- On waking: 5-7 mM
- Before meals: 4-7 mM
- 90 minutes after meals: 5-9 mM

The clinically relevant quantification range for glucose is generally 2-10 mM. This chapter discusses the enzymatic cascade and details the methods and procedures used to develop and evaluate the colourimetric reagent and the optical assay used for the quantification of cholesterol and glucose in whole blood.

3.2 Materials and Methods

Phosphate buffered saline (PBS) (10 mM phosphate buffer, 2.7 mM potassium chloride and 137 mM sodium chloride, pH 7.4) tablets, chromotropic acid disodium salt dihydrate (CTA), 4-aminoantipyrine (AAP), Horseradish peroxidase Type II essentially salt-free, lyophilized powder, 150-250 units/mg solid (using pyrogallol) (HRP), glucose, cholesterol, Triton X-100, cholesterol oxidase from *Streptomyces sp.* lyophilized powder, ≥ 20 units/mg protein (ChOx), glucose oxidase from *Aspergillus Niger* lyophilised powder ~ 200 units/mg protein (GLOx), hydrogen peroxide solution 30 wt. % in H₂O (H₂O₂) were all purchased from Sigma-Aldrich (Poole, UK). Defibrinated whole horse blood was purchased from TCS Biosciences (Buckingham, UK). Ultrapure water (18 M Ω cm) was obtained using a Milli-Q water system (Millipore Corp., Tokyo, Japan).

A Varioskan Flash spectral scanning multimode reader (ThermoScientific Ltd., UK) was used in conjunction with the PC software package SkanIt, to determine the absorbance values of the well plate assays performed in this project; all readings were

carried out at wavelengths of 590 nm or 650 nm, unless otherwise stated. Sample readings were carried out in 96-well Nunc-Immuno MaxiSorp flat bottom plates (Sigma-Aldrich, UK). Heraeus Fresco 17 Centrifuge (ThermoScientific, UK), Heraeus Megafuge 16R Centrifuge (ThermoScientific, UK) and Mini Star silverline microcentrifuge (VWR, USA) were used for sample preparation when necessary.

The concentration of cholesterol in samples was tested and quantified independently using an EasyTouch GC Blood Glucose/Cholesterol Dual-Function Monitoring System (Bioptik Technology, Taiwan). The concentration of glucose in samples was tested and quantified independently using an Optium Exceed Blood Glucose Monitoring System (Abbott, UK).

3.2.1 Buffers and Solutions

All solutions were prepared daily, protected from light, kept at the stated temperatures and allowed to return to room temperature until use.

- CTA stock solution (100 mM) was prepared by dissolving 400.3 mg CTA in 10 ml PBS pH 7.4 and kept at 4°C until use.
- AAP stock solution (100 mM) was prepared by dissolving 203.24 mg AAP in 10 ml PBS pH 7.4 and kept at 4°C until use.
- H₂O₂ solution concentrations 0-12 mM were prepared by diluting H₂O₂ 30%wt using PBS pH 7.4 and stored at 4°C until use.
- ChOx 100 units / ml was prepared by adding 1 ml PBS, pH 7.4 to 4.3 mg ChOx solid and stored at -20°C until use.
- GLOx 1000 units / ml was prepared by adding 1 ml PBS, pH 7.4 to 5.88 mg GLOx solid and stored at -20°C until use.
- HRP 1000 units / ml was prepared by adding 1 ml PBS, pH 7.4 to 6 mg HRP and stored at 4°C until use.
- Cholesterol was used as a substrate for ChOx and prepared according to the Sigma-Aldrich protocol (Sigma-Aldrich, 2013). A 100 mg of cholesterol solid was

dissolved in 1.0 ml of Triton X-100 by heating to 70-80°C and stirring, until the solution was clear. A 9.0 ml aliquot PBS pH 7.4 heated to 70-80 °C was added to get a final concentration of 100 mg / 10 ml (25.86 mM). Solutions of different concentration ranging from 1-10 mM were prepared similarly and stored at 4 °C until use. Cholesterol solution was allowed to return to room temperature before use.

3.2.2 Enzyme Specifications

Horseradish Peroxidase (HRP)

The properties of the enzyme HRP used in this work as listed (Sigma-Aldrich, 2014a) were as follows:

- Optimal pH range: 6.0–6.5 (activity at pH 7.5 is 84% of the maximum).
- PH stability: most stable in the pH range of 5.0–9.0.
- Storage/Stability: Store the product at 2–8 °C. The enzyme remains active for at least 2 years. Solutions show a loss of <2% of activity per week if stored at -20 °C.
- Specific Activity: 150–250 units mg solid (pyrogallol as substrate)
- Unit (U) definition (purpurogallin): 1 U will form 1.0 mg of purpurogallin from pyrogallol in 20 seconds at pH 6.0 at 20 °C. This unit is equivalent to ~18 mM units per minute at 25 °C.
- Unit definition (ABTS): 1 U corresponds to the amount of enzyme which oxidizes 1 μmol ABTS (Fluka No. 11557) per minute at pH 6.0 and 25°C.
- Molecular weight: ~44 kDa. Consists of at least 5 isoenzymes.
- Inhibitors: sodium azide, cyanide, L-cystine, dichromate, ethylenethiourea, hydroxylamine, sulphide, vanadate, p-aminobenzoic acid, and Cd²⁺, Co²⁺, Cu²⁺, Fe³⁺, Mn²⁺, Ni²⁺, and Pb²⁺ ions.

Cholesterol Oxidase (ChOx)

The properties of the enzyme ChOx used in this work as listed (Sigma-Aldrich, 2014b) were as follows:

- Optimal pH: 6.0
- pH Range: 6.0-8.0
- Optimum temperature : 60°C
- pH Stability : pH 5.0 – 10.0 (25°C, 20 hr)
- Thermal stability : Below 45°C (pH 7.0, 15 min)
- Specific activity: 20 units/mg protein
- Unit Definition: 1U will convert 1.0 μmol of cholesterol to 4-cholesten-3-one per min at pH 7.5 at 25 °C.
- Molecular weight: 50 kDa
- Inhibitors : Ionic detergents, Hg^{2+} , Ag^+

Glucose Oxidase (GLOx)

The properties of the enzyme GLOx used in this work as listed (Sigma-Aldrich, 2015) were as follows:

- Optimal pH: 5.5
- pH Range: 4.0-7.0
- Optimum temperature : 60°C
- pH Stability : pH 5.0 – 10.0 (25°C, 20 hr)
- Thermal stability : Below 45°C (pH 7.0, 15 min)
- Specific activity: 200 units/mg protein
- Unit Definition: 1U will convert 1.0 μmol of β -D-glucose to D-gluconolactone and H_2O_2 per min at pH 5.1 at 35 °C.
- Molecular weight: 186 kDa
- Inhibitors: Ag^+ , Hg^{2+} , and Cu^{2+} ions, phenyl mercuric acetate and p-chloromercuribenzoate.

3.2.3 Preliminary Investigation into Chromotropic Acid (CTA) and 4-Aminoantipyrine (AAP) Concentration.

1 ml samples containing HRP (5 U/ml), CTA (0-10 mM) and AAP (0-10 mM) were prepared from stock solutions. The reaction was started by adding H₂O₂ (12 mM). The sample was incubated for 10 minutes then the absorbance at 650 nm was measured in 100 µl. The sample was allowed to incubate for a further 10 minutes (20 minute total incubation time) and the absorbance was measured again.

A preliminary absorbance spectrum was produced from a 1 ml sample containing HRP (5 U/ml), CTA (2 mM), AAP (2 mM) and H₂O₂ (4 mM). The absorbance was measured in 100 µl after 10 minute incubation.

3.2.4 Investigation of CTA:AAP molar ratio.

Samples containing HRP (6 U/ml), CTA and AAP were prepared in PBS. The reaction was started by adding H₂O₂ (5 mM). Total sample volume was 1 ml. The sample was incubated for 2 minutes then the absorbance at 650 nm was measured. The sample was allowed to incubate for a further 8 minutes (10 minute total incubation time) and the absorbance was measured again. The molar ratios tested were 0-80 mM CTA with 10 mM AAP and 10 mM CTA with 0-80 mM AAP. The absorbance was measured in 100 µl of each sample.

An experiment was performed to induce AAP radical dimerization. H₂O₂ (5mM) was added to sample containing AAP (40 mM) and HRP (6 U/ml). Total sample volume was 1 ml.

Experiments were performed to determine which ratio of CTA:AAP should be used. Samples containing HRP (6 U/ml), CTA (0-40 mM) and AAP (10 mM) were prepared in PBS. The reaction was started by adding H₂O₂ (0-10 mM). Total sample volume was 1 ml. The assay was read after 2 minute incubation at a wavelength of 650

nm (n=3). The absorbance was measured in 100 µl of each sample. The absorbance was measured in a 1 in 10 dilution.

3.2.5 Optimisation of Horseradish Peroxidase (HRP) Concentration.

Samples containing HRP (1 U/ml), CTA (6 mM) and AAP (6 mM) were prepared in PBS. The reaction was started by adding H₂O₂ (4 mM). Total sample volume was 1 ml. The sample was incubated for 5 minutes then the absorbance at 650 nm was measured in 100 µl every 5 minutes up to 20 minute total incubation time. This process was repeated with HRP concentration 0-6 U/ml and H₂O₂ concentration 4 mM and 8 mM.

3.2.6 Optimisation of Cholesterol Oxidase (ChOx) Concentration.

Samples containing ChOx (0.25 U/ml), HRP (6 U/ml), CTA (6 mM) and AAP (6 mM) were prepared in PBS. The reaction was started by adding cholesterol (2.75 mM). Total sample volume was 1 ml. The sample was incubated for 5 minutes then the absorbance at 650 nm was measured in 100 µl every 5 minutes up to 20 minute total incubation time. This process was repeated with ChOx concentration 0-1 U/ml per sample and cholesterol concentration 2.75 and 8.9 mM.

3.2.7 Development of the Cholesterol Assay in Buffer.

Sample solutions containing ChOx (1 U/ml), HRP (6 U/ml), CTA (6 mM) and AAP (6 mM) were prepared in PBS. The reaction was started by adding cholesterol (2.75 mM). Total sample volume was 1 ml. The sample was incubated for 5 minutes and the absorbance at 650 nm was measured in 100 µl every 5 minutes up to 20 minute total incubation time. This process was repeated with cholesterol concentrations in the range 2.75 - 9.3 mM.

3.2.8 Development of the Cholesterol Assay in Plasma.

Defibrinated horse plasma was prepared by centrifuging defibrinated whole horse blood at 5000 RPM for 15 minutes and extracting the liquid fraction. Sample containing HRP (6 U/ml), CTA (6 mM), AAP (6 mM) and cholesterol (2.6 mM) in defibrinated horse plasma were prepared. The reaction was started by adding ChOx (1 U/ml). Total sample volume was 1 ml. The sample was incubated for 5 minutes. The absorbance at 650 nm was measured in 100 μ l every 5 minutes up to 20 minute total incubation time. This process was repeated with horse plasma with cholesterol concentrations in the range 2.6-9.8 mM.

3.2.9 Development of the Cholesterol Assay in Whole Blood.

Sample solutions containing HRP (12 U/ml), CTA (12 mM), AAP (12 mM) and cholesterol (0-12 mM) in defibrinated whole horse blood were prepared. The reaction was started by adding ChOx (2 U/ml). Total sample volume was 1 ml. The samples were then mixed thoroughly and left to incubate at room temperature for 5 minutes for the enzyme reaction to take place and for the colour to develop. The samples were then centrifuged for 5 minutes at 8000 RPM and the liquid fraction extracted. The absorbance at 650 nm was measured in 100 μ l after a total of 10 and 20 minutes incubation.

3.2.10 Optimisation of Glucose Oxidase (GLOx) Concentration.

Samples containing GLOx (0-50 U/ml), HRP (6 U/ml), CTA (20 mM) and AAP (10 mM) were prepared in PBS. The reaction was started by adding glucose (10 mM). Total sample volume was 1 ml. The sample was incubated for 2 minutes then the absorbance at 590 nm was measured in 100 μ l.

3.2.11 Development of the Glucose Assay in Buffer.

Sample solutions containing GIOx (20 U/ml), HRP (6 U/ml), CTA (20 mM) and AAP (10 mM) in PBS were prepared. The reaction was started by adding glucose (0-10 mM). Total sample volume was 1 ml. The sample was incubated for 2 minutes and the absorbance at 590 nm was measured in 100 μ l.

An experiment was performed to investigate the glucose assay reaction in buffer over time. Samples containing GIOx (20 U/ml), HRP (6 U/ml), CTA (20 mM) and AAP (10 mM) were prepared in PBS. The reaction was started by adding glucose (0-10 mM). Total sample volume was 1 ml. The sample was incubated for 5 minutes then the absorbance at 590 nm was measured in 100 μ l. Absorbance was measured again after 7, 10 and 30 minutes total incubation time.

3.3 Results and Discussion

The results from each stage of assay development are presented and discussed in detail in this section. Results are not necessarily presented chronologically. All plots utilise mean values of at least 3 absorbance readings taken at 590 nm or 650 nm and error bars are shown on all graphs representing ± 1 standard deviation. 590 nm is the theoretical peak of the absorbance curve produced by the blue quinoneimine dye of CTA and AAP (Wong *et al.*, 1981); 650 nm is the wavelength of a DVD optical drive laser. HRP concentration can be determined by either a kinetic or a fixed time method. As the fixed time method is more applicable in most clinical assays (Wong *et al.*, 1981), and this particular assay, it was chosen for this investigation. All absorbance values displayed on graphs have been standardised against the blank absorbance of the well plate containing samples with CTA, AAP, HRP, ChOx/GIOx and 0 mM substrate; blank solutions displayed < 5 % absorbance in all cases. All incubations were performed at room temperature.

3.3.1 Preliminary Investigation into Chromotropic Acid (CTA) and 4-Aminoantipyrine (AAP) Concentration.

The glucose and cholesterol assays involve the use of an enzymatic cascade to produce a blue dye with an absorbance correlating to substrate concentration. The reagents that combine to produce the dye are CTA and AAP. According to the reaction proposed by Wong *et al.*, Figure 3.1, 2M H₂O₂ reacts with 1M of CTA and 1M AAP in the presence of HRP with a molar ratio of CTA:AAP for maximum colour produced being 4:1 (Wong *et al.*, 1981).

1M cholesterol or glucose is oxidized, producing 1M H₂O₂. Cholesterol has a clinically relevant concentration range of 0-5 mM. A broad quantification range of 0-10 mM is important to provide emergence intervention if cholesterol concentration is significantly elevated. A solution consisting of CTA (6 mM) and AAP (6 mM) will give a broad cholesterol quantification range of 0-10 mM with a 2 mM excess. Glucose has a clinically relevant range of 0-10 mM; concentrations above 7 mM are seen as elevated, which is common after eating, and should be reduced (Diabetes UK, 2015). A broad quantification range of 0-20 mM is important to provide emergence intervention if glucose concentration is significantly elevated. A solution consisting of CTA (10 mM) and AAP (10 mM) will give a broad glucose quantification range of 0-20 mM.

It is necessary that the concentrations of CTA and AAP are sufficient to quantify substrate within the required detection range (0-10 mM). Experiments were performed to determine what concentration values and ratio of CTA:AAP are applicable to practice and produce a blue quinoneimine dye of required concentration.

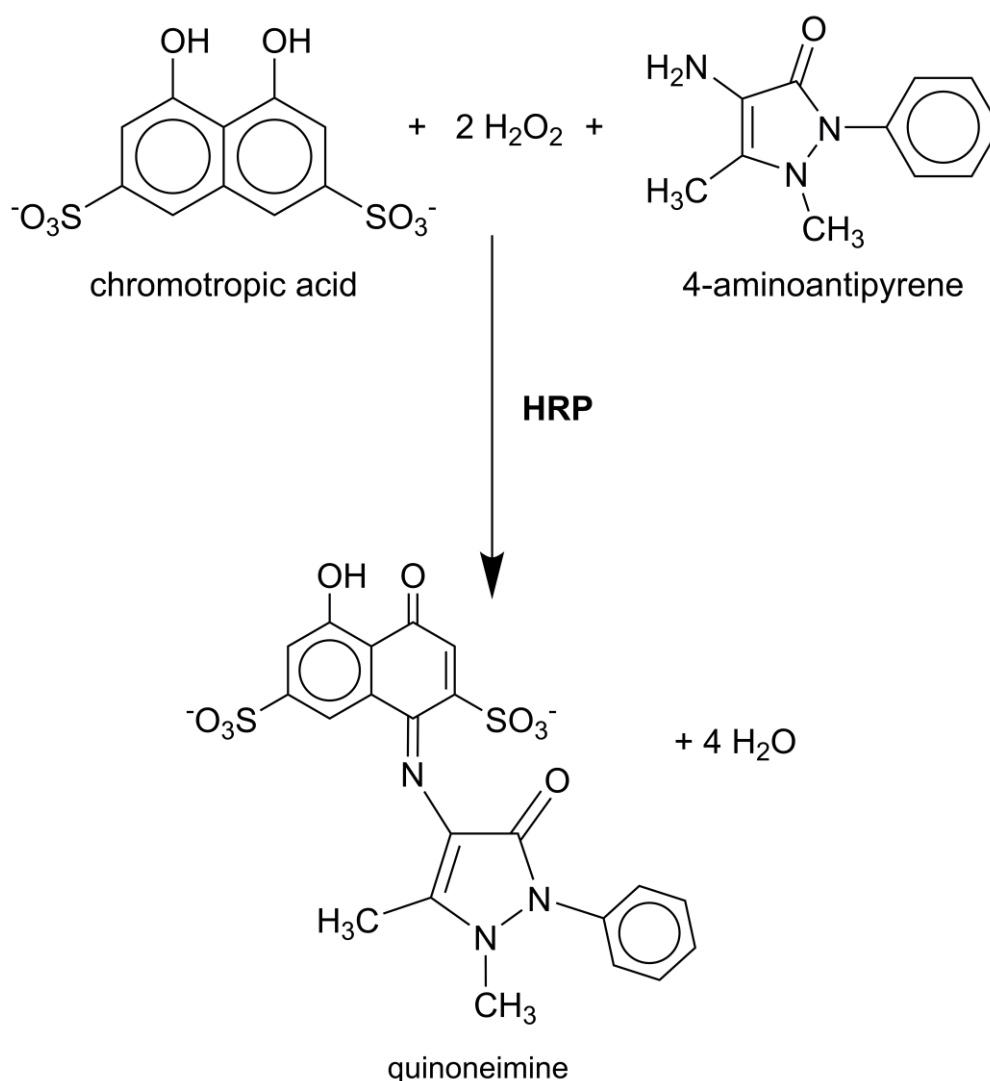


Figure 3.1: Proposed mechanism for peroxidase-catalysed formation of a quinoneimine dye (Wong *et al.*, 1981).

H_2O_2 solution was used as a substitute for the substrate in the optimisation of CTA+AAP solution concentration since the cholesterol+ChOx or glucose+GLOx reaction are unnecessary for this reaction. Removal of the cholesterol/glucose reaction would ensure that the concentration of CTA+AAP reagent solution could be determined quickly whilst preserving enzyme quantities. H_2O_2 is thermodynamically unstable and therefore is constantly decomposing over time to water and oxygen. As a result, the molar concentration of H_2O_2 provides an estimate for the concentration rather than

accurate concentration, and therefore its use may provide inaccurate recordings. However, since the concentration of H₂O₂ solution being used is across the clinically relevant range expected of an assay for cholesterol or glucose (0-10 mM) it will be sufficient for initial assay development and optimisation. If the assay reagents at the chosen concentrations and ratios give distinct absorbance for the H₂O₂ solutions then it will be suitable for the required quantification range of 0-10 mM. However, further testing over the entire substrate concentration range will be performed using substrate samples (cholesterol and glucose) to confirm this.

As these were the first attempts at working with the assay reagents and generating quinoneimine dye, assay/incubation times were greater than the objective (≤ 2 minutes). Previous studies conducted by Wong *et al.*, which aspects of this work was attempting to recreate, have used 5 - 60 minute incubation intervals (Wong *et al.*, 1981). Incubation times of 5 or 10 minute intervals were used initially, and then as optimisation progressed, incubation times of 2 minutes were used. The absorbance (A) of the samples was calculated automatically by the plate reader using the following metric:

$$A = \log \frac{I_0}{I} \quad (10)$$

Where I_0 = the intensity of incident light; I = intensity of transmitted light.

Samples containing HRP (5 U/ml), CTA (1 mM) and AAP (1 mM) were prepared in PBS. The reaction was started by adding H₂O₂ (12 mM). Total sample volume was 1 ml. The sample was incubated for 10 minutes then the absorbance at 650 nm was measured in 100 μ l. 100 μ l volume was chosen due to the size of the 96 well plates that were used to measure absorbance and the need for sufficient sample to fill the bottom of the well. The sample was allowed to incubate for a further 10 minutes (20 minute total incubation time) and the absorbance was measured again. This process was repeated with CTA (0-10 mM) + AAP (0-10 mM) solution. The increasing concentration of quinoneimine dye can be seen in Figure 3.2.

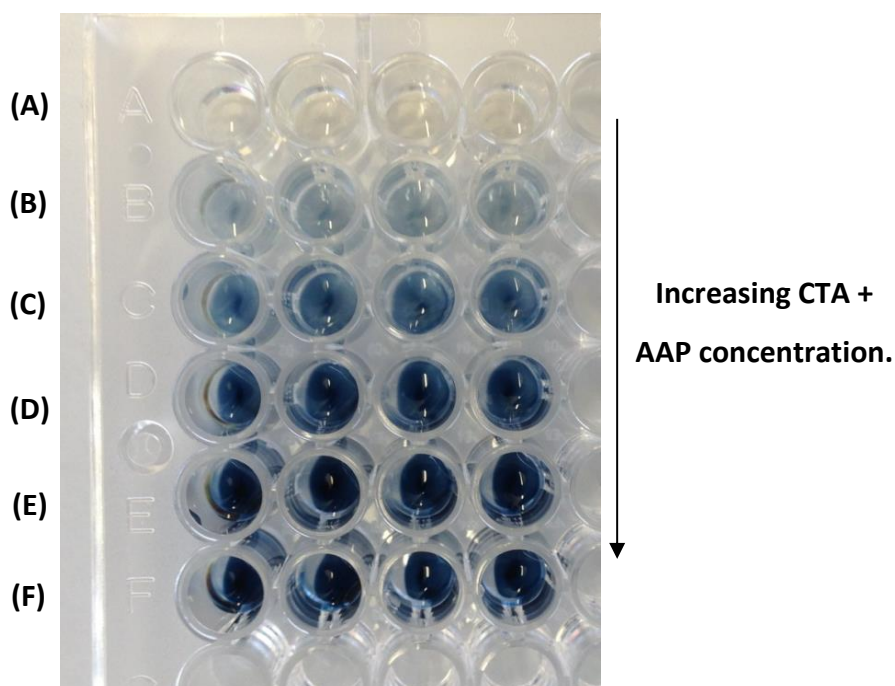


Figure 3.2: The image shows the increasing quinoneimine dye concentration observed as CTA+AAP concentration increases. Each well contains 100 μl taken from each 1 ml sample. Each sample contains HRP (5 U/ml), H_2O_2 (12 mM) and varying concentrations of CTA and AAP as follows: Line (A) CTA (0 mM), AAP (0 mM); (B) CTA (1 mM), AAP (1 mM); (C) CTA (3 mM), AAP (3 mM); (D) CTA (5 mM), AAP (5 mM); (E) CTA (6 mM), AAP (6 mM); (F) CTA (8 mM), AAP (8 mM).

The absorbance readings observed in the experiments were high (above 1 AU). It is well known in spectrophotometry, due to the Beer-Lambert Law, that when absorbance values exceed a value of 1, the accuracy of the results begins to decrease, and once a value of 2 AU is reached then the results are regarded as inaccurate and samples should be diluted or the sample path length reduced before analysis (Higson, 2004). Due to the potential inaccuracy of the data, one must be cautious when drawing conclusions from absorbance data in excess of 2 AU. However, the Varioscan plate reader has a linear measurement range of 0-4 AU when using a 96-well plate, as stated by the manufacturer, so the absorbance recorded is within the limits of accuracy for this specific piece of equipment.

In the presence of H_2O_2 and HRP, AAP and CTA combined to form a deep blue compound with a broad absorbance band between 550-650 nm with a peak at 590 nm, as shown in the preliminary spectrum in Figure 3.3. The broad absorbance peak introduces the flexibility for measuring absorbance across a wide range of wavelengths, with the absorbance and trend line shifting accordingly; this is demonstrated in section 5.3.1.

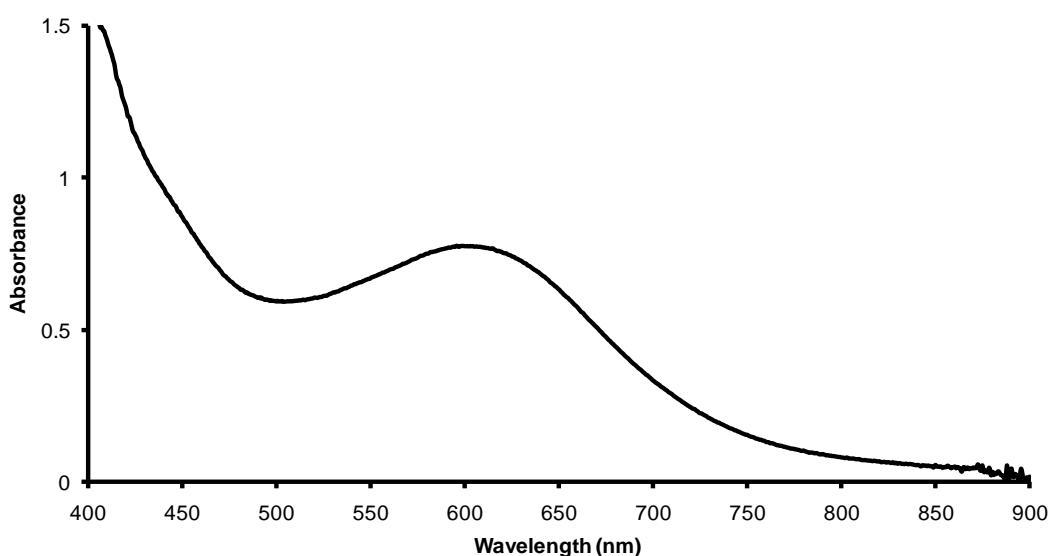


Figure 3.3: Preliminary absorbance spectrum produced from a 1 ml sample containing HRP (5 U/ml), CTA (2 mM), AAP (2 mM) and H_2O_2 (4 mM). The absorbance was measured in 100 μl after 10 minute incubation.

In the absence of either H_2O_2 or HRP, no absorbance within the 550-650 nm range was detected. The absorbance detected at 650 nm in 10 control/blank samples containing HRP (5 U/ml), CTA (6m M) and AAP (6 mM) can be seen in Figure 3.4. In all cases the observed absorbance of the control/blank samples was < 5 % of the observed absorbance at the lowest substrate concentration.

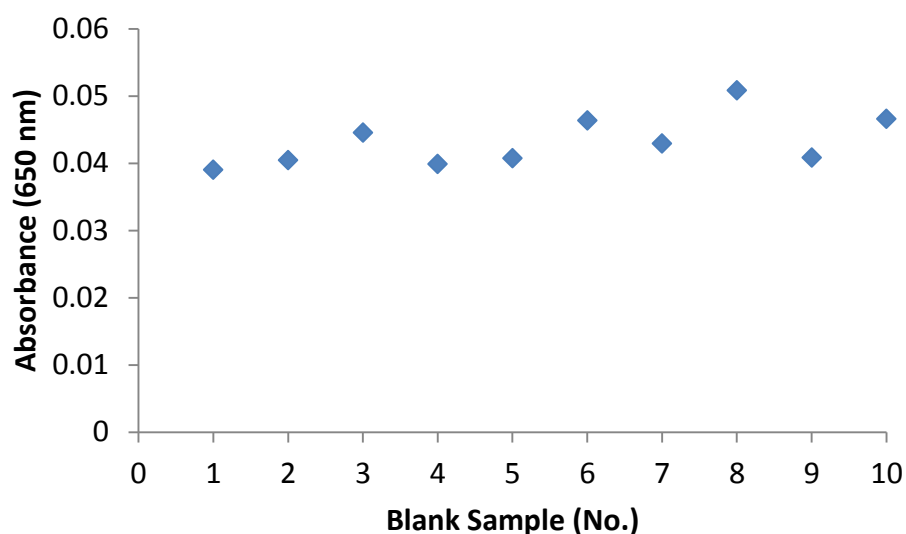


Figure 3.4: Absorbance detected in 10 control/blank solutions containing HRP (5 U/ml), CTA (6m M) and AAP (6 mM).

The preliminary results (data not shown) showed that as the CTA+AAP concentration increased the absorbance increased. The absorbance readings taken after 20 minutes incubation showed no further increase. Therefore, it was concluded that the reaction was complete after 10 minutes incubation. It was also seen from the data that the dye was stable for up to 20 minutes after the reaction, but the dye does appear to be unstable and break down over time. When samples were observed after extended periods of time (after an hour or more) the colour seen is more brown/black and cloudy. The stability of the dye produced over time needs further investigation. However, if absorbance is recorded within 5 minutes this should not be problematic for this assay, especially as the dye has been seen to be stable for up to 20 minutes.

Using the equations (Equation 7-9) originally proposed by Wong *et al.*, and subsequent testing based on these formulae, it was seen that a substrate concentration range of 0-10 mM can be measured colourimetrically using CTA (6 mM) and AAP (6 mM). A benefit of the blue dye absorbing in the 650 nm range is that it is a visible colour change with the potential for eye based analysis if there is a clearly distinguishable colour difference between substrate concentrations. Although this

qualitative approach is not acceptable for the quantification of substrates such as glucose or cholesterol, where accurate quantification is required for clinical and therapeutic purposes, it is acceptable for tests such as proteinuria which uses a 'dip-stick' colour change to determine the presence of protein in urine (bpac.org, 2013).

Preliminary testing of the CTA+AAP solution, using serial dilutions, showed that a large excess of AAP compared to CTA caused reduced blue quinoneimine dye production and instead resulted in a brown colouration. Having the CTA in excess compared to the AAP however, did not decrease the blue quinoneimine dye production. The effect of CTA:AAP molar ratio was investigated further in section 3.3.2.

3.3.2 Investigation of CTA:AAP molar ratio.

It was observed during the preliminary testing performed in section 3.3.1, that the molar ratio of CTA:AAP has an effect on the concentration of quinoneimine dye produced. Experimentation was performed to investigate this effect.

The absorbance difference with increasing concentration of CTA (0-80 mM) and fixed AAP (10 mM) can be seen in Figure 3.5 and is illustrated by Figure 3.6. A fixed 10 mM reagent concentration is employed rather than the 6 mM previously used (for a broad cholesterol range of 0-10 mM), as 10 mM is necessary for substrate quantification required in the broad glucose assay range (0-20 mM).

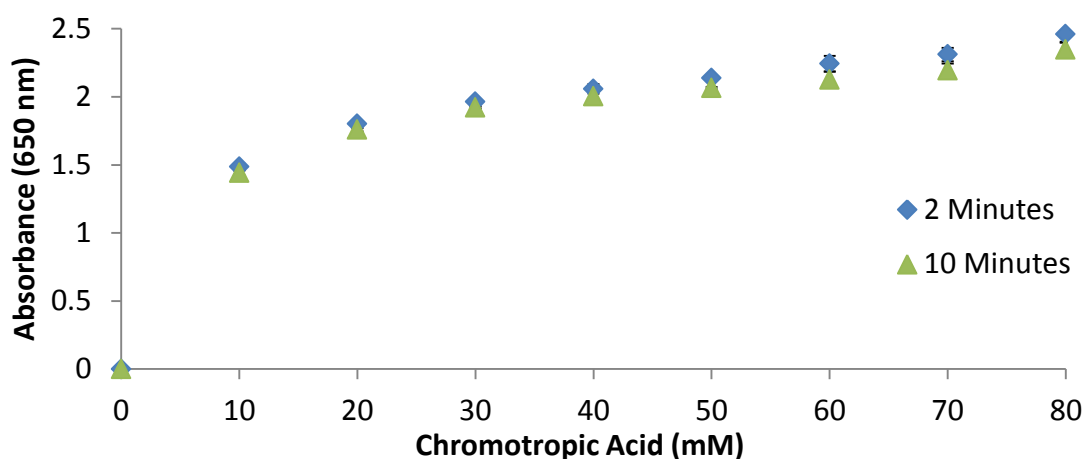


Figure 3.5: Change in absorbance recorded at a range (0-80 mM) of CTA concentrations with H₂O₂ (5 mM), HRP (6 U/ml) and AAP (10 mM) in PBS (n=3).

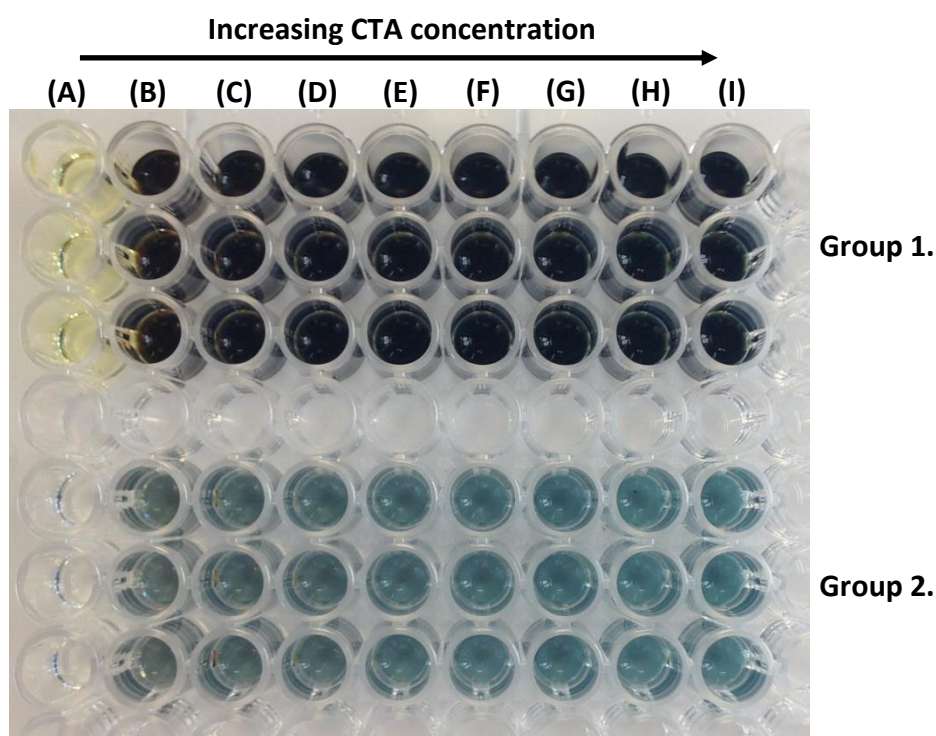


Figure 3.6: The image shows the quinoneimine dye concentration observed as CTA concentration increases. Group 1 is undiluted sample; group 2 is a 1 in 10 dilution. Each well contains 100 μ l taken from each 1 ml sample. Each sample contains HRP (6 U/ml), H₂O₂ (5 mM), AAP (10 mM) and varying concentrations of CTA as follows: Line (A) 0 mM; (B) 10 mM; (C) 20 mM; (D) 30 mM; (E) 40 mM; (F) 50 mM; (G) 60 mM; (H) 70 mM; (I) 80 mM.

As can be seen in Figure 3.5 and is illustrated by Figure 3.6, as the concentration of CTA increased, the absorbance detected increased; there was a 165% absorbance increase when the molar ratio of CTA:AAP was increased from 1:1 to 8:1. However, the strong absorbance detected (1.4-2 AU) at the lower CTA concentrations (10-40 mM) indicated that a low concentration ratio of CTA to AAP should be used to maintain accuracy. If the absorbance needed to be increased, then a higher concentration of CTA could be used. This demonstrated flexibility in the assay absorbance which could be adjusted to user requirements, however, this also introduced the potential for inaccuracy in the absorbance data, as imprecise quantification of assay reagents between stock solutions would result in different absorbance values generated in the assay reaction. The stability of the quinoneimine dye was also apparent, with <2% decrease in absorbance after 10 minutes incubation (Figure 3.5). The absorbance difference with fixed concentration of CTA (10 mM) and increasing AAP (0-80 mM) can be seen in Figure 3.7.

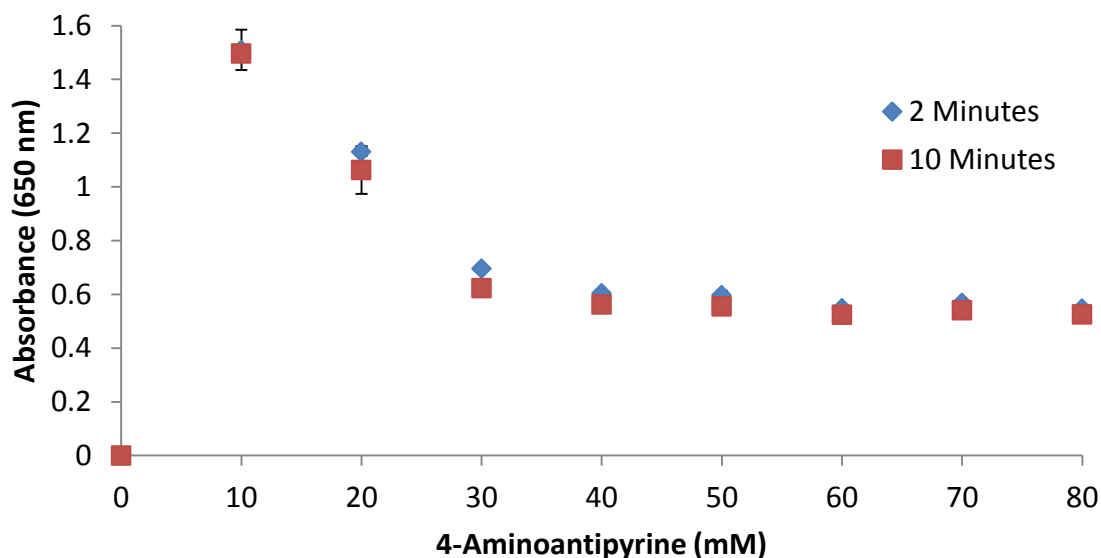


Figure 3.7: Change in absorbance recorded at a range (0-80 mM) of AAP concentrations with H₂O₂ (5 mM), HRP (6 U/ml) and CTA (10 mM) in PBS (n=3).

Figure 3.7 shows that, as the AAP concentration increased relative to that of CTA, absorbance decreased; there was a 65% absorbance decrease when the molar ratio of CTA:AAP was increased from 1:1 to 1:8. It could be seen that a high concentration of AAP compared to CTA decreased the quinoneimine dye intensity, and instead a murky brown colouration was formed, as can be seen in Figure 3.8.

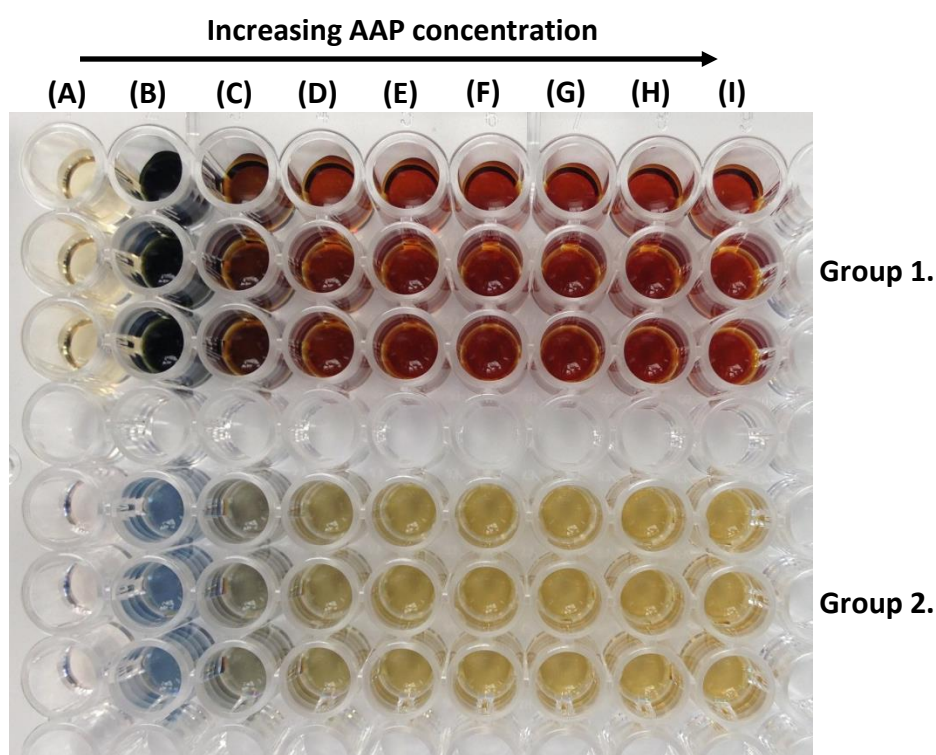


Figure 3.8: The image shows the quinoneimine dye concentration observed as AAP concentration increases. Group 1 is undiluted sample; group 2 is a 1 in 10 dilution. Each well contains 100 μ l taken from each 1 ml sample. Each sample contains HRP (6 U/ml), H_2O_2 (5 mM), CTA (10 mM) and varying concentrations of AAP as follows: Line (A) 0 mM; (B) 10 mM; (C) 20 mM; (D) 30 mM; (E) 40 mM; (F) 50 mM; (G) 60 mM; (H) 70 mM; (I) 80 mM.

Nicell and Wright explain how increased concentration of AAP with respect to phenol in an oxidised HRP colourimetric reaction results in dimerization of AAP radicals and decreased dye production (Nicell and Wright, 1997). An experiment was performed to induce AAP radical dimerization to confirm if this is occurring in the

CTA+AAP reaction. H_2O_2 (5mM) was added to sample containing AAP (40 mM) and HRP (6 U/ml). Total sample volume was 1 ml. The results can be seen in Figure 3.9.

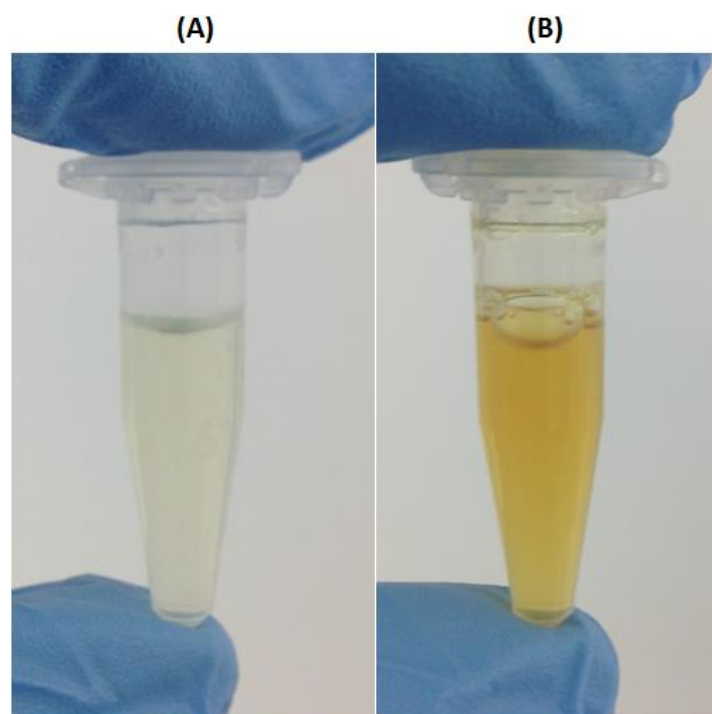


Figure 3.9: 1 ml samples containing HRP (6 U/ml) and AAP (40 mM) in PBS after 5 minutes incubation. (A) Contains no H_2O_2 ; (B) contains H_2O_2 (5 mM).

As can be seen in Figure 3.9, the sample becomes visually much darker when H_2O_2 is added. In the CTA+AAP reaction, CTA is oxidised by HRP producing CTA radicals. The CTA radicals then react with AAP to produce AAP radicals and CTA. AAP radicals then react with CTA radicals in solution and H_2O_2 to produce the blue quinoneimine dye. Increasing the AAP in the reagent mixture increases the probability of direct oxidation of AAP by oxidised HRP, which then increases the concentration of aminyl radicals and subsequently the probability of their dimerization (Nicell and Wright, 1997). The result of this is a decreased concentration of blue quinoneimine dye and an increased concentration of AAP dimers, the source of the brown colouration seen. By maintaining a high concentration of CTA with respect to AAP, the blue dye reaction pathway should be enhanced.

From these experiments assay optimisation has progressed and it is important that CTA is always in excess to AAP to prevent the direct competition between CTA and

AAP for oxidised HRP and increase the blue quinoneimine dye production reactional pathway.

As it was observed that increasing molar ratio of CTA:AAP increases absorbance, it was concluded that a low (1:1-4:1) concentration ratio of CTA:AAP would be appropriate. Experiments were performed to determine which ratio of CTA:AAP should be used, ensuring that the chosen CTA and AAP concentrations are capable of quantifying a 0-10 mM substrate range. The results are shown in Figure 3.10.

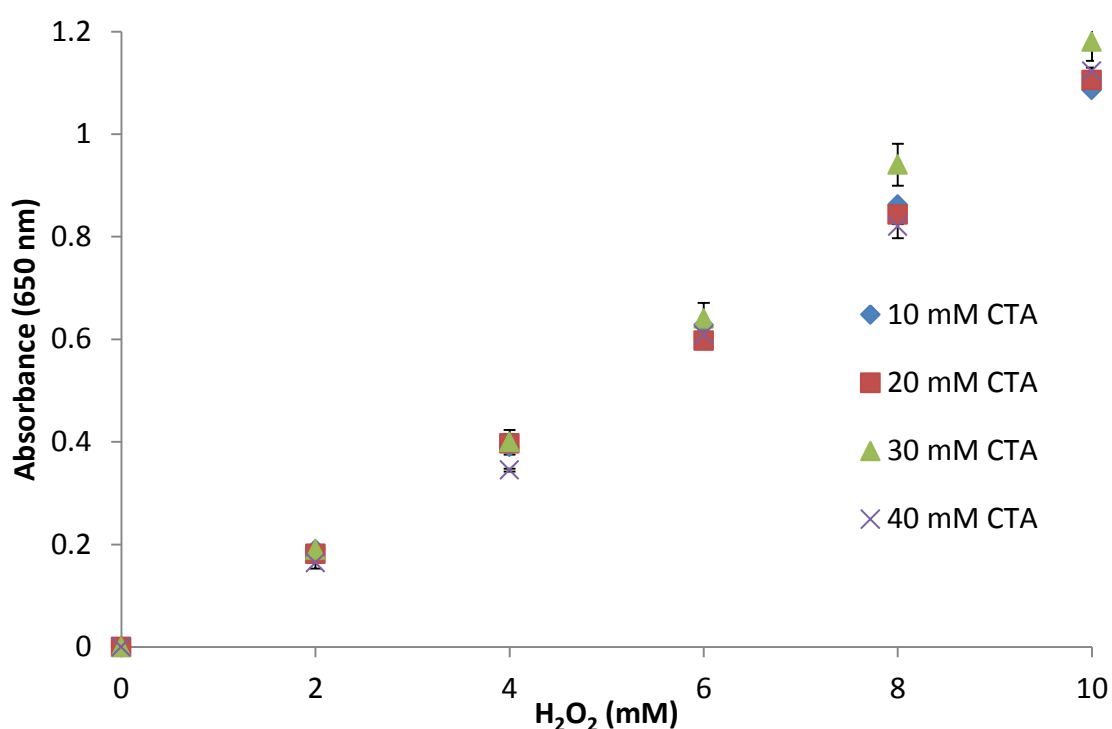


Figure 3.10: Change in absorbance recorded at a range (0-10 mM) of H₂O₂ concentrations with HRP (6 U/ml) and AAP (10 mM) in PBS (n=3).

As can be seen in Figure 3.10, there is a (<10%) observable difference between the investigated concentrations of CTA at 10 mM H₂O₂ and all are capable of producing an absorbance curve for H₂O₂ (0-10 mM). The absorbance detected for 30 mM CTA shows a slightly greater absorbance (5%) than the other concentrations. However, the error observed puts the absorbance within range of the other data. The results show that a 1:1 ratio of CTA:AAP could be used to measure a substrate range of 0-10 mM,

but, due to the reduction in absorbance observed when AAP is greater, it was determined that a ratio of 2:1 CTA:AAP would be used in the assay to ensure that the concentration of CTA is always greater than that of AAP and that the quinoneimine dye remains stable. In addition, a concentration of CTA (20 mM) and AAP (10 mM) should be capable of quantifying broad ranges of both cholesterol (0-10 mM) and glucose (0-20 mM), therefore, a concentration of CTA (20 mM) and AAP (10 mM) will be used in the assay in subsequent testing.

It should be noted that the work performed in this section occurred after the HRP (section 3.3.3), ChOx (section 3.3.4) and cholesterol assay optimisation (section 3.3.5-3.3.7) which is why a higher concentration of HRP is utilised (6 U/ml) and neither the CTA (20 mM) and AAP (10 mM) concentrations or molar ratio of CTA:AAP of 2:1 were applied to those stages of assay development.

3.3.3 Optimisation of Horseradish Peroxidase (HRP) Concentration

Experiments were performed to determine the necessary concentration of HRP for an acceptable (<5 minutes) reaction rate. PBS pH 7.4 is used as the solution medium in order to mimic physiological conditions. Its use would also provide easy identification of lower reaction rate at specific enzyme concentrations, allowing increased enzyme concentration to be used to compensate without needing sample pre-treatment, which is undesirable for a POC assay. While the optimum pH for HRP activity is 6-6.5, at pH 7.5 the activity is 84% (section 3.2.2), which is an acceptable activity without needing increases in enzyme concentration to compensate.

4 mM and 8 mM H₂O₂ concentrations were used as 4 mM substrate lies within the clinically relevant range for cholesterol (0-5 mM) and 8 mM lies above this range. H₂O₂ was used as a substitute for cholesterol/ChOx in this reaction to reduce the potential for interference and to conserve ChOx. In all cases, blue quinoneimine dye in the 650 nm region was produced, with the colour intensity increasing as the sample

H₂O₂ concentration increased. In the absence of either H₂O₂ or HRP no blue dye was produced and no absorbance at 650 nm was detected.

At 4 mM substrate there was no observable absorbance difference between the different HRP concentrations across all incubation periods ranging from 5-20 minutes with the reaction reaching completion within 5 minutes. This suggested that a HRP concentration of 0.5 U/ml would be sufficient for this assay. However, Figure 3.11 showed that as the substrate concentration is increased to 8 mM (above the clinically relevant cholesterol and glucose detection range of 0-5 mM and 4-7 mM respectively but within the broad detection ranges of cholesterol 0-10 mM and glucose 0-20 mM), the difference in reaction rate becomes apparent. It can be seen in Figure 3.11 that after 20 minutes incubation all HRP concentrations had reached reaction completion. HRP concentrations less than 2 U/ml were insufficient to ensure completion of the reaction within 5 minutes and a HRP concentration of 1 U/ml displayed incomplete reaction after 15 minutes incubation.

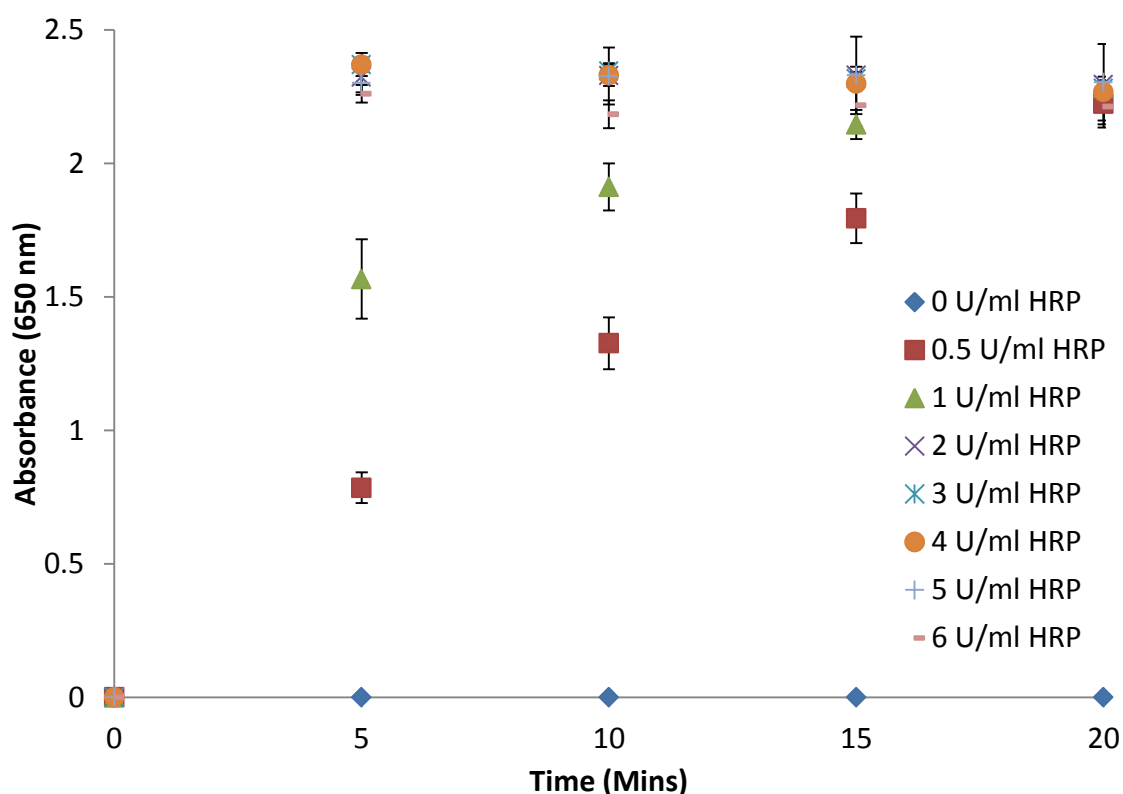


Figure 3.11: Change in absorbance recorded at a range (0-6 U/ml) of HRP concentrations with H₂O₂ (8 mM), CTA (6 mM) and APP (6 mM) in PBS (n=3).

The data shows that an enzyme concentration of 3 U/ml was sufficient to complete the reaction containing 8 mM substrate within 5 minutes. However, due to the increased clinically relevant quantification range of glucose (0-20 mM) and the additional enzyme reaction step yet to be implemented (ChOx/GlOx) it was decided that a HRP concentration of 6 U/ml would be used to maintain a reaction time ≤ 5 minutes. In addition, a concentration of 6 U/ml would reduce any impact that resulting from decreased HRP enzyme activity (84% at pH 7.5) due to the assays' environmental conditions (blood has approx. pH 7.4). It should also be noted that the results display no absorbance interference due to the HRP concentration. High absorbance was detected (above 2 AU) therefore samples may need to be diluted as the assay optimisation continues, to increase accuracy of readings.

3.3.4 Optimisation of Cholesterol Oxidase (ChOx) Concentration

Investigations were performed to try to determine the necessary concentration of ChOx for a reaction rate < 5 minutes. PBS pH 7.4 is used as the solution medium in order to mimic blood conditions; it would also provide easy identification of lower reaction rates at specific enzyme concentrations allowing increased enzyme concentration to be used to compensate, without a requirement for sample pre-treatment. It should be noted that at this stage in the project quantities of ChOx available for assay optimisation was severely limited. As a result, the use of ChOx was restricted in an attempt to conserve enzyme.

The primary issue encountered with the ChOx assay, and subsequent testing involving cholesterol, was concerned with preparing the cholesterol solution. Due to its strongly hydrophobic properties, a high concentration of surfactant and high temperatures are needed to encourage cholesterol solids to dissolve in the water based solution. When preparing the cholesterol solution, the cholesterol would dissolve in Triton X-100 when heated to 70-80°C. Upon addition of PBS pH 7.4 and when heated to 70-80°C, the solution becomes cloudy due to the cholesterol forming an emulsion. When cooled the solution clarifies again and forms 2 distinct phases.

When the phases are mixed thoroughly, a precipitation of cholesterol can be seen in the form of white crystals. Despite numerous efforts these crystals could not be dissolved. In addition, the high concentration of surfactant would cause bubbles to form in the sample that could not be removed and that interfered with the absorbance detected. As a result, testing was difficult whenever cholesterol solution was used and the tests had to be repeated many times.

Independent quantification of cholesterol concentration was sought to establish the concentrations in solution. It would have been preferential to use a commercial cholesterol quantification assay kit for use with the plate reader, such as those offered by Sigma-Aldrich (Poole, UK) (Sigma-Aldrich, 2014c), for greater accuracy, however, due to cost this was not possible. Therefore, an Easy Touch GC monitor (Bioptik Technology, Taiwan), was used to determine the cholesterol concentrations of the samples; this is a low-cost (£30) POC electrochemical sensor. As discussed in section 2.2.2, POC tests are inherently inaccurate and this particular device and associated company websites are currently unavailable at the time of writing. As a consequence the displayed cholesterol concentration values varied significantly from the prepared concentration by up to ± 1.8 mM as seen in Table 3.1. Despite the lack of accuracy in independently quantifying the cholesterol concentration, a trend line was still investigated, however, a quantification method with greater accuracy will be utilised for any future cholesterol assay optimisation that takes place after this project.

Table 3.1: Cholesterol solution concentration as prepared and the concentration stated using an Easy Touch GC monitor (Bioptik Technology, Taiwan) approx. 10 minutes after preparation (n=6).

Prepared Concentration	Tested Concentration
3 mM	2.75 mM \pm 1.3
5 mM	5.5 mM \pm 1.6
7 mM	7.6 mM \pm 1.5
8 mM	8.9 mM \pm 1.8
10 mM	9.3 mM \pm 1.4

After 30 minutes from preparation, further cholesterol precipitation was observed and the solution became cloudy and heterogeneous. This solution gave varying concentrations, rendering it unusable. While it is possible to purchase cholesterol solution, the cholesterol is dissolved in chloroform. Chloroform causes denaturation and precipitation of proteins in solution and does not mix with water. Thus it was decided that it would not be used, to prevent enzymatic damage in the assay.

ChOx has been used in cholesterol assays for many years, however, there are several different sources of ChOx isolated from *Nocardia*, *Streptomyces*, *Mycobacteria*, *Brevibacterium*, *Schizophyllum*, *Pseudomonas fluorescens*, *Cellulomonas*, and *Brevibacterium*. ChOx from *Streptomyces* was chosen for use, as Lolekha *et al.* suggested it is superior in terms of increased stability and lower cost compared with ChOx from other sources (Lolekha and Jantaveesirirat, 1992). The Clinical Chemistry Standardization Section of Centers for Disease Control uses the *Streptomyces* enzyme for cholesterol determination (Warnick, 1986). Experiments performed by Lolekha *et al.* also came to the conclusion that ChOx from *Streptomyces* is recommended for the determination of serum cholesterol by enzymatic methods (Lolekha *et al.*, 2004).

In all cases, blue quinoneimine dye with an absorbance peak in the 650 nm region was produced, with the colour intensity increasing as the cholesterol concentration increased and over time as the reaction continued. In the absence of either cholesterol or ChOx, no blue dye was produced and no absorbance in the 650 nm wavelength range was detected. Figure 3.12 shows that, at 2.75 mM of cholesterol, 0.5 U/ml ChOx is sufficient to complete the reaction within 5 minutes. This, however, is towards the lower end of the detection range.

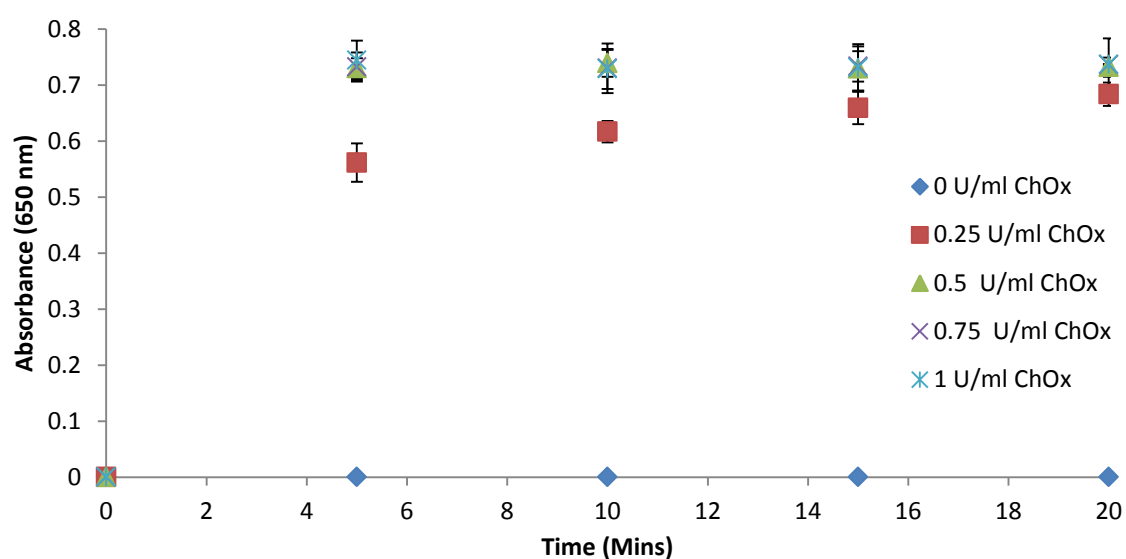


Figure 3.12: Change in absorbance recorded at a range (0-1 U/ml) of ChOx concentrations with cholesterol (2.75 mM), HRP (6 U/ml), CTA (6 mM) and AAP (6 mM) in PBS (n=3).

Figure 3.13 shows that as cholesterol concentration increased to 5.5 mM, 1 U/ml ChOx required over 10 minutes to complete the reaction and 0.5 U/ml required up to 20 minutes.

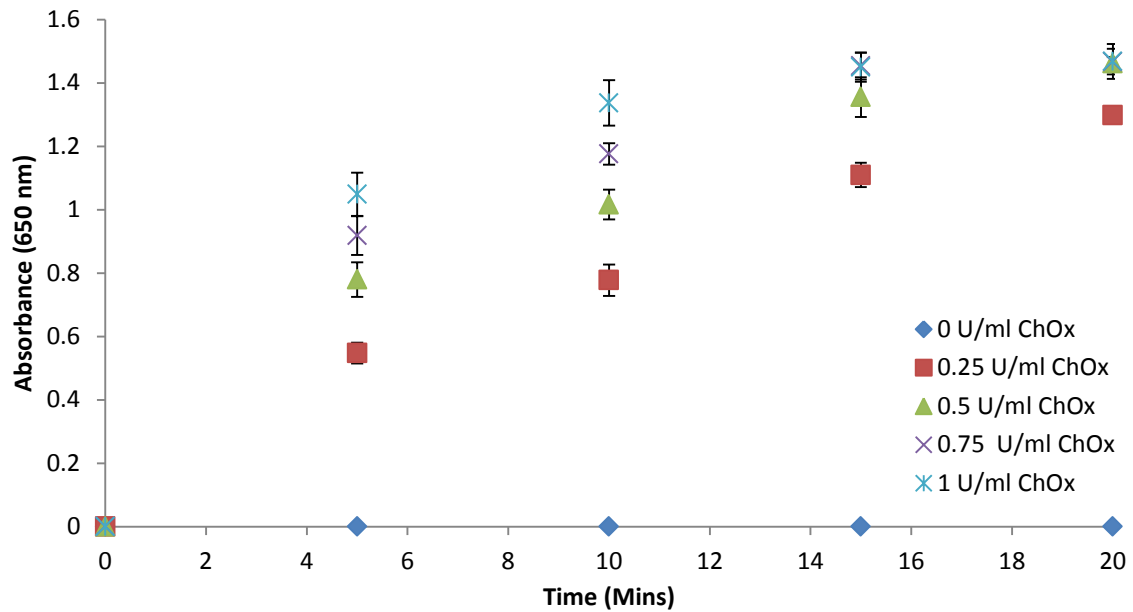


Figure 3.13: Change in absorbance recorded at a range (0-1 U/ml) of ChOx concentrations with cholesterol (5.5 mM), HRP (6 U/ml), CTA (6 mM) and AAP (6 mM) in PBS (n=3).

Figure 3.14, shows that at a cholesterol concentration of 7.6 mM, a ChOx concentration of <1 U/ml was unable to complete the reaction within 20 minutes.

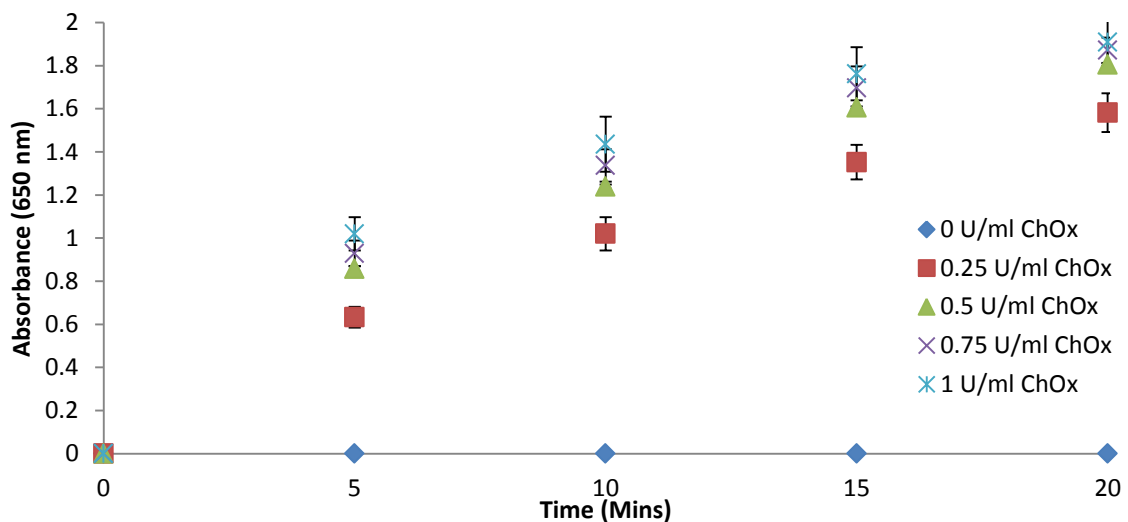


Figure 3.14: Change in absorbance recorded at a range (0-1 U/ml) of ChOx concentrations with cholesterol (7.6 mM), HRP (6 U/ml), CTA (6 mM) and AAP (6 mM) in PBS (n=3).

The slow reaction rate at high cholesterol concentrations is confirmed by Figure 3.15 for 8.9 mM cholesterol. The reaction was incomplete within 20 minutes at ChOx concentrations <1 U/ml.

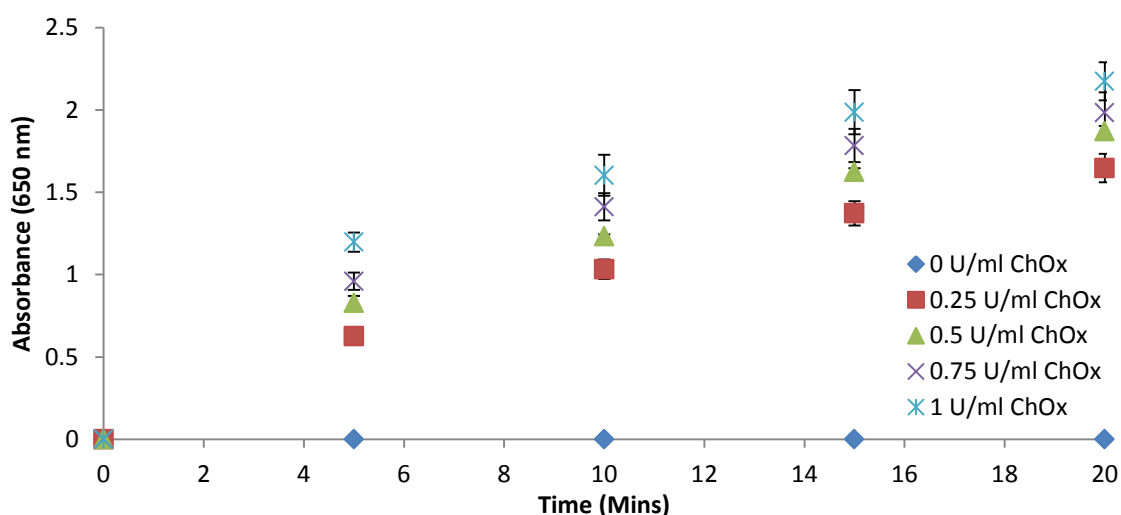


Figure 3.15: Change in absorbance recorded at a range (0-1 U/ml) of ChOx concentrations with cholesterol (8.9 mM), HRP (6 U/ml), CTA (6 mM) and AAP (6 mM) in PBS (n=3).

As the HRP concentration is capable of completing a reaction of 8 mM H_2O_2 within 5 minutes, it can be assumed that the rate limiting factor is the ChOx concentration. The enzyme concentrations employed in these reactions are lower than ideal, resulting in slower reaction rates; it would be preferential to investigate a ChOx concentration range of 0-10 U/ml and observe the reactions. However, if incubation time and temperature is controlled, it is still possible to take a measurement of cholesterol concentration without requiring reaction completion. For example, when the 1 U/ml ChOx absorbances are plotted after 5 minutes incubation, Figure 3.16, the general trend in increasing absorbance can be seen.

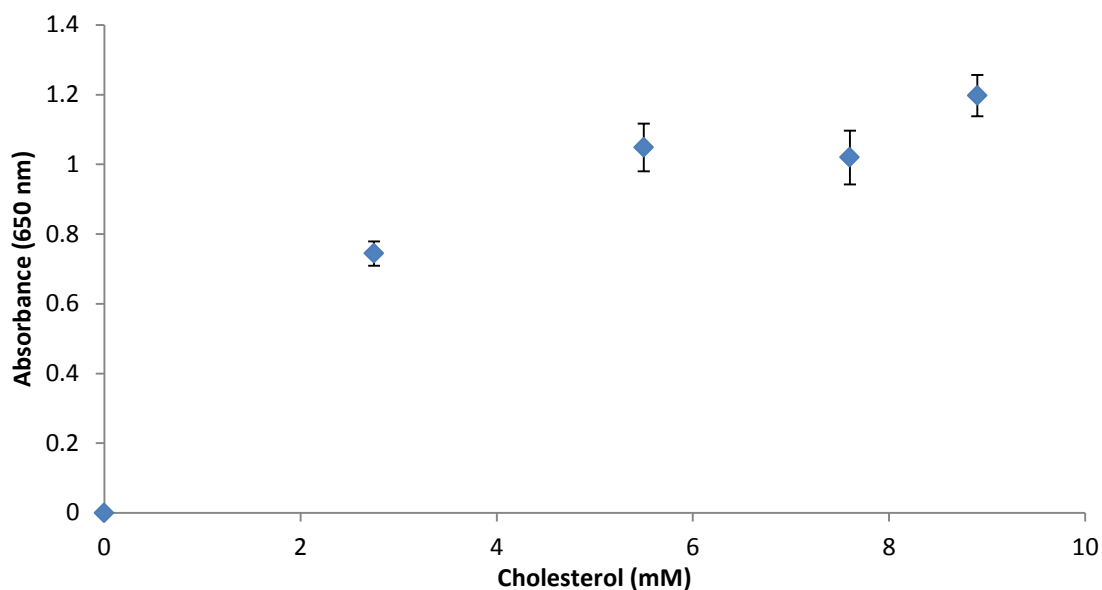


Figure 3.16: Change in absorbance recorded at a range (0-8.9 mM) of cholesterol concentrations with ChOx (1 U/ml), HRP (6 U/ml), CTA (6 mM) and AAP (6 mM) in PBS (n=3).

A ChOx concentration of 1 U/ml will be used for future work. It should also be noted that the results displayed no absorbance interference due to the ChOx concentration.

3.3.5 Development of the Cholesterol Assay in Buffer

The first stage of the combined assay testing involved the use of buffer solution spiked with cholesterol solution, as shown in Figure 3.17.

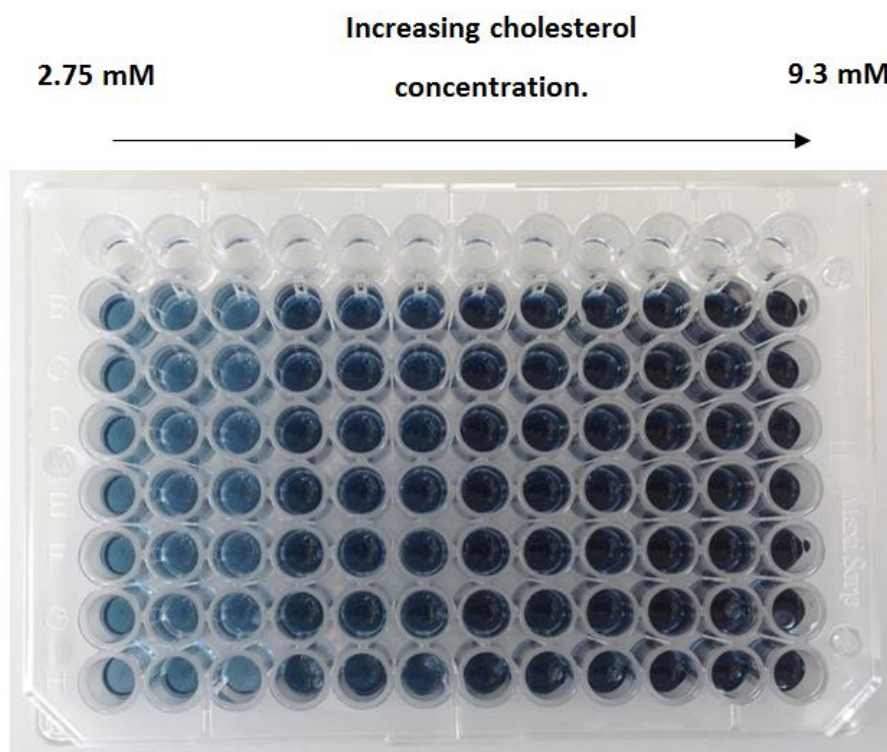


Figure 3.17: The image shows the quinoneimine dye concentration observed as cholesterol concentration increases after 5 minutes incubation. The assay contains cholesterol (0-9.3 mM), ChOx (1 U/ml), HRP (6 U/ml), CTA (6 mM) and AAP (6 mM).

In all cases, blue quinoneimine dye in the 650 nm region was produced, as can be seen in Figure 3.17, with the colour intensity increasing as the cholesterol concentration increased and over time as the reaction continued. In the absence of cholesterol no blue dye was produced and no absorbance at 650 nm was detected.

After 5 minutes of incubation, a clear correlation between concentration and absorbance can be seen, as shown in Figure 3.18. The absorbance increases as the incubation time increases and the reaction continues. The long reaction time observed highlights the low ChOx concentration of 1 U/ml and reiterates the need for increased ChOx enzyme in the final assay. The distinct absorbance produced at each cholesterol concentration shows that the combined assay can quantify cholesterol in solution.

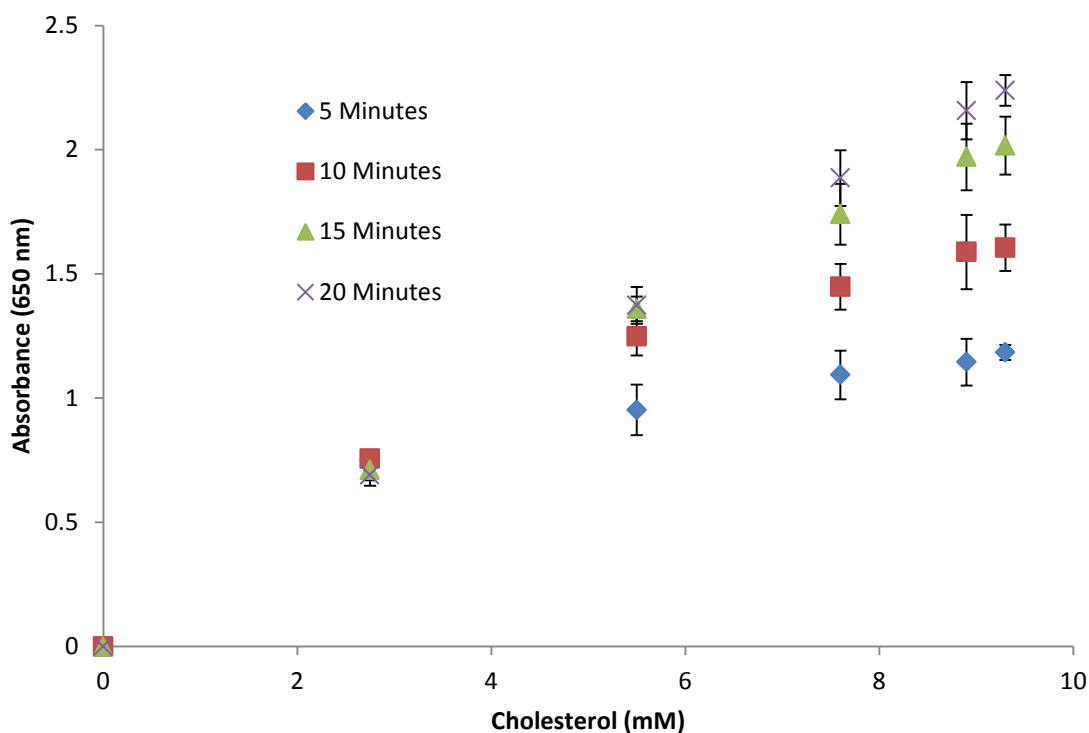


Figure 3.18: Change in absorbance recorded at a range (0-9.3 mM) of cholesterol concentrations with ChOx (1 U/ml), HRP (6 U/ml), CTA (6 mM) and AAP (6 mM) in PBS (n=7).

3.3.6 Development of the Cholesterol Assay in Plasma

The second stage of the combined assay testing used horse plasma spiked with cholesterol solution as the sample. The unspiked horse plasma was tested for the baseline cholesterol already present in the sample; it was then spiked with cholesterol solutions to produce the necessary sample concentrations. The concentration of the cholesterol solution used to spike the plasma was increased so that the sample would be diluted as little as possible.

Defibrinated horse blood was used as it contains no anticoagulant, reducing the risk of interference with assay reagents. Risk of infection by blood samples is null, so vaccinations are not required, but safe handling must be adhered to, as with any laboratory based reagents. It is also low-cost (approximately £10 per 100 ml) and

readily available. For this project, the blood samples are used to demonstrate the assay functionality, specifically colour generation, in whole blood and, as the project progresses, blood separation within 3D-printed devices. Thus horse blood samples fulfil this role adequately.

The horse plasma was prepared by centrifuging defibrinated whole horse blood at 5000 RPM for 15 minutes and extracting the liquid fraction. Ideally, transparent, pale yellow plasma would be extracted after centrifugation. However this was not possible, regardless of centrifugation time and speed. Several different preparations of horse blood were tested for their plasma properties, including defibrinated horse blood and oxalated horse blood. Cell solids would separate in defibrinated horse blood and horse blood in oxalate, but the resulting liquid fraction was still red, rather than the pale yellow colour that is expected when human blood is separated. It was suspected that the red colouration present in the plasma was due to cell lysis releasing cell protein, which became dissolved in the plasma. The reason for the cell lysis is suspected to be due to the blood not being freshly harvested before each use; there was always a minimum of 24 hours between the blood being harvested and the earliest possible testing.

As the absorbance of the blue quinoneimine dye is in the 550-650 nm wavelength range, the impact on absorbance measurements of the red plasma should be minimal. However, it would complicate readings being performed by eye without a spectrophotometer. As can be seen in Figure 3.19, the plasma obtained had a strong red colour. Defibrinated whole horse blood was used in all assay testing due to the lack of anticoagulant (such as oxalic acid in oxalated blood) which may introduce cross-reactivity in the assay.



Figure 3.19: Transparent red plasma after defibrinated whole horse blood was centrifuged at 5,000 RPM for 15 minutes.

The solution to this was to ‘wash’ the blood. 1 ml of defibrinated whole horse blood was centrifuged for 2 minutes in 1.5 ml Eppendorf tubes using a benchtop microcentrifuge at 6000 RPM to separate the solid blood cells from the liquid plasma. The 500 μ l of liquid component was then extracted, ensuring no solid was removed, and replaced with the same volume of PBS pH 7.4 solution. The blood solution was then mixed thoroughly and the red blood cells resuspended. This process was repeated once more until the red colouration was not visible in the liquid component produced after centrifugation. There is a slight colour difference observed between the raw blood and the ‘washed’ blood, however, this should not influence blood separation results. Images can be seen in Figure 3.20. In addition, there would likely be a change in viscosity between the raw and ‘washed’ blood, with the raw blood being more viscous and therefore requiring more force to separate the blood cells. However, this should not significantly impact experimentation at this stage of preliminary development.

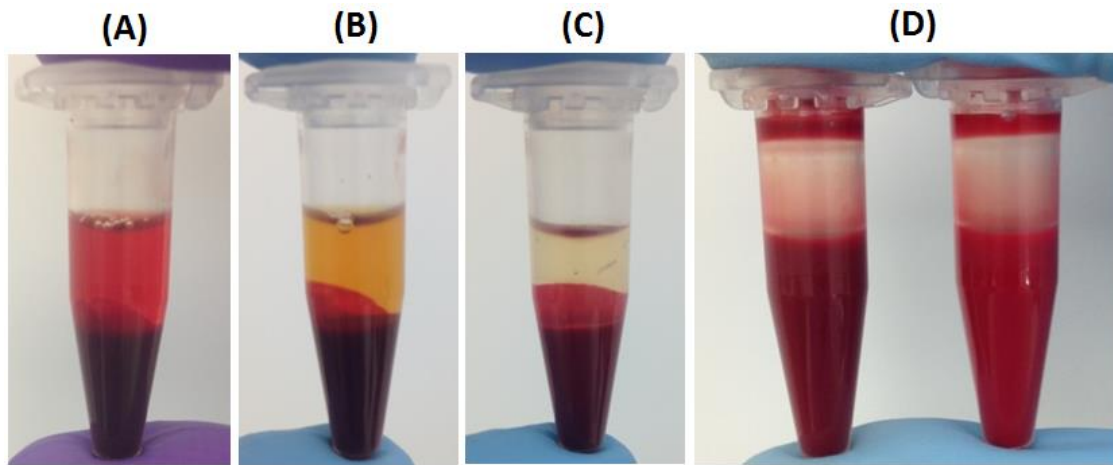


Figure 3.20: Defibrinated whole horse blood after centrifugation, (A) wash 0; (B) wash 1; (C) wash 2; (D) suspended whole horse blood before (left) and after (right) washing.

As the experimentation using whole blood in this project was to demonstrate that blood cells can be separated within a 3D-printed device using a standard DVD optical drive and that a DVD optical drive is capable of applying sufficient centrifugal force necessary to separate blood cells within the desired time period (≤ 2 minutes), it was concluded that this protocol of ‘washing’ the blood to produce a colourless/pale yellow liquid component from whole blood was sufficient for this project, and this stage of assay/device development, to demonstrate the blood separation capabilities of the platform/device. It should be noted that the blood washing protocol was not investigated before the cholesterol assay development and only implemented when assay development progressed to the stage of whole blood separation and glucose assay performance in 3D-printed devices (section 5.3.1).

Experimentation of the cholesterol assay in horse plasma was performed. Two control sample tests were performed. The first contained horse plasma with no assay reagents added, with the aim of testing for interference introduced by the red plasma. The second control contained HRP (6 U/ml), CTA (6 mM) and AAP (6 mM) in horse plasma with no ChOx, in order to test for possible interactions between the plasma and the reagents, which may introduce interference. In all cases, blue quinoneimine dye in the

650 nm region was produced with the colour intensity increasing as the cholesterol concentration increased and over time as the reaction continued, as seen in Figure 3.21.

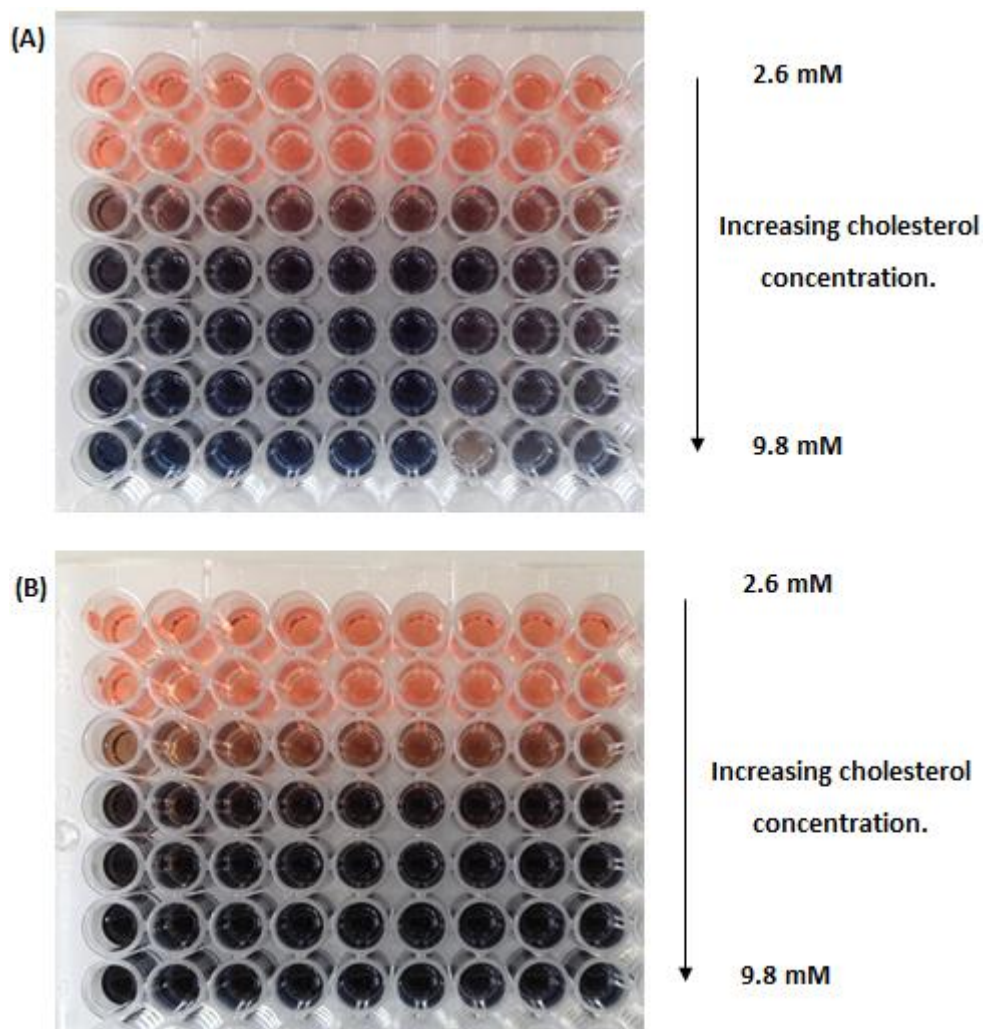


Figure 3.21: The image shows the quinoneimine dye concentration observed as cholesterol concentration increases. (A) Colour immediately after sample application (0 minutes incubation); (B) colour after 5 minutes incubation.

Figure 3.22 shows that the combined assay produces clearly distinguished absorbance values quantifying cholesterol in plasma. As the cholesterol concentration increased so did the absorbance. No absorbance was detected in control 1, so it can be concluded there was no interference introduced through the use of red plasma. In the absence of ChOx in control 2, no blue dye was produced and no absorbance at 650 nm

was detected and so it is concluded that there were no observable reactions/matrix effects between the plasma and reagents.

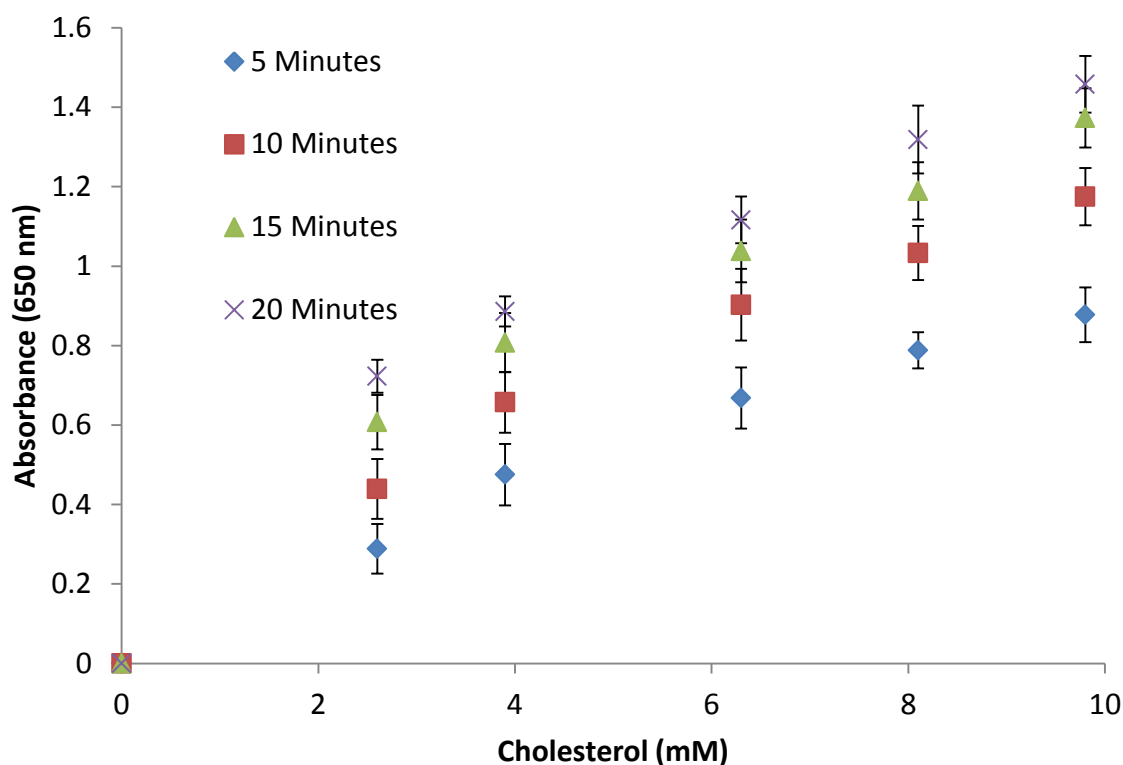


Figure 3.22: Change in absorbance recorded at a range (0-9.3 mM) of cholesterol concentrations with ChOx (1 U/ml), HRP (6 U/ml), CTA (6 mM) and AAP (6 mM) in horse plasma (n=9).

3.3.7 Development of the Cholesterol Assay in Whole Blood

The final stage of the combined assay testing was undertaken using whole horse blood spiked with cholesterol solution as the sample. The untreated whole horse blood was tested for the cholesterol already present in the sample. It was then spiked with cholesterol solution to produce the necessary sample concentrations. The concentration of the cholesterol solution used to spike the plasma was increased so the sample would be diluted as little as possible. According to the supplier, defibrinated whole horse blood has a guaranteed packed cell volume of 40-50% (Tcsbiosciences.co.uk, 2015) and it was established from plasma testing that

approximately 50 μl plasma is obtained from 100 μl whole blood. This results in an increased reagent concentration of approximately 100% when whole blood is used rather than PBS/plasma. It was decided that reagent quantities (ChOx, HRP, CTA, and AAP) would not be adjusted accordingly so the established quantities would remain acceptable in both plasma and whole blood samples of the same volume. However, it is expected that the reaction rate in whole blood will increase due to the increased concentration of reagents relative to PBS/plasma.

Sample solutions containing HRP (12 U/ml), CTA (12 mM), AAP (12 mM) and cholesterol (0-12 mM) in defibrinated whole horse blood were prepared. The reaction was started by adding ChOx (2 U/ml). Total sample volume was 1 ml. The samples were then mixed thoroughly and left to incubate at room temperature for 5 minutes for the enzyme reaction to take place and for the colour to develop. The results are shown in Figure 3.23.

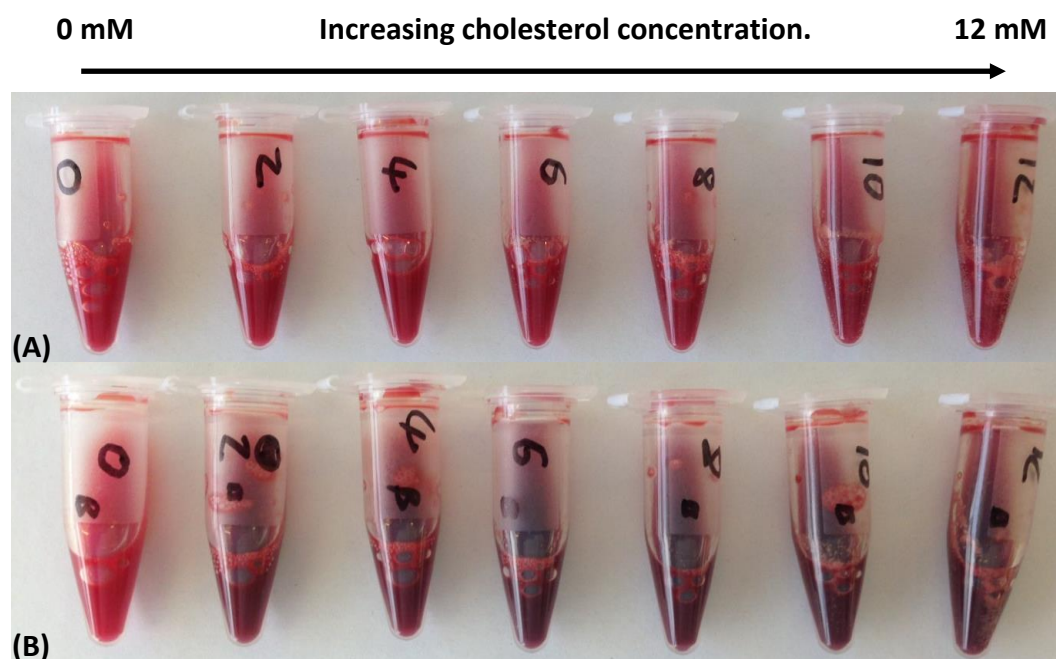


Figure 3.23: The image shows the quinoneimine dye concentration observed in whole horse blood as cholesterol concentration increases. (A) Before addition of ChOx; (B) after addition of ChOx (2 U/ml) and 5 minutes incubation.

The samples were then centrifuged for 5 minutes at 8000 RPM and the liquid fraction extracted, as shown in Figure 3.24.

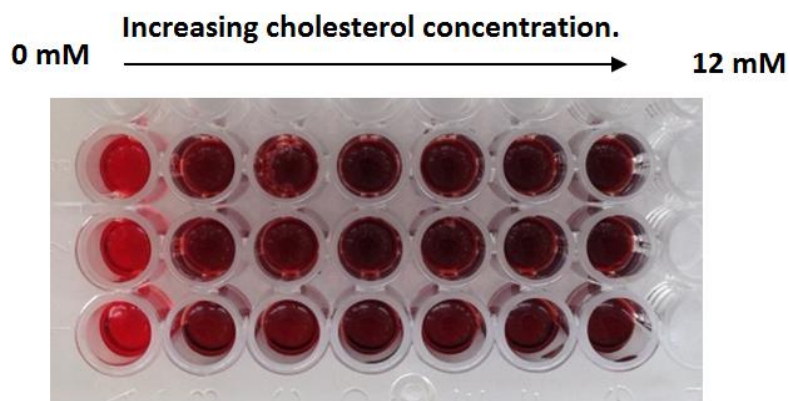


Figure 3.24: The image shows the quinoneimine dye concentration observed as cholesterol concentration increases in plasma extracted from whole horse blood.

The absorbance at 650 nm was measured in 100 μ l after a total of 10 minutes, after the initiation of the reaction (5 minutes incubation and 5 minutes centrifugation) and then again after a further 10 minutes (20 minutes total), to monitor any absorbance changes. A control was run containing HRP (12 U/ml), CTA (12 mM) and AAP (12 mM) in whole horse blood but no ChOx enzyme. Figure 3.25 shows that the combined assay can be used to quantify cholesterol in whole blood with absorbance increasing as cholesterol concentration increases.

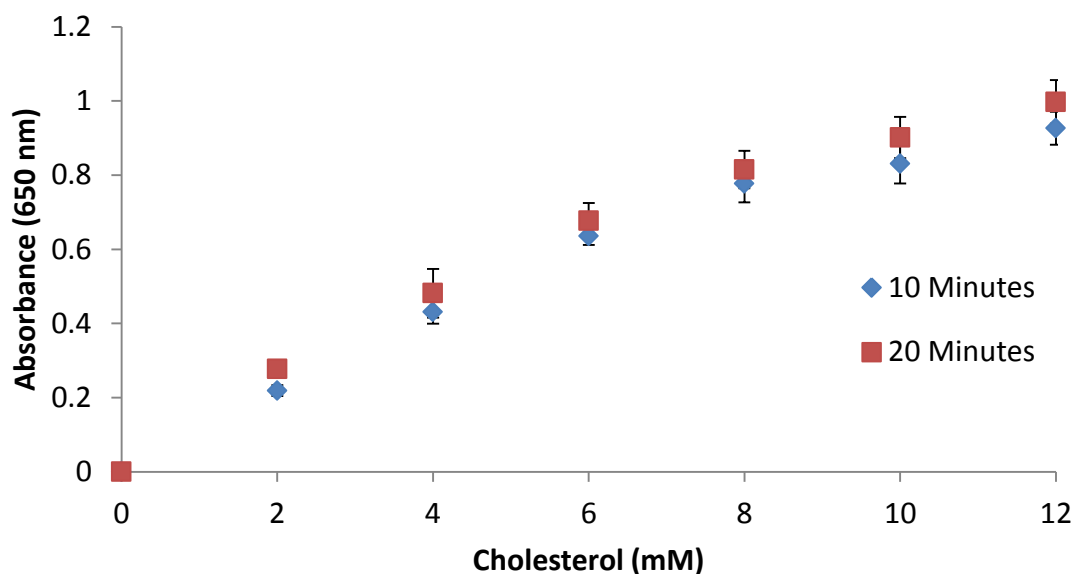


Figure 3.25: Change in absorbance recorded at a range (0-12 mM) of cholesterol concentrations with ChOx (2 U/ml), HRP (12 U/ml), CTA (12 mM) and AAP (12 mM) in whole horse blood (n=6).

There was a minor increase in absorbance (<2%) across all concentrations after 20 minutes total incubation time indicating that the reaction was largely complete after 10 minutes; this is due to the 100% increased enzyme concentration in whole blood relative to plasma. The experiments performed showed that ChOx, HRP, CTA and AAP when mixed together produce an enzymatic cascade and optical reaction that can distinguish between a range of cholesterol concentrations in various solution mediums including whole blood. There was clear correlation between the different cholesterol concentrations and absorbance produced; as cholesterol concentration increases, absorbance increases. The current study was quantifying free cholesterol in whole blood. The reaction could be expanded to quantify total cholesterol in blood through the addition of cholesterol esterase into the enzyme mixture. However this has yet to be implemented at this stage. The application of this assay for the detection of cholesterol in whole blood has previously not been published.

The work presented so far has demonstrated the capability of the assay for the quantification of cholesterol in plasma and whole blood samples. The assay can be altered for the detection and quantification of other compounds that can be reacted to produce H₂O₂. Compounds such as lactate and glucose could be assayed by simply replacing ChOx with lactate oxidase or GLOx respectively. Assay development for the quantification of glucose is now detailed.

3.3.8 Optimisation of Glucose Oxidase (GLOx) Concentration

GLOx from *Aspergillus Niger* was used in this assay as it is the most commonly used source of GLOx in glucose assays and is widely available (Bankar *et al.*, 2009). Experiments were performed to try to determine the necessary concentration of GLOx for an acceptable reaction time (≤ 2 minutes). PBS pH 7.4 is used as the solution medium in order to mimic blood conditions, and to provide easy identification of reaction rates at specific enzyme concentrations, allowing increased or decreased enzyme concentration to be used where required compensating for device limitations without needing sample pre-treatment, which is undesirable for this assay. The

optimum pH range for GLOx is 4-7, so at pH 7.4 the reaction rate should not be impacted. However, should the reaction rate be too slow, a higher quantity of enzyme can be used to help negate this. It was decided to observe the reaction rate at a single substrate concentration at the high end of the clinically relevant glucose range of the substrate detection scale (10 mM) and at a single incubation time reasonable for a point-of-care device (POC) (2 minutes). This would be sufficient to determine what concentration of GLOx would be necessary for an acceptable assay rate without requiring excessive consumption of enzyme and reagents.

In all cases, blue quinoneimine dye was produced and visible with the colour intensity increasing as GLOx concentration increased. In the absence of GLOx no blue dye was produced. Figure 3.26 shows the absorbance produced using 10 mM glucose solution with varying GLOx concentration after 2 minutes incubation. There was an approximate 34% increase in absorbance between 5 U/ml and 50 U/ml; the greater the GLOx concentration the greater the absorbance detected due to the greater reaction rate. The data showed that the reaction time can be controlled by adjusting enzyme concentrations.

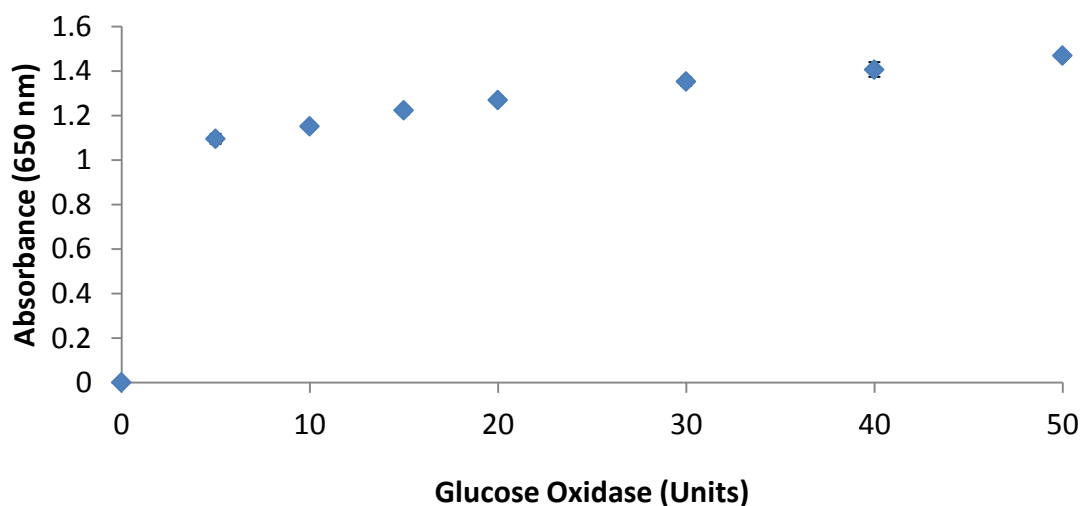


Figure 3.26: Change in absorbance recorded at a range (0-50 U/ml) of GLOx concentrations with glucose (10 mM), HRP (6 U/ml), CTA (20 mM) and AAP (10 mM) in PBS (n=3).

A GLOx concentration of 20 U/ml of sample will be used for future work as this will provide an acceptable reaction time (≤ 2 minutes). By increasing or decreasing GLOx concentration, the reaction rate can be changed and therefore shift the absorbance curve up or down according to requirements. While higher concentrations would decrease the reaction time, this would put more emphasis on precise incubation time and potentially introduce discrepancies/errors should absorbance readings be taken too early or late. When moving towards on-device testing, smaller enzyme quantities could be used whilst maintaining the relative concentration and reaction rates due to smaller sample volumes and therefore, smaller glucose quantities being used. It should also be noted that the results display no absorption interference due to the GLOx concentration.

3.3.9 Development of the Glucose Assay in Buffer

The first stage of glucose assay testing uses PBS buffer pH 7.4 spiked with glucose solution as the sample, as shown in Figure 3.27. The assay combines concentration data obtained from the previous experiments on CTA and AAP (section 3.3.2), HRP (section 3.3.3) and GLOx (section 3.3.8). In all cases blue quinoneimine dye in the 590 nm region was produced, as can be seen in Figure 3.27, with the colour intensity increasing as glucose concentration increased as can be seen in Figure 3.28. In the absence of glucose, no blue dye was produced and no absorbance at a wavelength of 590 nm was detected.

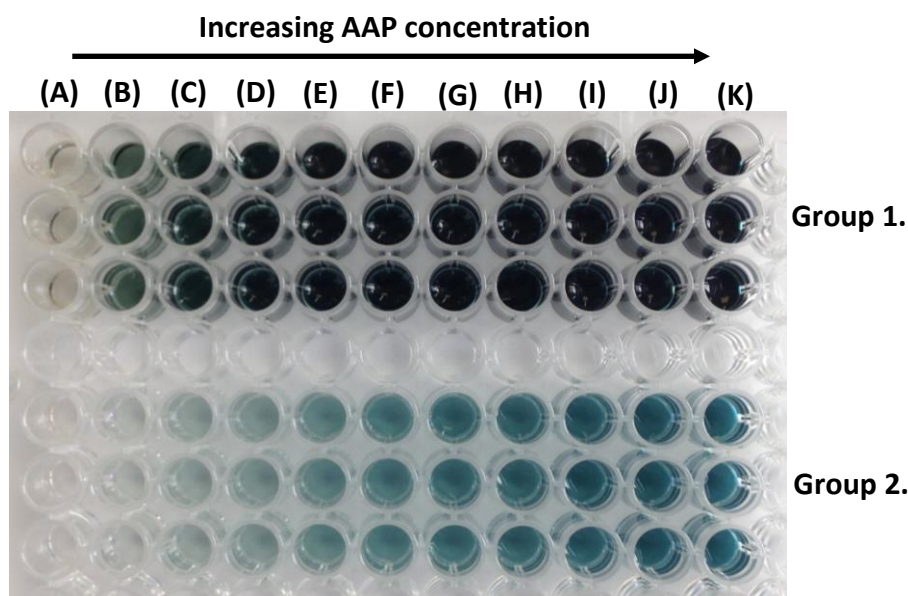


Figure 3.27: Glucose assay in buffer. The image shows the quinoneimine dye concentration observed as glucose concentration increases. Group 1 is undiluted sample; group 2 is a 1 in 10 dilution. Each well contains 100 μ l taken from each 1 ml sample. Each sample contains GLOx (20 U/ml), HRP (6 U/ml), CTA (20 mM), AAP (10 mM) and varying concentrations of glucose as follows: Line (A) 0 mM; (B) 1 mM; (C) 2 mM; (D) 3 mM; (E) 4 mM; (F) 5 mM; (G) 6 mM; (H) 7 mM; (I) 8 mM; (J) 9 mM; (K) 10 mM.

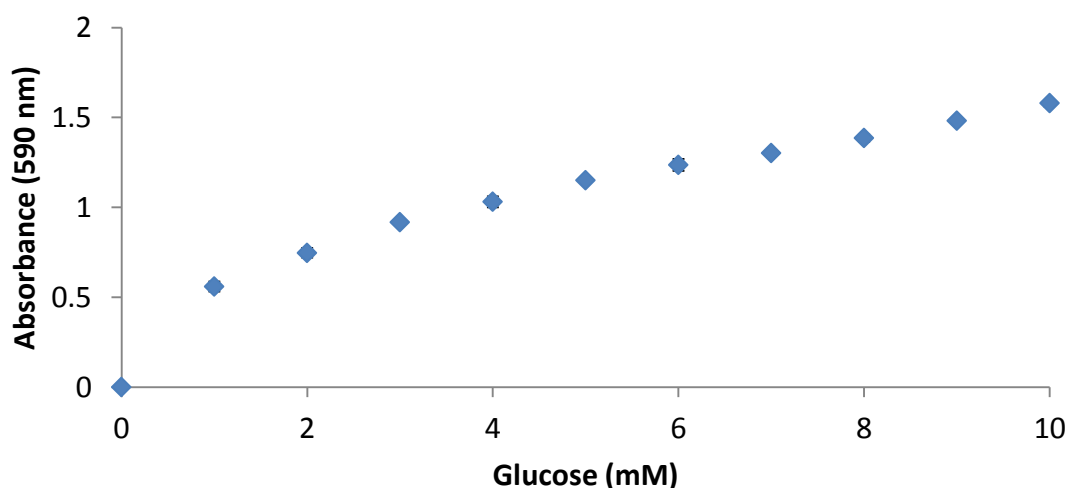


Figure 3.28: Change in absorbance recorded at a range (0-10 mM) of glucose concentrations with GLOx (20 U/ml), HRP (6 U/ml), CTA (20 mM) and AAP (10 mM) in PBS (n=3).

An experiment was performed to investigate the glucose assay reaction in buffer over time. The intention was to monitor reaction progression with longer incubation periods and to identify a time range in which the quinoneimine dye remains stable and can be used to quantify glucose concentration. The sample was incubated for 5 minutes then the absorbance at 590 nm was measured in 100 μ l. Absorbance was measured again after 7, 10 and 30 minutes total incubation time. In all cases blue quinoneimine dye in the 590 nm region was produced with the colour intensity increasing as glucose concentration increased and over time up to 10 minutes as the reaction continued, as seen in Figure 3.29.

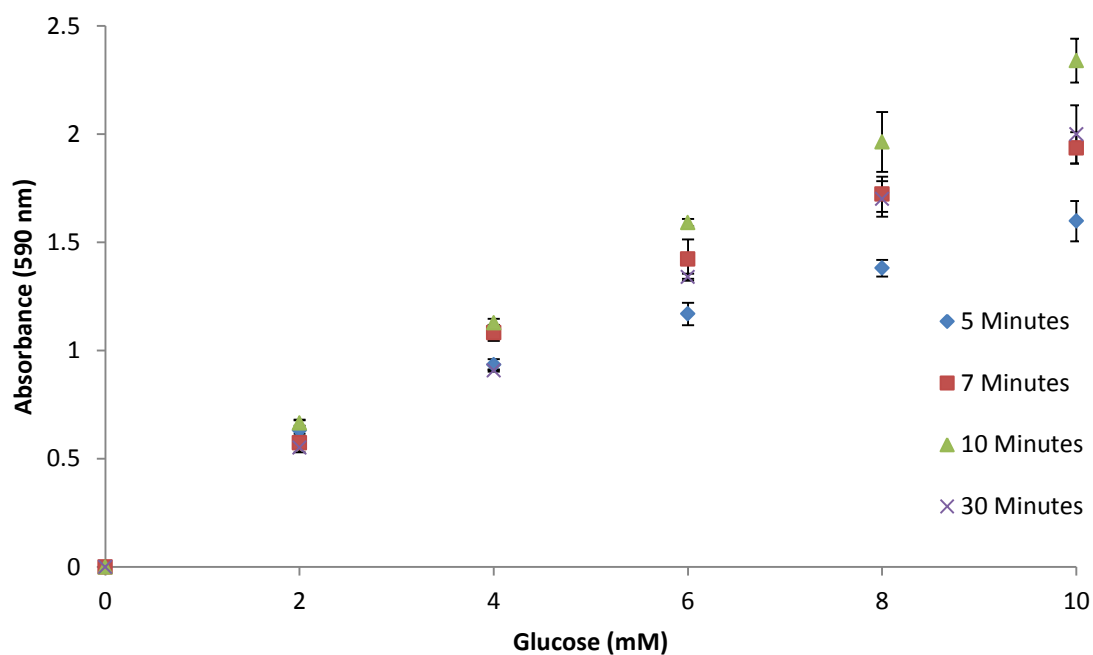


Figure 3.29: Change in absorbance recorded at a range (0-10 mM) of glucose concentrations with GIOx (20 U/ml), HRP (6 U/ml), CTA (20 mM) and AAP (10 mM) in PBS (n=3).

As can be seen in Figure 3.29, the absorbance measured after each period of incubation increases as the glucose concentration increases. The absorbance curve

shifts up as the incubation time increases and as the reaction continues. Between 10-30 minutes incubation the absorbance begins to decrease. This illustrates the stability of quinoneimine dye over 10 minutes, after which decomposition begins and absorbance drops. However, as the assay is intended to generate results within 2 minutes in a POC setting, this is not problematic. The reaction can be completed within this time period simply by increasing enzyme concentration if necessary. The distinct absorbance produced at each glucose concentration shows that the assay can quantify glucose in solution and the absorbance curve can be shifted by changing incubation time: shorter incubation time results in lower absorbance, longer incubation results in higher absorbance up to 10 minutes. Assay optimisation will continue, however, this shows that it is possible to quantify glucose concentration in buffer with a range of 0-10 mM as required for the project aims and objectives.

3.4 Conclusions

It was shown that HRP, CTA and AAP when mixed together with either ChOx or GLOx, produce an enzymatic cascade and blue quinoneimine dye with a correlation between absorbance and substrate (cholesterol/glucose) concentration. A substrate range of 0-10 mM was quantified in various solution mediums including whole blood. The experiments presented demonstrate a quantification method for cholesterol in whole blood that has not been published previously. The final assay reagent concentrations were CTA (20 mM), AAP (10 mM), HRP (6 U/ml), ChOx (1 U/ml) and GLOx (20 U/ml).

The ChOx concentration was found to be the primary rate limiting factor encountered in the cholesterol assay, however, as demonstrated in section 3.3.7, this did not prevent the quantification of cholesterol in whole blood or the generation of a trend line within a 5 minute incubation period; as cholesterol concentration increased the absorbance increased. The low reaction rate seen could be corrected through the use of an increased concentration of ChOx in the assay. However, in an attempt to conserve ChOx quantities, the increased concentration was not implemented. Despite

long/incomplete reaction times seen in the combined assay, with optimisation and a fixed time assay, cholesterol quantification could still be performed by generating a calibration curve using lower absorbance values.

Difficulties were encountered during testing regarding the making of cholesterol solution, the independent quantification of cholesterol and the red coloured plasma obtained from the whole horse blood. The results showed that the red plasma had a minimal effect on absorbance and the 'blood washing' protocol that was developed would aid in observing blood cell separation performed in a LOAD device. The use of a low cost POC electrochemical assay for the independent quantification of cholesterol in solution was not ideal due to the inaccuracy displayed, however, absorbance trend lines were obtained regardless; a cholesterol quantification method with improved accuracy will be used in future work.

An enzymatic assay capable of quantifying 0-10 mM glucose concentration in buffer has been developed and optimisation has progressed. The experiments performed showed that GLOx, HRP, CTA and AAP, when mixed together, produce an enzymatic cascade and optical reaction that can distinguish between a range of glucose concentrations in PBS pH 7.4 solution.

There was clear distinction between the different glucose concentrations and absorbance produced; as the glucose concentration increased, the absorbance increased, but the protocol needs optimisation for use in the intended assay platform to standardise the absorbance values and to generate a calibration curve for on-device testing. When using H₂O₂ in lieu of glucose and GLOx, the reactions were complete within 5 minutes of incubation. However, when glucose and GLOx were used the reaction rate dropped, although not significantly, this being due to the incorporation of an additional reaction step. As discussed in section 3.3.8, the reaction rate can be increased or decreased by increasing or decreasing the GLOx concentration respectively, however, a GLOx concentration of 20 U/ml was sufficient at generating an absorbance trend line within 5 minutes incubation.

The testing showed that the absorbance curves can be shifted up or down according to incubation time, enzyme concentration and, to a lesser extent, CTA concentration. This allows the assay to be adjusted by increasing or decreasing the colour intensity.

Due to the dimerization of AAP it was decided that a molar ratio of 2:1 CTA:AAP must be maintained, therefore a concentration of CTA (20 mM) and AAP (10 mM) was used. This concentration will be used for both cholesterol and glucose testing that takes place in future work so the assay solutions can be used to quantify both substrates without requiring a change in concentration; glucose has a higher clinically relevant quantification range and therefore requires a higher concentration of reagents relative to cholesterol. In addition, CTA, AAP and enzyme quantities in solution were not adjusted for whole blood relative to plasma as this provides flexibility in what samples can be tested without requiring a change in reagent quantities.

Cholesterol and glucose colourimetric assays have been developed that produce distinct absorbance curves in the 650 nm region, the wavelength of the laser used in a DVD optical drive. Therefore, a standard unmodified DVD optical disc drive (ODD) could be used to quantify absorbance changes in these assays. The next stage of assay testing will involve the use of whole blood spiked with glucose solution, moving towards using 3D-printed devices, such as cuvettes and microfluidic channels, in which to quantify substrate. The testing will explore the problems and limitations of 3D-printed objects for assay device development and how to minimise them.

Chapter 4: Lab-On-A-Disc Platform Design and Manufacture

4.1 Introduction

The ability to manufacture detailed and complex prototypes in a fast and efficient way has led to rapid prototyping technology becoming a fundamental tool for many areas of research and development. Fused deposition modelling (FDM) based 3D printers are readily available for purchase, either as self-assembly kits or as pre-assembled units; they are already being used to develop components for research, as an on-site 3D printer allows for a rapid print, test and redesign sequence until an optimised product is achieved. Although design and manufacture takes time, the ability to make distinct items in the testing environment is highly advantageous regarding time and cost effectiveness when compared to external sourcing. The fact that a computer aided design CAD model is produced as part of the design process also means that it can be used with other computer aided manufacturing processes should the 3D printing technology not allow fabrication of devices with the required properties.

The rapid advancement of low-end 3D-printing technology (< £2000) is largely due to the development of free and open source software and hardware (Zhang *et al.*, 2013). The large open community that surrounds the use of rapid prototyping technology is actively altering and improving the 3D printers, accelerating the advance of the technology. In addition, there is a large library of CAD models available freely, which provides shortcuts to product development.

The aim of the work presented in this chapter is to design, create and test 3D-printed objects with optical transparency such that colour change can be viewed and ultimately quantified within the object. Optical transparency is the physical property of allowing light to pass through the material without being scattered. The attenuation of light of all frequencies and wavelengths is due to the combined mechanisms of absorption and scattering (Fox, 2001). The results of the investigations could then be applied to the development of a lab-on-a-disc (LOAD) microfluidic platform for the colourimetric quantification of substrates in whole blood. The primary goals are to investigate manufacturing and post-production techniques to, (A) improve optical

transparency of low-cost 3D-printed objects and (B) form imbedded water-tight microfluidic channels within 3D-printed devices. The primary stages involved in making a 3D-printed product are creation of a CAD file, conversion and preparation of the file using a slicer program, then uploading the file to the printer and the physical creation of the object. The process from CAD model to completed printed object will be detailed and demonstrated.

4.2 Materials and Methods

The materials, equipment and software that were used are detailed in this section. Schematics of 3D-printed objects that were used as test samples are also included.

4.2.1 3D-Printer

All 3D printed models were fabricated using an Ultimaker 2+ 3D printer (cost: ~£1500) using a 0.4 mm nozzle size (Ultimaking Ltd., Netherlands) Figure 4.1.

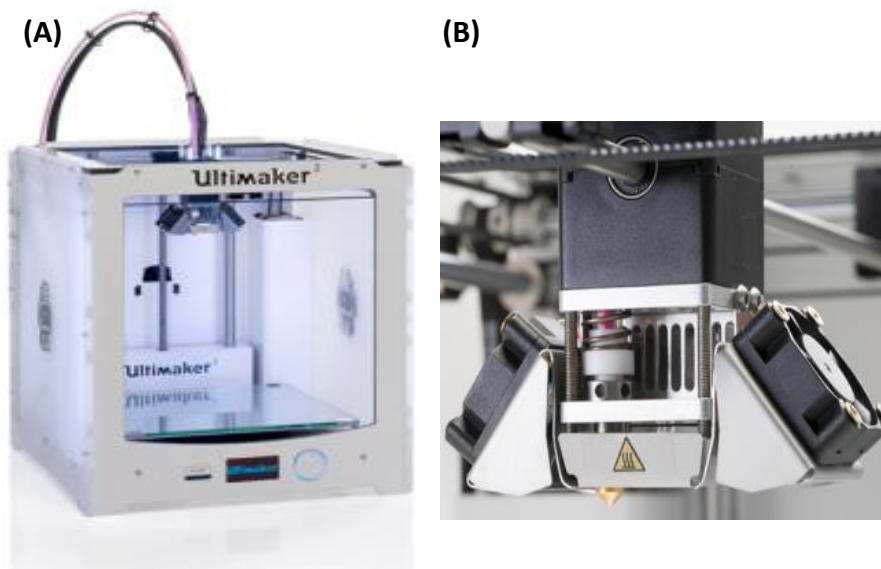


Figure 4.1: Ultimaker 2+, (A) 3D-printer; (B) print head/extruder (Ultimaker Ltd., 2014).

The Ultimaker 2+ printer uses a filament diameter of 2.85 mm and is equipped with a single print head/extruder. The build table moves vertically along the z-axis, while the print head moves horizontally in the x-y plane. The positional accuracy of the printer in the X, Y and Z dimension is 12.5, 12.5 and 5 μm respectively. The nozzle size of 400 μm allows for the design and constructions of features (such as channels) over a range of 20 μm to 200 μm layer resolution/layer height. The available build volume is 230 mm x 225 mm x 205 mm. The print layer resolution/layer height (Z-axis) is up to 20 μm for high quality/fine detail prints. The print speed can range up to 300 mm/s. The nozzle temperature during operation is variable from 180 – 260°C and the printer is equipped with a heated build table variable from 50 – 100°C. The heated build table reduces warping issues that can be severe for elongated, rectangular shaped objects and allows for printing using acrylonitrile butadiene styrene (ABS) (MakerGeeks.com, 2014). The warping of the printed structure primarily occurs at the contact surface of the printed object and the build table due to the large temperature difference between the hot melt extrusion and the colder table; the first layers deposited cool down quicker and shrink, which causes the lower parts of the model to bend up at the edges. Heating up the build table reduces this temperature difference which reduces the shrinkage that occurs when the plastic cools quickly, therefore, warping issues are significantly reduced (Wang *et al.*, 2007; Kantaros and Karalekas, 2013). In polylactic acid (PLA) models, less shrinkage occurs during cooling compared to ABS which is prone to shrinkage and warping; as a result PLA tends not to require a heated build table whereas it is required when printing in ABS (Grieser, 2016).

When printing in PLA, the heated build table of the 3D-printer is set to 60 °C as PLA has a glass transition temperature of 60-65 °C (Grieser, 2016). The glass transition temperature is the range over which the mobility of polymer chains increases significantly compared to colder temperatures. By printing on to a surface which is at the glass transition temperature it is suspected that polymer chain mobility is maintained which may cause the deposited polymer strands to have increased merging which could result in improved layer homogeneity.

4.2.2 Software

The software used in this work is as below:

- Sketchup (Trimble Navigation Ltd., USA): 3D CAD modelling.
- Cura (Ultimaker Ltd., Netherlands): CAD model slicer and printer control.
- SpectraSuite (Ocean Optics, USA): Spectrum generation and analysis.
- Image J (ImageJ.net): OCT image analysis.

4.2.3 3D-Printing Process

When using 3D-printing, several stages are required in order to progress from a conceptual idea to a physical model. The protocol followed in this thesis is as follows:

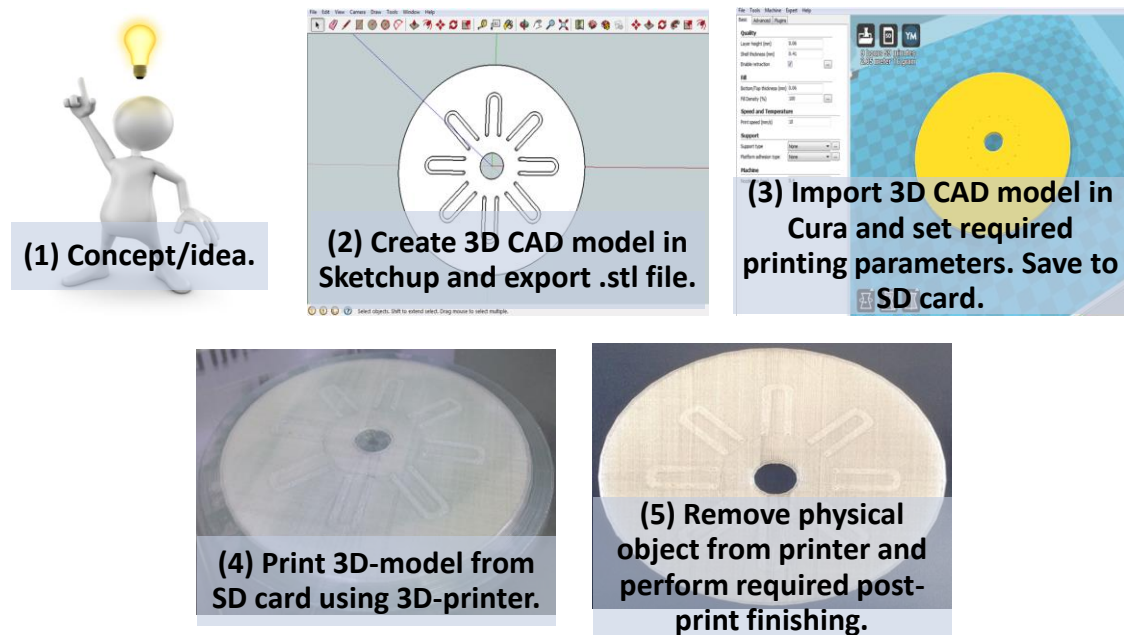


Figure 4.2: 3D-printing protocol followed in this thesis.

4.2.4 Print Material

There are several different materials available for use with FDM 3D printers, each with their own strengths, weaknesses and distinct characteristics. For this project,

the primary factor to be considered when choosing a print material is the transparency of the final item. Factors such as strength, extrusion temperatures and warping tendencies are also important. Currently the most commonly used materials for FDM 3D printing are PLA and ABS; both are classed as thermoplastics, PLA is further classed as a polyester plastic, ABS is further classed as a styrenic plastic (Makeitfrom.com, 2017). Table 4.1 contains a summary of quick reference, non-technical differences to be considered when working with ABS or PLA. Table 4.2 contains a comparison between the thermal properties of ABS and PLA. Table 4.3 contains a comparison of ABS and PLA material properties. Currently, there are several types of printing filament that are being marketed as natural, transparent or clear, but the actual optical transparency of the printed items tends to be poor for use in an optical device. The devices produced are not transparent but rather are translucent/ cloudy. Despite this, advances in 3D printing materials, like the printers themselves, have been and continue to be rapid and consistent, with new products becoming available daily.

Table 4.1: Quick reference of differences between ABS and PLA (English, 2012).

Acrylonitrile Butadiene Styrene	Poly(lactic Acid)
<ul style="list-style-type: none"> • Extrude at ~225°C • Requires heated build table • Does not required cooling • Adheres best to polyimide tape • Filament tolerances are usually tighter • Prone to cracking, delamination, and warping • More flexible • Can be bonded using adhesives or solvents (Acetone or MEK) • Fumes are unpleasant in enclosed areas • Oil Based 	<ul style="list-style-type: none"> • Extrude at ~180-200°C • Benefits from heated build table • Requires cooling while printing • Adheres to a variety of surfaces • Finer feature detail possible on a well calibrated machine • Prone to curling of corners and overhangs • More brittle • Can be bonded using adhesives • More pleasant smell when extruded • Plant Based

Table 4.2: Reference of thermal properties of ABS and PLA (Grieser, 2016).

Thermal Properties	ABS	PLA
Melt volume index	9.7 cm ³ /10 min	10.3 cm ³ /10 min
Glass transition temperature	105 °C	60-65 °C
Slumping temperature	110-125 °C	70-80 °C
Melting temperature	210-240 °C	160-190 °C
Printing temperature	230-250 °C	190-220 °C
Recommended build table temperature	80-120 °C (heated build table required)	50-70 °C (heated build table not required)

Table 4.3: Reference of material properties of ABS and PLA (Makeitfrom.com, 2017).

Material Properties	ABS	PLA
Density	1.0 to 1.4 g/cm ³	1.3 g/cm ³
Elastic (Young's, Tensile) Modulus	2.0 to 2.6 GPa (0.29 to 0.38 x 10 ⁶ psi)	3.5 GPa (0.51 x 10 ⁶ psi)
Elongation at break	3.5 to 50 %	6.0 %
Flexural Modulus	2.1 to 7.6 GPa (0.3 to 1.1 x 10 ⁶ psi)	4.0 GPa (0.58 x 10 ⁶ psi)
Flexural Strength	72 to 97 MPa (10 to 14 x 10 ³ psi)	80 MPa (12 x 10 ³ psi)
Strength to Weight Ratio	37 to 79 kN-m/kg	38 kN-m/kg
Tensile Strength: Ultimate	37 to 110 MPa (5.4 to 16 x 10 ³ psi)	50 MPa (7.3 x 10 ³ psi)

The quality of the final product largely depends on the printing parameters and post-print-finishing, so even if a particular material does not produce an acceptable optical transparency solely from the print, that does not mean it cannot be improved with post-print treatment. In this work experiments have been performed using a

variety of filaments and post-print finishing techniques to arrive at an acceptable material and manufacturing process.

Due to the properties listed above, the primary printing material will be PLA; with the goal ultimately to produce a LOAD platform, PLA's improved fine detail potential compared to ABS makes it a logical choice for initial designs, as precision is key when attempting to design and manufacture microfluidic channels; in addition, the use of PLA in biochemical devices is already established (Kadimisetty *et al.*, 2016; Pioggia *et al.*, 2007). While a number of materials can be used for 3D-printing, as the aim of the project is to investigate the capabilities of low-cost, commercially available 3D-printing resources for the development of point-of-care (POC) diagnostic devices, all print materials will be 750 g filament spools purchased from Ultimaker.com (Ultimaking Ltd., Netherlands). A number of different batches and makes of transparent filaments were used. The filaments tested include: Ultimaker PLA Translucent, Ultimaker PLA Transparent, Innofil PLA Natural and InnoPET Natural.

4.2.5 Other Materials

Acetone and isopropyl alcohol were purchased from Sigma-Aldrich (Poole, UK). Microscope images were taken using an Olympus BX51 microscope (Olympus Corporation, Japan).

4.2.6 Instrumentation Used to Measure Attenuation

Instrumentation (Figure 4.3) was assembled to quantify the difference in optical attenuation between the 3D-printed plastic samples. Plastic samples were supported at a fixed distance in front of a Newport 1825-C Optical Power / Energy Meter (Newport, USA). The sample was then illuminated with a helium-neon gas laser (Uniphase, UK), operating at 633 nm with an output power of 0.8 mW fitted with a beam expander to create a spot diameter of 20 mm on the plastic sample. The

attenuation of the sample was recorded as the difference between the transmitted power with and without the sample under test in the beam path.

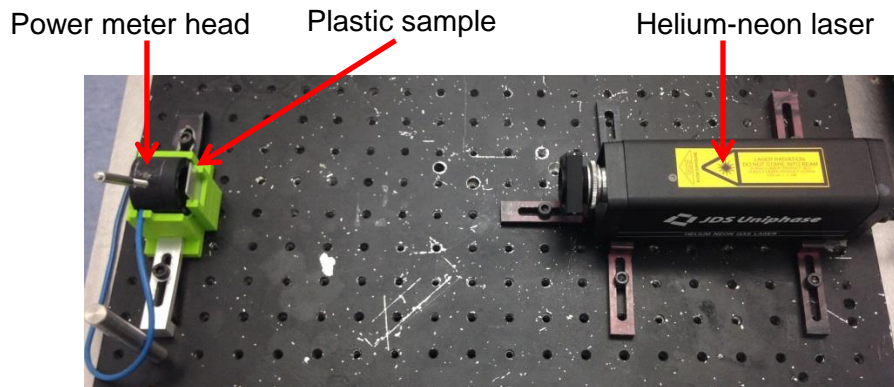


Figure 4.3: Instrumentation used to measure attenuation.

4.2.7 Optical Coherence Tomography Instrumentation

Fourier Domain Optical Coherence Tomography (OCT) is an interferometric, noninvasive tomographic imaging technique that is traditionally used to obtain subsurface cross-sectional images of a sample with micron-level resolution. A 930 nm Fourier Domain Thorlabs OCT system (Thorlabs Inc., New Jersey, USA) was used to generate surface trace images of channel samples (Figure 4.4). A broadband (i.e. a low temporal-coherence) light source illuminates a Michelson interferometer which splits the light into a reference path and sample path. The reference path terminates with a mirror, while the sample path contains an imaging lens that focuses the light onto the sample. The imaging lens collects light that is backscattered or reflected from the sample. The light returned from both paths is recombined and directed into a spectrometer, which forms the interference pattern that is then analyzed to yield the spectral OCT image. Interference fringes form when the optical path length difference between the reference and sample beams is less than the source coherence length. This technique provides precise axial positioning of an object in the direction of light propagation achieving precision on the order of microns. Typical scan depths for highly scattering biological samples range from 1 mm to several mm depending on the

scattering properties of the sample (Thorlabs Inc., 2007; Drexler and Fujimoto, 2015). Samples with highly reflecting surfaces are usually tilted so surface reflections of high intensity are reduced in favour of reflections at inner structures (Berer *et al.*, 2015). Therefore, samples were positioned at a 20 degree incline.

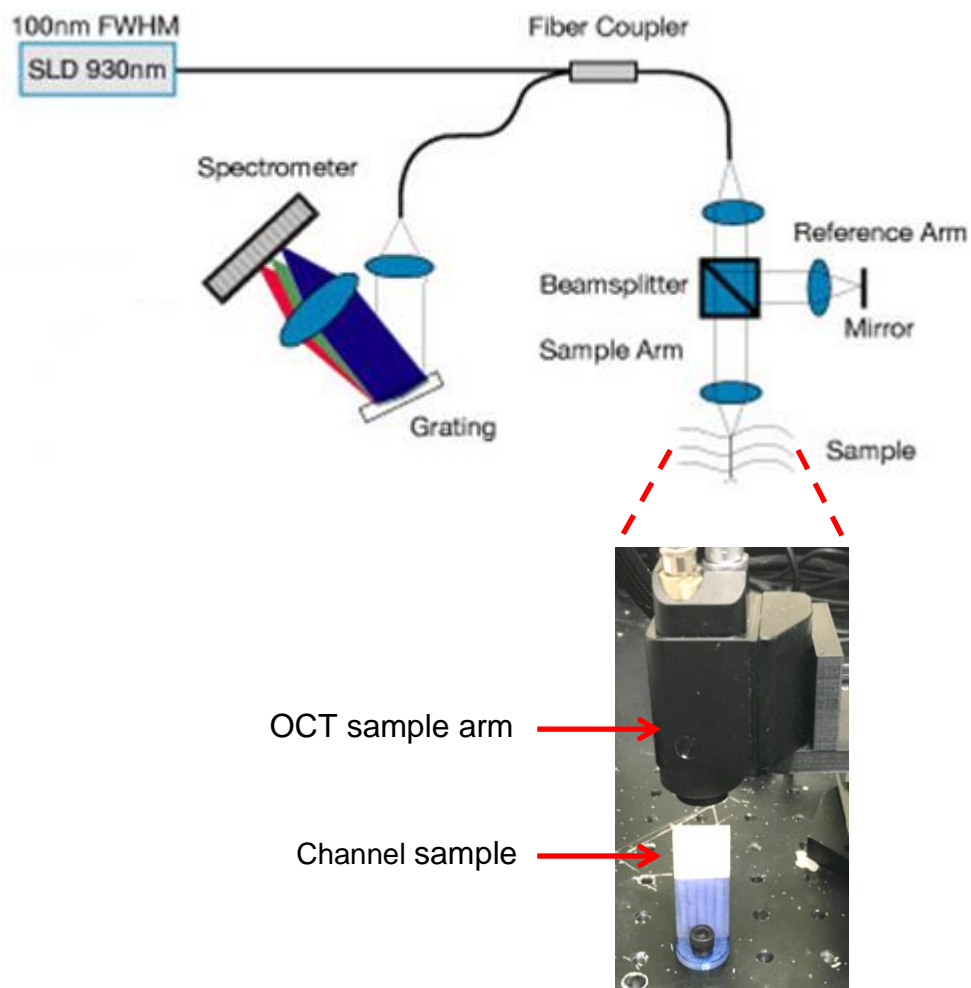


Figure 4.4: Schematic of instrumentation used for optical coherence tomography (Thorlabs Inc., 2007).

4.2.8 Plastic Samples

A plastic sample (Figure 4.5) was designed as a means to quantify changes in optical transparency during experimentation. The sample was made using Ultimaker PLA Translucent with the back-side surface on to the heated build table; the square

region from which readings were taken was 400 mm^2 with $400 \text{ }\mu\text{m}$ thickness. An additional support structure borders the plastic sample for handling and identification, so that physical contact with the plastic sample was minimised and the risk of damage occurring when removing the plastic sample from the 3D-printer build plate was reduced. The back side was printed down onto the build table.

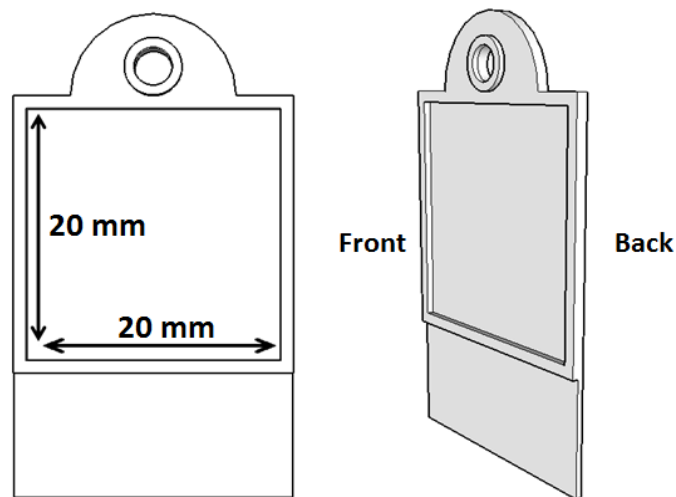


Figure 4.5: Schematic of plastic sample.

4.2.9 Open Face Plastic Channel Samples

An open face channel sample, Figure 4.6, was designed as a means to quantify changes in channel surface roughness during experimentation. The test samples were made using Ultimaker PLA Translucent with the bottom surface on to the heated build table; the channel region from which readings were taken was 1 mm wide with $400 \text{ }\mu\text{m}$ depth. All samples were printed at a print speed of 10 mm/s with 0.06 mm layer height. The top side was printed down onto the build table.

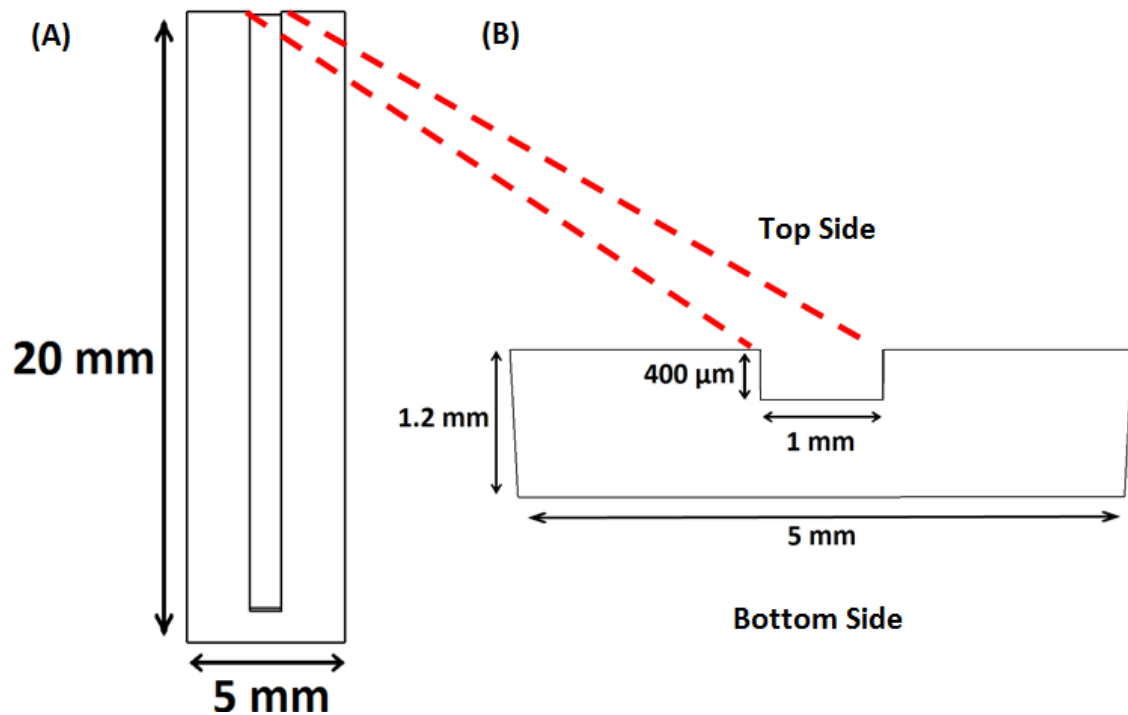


Figure 4.6: Schematic of the microfluidic channel. (A) Channel specifications; (B) cross-sectional specifications.

4.2.10 Effect of Layer Height and Print Speed on Optical Transparency

Plastic samples (section 4.2.9) were printed at different speeds (5 – 10 mm/s) and layer heights (0.06 – 0.25 mm), described fully in section 4.3.1. The distance between the print head and build table was < 0.05 mm. The optical transparency of each sample was measured using instrumentation described in section 4.2.6.

4.2.11 Effect of 3D-Printer Print Head Position in Relation to Printer Build Table on Optical Transparency

Plastic samples (section 0) were printed when the distance between the print head and build table was < 0.05 mm and then 0.25 mm. All samples were printed at 10 mm/s with 0.06 mm layer height. The difference in attenuation was recorded using the plastic sample attenuation instrumentation (section 4.2.6).

4.2.12 Effect of Acetone Vapour Treatment on Optical Transparency

Plastic samples (section 0) were exposed for differing times to acetone vapour and the difference in attenuation was recorded using the plastic sample attenuation instrumentation (section 4.2.6). Acetone liquid was added to a glass jar on a heat plate. The acetone was then boiled by setting the heat plate to 150 °C. An acetone vapour cloud was generated in the glass jar; the plastic samples were immersed in the acetone vapour cloud for varying times then allowed to dry. All samples were printed at 10 mm/s with 0.06 mm layer height and the distance between the print head and build table was < 0.05 mm.

4.2.13 Effect of Acetone Liquid Treatment on Optical Transparency

Plastic samples (section 0) were exposed to liquid acetone (0-100%) and the difference in attenuation was recorded using the plastic sample attenuation instrumentation (section 4.2.6). Acetone liquid was diluted using isopropyl alcohol and the samples were immersed fully into the solutions then removed. Excess liquid was allowed to flow off the plastic sample and it was then allowed to dry. All samples were printed at 10 mm/s with 0.06 mm layer height and the distance between the print head and build table was < 0.05 mm.

4.2.14 Effect of Acetone Liquid on Channel Surface Roughness

Open face channel samples (section 4.2.9) were exposed to liquid acetone (0-100%). OCT instrumentation as described in section 4.2.7 was used to image the channel cross-sections before and after treatment so the change in surface roughness could be quantified. All samples were printed with plate 1 surface (top side) being printed onto the build table at 10 mm/s with 0.06 mm layer height and the distance between the print head and build table was < 0.05 mm.

4.3 Results and Discussion

The investigation of the use of 3D printed plastics for microfluidic devices had two key aims. Firstly, the optimisation of the 3D printing methodology to produce plastic samples of sufficient optical quality to allow optical interrogation of internal cavities. Secondly, the production of microfluidic channels imbedded in a 3D-printed device. The process of optimisation of the 3D printing methodology focussed initially on the layer height and the print speed. It then progressed to an investigation of post-print treatments. Error bars shown on graphs represent ± 1 standard deviation.

4.3.1 Effect of Layer Height and Print Speed on Optical Transparency

As previously discussed in section 2.4.1 and 4.2.4, many factors can influence a 3D-printed object; it can take several print attempts and varying conditions to produce an object with the desired properties. The FDM printer used here deposits individual strands of polymer which merge together to form a layer; layers are built up on top of each other to form the object. Thinner layers result in better quality objects at the cost of increased print time. Therefore, an important parameter when printing an object is the height of the individual layers.

The influence of the layer height on the attenuation of the transmitted light was investigated by characterising the 3D-printed solid plastic samples as described in section 0. The difference in attenuation was recorded using the plastic sample attenuation instrumentation (section 4.2.6). These samples were fabricated at a print speed of 10 mm/s, with varying layer height of the plastic. Layer height and print speed is controlled using the Cura software. The results can be seen in Figure 4.7.

An important factor observed during initial printing attempts was the difference in sample surface quality. From visual examination, the sample surface that was in contact with the heated build table was polished/smooth and had visibly improved form, structure and optical transparency; the top face is visibly rough and cloudy by comparison. It is possible that by ensuring that the most suitable surface is

printed face down on the build table, the object will have improved characteristics for its intended purpose. It was hypothesised that the rough surface may cause increased scattering relative to the smooth surface which could affect attenuation. Attenuation is the loss of flux intensity that occurs through a medium; attenuation is caused by absorbance, reflection and scattering. The attenuation in plastic samples was calculated by measuring the difference in beam intensity when the samples were placed in the laser beam path; $(I_0 - I)$ where I_0 is the beam intensity detected without the sample and I is the beam intensity detected with the sample. Attenuation results were taken from the front-side of the plastic sample (rough surface away from heated build table) and then the back-side of the plastic sample (smooth surface on to the heated build table). This was done by placing the plastic sample with the relevant face towards the incident beam in the experimental setup so the difference could be investigated; 'rough' measurements had the rough face towards the incident beam as was the case with 'smooth' measurements. Results have been normalised.

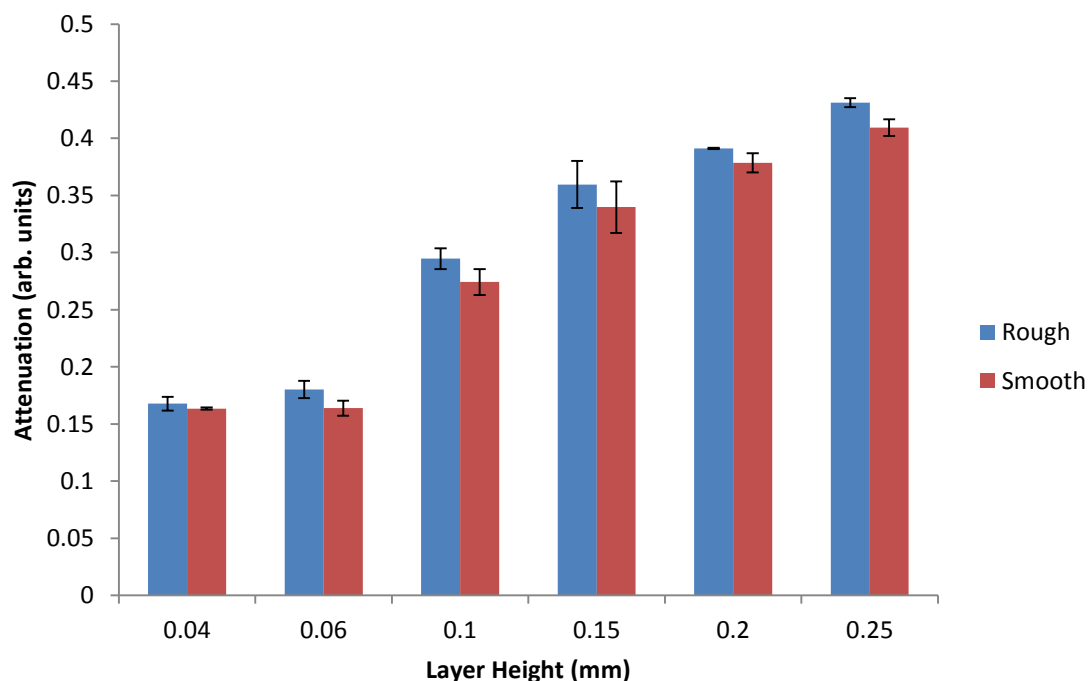


Figure 4.7: Attenuation measured at a wavelength of 633 nm in 400 μm thick plastic samples made from Ultimaker PLA Translucent using 6 different layer-heights (n=3).

As shown in Figure 4.7, an increase in the layer-height increases the attenuation of the transmitted light; as layer height increased from 0.06 – 0.25 mm, attenuation detected in samples increased by up to 252%. However, at 0.04 mm and 0.06 mm layer-heights the difference between the attenuation measurements was less than the experimental error. It is postulated that as layers are deposited, air can be trapped between the layers, reducing homogeneity. Such air pockets and the corresponding reduction in the merging of the polymer layers is thought to be responsible for the clouding observed in the printed samples and the measured increase in attenuation. Where homogeneity between layers was improved, it was observed by eye that the optical transparency increased, even if intermittently and not across the entire object. It might be expected that by increasing the layer height the optical transparency would also increase, as there would be fewer layers and therefore less potential for air gaps. However, it is proposed that as the layer height increases the circular nature of the FDM extruded plastic causes the air pockets to become larger, increasing attenuation and decreasing optical transparency.

A proposed solution to the formation of air gaps was to vary the print speed to allow the plastic time to flow into the gaps. However, as shown in Figure 4.8, the variation of the print speed had a mixed impact on the attenuation of the samples made using the PLA Translucent plastic. For 0.06 mm layer height, increased print speeds reduced the attenuation by up to 16%. Layer heights of 0.15 mm and 0.25 mm showed an increase in attenuation, up to 27% and 15% respectively, with speed. It was also seen that while there was a decrease in attenuation results taken from the smooth face compared to the rough face, there is little difference (<10%). All subsequent results were taken from the front (rough) surface.

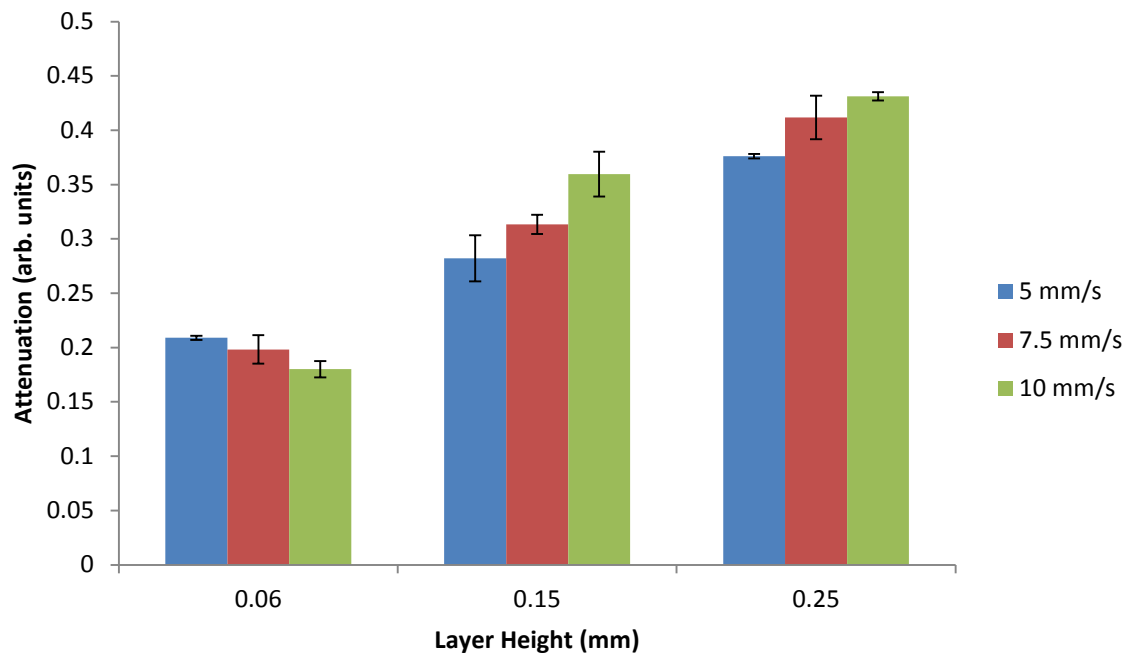


Figure 4.8: Attenuation in Ultimeker PLA Translucent plastic samples made with 3 different layer heights at 3 different speeds (n=3).

Further experiments were undertaken at a range of higher print speeds, but this increased the failure rate of the prints. It has been documented that at higher print speeds the chance of print failure increases. This is due to the increased risk of the print not sticking to the build table, overheating, layer shifting and misalignment, grinding of the filament by the feed motor leading to interruption of feed, and increased vibrations impacting the quality of fine details (Simplify3D, 2016). This results in either incomplete, inadequate quality or aborted prints. All further prints were done at a layer height of 0.06 mm and at a print speed of 10 mm/s, as this appears to offer the best compromise between optical transparency, print success and print time.

4.3.2 Effect of 3D-Printer Print Head Position in Relation to Printer Build Table on Optical Transparency

As it was postulated in section 4.3.1 that air pockets between filament strands and layers have a direct impact on attenuation and optical transparency, reducing this is paramount. Through preliminary testing using the 3D-printer it was discovered that the print build table position in relation to the printer nozzle can change the deposition of strands and change the homogeneity of layers, therefore affecting optical transparency. The manufacturer provides a 'calibration card' that is to be used to calibrate the position of the build table; the calibration protocol states that there should be slight friction when moving the calibration card between the printer nozzle and the build table (Ultimaker.com, 2016b). The thickness of the calibration card was 0.15 mm (± 0.01 mm) when measured using a digital Vernier calliper.

It was hypothesised that by reducing the space between the printers build table and print nozzle, the printer nozzle could physically smooth the previous layer as it moves over while depositing the next layer. This could improve strand merging and force the new layer into the previous, rather than just laying it on top. This process forces out air from the layers and improves homogeneity and decreases attenuation which improves optical transparency. This process of forcing or squashing the strands and layers together is how the recently introduced Dolomite Fluidic Factory seeks to improve optical transparency and water sealing of microfluidic chips (Dolomite, 2016) as illustrated in Figure 4.9.

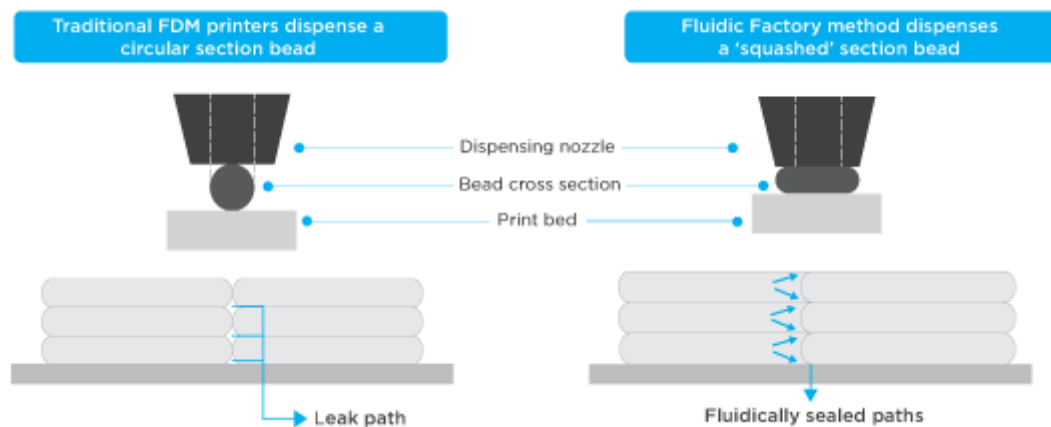


Figure 4.9: Illustration of squashed filament strand (bead) compared to traditional circular strand (bead) (Dolomite, 2016).

The difficulty encountered with calibrating the print head position was the difficulty in monitoring the build table position in relation to the print head. The position changed over time as the machine was in use, presumably due to vibrations and the action of the moving parts. As a result, the build table needed to be recalibrated before each printing session. This was performed by eye during printing by adjusting the positioning screws in the build table. There was a limited build table position range (approximately 0-0.25 mm), discovered during testing, in which the printer could produce objects; operation outside this range could result in damage to the machine (if too close) or unsuccessful prints (if too far).

Experiments were performed to illustrate the difference in optical transparency of objects fabricated using a machine with calibrated build table positioning and that of objects fabricated with the machine in an uncalibrated configuration. Plastic samples were made on a calibrated build table position (distance between print head and build table < 0.05 mm) and an uncalibrated build table position (distance between print head and build table 0.25 mm). The distance between print head and build table was measured using steel feeler gauges, the thinnest being 0.05 mm thick, hence the calibrated build table position being stated as < 0.05 mm as this thickness of feeler gauge was unable to pass between the build table and print head after calibration.

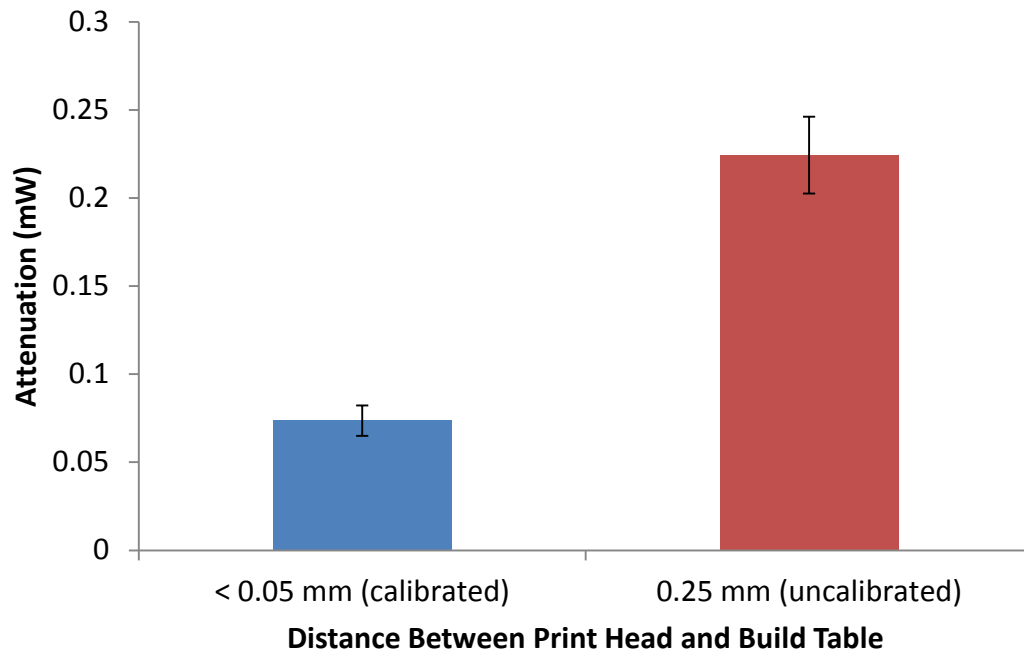


Figure 4.10: Attenuation in Ultimaker PLA Translucent plastic samples made with two different print head to build table distances (n=3).

As can be seen in Figure 4.10, the plastic samples printed on a machine with a calibrated build table have far greater optical transparency than those printed on a machine with an uncalibrated build table. The increase in attenuation was almost 200% for the uncalibrated plastic samples compared to the calibrated plastic samples. Printing was not possible with a distance >0.25 mm as the print strands could not adhere to the build table. There is a visible difference between the plastic samples produced; the calibrated plastic samples are significantly clearer than the clouded uncalibrated plastic samples. Examples of the plastic samples can be seen in Figure 4.11.

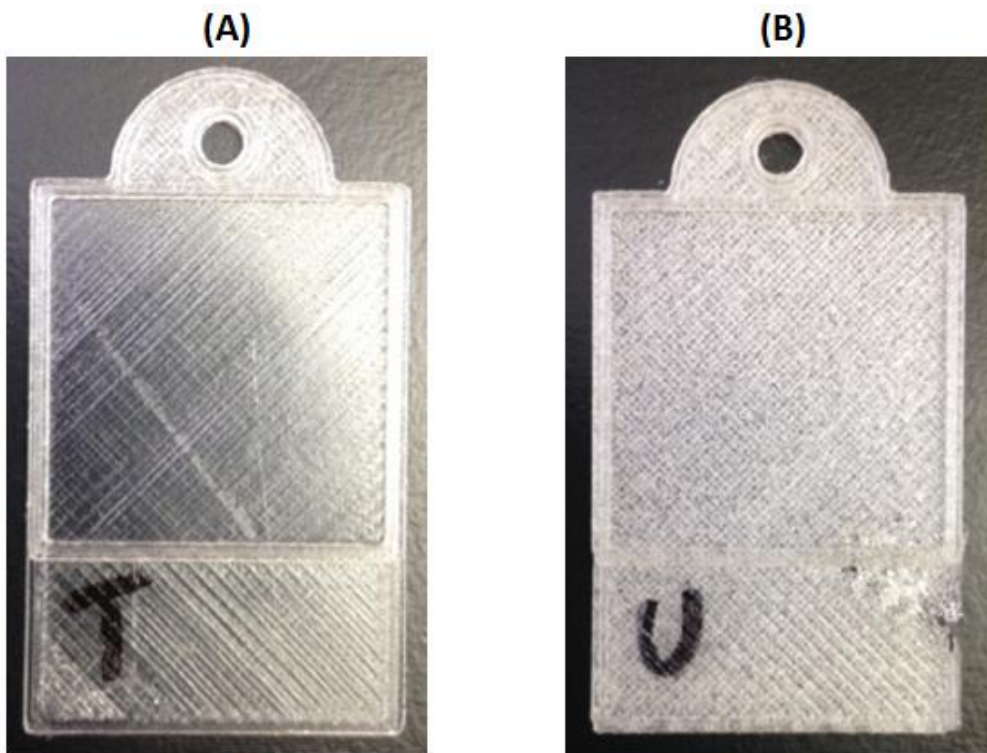


Figure 4.11: Plastic samples printed on a machine with calibrated and uncalibrated print head to build table distance. (A) Calibrated (< 0.05 mm); (B) Uncalibrated (0.25 mm).

Detailed images of the plastic sample surface taken using a microscope can be seen in Figure 4.12. With the calibrated plastic samples only the strands in the last deposited layer can be seen (the diagonal lines are the strand edges), due to the fusion of the preceding layers into a single homogenous layer. With the uncalibrated plastic samples, multiple layers in the sample can be seen as a lattice effect in the images. This is due to reduced fusion of the strands and layers in the sample, resulting in decreased homogeneity.

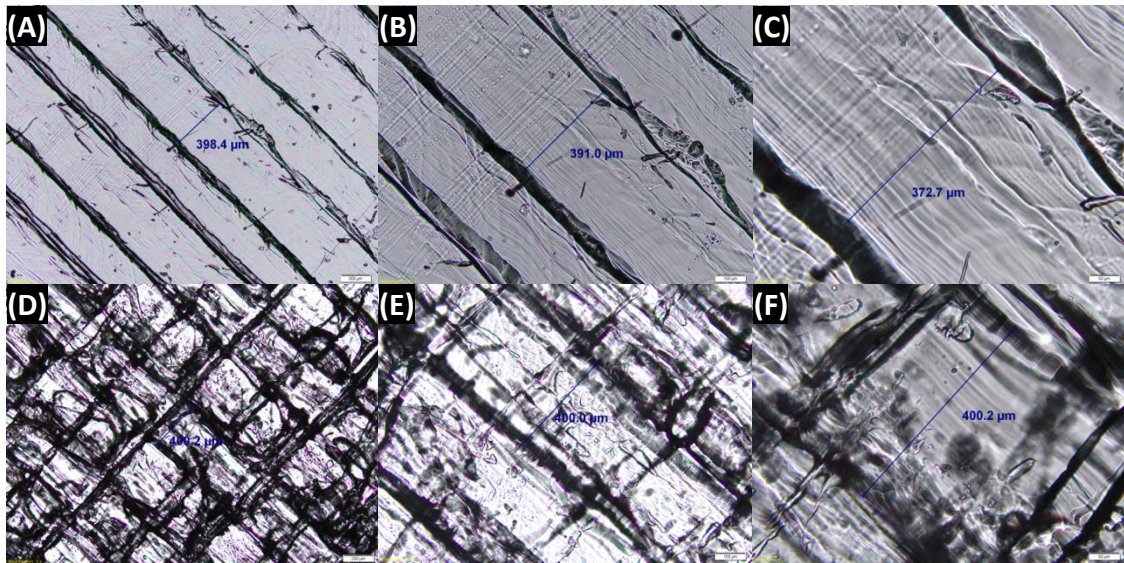


Figure 4.12: Microscope pictures taken of plastic samples printed on a machine with calibrated (< 0.05 mm) and uncalibrated (0.25 mm) print head to build table distance. (A) calibrated 5x magnification; (B) calibrated 10x magnification; (C) calibrated 20x magnification; (D) uncalibrated 5x magnification; (E) uncalibrated 10x magnification; (F) uncalibrated 20x magnification.

This shows that a calibrated print build table position is of utmost importance when printing devices for optical detection as an uncalibrated position can impact the optical characteristics of the object produced.

4.3.3 Effect of Acetone Vapour Treatment on Optical Transparency

After improving the optical transparency of the printed objects by changing the printing parameters, the next stage was to explore the use of post-print treatments to further improve the transparency. The most common post-print technique for finishing 3D-printed objects involves the use of acetone to treat the surface; acetone acts as a plasticiser and induces crystallisation (Naga *et al.*, 2013), reducing imperfections and leaving a smooth finish. By removing imperfections from the exposed surfaces of the plastic sample it may be possible to improve optical transparency by reducing scattering.

An experiment was performed to investigate the effect of acetone vapour treatment on 3D-printed plastic samples. The results are displayed in Figure 4.13, negative attenuation change signifies an improvement in optical transparency.

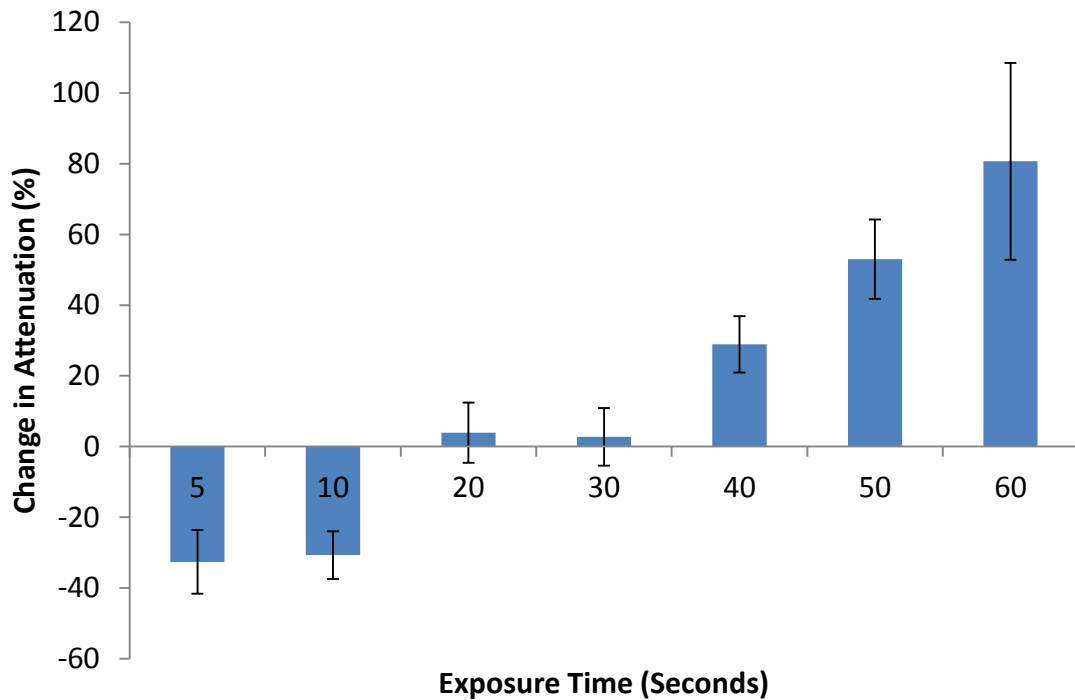


Figure 4.13: Changes in the attenuation of Ultimaker PLA Translucent plastic samples exposed to acetone vapour for a range of durations (n=3).

The influence of the duration of the exposure to acetone vapour on the transparency of the printed samples is shown in Figure 4.13. At low exposure times, ≤ 10 seconds, the transmission is improved by up to 30%. For exposure times > 10 s, the transparency decreases significantly, falling below the pre-treatment value, with the surface of the sample becoming cloudy and whitened. The change in surface structure is visible as the exposure time increases, as shown in Figure 4.14. The individual filament strands and demarcation become less apparent. This shows that brief exposure to acetone vapour (≤ 10 seconds) can be used to improve optical transparency. While this is a promising post-fabrication treatment, its use is limited by

the ability to control uniform exposure across the surface of the object. This approach would be difficult to deploy in imbedded microfluidic channels.

Current methods involve simply immersing the entire object in a cloud of acetone vapour (Naga *et al.*, 2013) and, while exposure time can be controlled, it is not possible to ensure that all surfaces experience uniform exposure and that the cloud itself is uniform in concentration. Condensation of the acetone vapour on surfaces also occurs; the acetone droplet then runs and leaves a white trail on the PLA that could be difficult to remove. If acetone vapour treatment was to be used for internal surface treatment, such as those of the microfluidic channels, it would be difficult to introduce the vapour into the channels and to remove it in a controlled fashion without condensation of the acetone occurring inside the channels.

An unexpected consequence of the acetone vapour treatment was a change to the physical properties of the plastic samples. As exposure time increased, the plastic samples became increasingly pliable, taking on a more rubbery texture and becoming increasingly elastic, whereas the samples before treatment are hard and brittle. While the impact this could have on microfluidic devices is unknown, it is likely that making the surface more elastic could cause drooping or sagging, resulting in obstruction within channels. Another effect of the acetone vapour treatment was warping of the plastic samples, which increased as exposure time increased. This effect must be taken into account for devices that are thin, especially those with a large cross section such as LOAD platforms which are particularly prone to warping.

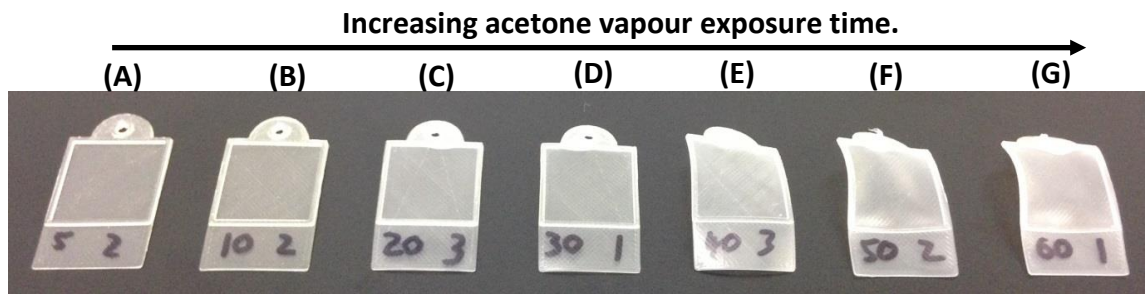


Figure 4.14: Images of plastic samples after acetone vapour treatment. As exposure time increases, warping and clouding increase. Exposure time: (A) 5 seconds; (B) 10 seconds; (C) 20 seconds; (D) 30 seconds; (E) 40 seconds; (F) 50 seconds; (G) 60 seconds.

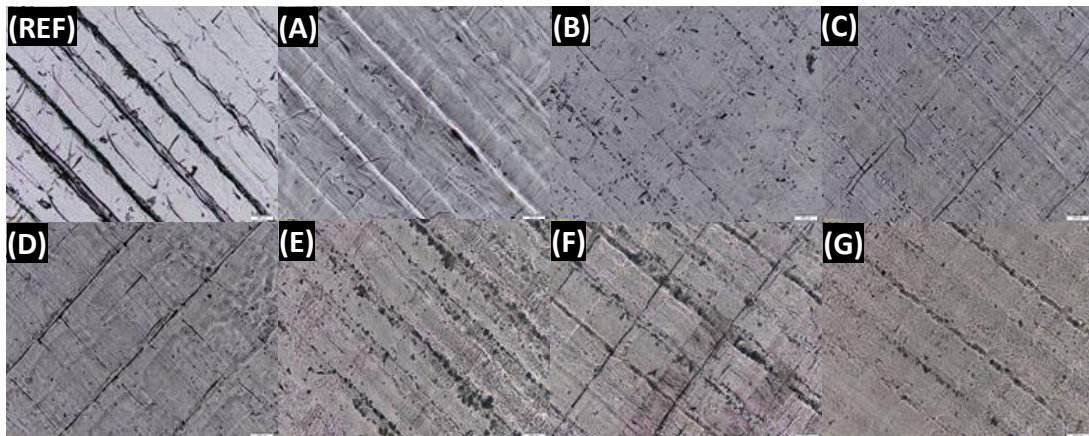


Figure 4.15: Microscope pictures taken of plastic samples after acetone vapour treatment (5 x magnification). Exposure time: (REF) 0 seconds; (A) 5 seconds; (B) 10 seconds; (C) 20 seconds; (D) 30 seconds; (E) 40 seconds; (F) 50 seconds; (G) 60 seconds.

The microscope images, Figure 4.15, show in detail the changes in surface structure that occur as exposure time increases; the individual strands and demarcation become less apparent, the objects also get gradually darker as the cloudiness increases and optical transparency decreases.

4.3.4 Effect of Acetone Liquid Treatment on Optical Transparency

An alternative to acetone vapour treatment was tested to see if better results could be achieved. Liquid acetone of varying concentration (0-100%) was used to treat the plastic samples and the results can be seen in Figure 4.16.

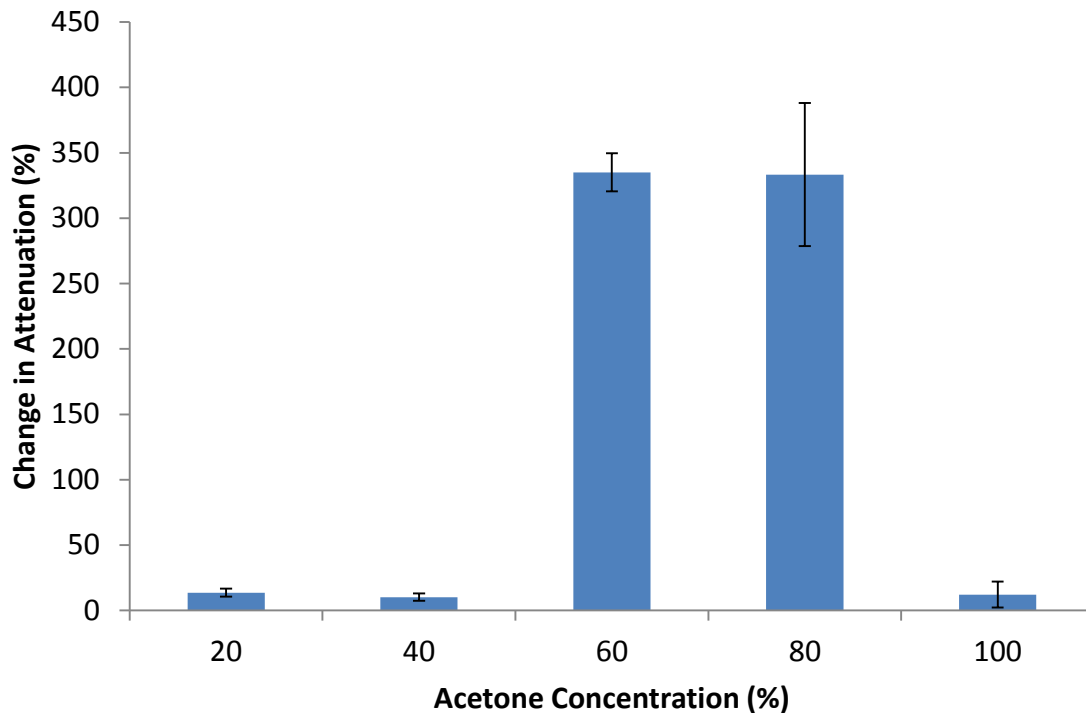


Figure 4.16: Change in attenuation in Ultimaker PLA Translucent plastic samples exposed to acetone solution of increasing concentration (n=3).

In all cases, attenuation is increased and optical transparency is decreased. At 20% and 40% acetone concentrations, the increases in attenuation are 13% and 10% respectively and there is little visible change to the transparency of plastic samples. However, at 60% and 80% acetone concentrations, the attenuation is increased by 335% and 333%, respectively, and the surfaces of the plastic samples have become opaque, as can be seen in Figure 4.17. It was also observed that at 100% acetone concentration, the difference in attenuation following treatment was similar to those observed at low acetone concentrations (20-40%), with an increase in attenuation of 12%. It is believed that the isopropyl alcohol affected the evaporation rates of the

solutions. The 100% acetone evaporated more quickly than the 60% and 80% solutions so that surface damage was limited. It is possible that the surface damage that occurred at 60% and 80% could have been reduced by including a rinsing step using isopropyl alcohol following immersion in the acetone solutions for all plastic samples however, this was not performed. The 0-40% concentration solutions did not have a significant effect on the surface before complete evaporation occurred.

Whilst best efforts were made to drain all excess solution from the plastic samples after immersion, the effects of liquid that pooled can be seen, particularly along the bottom support of the plastic samples, as seen by the white plaque formation in Figure 4.17(F). This emphasises a problem with the use of liquid acetone of any concentration: if it is allowed to remain on a PLA surface, damage will occur resulting in opaque white colouration. Thus control of surface exposure to acetone liquid is of utmost importance.

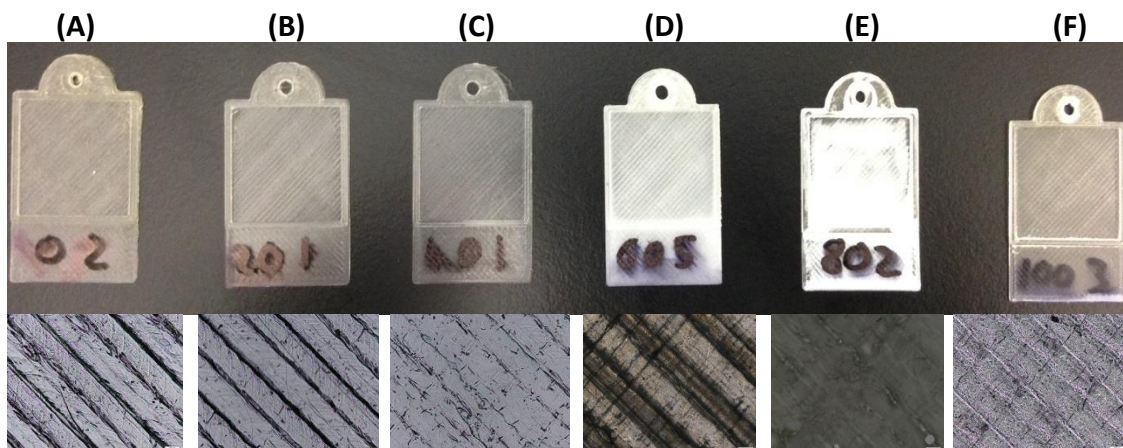


Figure 4.17: Images of plastic samples after acetone liquid treatment and microscope pictures (5 x magnification). As acetone concentration increases clouding increases. Concentration: (A) 0%; (B) 20%; (C) 40%; (D) 60%; (E) 80%; (F) 100%.

When liquid acetone was used there was no warping or change of the physical properties of the plastic samples. This was presumably due to the shorter exposure time to the acetone, as each plastic sample was immersed for approximately 1 second

during the dipping process and was then left to dry as the acetone solution evaporated, so the exposure rate was primarily controlled by rate of evaporation.

Further investigations into the use of liquid acetone could be undertaken in an attempt at improving optical transparency. It is possible that by using a low concentration of acetone ($\leq 5\%$) and by flowing the solution over the surface, more controllable exposure could be achieved, particularly for treatment of internal surfaces such as those of the microfluidic channels, where it may be easier to control and manage liquid rather than vapour. In addition, the ability of acetone to 'smooth' surfaces of 3D-printed devices does present other possible uses; if controlled application of acetone liquid can minimise the destructive effect on optical transparency, there is potential to reduce imperfections of internal channel surfaces that acetone vapour would be unsuitable for.

4.3.5 Development of a FDM 3D-Printed LOAD Platform

The second area to be investigated regarding the use of 3D-printing for microfluidic diagnostic devices is the development and manufacture of a LOAD diagnostic device with imbedded microfluidic channels. An aim of the research presented in this thesis is that the LOAD device should be suitable for use in conjunction with an unmodified optical drive that will act as a centrifugal driver and reader platform. Referring back to the project aims and objectives, the LOAD device is intended to be a vessel in which centrifugal separation of whole blood and colourimetric quantitative assays for analytes in whole blood can be performed. The device must have sufficient optical transparency such that colourimetric assays can be quantified within the channels. The channels must have a volumetric capacity of $\leq 50 \mu\text{l}$ (a drop of blood) and be water tight to the point that centrifugally driven separation of blood plasma from whole blood can be performed within.

Initial device design specifications were based on an optical disc, so the device could be spun using an unmodified ODD. According to the Guidelines on the

Production and Preservation of Digital Audio Objects (web edition), optical discs should adhere to the universal standards, listed within the publication, so that “discs are writable or playable on different manufacturers’ machines”. Therefore, it can be assumed that the specifications of optical disc drives adhere to the standardised specifications of optical discs, those being 80 mm or 120 mm in diameter, 1.2 mm thick with a 15 mm diameter spindle hole (IASA Technical Committee, 2009).

When the internals of several ODDs were investigated, it was seen that the restrictions applied to the LOAD design would, in actuality, be primarily dictated by the specifications of the ODD being used to spin the device; specifically the drive spindle. While ODD drive spindle specifications are standard to fit the discs (15 mm diameter), two types of ODD spindle were encountered: one with locking clips and one without, as can be seen in Figure 4.18. The clips are intended to secure the disc onto the spindle to reduce vibration at high speeds, and have precise specifications to lock the 1.2 mm disc in place. Therefore, drive spindles with locking clips cannot accommodate a disc with a thickness > 1.2 mm. Due to the absence of locking clips on the alternative spindle design, it was assumed that a disc with thickness > 1.2 mm could be spun, although, the maximum thickness of disc that could be spun was unknown. It was decided that initial LOAD specifications would be of an optical disc (diameter 120 mm, thickness 1.2 mm, spindle hole diameter 15 mm), however, should it be necessary, the disc diameter could be reduced and the thickness increased.

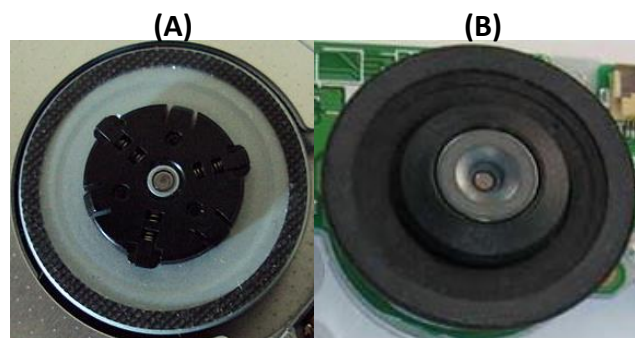


Figure 4.18: Optical disc drive spindles. (A) with disc locking clips (Study.com, 2014); (B) without disc locking clips (Ausgamestore.com, 2008).

The initial channel design was based on a U-bend as this is a simple design that allows for two input/exits required to allow for pressure equalisation for capillary action to draw sample into the channel (Figure 4.20(B)). In addition, a U-bend design allows for centrifugal motion without requiring plugs to seal channel entry points as the force draws sample away from the openings.

The LOAD device design process envisaged the disc as consisting of 3 distinct plates printed consecutively on top of each other to form one disc:

- Plate 1 is the top plate; it is used to both seal the top of the internal channels and provide 'windows' into the internal channels, allowing visual interrogation of the channel interior. It also has openings/pores to allow for sample application and air release.
- Plate 2 is the internal plate; it contains the channel space.
- Plate 3 is the base plate; used to seal the internal chambers.

The first LOAD design had a 120 mm diameter, 15 mm diameter central spindle hole and was 1.2 mm thick. Each plate was 400 μm thick, with 8 U-bend channels (2 mm wide, 400 μm depth, approximately 52.5 mm long in total, 3 mm radius U-bend curvature of the inside wall) and 1 mm diameter pores. 8 channels were to be imbedded in order to maximise the space on the device that could be used for sample quantification, and to allow observation of any differences that may occur between channels printed within the same device. The channel volume was approximately 42 μl . The schematics designed using Sketchup can be seen in Figure 4.19.

The first print of the disc was completed using PLA Translucent with the aim of establishing that the disc would print and to assess the initial properties. The disc was printed using 'normal print' factory settings with the plate 3 surface being onto the build table. The settings to note are the print speed (50 mm/s) and layer height (0.1 mm). The print time was approximately 5 hours and consumed approximately 18 g of plastic filament. When the disc was printed with settings determined from previous experimentation as detailed in section 4.3.1 (print speed: 10 mm/s, layer height 0.06 mm), the print time per disc was approximately 10 hours. It should be noted that

decreasing the layer height of a print will increase print time, independently of the print speed setting. Figure 4.20 shows the disc immediately after printing and before post-print finishing.

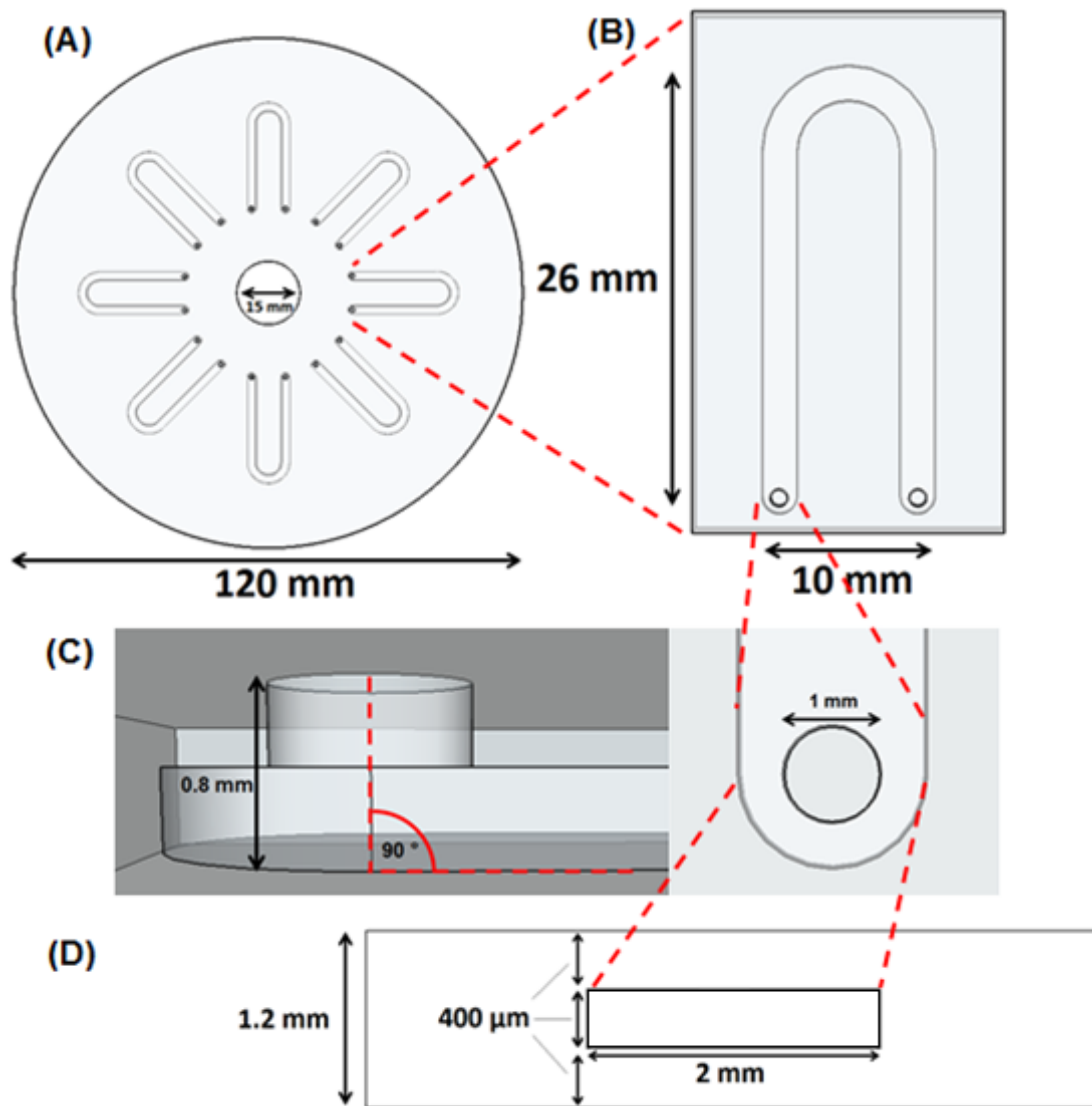


Figure 4.19: Schematic of first LOAD device. (A) Disc specifications and channel layout; (B) channel specifications; (C) pore schematic; (D) cross-sectional specifications.

The disc felt similar to an optical disc with no warping being visible; any warping could render the disc unusable due to instability that could arise when the

disc is spun. There were noticeable differences between the surface of plate 3, which was printed onto the heated build table, and the surface of plate 1 which was not.

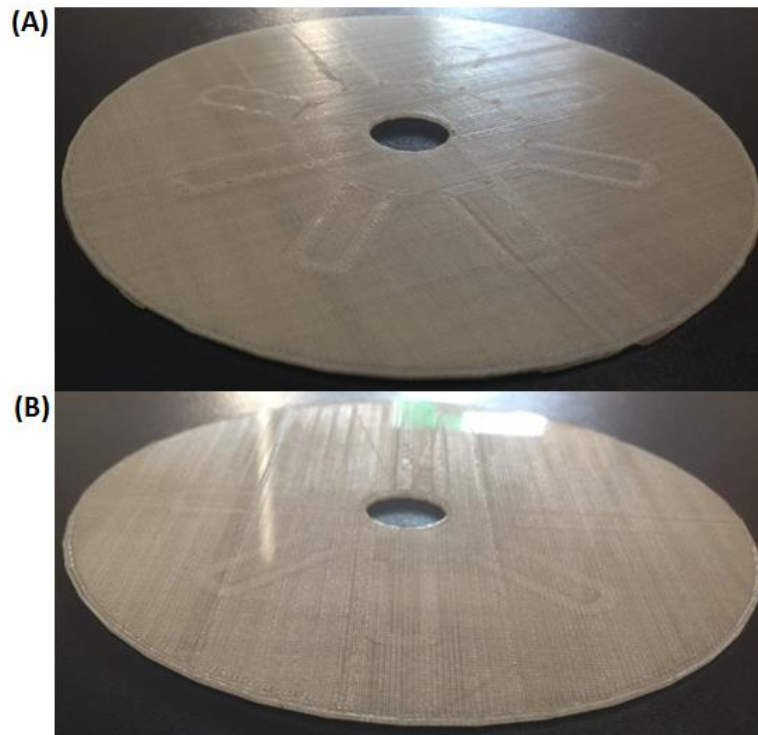


Figure 4.20: Angled view of printed disc faces to show different surface quality. (A) The surface of plate 1; (B) The surface of plate 3.

The surface of plate 1, Figure 4.20(A), felt rough to touch and visible layers and strands could be seen and felt. There are visible integrity issues in the plate 1 windows over the channels with some bulging and sagging noticeable, in some cases the internal channel are exposed. In addition, the pores were not formed properly/circular as designed, but were visibly broken/misshapen. The surface of plate 3 which was printed onto the heated build table, Figure 4.20(B), displayed a superior finish and transparency, and is more glass like in appearance than the surface of plate 1. It would appear that direct contact of the face with the heated bed has maintained the strand melt temperature and allowed the printed strands to blend together, allowing for a homogenous layer. It is assumed that as subsequent layers were deposited, and distance from the bed increased, the strand/layer merging decreased and transparency was diminished.

When using a FDM printer there will be visible print layers and strands to some degree regardless of the print quality and print resolution; obtaining a smooth finish, as seen in injection moulding, is unfeasible when using a FDM 3D printer unless post-print finishing is performed (Benchhoff, 2013). Printer calibration, print optimisation and post-print finishing offer the potential for significant improvement of final device quality.

There were two fundamental issues that needed to be overcome. The first was the window surface integrity of the microfluidic channels, i.e. the plastic layer laid on top of the channel to seal it in plate 1; the visible gaps in the windows suggested that the channels were not being sealed properly during printing and therefore were not water tight. The second issue was the channels after printing; the channels were usually blocked and obstructed with plastic. These issues were linked directly, as the plate 1 windows, which should be sealing the channels, were sagging into the channel interior, blocking the channel and leaving gaps in the plate 1 windows.

It was presumed that optimisation of the channel design may result in the formation of sealed imbedded microfluidic channels. The initial channel designed (Figure 4.19) was 2 mm wide, and it was the relatively large (2 mm) width of the overhang space on top of the channel that caused the problems; the plastic being laid on top would sag or drop between the channel walls. Different channel designs were investigated, examples of which are displayed below. All samples were printed at 10 mm/s with 0.06 mm layer height.

Channels with a circular cross-sectional geometry (Figure 4.21) were designed using Sketchup and printed with a range of diameters (0.5 mm, 0.75 mm, 1 mm, 1.1 mm). Due to the 1.2 mm height constraint, sealed channel formation was not possible with a channel diameter >1 mm. A channel diameter of 1 mm could be formed, however as can be seen in Figure 4.21, the issue regarding plastic dropping and obstructing the channels was still present. A channel with a diameter of <1 mm would not form. A fundamental issue introduced by circular channels is that of shifting channel path length. As interrogation of the assay in the LOAD device is to be

performed perpendicular to the channel, top down through the disc from plate 1 to plate 3, the circular channels have a different pathlength depending on the position the reading takes place over the channel. For example, if the reading takes place at the edge of the channel cross-section, the path length will be shorter than if the reading takes place in the centre of the channel cross-section; the path length of the sample must be maintained to reduce inaccuracy.

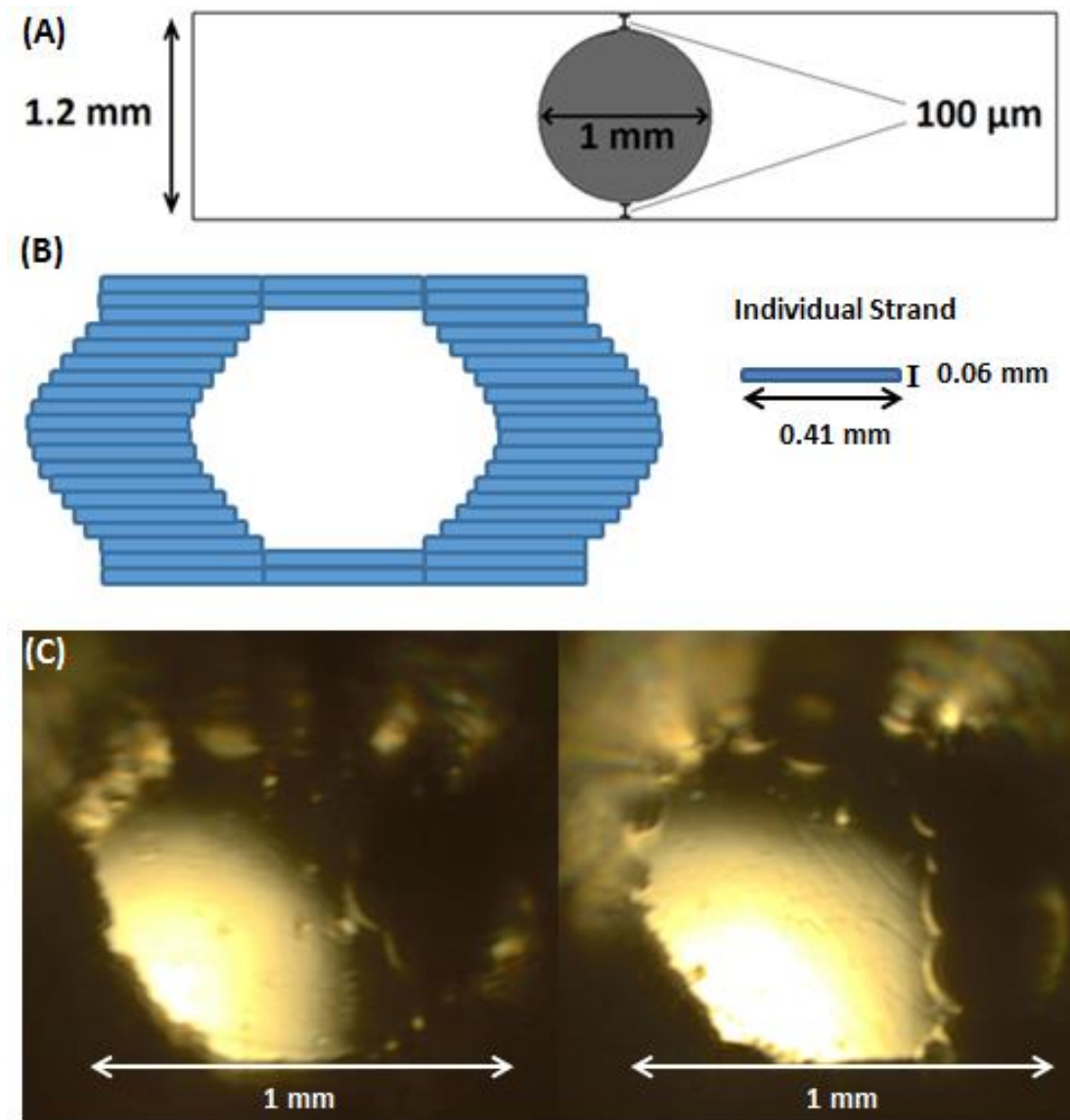


Figure 4.21: (A) Schematic of circular channel. (B) Illustration of how strands are deposited to form the channel. (C) Microscope pictures taken of circular channel samples (5 x magnification).

Channels with a triangular cross-sectional geometry (Figure 4.22) were also investigated. Sealed channels with this geometry could be formed with a channel width up to 4 mm and height up to 0.8 mm; obstructions within the channels were also reduced. It is speculated that the way in which the layers are built up to form channels with triangular geometry, results in less plastic over-hang, and therefore improved channel formation, as illustrated in Figure 4.22 (B).

Despite this success, the issue of shifting path length remains. The ultimate goal is to produce a diagnostic device that can be interpreted utilising optical absorbance quantification methods such as spectroscopy. Therefore the shifting path length introduced by a non-uniform design renders channel designs such as triangular or circular unusable.

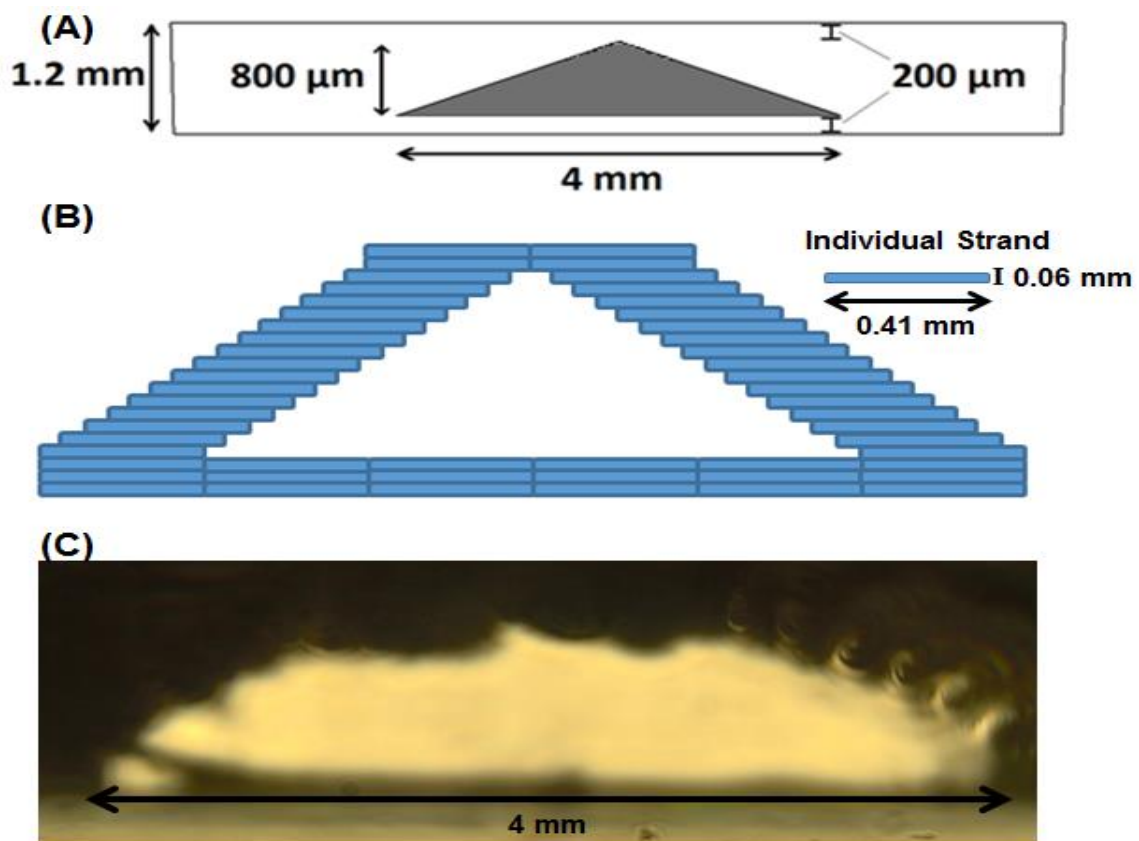


Figure 4.22: (A) Schematic of triangular channel; (B) Illustration of how strands are deposited to form the channel. (C) Microscope picture taken of triangular channel sample (5 x magnification).

It was decided that focus should be on printing sealed channels with a square/rectangular cross-sectional geometry as this geometry must be used to minimise shifting path length within the channel. The primary reason that the channels were not sealing was due to sagging and dropping of the plastic layers being laid on top of the open channel; it was speculated that this could be reduced by adjusting the plastic extrusion temperature.

It was hypothesised that increasing the extrusion temperature would increase the fluidity of the plastic resulting in improved strand and layer merging. However, it could also introduce structural integrity issues when constructing the internal microfluidic channels, as increased fluidity of the plastic could cause increased sagging and dropping, and ultimately collapsing, of the channel. The converse would also be true; a lower extrusion temperature decreases plastic fluidity resulting in decreased strand and layer merging, however, channel formation is improved, as less fluidic plastic is being laid over open space.

Samples were printed with up to 2 mm² channels at a range of extrusion temperatures (180-210 °C) and the channels examined under a microscope. An extrusion temperature of 200 °C was found to be most successful for the formation of imbedded channels; the standard extrusion temperature of the printer is 210 °C. The reduction in extrusion temperature resulted in reducing the plastic sagging and dropping, allowing for increased freedom in channel specifications, as can be seen in Figure 4.23. Although there was still sagging, channels of cross sectional area up to 2 mm² could be formed without obstruction. At an extrusion temperature <200 °C, the prints were seen to delaminate due to inadequate strand and layer merging.

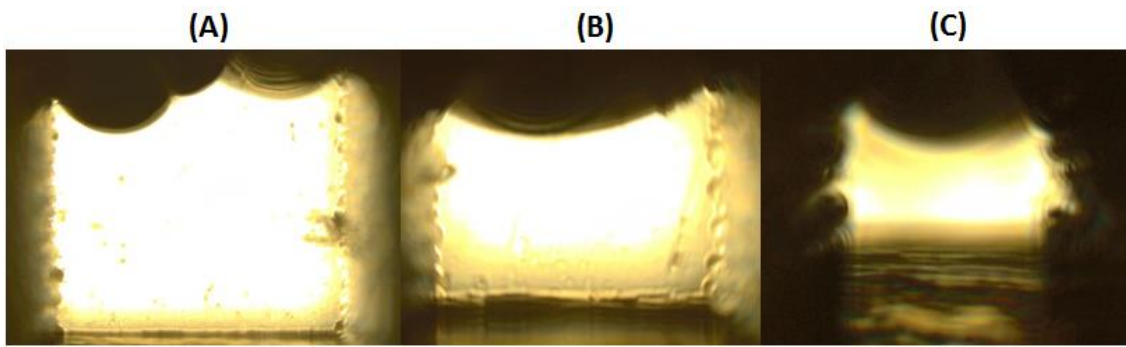


Figure 4.23: Microscope pictures taken of square channel samples printed with extrusion temperature at 200 °C (5 x magnification). (A) 2 mm²; (B) 1 mm²; (C) 0.5 mm².

As was previously mentioned in this section (4.3.5), another area of concern was the pore formation required for channel access for sample application. Precise pore formation was unsuccessful when printing the LOAD devices. It was suspected that this was due to the pore being located above the channel, which made precise strand placement impossible due to it being over open space. This was solved by printing the LOAD disc with plate 1 (which contains the pores) down onto the build table. This means the pores are formed and built on the build table rather than in open space. This also results in improved transparency for the channel window, making it easier to view the assay in the channel.

It was also observed that the plate printed onto the build table required fewer layers to seal the channels. It was assumed this was due to the heated build table improving strand and layer merging, therefore producing a better seal. This allowed for the plate being printed onto the build table, plate 1, to be made thinner as fewer layers were required to seal the channels. This meant plate 2 and plate 3 could be made thicker as required whilst maintaining a total LOAD thickness of 1.2 mm.

Following the improvement of the print process and print parameters that have been discussed in this section 4.3.1 and 4.3.5, a LOAD device with embedded microfluidic channels was developed. Each ‘U’ channel is distinct from the other

channels and must be filled individually; this facilitates multiple individual assays to be performed on a single device without cross-contamination or reagents or samples. The schematics are shown in Figure 4.24. The outer region of the disc was minimised to reduce print time and filament consumption. Channel volume was approximately 23 μl . Plate 1 was 200 μm thick, plate 2 was 400 μm thick and plate 3 was 600 μm thick. The channels were 1 mm wide, 400 μm deep and the pore design remained unchanged from Figure 4.19 (C).

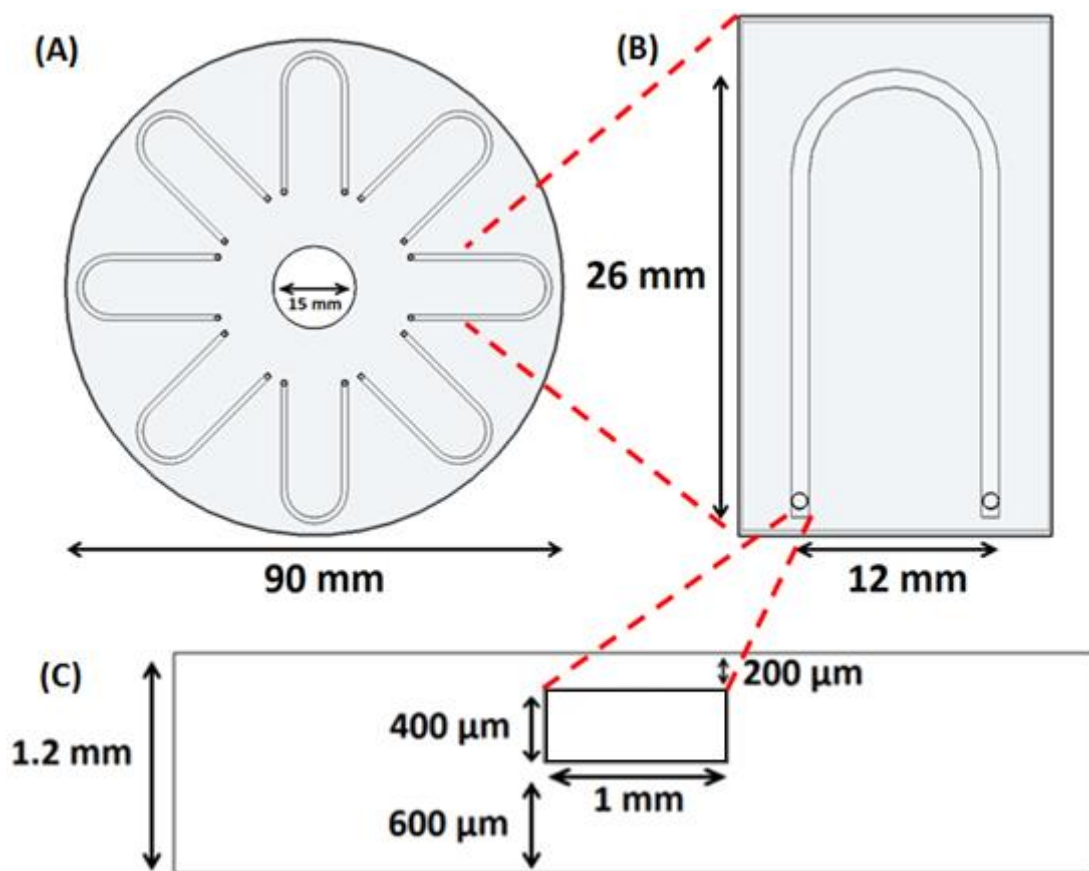


Figure 4.24: Schematic of second LOAD device, channel capacity $\sim 23 \mu\text{l}$. (A) Device specifications and channel layout; (B) channel specifications; (C) cross-sectional specifications.

The print time for the disc using optimum settings (10 mm/s speed, 0.06 mm layer height) was approximately 5.5 hours and consumed 9g of plastic filament; the

extrusion temperature was 200 °C. The disc size reduction decreased print time and material consumption by approximately 45%. The disc was printed with the surface of plate 1 down on to the heated build table so pore formation could occur. The successful formation of imbedded microfluidic channels is illustrated in Figure 4.25, where the channels of a printed disc have been filled with red dye solution. This demonstrates that not only can embedded microfluidic channels be printed using a low-cost hobbyist FDM 3D-printer, but that optical transparency has been improved to the point that colour can be viewed within the channels. Samples were applied to the channels using a syringe and hypodermic needle; the needle is inserted through the pore (plate 1), into the channel (plate 2) and the sample forced into the channel via the syringe. The sample would not flow easily through the channel unless the needle was inserted into the channel and pressure was applied, this was presumed to be due to the surface roughness of the channel impeding the sample flow and preventing capillary action drawing the sample through the channel naturally.

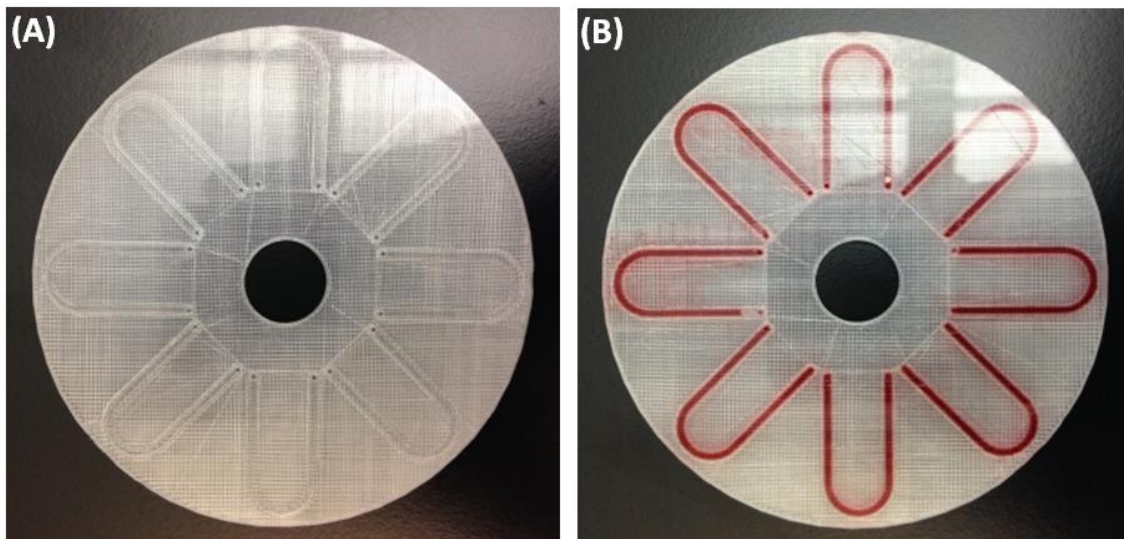


Figure 4.25: (A) 3D-printed LOAD device printed using PLA Translucent; (B) LOAD channels filled with red dye solution to illustrate improved optical transparency and successful formation of imbedded microfluidic channels.

Despite the successful formation of imbedded microfluidic channels in a LOAD device, the introduction of red dye solution into the channels revealed that the channels were not water tight. Within 30 seconds of the dye being introduced to the channels, there was visible permeation of the dye into the surrounding plastic.

A time lapse observation was performed to quantify the approximate rate of passive liquid loss when no centrifugal force is being applied (Figure 4.26). Assuming that channel formation is ideal (ideal cross section = 1 mm x 400 μm) and fill at time 0 is 100%, the volume is approximately 23 μl per channel and approximately 184 μl in total across all 8 channels. Images were taken at the specified times. The fluid loss in each channel was calculated by measuring the fluid loss in mm which was then converted into volume loss based on the channel dimensions. Although this would not be as accurate as directly quantifying the volume present in the channel, this method was the most practical for quantifying the fluid loss at multiple time points over an extended period.

The following metric was used to calculate total percentage liquid loss across all channels (total % channel liquid loss):

$$100 \frac{V_T - \sum_{i=1}^N (V_{x_i})}{V_T} \quad (11)$$

Where V_T is total approximate volume across all channels (184 μl), V_{x_i} is the approximate volume difference per channel.

It was expected that there may be liquid loss due to evaporation, however this was not factored in to calculations at this stage of investigation.

- After 12 hours: mean liquid loss was calculated at approximately 48% across all channels.
- After 24 hours: mean liquid loss was calculated at approximately 78% across all channels.

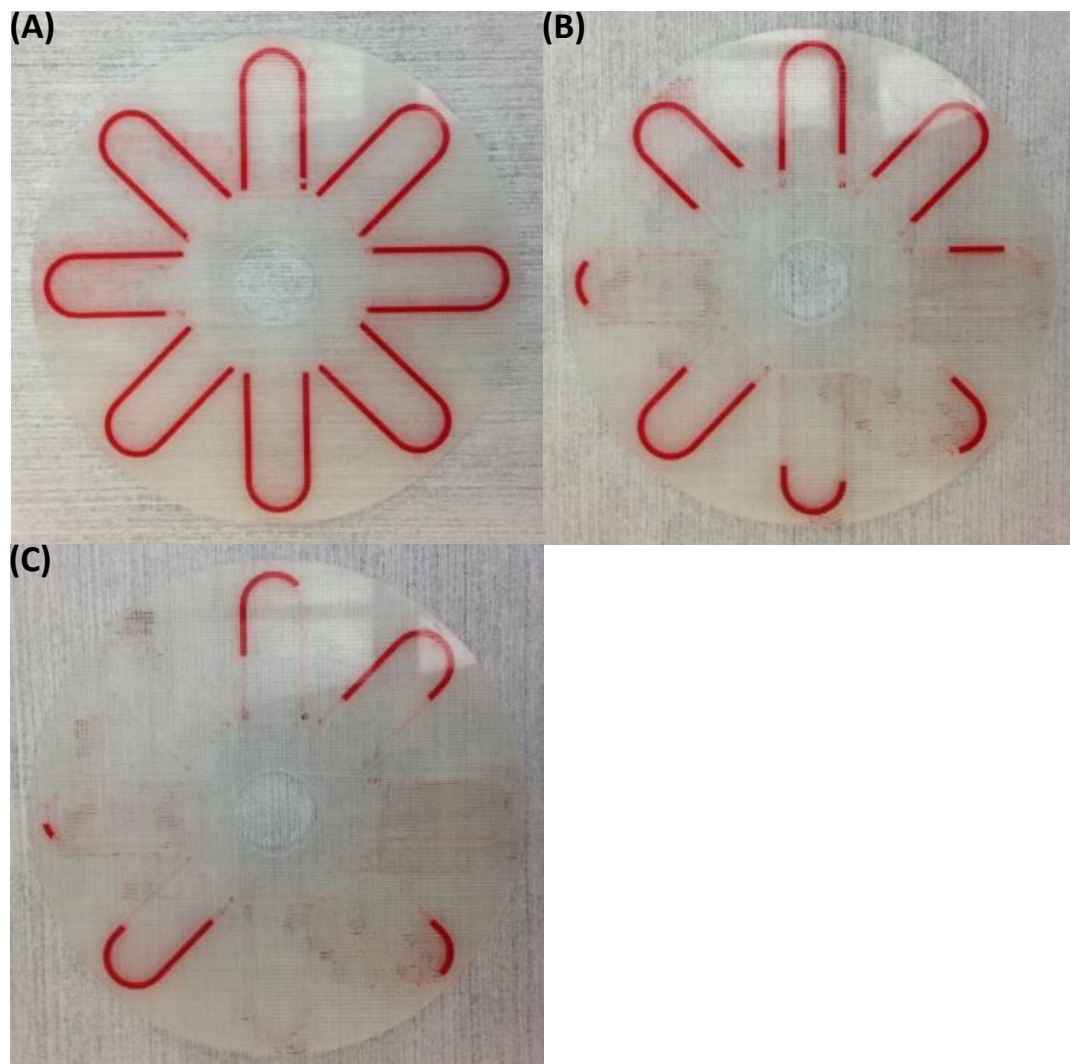


Figure 4.26: Time lapse series to quantify fluid loss from disc channels; (A) 0 hours; (B) 12 hours; (C) 24 hours.

The results show that there is liquid loss from the channels, with 78% liquid lost over 24 hours, however, the platform will not be expected to remain accurate for 24 hours after sample introduction. Assay results are intended to be generated and read within 5 minutes, a liquid loss of 3-4% per hour should allow for result generation without impacting the assay performance or accuracy; a liquid loss of 4% per hour translates to 0.33% (or 0.076 μl per 23 μl channel) in 5 minutes which is within the experimental error seen in section 3.3.9. However, the results display a weakness in

the channel structure. The 3-4% liquid loss per hour is via passive diffusion, with no force being applied to the sample. While this degree of water-tightness would be acceptable for current POC microfluidic chips with a time-to-result of <10 seconds, the LOAD device is intended to perform centrifugally in an optical disc drive, being subjected to high RPM and g-force to separate blood plasma. For example, a 4x optical drive is intended to rotate at 800-2000 RPM while transferring data. This translates to an approximate g-force of 32-200 *g* being applied at the disc circumference with a radius of 45 mm. Any passive liquid loss recorded at this stage of device development is undesirable if the end goal of centrifugally separating blood plasma from whole blood within the device is to be realised, as the device is unlikely to remain water tight duration centrifugation. It is possible that a higher extrusion temperature (210°C) may improve strand and layer merging, therefore improving the water tight seal. However, as discussed in section 4.3.5, this would result in sagging and collapsing of the channels. There is potential that post-print heat treatment (section 2.4) could be used to improve strand and layer merging and seal the channels without causing structural deformation to the channels; this is investigated in section 5.3.4.

4.3.6 Effect of Acetone Liquid on Channel Surface Roughness

It has been shown in section 4.3.5 that it is possible to form imbedded microfluidic channels, however, the surface structure remains an area of concern. Obstructions and imperfections could introduce differences in sample-reagent mixing, sample volume, or influence the blood separation. This could lead to inaccurate assay results with poor reproducibility and therefore incorrect diagnostic evaluation. Due to the previous success of using acetone to reduce surface imperfections in 3D-printed samples as seen in section 4.3.3, acetone was investigated for its potential in reducing surface imperfections within channel formations.

Surface roughness is traditionally used to compare manufacturing techniques (Hobson and Le, 2012), and is often quantified by the deviations in the direction of the normal vector of a real surface from its 'ideal' form. Surface roughness can have a

large impact on how an object interacts within its environment. For example, rough surfaces have higher friction coefficients, promote adhesion and are more prone to wear. Rough surfaces can also have reduced lifespan compared to smooth surfaces, as irregularities in the surface may create sites for cracks or corrosion (Photometrics Inc., 2016). Manufacturing processes intended to control and reduce roughness can be expensive, therefore there is often a compromise between a components manufacturing cost and its performance.

While there are several methods of quantifying and evaluating surface roughness, in general there are three different ways through which surface roughness can be represented. The arithmetic average (R_a) is the mean value of the deviation of the surface compared to the 'ideal surface' (Thorlabs Inc., 2016). This shows the location of the average surface position in relation to the ideal in the Y-axis.

$$R_a = \frac{1}{N} \sum_{i=1}^N |y_i| \quad (12)$$

Where y_i is the height difference from the ideal surface for each point of measurement and N is the number of measurements. The root mean squared (R_q) produces information about the mean value of the deviation of the surface compared to the ideal surface and statistical error (Thorlabs Inc., 2016). This is the most typically used method for quantifying surface roughness relative to the ideal surface.

$$R_q = \sqrt{\frac{1}{N} \sum_{i=1}^N y_i^2} \quad (13)$$

Where y_i is the height difference from the ideal of each point and N is the number of measurements. The final method is the most basic, the peak-to-valley distance (PV). The PV is simply a measure of the distance between the highest and lowest points overall within a sample length; it provides no information on mean values or statistical variation (Thorlabs Inc., 2016).

An experiment was performed in which channel samples were printed then treated using acetone liquid solution of a range of concentrations (0-100%). All samples tested in the following section were printed at 10 mm/s, 0.06 mm layer height

with plate 1 surface being printed onto the build table. OCT instrumentation as described in section 4.2.8 was used to image the channel cross-sections before and after treatment so the change in surface roughness could be quantified. OCT is a non-invasive imaging technique used to generate cross-sectional images of samples. The Images produced from OCT allows the surface trace, and therefore the surface roughness, to be analysed.

Initial channel samples were of the same specifications as determined in the previous successful channel formation experiments, described in section 4.3.5, however it was found that plate 1, at 200 μm thick, was preventing OCT light transmission from imaging the base surface. As the surface of plate 1 has higher reflectivity relative to the channel surface due to being printed onto the heater build table, it is possible that the signal returned from the plate 1 surface is much larger than that of the channel, and thus, with the intensity scaling adopted for the image, the effective signal-to-noise-ratio of light reflected at the bottom of the channel was too low. This can be seen in Figure 4.27 from the horizontal white lines at the top of the image on the plate 1 surfaces indicating high reflectance.

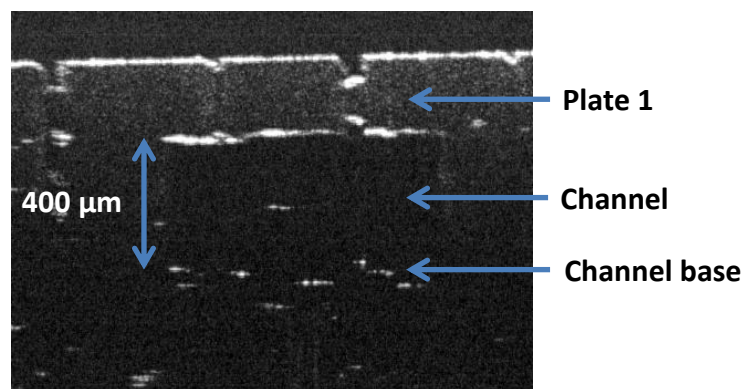


Figure 4.27: OCT image of 3D-printed channel sample (schematic: section 4.3.5).

As a result, a new design with a thinner plate 1 was designed. The samples had channels of 1 mm wide and 400 μm depth (plate 2), positioned with plate 1 being 100

μm thick and plate 3 being $700\ \mu\text{m}$ thick (Figure 4.28(A)). Inspection of the images (Figure 4.28(B)) revealed that the channel base surface was most prone to surface roughness and irregularities, having far greater peaks and troughs relative to the surface of plate 1 (channel ceiling). Although image quality was improved relative to the previous channel (Figure 4.27), this design still produced poor image quality of the bottom of the channel when using the OCT equipment.

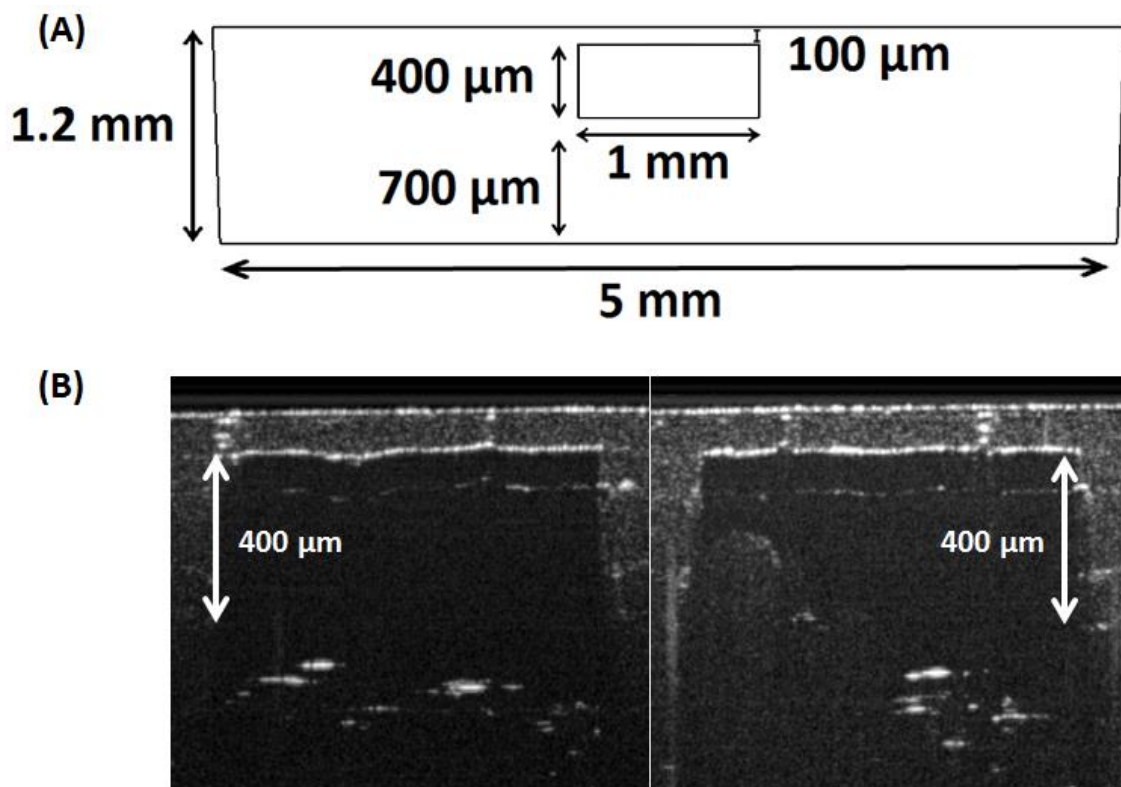


Figure 4.28 : (A) Schematic of channel sample. (B) OCT images of channel samples printed using schematic (A).

In order to accurately image, and subsequently quantify any changes in surface roughness, improved image quality was required. It was determined after further trials of channel samples that the channels must be open-faced for the best possible imaging of the base channel surface, which is the surface most affected by surface roughness. By printing open face channels, reflection is reduced and better cross-sectional images

can be generated of the channel base. Also acetone treatment can be applied with greater control and any opaque white plaque that forms within the channel as a result of the acetone solution will not prevent imaging from being possible. Therefore, the optimised channel depth of 400 μm , as determined in section 4.3.5, was used and the open-faced channel schematic shown in section 4.2.10 used. Channel samples were printed open-face down to emphasise the roughness of the channel base surface, as would be the case in a LOAD device printed with plate 1 surface down onto the build table. Cross-sectional OCT images were taken at a fixed location marked by scoring the plate 1 surface using a scalpel. Acetone solutions of 0-100% concentration were prepared, applied to the channels and allowed to air dry. Then cross-sectional OCT images were taken and the surface trace of the channel base was then analysed. Figure 4.29 illustrates an OCT image with annotations highlighting the image features.

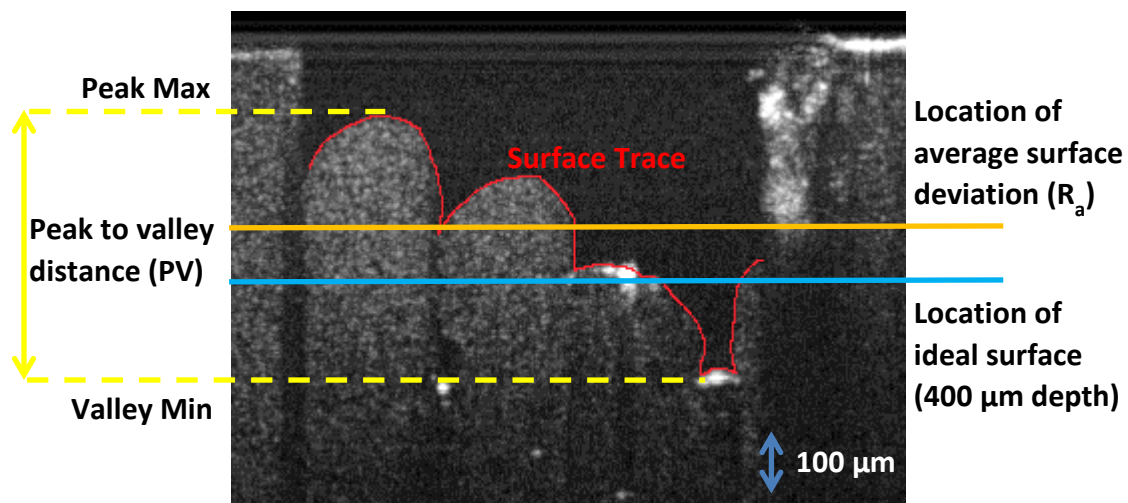


Figure 4.29: OCT image of channel surface with surface roughness features highlighted.

The first stage in image analysis was calculating the R_a of the channel surface relative to the 'ideal surface' as defined by the CAD model. The 'ideal surface' position of 400 μm depth was applied to the images so the mean deviation of the channel

surface could be calculated using Equation 12 and the difference before and after acetone treatment quantified. The results can be seen in Table 4.4.

Table 4.4: Mean deviation (R_a) of channel surface trace from the ideal surface (μm).

Concentration of acetone in IPA	R_a (μm)		
	Pre-treatment	Post-treatment	Difference
0%	-79.3	-88.0	-8.8
20%	134.4	130.7	-3.8
40%	-84.5	-95.7	-11.1
50%	-120.4	-123.8	-3.4
60%	-8.1	-9.8	-1.7
80%	108.2	158.3	50.2
100%	70.2	158.3	88.1

The R_a data (Table 4.4 pre-treatment) revealed that the average channel surface position can fluctuate, with the position ranging from 120.4 μm below the ideal surface to 134.4 μm above the ideal surface in the Y-axis position. This emphasises how unpredictable/inaccurate 3D-printing can be and how large variations can be seen between models produced under identical conditions. In addition it revealed how the average surface position can shift in relation to the ideal surface following acetone treatment (Table 4.4 post-treatment); at 40% acetone concentration, the R_a shifted down by approximately 11 μm whereas at 80% concentration the R_a shifted up by approximately 50 μm . This was presumed to be due to the repositioning of polymer within the channels that takes place during the treatment.

Due to the shifting average surface position, the definition of an 'ideal surface' from which surface roughness could be calculated became problematic and introduced potential variables not seen in other forms of manufacturing. As the position and structure of the channels within the samples varied, the application of an ideal surface from which surface roughness quantification could be performed was not relevant.

Therefore the R_a , as a method of quantifying surface roughness, is biased and inaccurate in this context.

For example, a channel may be perfectly smooth but placed significantly above or below the 'ideal' channel location within the sample, as a result, the smooth surface would appear to have high surface roughness when average deviation (R_a) from the ideal is calculated. In addition, the apparent effectiveness of the acetone treatment on improving surface roughness would be diminished or inaccurate if the R_a had shifted away from the ideal despite actual roughness decreasing. The R_q , as calculated from the ideal using Equation 13, is displayed in Table 4.5 and OCT images shown in Figure 4.30 to demonstrate the inaccuracy of using R_a as a method of quantifying surface roughness in this context.

Table 4.5: Root mean squared deviation (R_q) of channel surface trace from the ideal surface (μm).

Concentration of acetone in IPA	R_a (μm)			Difference (%)
	Pre-treatment	Post-treatment	Difference	
0%	141.6	146.5	4.8	3.4
20%	187.3	182.1	-5.2	-2.8
40%	105.7	113.1	7.5	7.1
50%	135.5	134.9	-0.5	-0.4
60%	58.2	40.6	-17.6	-30.3
80%	167.2	182.1	14.9	8.9
100%	148.2	181.5	33.4	22.5

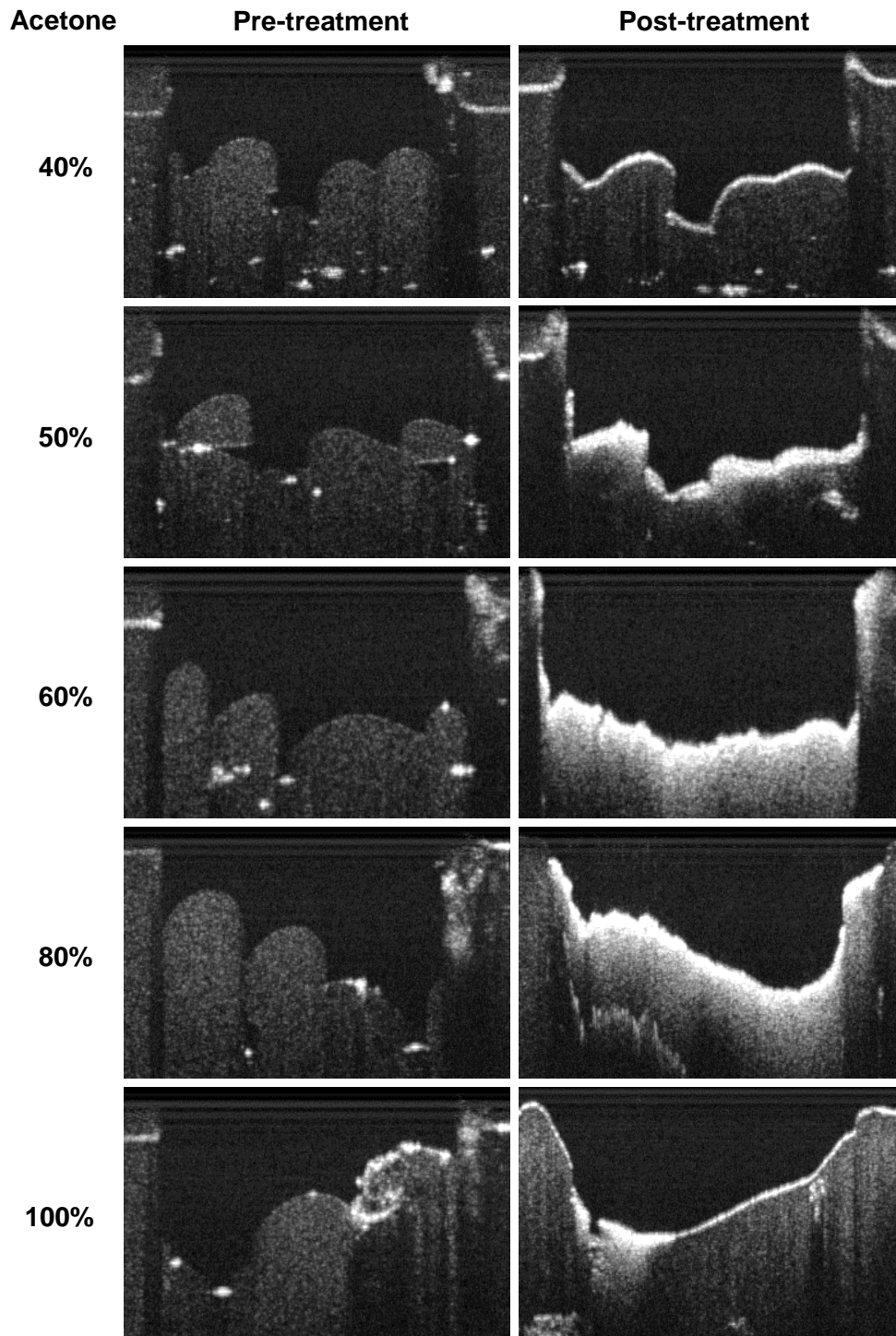


Figure 4.30: OCT images focused on channel surface, pre and post acetone treatment.

As can be seen from Figure 4.30, as acetone concentration increased, there was a visible decrease in the surface roughness. However, according to the R_q calculated from the ideal (Table 4.5), the roughness increased. This was due to the R_a shifting away from the ideal as seen in Table 4.4. For example, at an acetone concentration of 100%, the R_q in relation to the ideal surface increased by approximately 22.5% despite the figure displaying a visible decrease in surface roughness following treatment Figure 4.30 (100%).

This bias, due to the shifting R_a relative to the ideal, was confirmed when the PV profile was investigated (Table 4.6). It was seen that the maximum peak to valley distance was reduced following treatment despite the roughness apparently increasing, according to Table 4.5. For 100% acetone, a PV decrease of approximately 18% was observed, signifying a decrease in surface roughness.

Table 4.6: Peak to valley distance (PV) (μm).

Concentration of acetone in IPA	R_a (μm)			Difference (%)
	Pre-treatment	Post-treatment	Difference	
0%	427.0	427.0	0.0	0.0
20%	535.5	549.5	14.0	2.6
40%	252.0	227.5	-24.5	-9.7
50%	220.5	213.5	-7.0	-3.2
60%	280.0	150.5	-129.5	-46.3
80%	448.0	259.0	-189.0	-42.2
100%	395.5	325.5	-70.0	-17.7

As this line of experimentation was investigating the potential use of acetone treatment for improving surface roughness, the R_q was not calculated relative to the 'ideal surface' but rather as a deviation from the average surface (R_a). This would more accurately represent the difference in surface roughness following acetone treatment by removing any bias that would arise from the R_a shifting away from the ideal. The results can be seen in Table 4.7.

Table 4.7: Root mean squared deviation (R_q) of channel surface trace from the average surface (R_a) (μm).

Concentration of acetone in IPA	R_a (μm)			Difference (%)
	Pre-treatment	Post-treatment	Difference	
0%	117.4	117.1	-0.3	-0.3
20%	130.5	126.9	-3.6	-2.8
40%	63.4	60.4	-3.0	-4.7
50%	62.0	53.6	-8.4	-13.6
60%	57.6	39.4	-18.3	-31.7
80%	127.5	90.0	-37.5	-29.4
100%	130.5	88.9	-41.6	-31.9

As can be seen from the images in Figure 4.30 and R_q in Table 4.7, in all cases, liquid acetone treatment can be used to reduce surface roughness in PLA microfluidic channels. At a concentration of 100%, surface roughness was decreased by approximately 32%.

However, R_q does not convey accurately the surface and structural changes that have occurred. White plaque formation becomes increasingly prevalent as concentration increases; as before, this is of concern as the white plaques are opaque and reduced optical transparency as discussed in section 4.3.4. As a primary point of investigation in this project is improving the optical transparency of 3D-printed devices, the white plaque formation is detrimental to this goal. In addition to the plaque formation, the destructive nature of acetone on PLA becomes apparent as the acetone concentration increases; there is visible damage and deformation to the fundamental channel structure, particularly evident in samples exposed to acetone concentrations $\geq 60\%$. At concentrations of 80% and 100% the channel walls have been dissolved to the point where one would expect perforation of the channels. A point of interest however, is that despite channel destruction witnessed, plaque formation at 100% acetone solution is minimal compared to 60% and 80%. This mimics results seen from previous use of liquid acetone treatment (section 4.3.4).

The results presented in Table 4.7 show that, generally, as the acetone concentration is increased, the surface roughness decreased. 60% acetone solution provided the most improvement in PV with approximately 46% reduction and an improvement in surface roughness (R_q) of approximately 32% reduction; but, as stated previously, caused significant plaque formation. 80-100% acetone solutions, although successful in reducing PV and R_q , were destructive to the point of causing severe damage to integral channel structure; 80% acetone concentration reduced PV and R_q by approximately 42% and 29% respectively, 100% acetone concentration reduced PV and R_q by approximately 18% and 32% respectively. 50% acetone concentration decreased surface roughness by approximately 14% without causing significant structural damage or plaque formation. Therefore a concentration of 50% acetone provides the best compromise between smoothing effect and diminished optical transparency; whereas 60% acetone provides the best compromise between smoothing effect and structural damage to the channel.

As stated at the beginning of this section, improving surface roughness is a key challenge in manufacturing. In the case of microfluidic channels for use within an optical LOAD platform, the channels serve as both vessel and window. Therefore, difficulties arising from surface roughness are compounded. In optical sensing it is usually desirable to have as little roughness as possible, so that light is scattered as little as possible (ZYGO, 2016). In a microfluidic channel, surface roughness can introduce variations in volumetric capacity, which is of particular concern in POC devices as control of sample volume is key to minimising variability in results (Gubala *et al.*, 2012). In addition, roughness impacts on the capillary effect necessary for sample flow within POC microfluidic devices (Yuan and Lee, 2013) and introduces turbulence within the fluid sample, all of which can affect assay results and subsequent diagnostic evaluation. Reducing channel roughness will improve sample flow, however, turbulence may aid sample-reagent mixing should assay reagents be deposited in the channel to be dissolved and distributed within the sample.

It has been demonstrated that significant improvement to surface roughness of PLA microfluidic channels using acetone solution is possible, and acetone remains a

potential low-cost post-print treatment method for sealed internal cavities where other methods are inapplicable.

4.3.7 Problems

As is the case with any emerging and evolving technology, one will naturally encounter problems. A significant problem involves filament feed. The filament is fed from a supply spool on the back of the printer, through a feed motor, up through rigid plastic tubing to the printer head. Often during printing the filament feed would stop which was inconvenient especially on prints with long print times (the average print time for a LOAD device was 5 hours). It was discovered that the filament would jam in the print head during the printing process, stopping all subsequent printing and requiring the filament to be forcibly removed, which would often require disassembly of the print head. Investigations were performed to try and reduce the occurrence of this. Initially it was thought that dust on the filament was being dragged into the print head, burning and building up an obstructive layer that blocked the nozzle. To prevent this, a dust filter was installed to try and clean the filament before it enters the feed mechanism; this did not improve the situation.

After more investigation, swelling of the filament was identified as the most probable cause of blockage; when stored improperly, PLA filament absorbs water from the air and swells, exceeding the 2.85 mm diameter requirement of the printer (RepRage.com, 2015). As a result, the filament could not be fed into the printer head and filament flow stopped. Following this, all filaments were stored in air tight bags with desiccant when not in use which improved the situation. In addition, the 3D-printer was upgraded to a geared feeder mechanism which also significantly reduced filament feed issues. Filament feed problems still occurred, primarily due to the filament randomly forming a plug when heated and obstructing flow, however this was less frequent.

Another serious problem encountered during the project concerned the nozzle thermostat in the printer head. It malfunctioned, resulting in the 3D-printer being

unusable for approximately 6 months as several replacements had to be ordered, fitted and tested until the repair was successful.

Other problems encountered involved the unpredictable state of printed objects. There was a lot of variation in the quality and finish of printed objects, even between those made during the same print session. This could range from several missed/faulty layers in a model to the entire surface, internal and external, being extremely rough and covered in extrusions and nodules. When attempting to print objects that need to be water tight and optically transparent, any differences or imperfections could render them unusable. The occurrence of such imperfections appeared to be reduced when models were printed individually rather than in batches, however, this significantly increased labour and manufacturing time and reduced the number of objects that could be made.

4.4 Conclusions

A combination of print optimisation and post-print finishing techniques were used to improve optical transparency of 3D-printed objects significantly; the poor optical transparency of 3D-printed polymers is a fundamental obstacle that limits the potential for optical quantification and application of 3D-printing technology.

Optimisation of the layer height, print speed and position of the build table in relation to the print nozzle all contributed to an improvement in optical transparency resulting in the ability to print objects in which colour change reactions can be viewed. It is believed that these parameters increased strand and layer merging in the prints which resulted in the increased optical transparency observed. Optimisation of the layer height and build table position displayed a decrease in attenuation in samples of up to 252% and 200% respectively. All further prints will be done at a layer height of 0.06 mm and at 10 mm/s print speed as this appears to offer the best compromise between optical transparency, print success and print time.

When acetone vapour treatment was used, it was possible to improve transparency of plastic samples by up to a further 30%. Initial experimentation with acetone liquid treatments were unable to improve optical transparency, however, acetone liquid treatments was seen to reduce surface roughness in channel samples by up to 32%. In imbedded microfluidic channels it is not possible to directly access the channel surface in order to decrease surface roughness via cutting or sanding; a liquid treatment that could be pumped into the channels to decrease surface roughness without requiring the user having direct physical access, has the potential of being highly advantageous.

A lab-on-a-disc device has been designed and developed with imbedded microfluidic channels with a volumetric capacity of approximately 23 μl , 54% better than target of $\leq 50 \mu\text{l}$. Optimisation of print extrusion temperature (200 °C) has resulted in sealed channels that would be suitable vessels for performing assay reactions and optical transparency is such that colour is clearly visible within the channels. The LOAD devices were produced as a single manufacturing step and did not require post print treatments to successfully form the imbedded channels or improve optical transparency. However, the channels did not have a sufficient water seal to withstand the application of centrifugal force, which is necessary for the separation of plasma from whole blood. Experimentation with post-print heat treatment will be investigated as a potential means of adequately sealing the microfluidic channels in section 5.3.4. Testing will progress towards performing quantitative assays and whole blood separation within 3D-printed devices.

Chapter 5: The Performance of a Whole Blood Colourimetric Assay in a 3D-Printed LOAD Device

5.1 Introduction

Experimentation and investigation thus far has resulted in an optimised assay for the quantification of cholesterol and glucose, significantly improved optical transparency of fused deposition modelling (FDM) 3D-printed devices and the formation of imbedded microfluidic channels in a lab-on-a-disc (LOAD) device. The final stages of device development involve proving and demonstrating the two final fundamental principles of the project:

- (1) That optical assays can be performed and quantified in a low-cost FDM 3D-printed device,
- (2) That centrifugation based whole blood separation can be performed in a low-cost FDM 3D-printed device.

Once these principles have been proven, they can be applied to the development of the 3D-printed LOAD device in an attempt to combine them and produce a LOAD device capable of centrifuging whole blood and performing optical quantitative assays in one step.

The objectives of the work presented in this chapter were to progress assay development and to perform the glucose assay in a 3D-printed microfluidic device, with the goal of recording absorbance data and generating a glucose concentration calibration curve in a low-cost FDM 3D-printed microfluidic device. Glucose assay experimentation will progress towards using whole blood samples. Then experimentation will investigate the separation of blood plasma from whole blood samples in FDM 3D-printed devices. A serious obstacle to this is the inherent lack of adequate water-tightness in FDM 3D-printed devices due to the manufacturing method discussed previously. Finally, optimisation and development of the LOAD device will continue with the ultimate objective being the performance of the glucose assay in whole blood within the device, performing centrifugation based whole blood separation and the generation of coloured plasma visible in the LOAD microfluidic channels.

5.2 Materials and Methods

Phosphate buffered saline (PBS, 10 mM phosphate buffer, 2.7 mM potassium chloride and 137 mM sodium chloride, pH 7.4) tablets, chromotropic acid disodium salt dihydrate (CTA), 4-aminoantipyrine (AAP), Horseradish peroxidase Type II essentially salt-free, lyophilized powder, 150-250 units/mg solid (using pyrogallol) (HRP), D-glucose, glucose oxidase from *Aspergillus Niger* lyophilized, powder, ~200 units/mg protein (GLOx), were all purchased from Sigma-Aldrich (Poole, UK). Ultrapure water (18 MΩcm) was produced using a Milli-Q water system (Millipore Corp., Tokyo, Japan). Defibrinated whole horse blood was purchased from TCS Biosciences (Buckingham, UK). The concentration of glucose in samples was tested and quantified independently using an Optium Exceed Blood Glucose Monitoring System (Abbott, UK). Mini Star Silverline microcentrifuge (VWR, USA) was used for sample preparation when necessary. Camlab Carbolite NR30 oven (Camlab, UK) was used for heat-treatment of samples.

5.2.1 Buffers and Solutions

- Phosphate Buffered Saline pH 7.4 was prepared by using PBS tablets with a final volume of 1 L using dH₂O.
- Horse blood was prepared by following the protocol detailed in section 3.3.6.
- GLOx 1000 units / ml was prepared by adding 1 ml PBS, pH 7.4 to 5.88 mg GLOx solid and stored at -20°C until use.
- CTA solution was prepared by dissolving the appropriate concentration of CTA in PBS pH 7.4.
- AAP solution was prepared by dissolving the appropriate concentration of AAP in PBS pH 7.4.
- HRP 1000 units / ml was prepared by adding 1 ml PBS, pH 7.4 to 6 mg HRP and stored at 4°C until use.
- Glucose solution was used as a substrate for GLOx and prepared by dissolving the appropriate concentration of glucose in PBS pH 7.4.

5.2.2 Microfluidic Cuvette Devices

Microfluidic cuvettes were designed as microfluidic vessels with decreased fluidic capacity and path length in which to perform the glucose assay and monitor the absorbance readings and how the assay performs in a 3D-printed microfluidic device. The microfluidic device was a 12 x 12 x 42 mm cuvette which had an internal microfluidic cavity with a thickness of 500 μm and volumetric capacity of $\sim 190 \mu\text{l}$. The cuvette design is shown in Figure 5.1. The chamber walls were 400 μm thick. The circular tube to one side allowed total filling of the cavity. All samples were printed at 10 mm/s with 0.06 mm layer height. Devices took 1 hour to print and consumed approximately 2 g of plastic filament per device. The microfluidic cuvettes were also used as example fluidic vessels from which inter- and intra-variability of devices could be investigated. Cuvettes were made from Ultimaker PLA Transparent, Ultimaker PLA Translucent, Innofil PLA Natural and InnoPET Natural where stated.

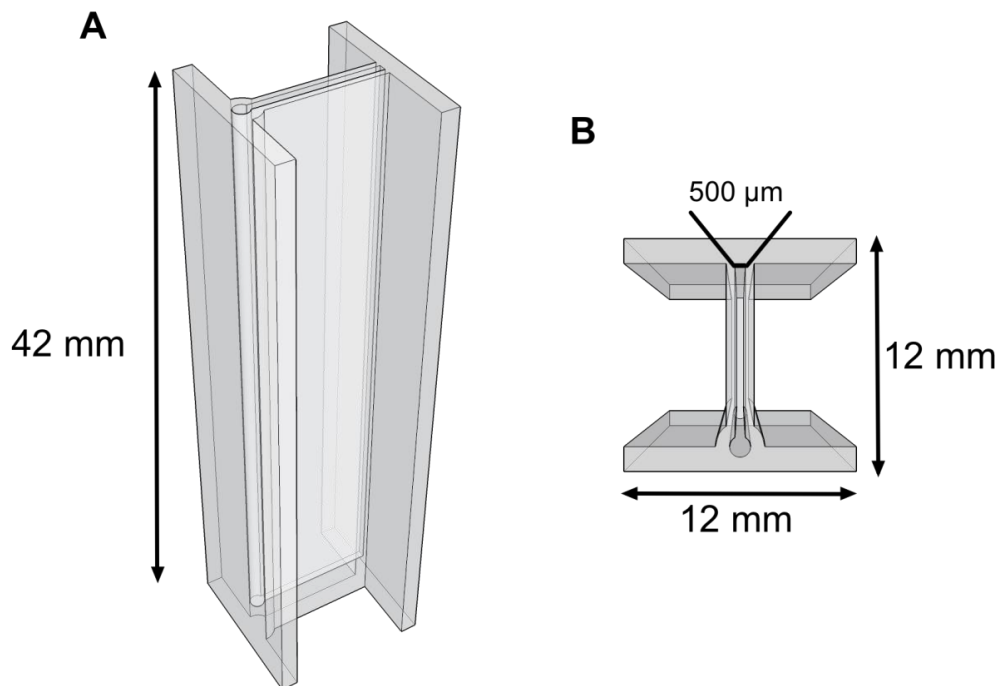


Figure 5.1: Schematic of the microfluidic device.

5.2.3 Spectral Analysis Instrumentation

The absorbance of the substrate assay reaction in the 3D-printed microfluidic devices was quantified by analysing the transmission spectrum of the assay using a fibre coupled tungsten halogen light source (Ocean Optics ecoVis, Ocean Optics, USA) and a CCD spectrometer Ocean Optics ADC1000-USB spectrometer (Ocean Optics, USA). The light source has an integrated cuvette holder which was adapted to hold the microfluidic devices. The light source and the spectrophotometer were connected using a short length (10 cm) of multimode optical fibre. The instrumentation can be seen in Figure 5.2.

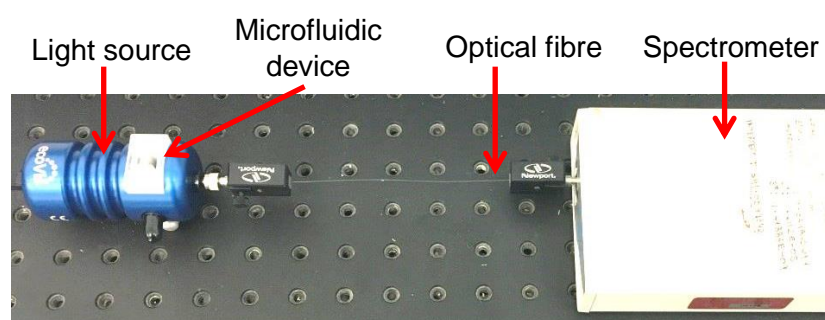


Figure 5.2: Instrumentation used for spectral analysis.

5.2.4 Centrifuge Pellet Device

Pellets were designed to investigate blood separation in a 3D-printed device. They were designed to fit inside a standard 1.5 ml Eppendorf tube for use within the benchtop microcentrifuge. The pellets are 8.5 x 2.82 x 17 mm with 0.5 mm sample walls. The sample cavity was 4 x 2 x 14 mm with a volume of $\sim 112 \mu\text{l}$. The schematic can be seen in Figure 5.3. Pellets were made from PLA Translucent. All samples were printed at 10 mm/s with 0.06 layer mm height. Devices took 36 minutes to print and consumed approximately 1 g of plastic filament per device.

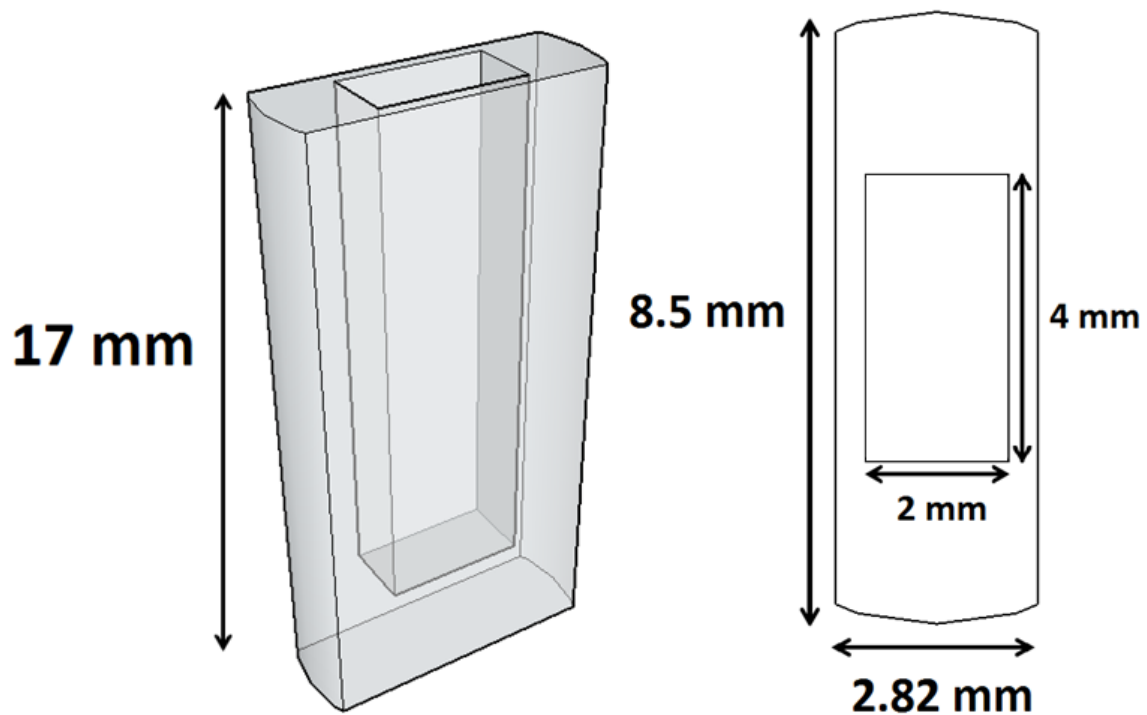


Figure 5.3: Schematic of the 3D-printed centrifuge pellet.

5.2.5 Glucose Assay in 3D-Printed Microfluidic Cuvette Device

Glucose assay reagent solution was made by dissolving CTA (20 mM), AAP (10 mM), GIOx (20 U/ml) and HRP (6 U/ml) in PBS solution or CTA (40 mM), AAP (20 mM), GIOx (20 U/ml) and HRP (6 U/ml) in defibrinated whole horse blood. The reaction was started by adding glucose solution (0-10 mM). The assay was read after 2 minute incubation and the absorption spectrum recorded; blood samples were centrifuged for 2 minutes at 6000 RPM and the liquid component isolated before analysis. The assay was performed in a microfluidic cuvette device (section 5.2.2) and the absorbance spectra assessed using the equipment described in section 5.2.3.

5.2.6 Blood Separation in a 3D-Printed Pellet Device

Pellets (section 5.2.4) were printed and filled with defibrinated whole horse blood. Pellets were placed inside 1.5 ml Eppendorf tubes and centrifuged for 2 minutes. A selection of pellets were also subjected to heat-treatment, consisting of 2 hour incubation at 60 °C in an oven before centrifugation testing.

5.2.7 Glucose assay in LOAD Platform

A generic usb optical disc drive (ODD) (HL-DT-ST DVDRRW GSA-2164D USB) was used to perform centrifugation experiments involving LOAD devices. The drive was unmodified other than the removal of the outer case to give access to the spindle whilst the drive is operational. Attempts at using software to manually control the drive were unsuccessful and the drive firmware prevents the drive from operating or spinning without a signal detected from an optical disc, therefore, the simplest solution was to place the LOAD devices on top of a data disc which was spun by the drive, as can be seen in Figure 5.3. The same data disc was used to activate the drive in all testing. The average RPM of the drive whilst reading the data disc was 1270 – 3175 (6.35x constant angular velocity) as determined using the software Nero Disc Speed (Nero AG, Karlsruhe, Germany). This translates to approximately 81 - 507 g-force being applied at the circumference of the LOAD device with a radius of 45 mm. Conventional protocols utilising centrifuges often apply 1000-2000 g-force for 10 minutes.

Glucose assay reagent solution was made by dissolving CTA (40 mM), AAP (20 mM), GLOx (20 U/ml) and HRP (6 U/ml) in defibrinated whole horse blood. The reaction was started by adding glucose solution (10 mM). The assay was applied to the LOAD channels, incubated for 2-minutes and then centrifuged using the optical disc drive for approximately 10 seconds.

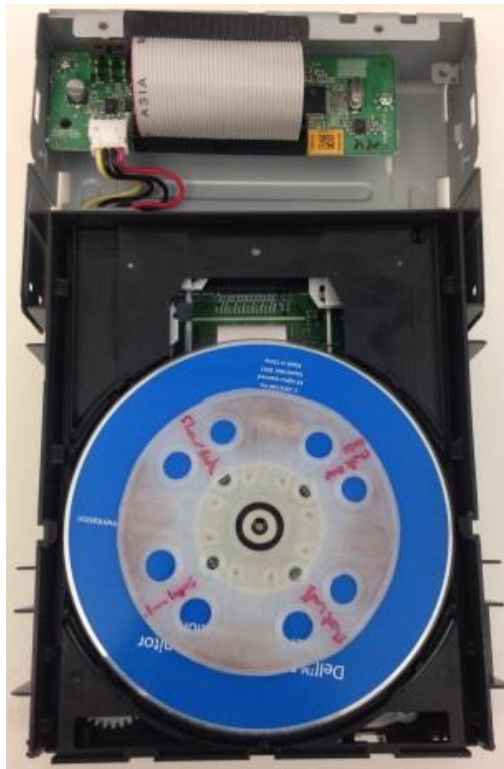


Figure 5.3: Generic optical disc drive with 3D-printed LOAD device placed on top of a data disc.

5.3 Results and Discussion

The following section describes the development process of two key aims. Firstly, the demonstration of filling and reading a biological assay within a 3D-printed microfluidic device. Secondly, the centrifugation and separation of plasma from whole blood within a 3D-printed microfluidic device. Finally, the development and optimisation of a microfluidic LOAD device is detailed, culminating in the performance of the whole blood glucose assay and plasma separation within a LOAD device. It should be noted that the blood washing protocol as discussed in section 3.3.6 has been implemented from section 5.3.1 onwards.

5.3.1 Glucose Assay Performed in a 3D-Printed Microfluidic Device.

Following the optimisation of the 3D-printing methodology to produce plastic samples of sufficient optical quality to allow the optical interrogation of internal cavities and the formation of viable microfluidic channels, the next stage was to demonstrate the filling and reading of the glucose assay within a 3D printed microfluidic device.

Cuvette design progressed from a 1 cm path length design, common in laboratories, to the microfluidic 500 μm path length cuvette demonstrated here. The microfluidic devices manufactured for use with the glucose assay were printed at a rate of 10 mm/second with a layer height of 0.06 mm using PLA Translucent. The glucose assay was performed in the 3D-printed microfluidic device as described in section 5.2.2. Samples were prepared using the chemical and enzyme concentrations described in section 5.2.5. The reaction was started by adding glucose solution of the desired concentration. Figure 5.5 shows a photograph of the microfluidic channel before and after the glucose assay reaction. The limits of the 3D-printers capabilities were tested through the design and manufacture of a 100 μm path length microfluidic cuvette and an S-shaped channel 2 mm wide with 500 μm path length, also shown in Figure 5.5. These are included to show the range of designs possible with the use of 3D-printing. An important point to note is that the 3D-printed cuvette devices all appeared to be water-tight, no evidence of fluid dissemination was observed outside the microfluidic channels.

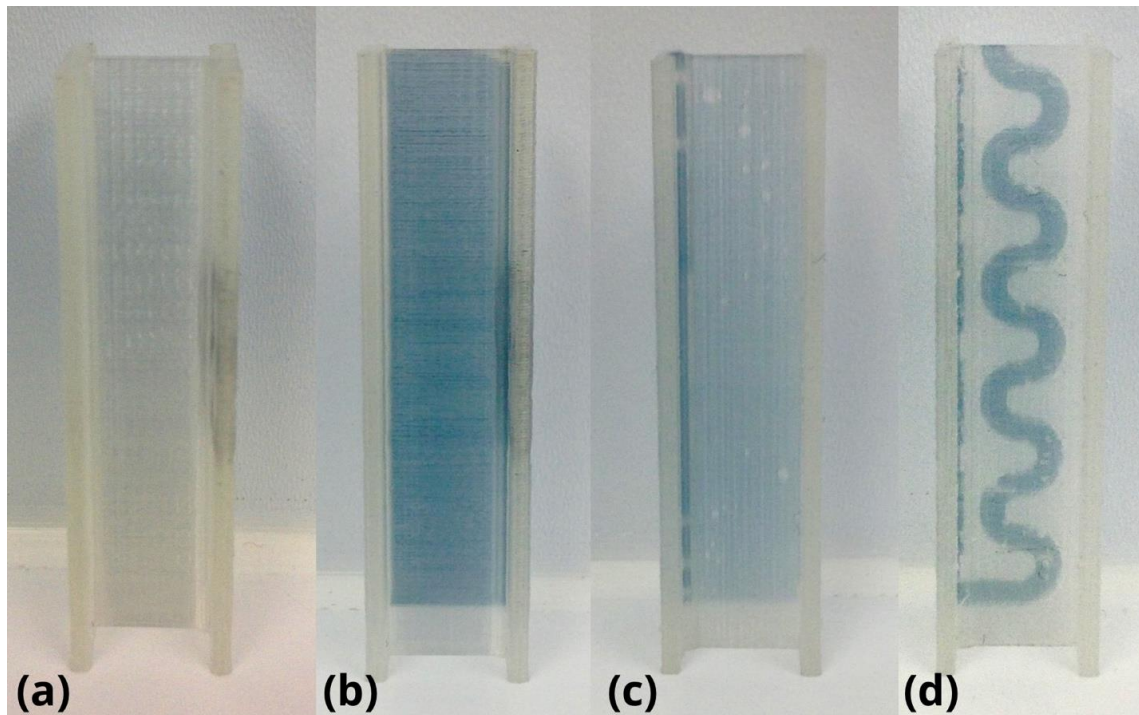


Figure 5.5: Microfluidic cuvette, (A) before glucose assay; (B) after glucose assay. Also shown are microfluidic cuvettes prepared with, (C) 100 μm thick chamber; (D) S shaped channel.

The absorbance spectra of the 500 μm thick chamber cuvette, Figure 5.5(B), were recorded using the methodology described in section 5.2.3. The resulting spectra shown in Figure 5.5 are a mean of 3 separate samples intensity readings taken from the 500 μm pathlength cuvette.

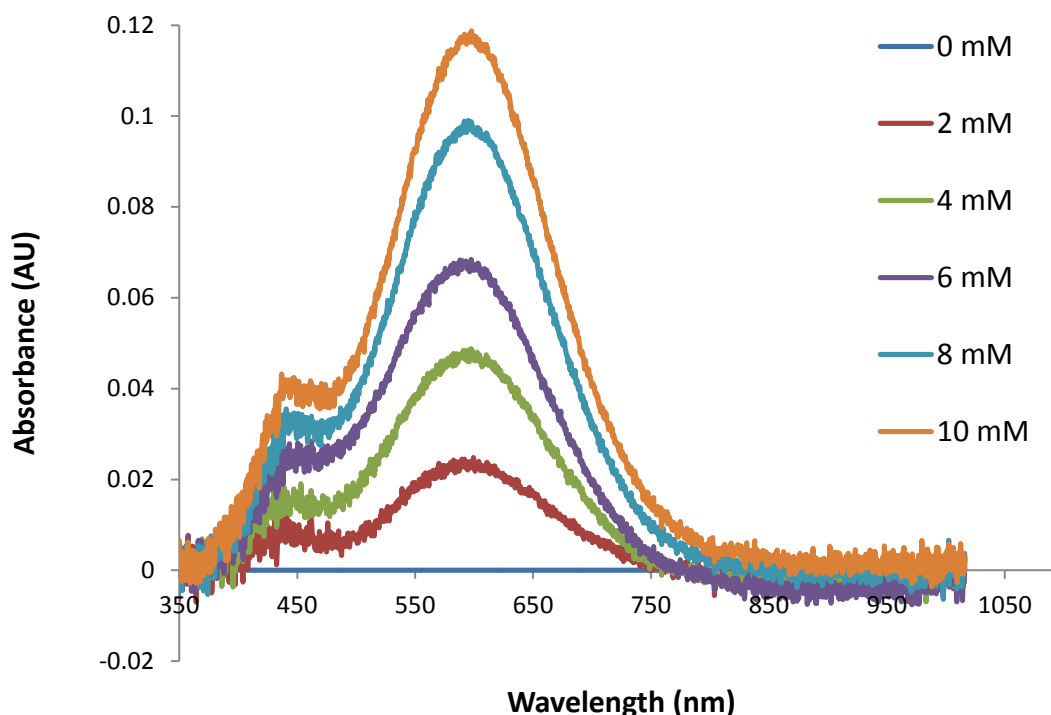


Figure 5.5: Change in the quinoneimine dye absorbance spectra with glucose concentration. Glucose (0-10 mM), CTA (20 mM), AAP (10 mM), GIOx (20 U/ml) and HRP (6 U/ml) in PBS solution. The assay was read after 2 minute incubation. Assay performed in 500 μm pathlength cuvette.

As the glucose concentration increases, the quinoneimine dye concentration also increases, resulting in an increase in absorbance centred around 590 nm. The spectra produced illustrate the range over which absorbance can be quantified. In this work, the absorbance of quinoneimine dye has been quantified at 590 nm, the approximate peak absorbance of the quinoneimine dye, and at 650 nm, the wavelength that an optical DVD drive operates at. Both sets of absorbance data have been shown in Figure 5.7 to illustrate how shifting the detection wavelength from the peak of 590 nm shifts the trend line accordingly; linearity is unaffected, but sensitivity is decreased.

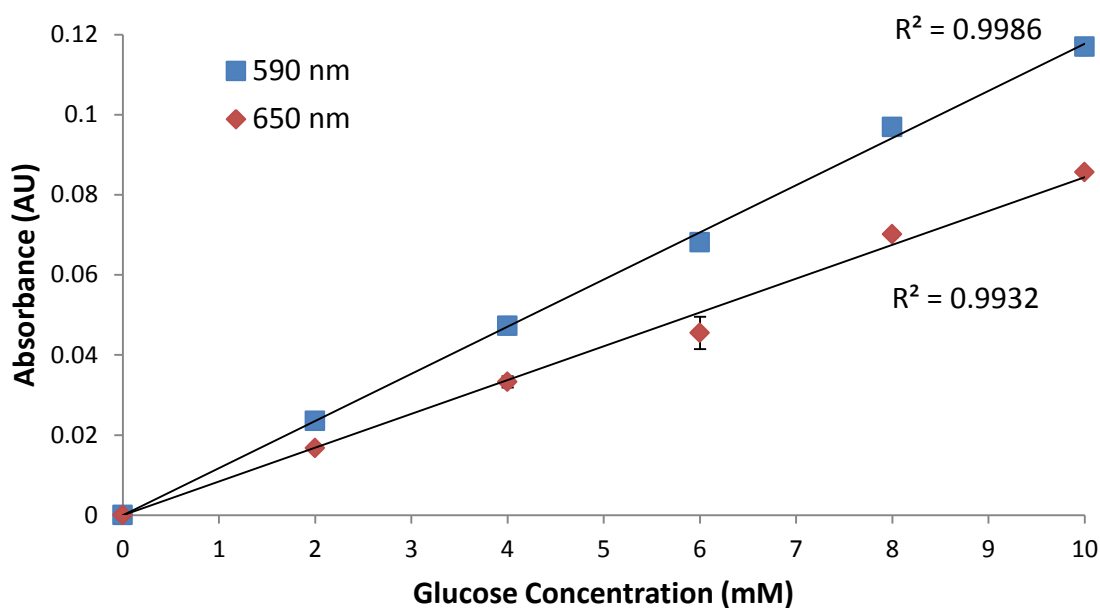


Figure 5.7: Difference in the absorbance of glucose concentration at 590 nm and 650 nm, n=3. Glucose (0-10 mM), CTA (20 mM), AAP (10 mM), GLOx (20 U/ml) and HRP (6 U/ml) in PBS solution. The assay was read after 2 minute incubation.

The data displayed in Figure 5.7 shows a linear absorbance trend line at 650 nm for increasing glucose concentrations with an R-squared of 0.99. This establishes that it is feasible to measure glucose concentration using a colourimetric assay in a 3D-printed microfluidic PLA device. The full range of glucose concentrations at 590 nm are shown in Figure 5.8, alongside the data from previous plate reader based experiments from section 3.3.9.

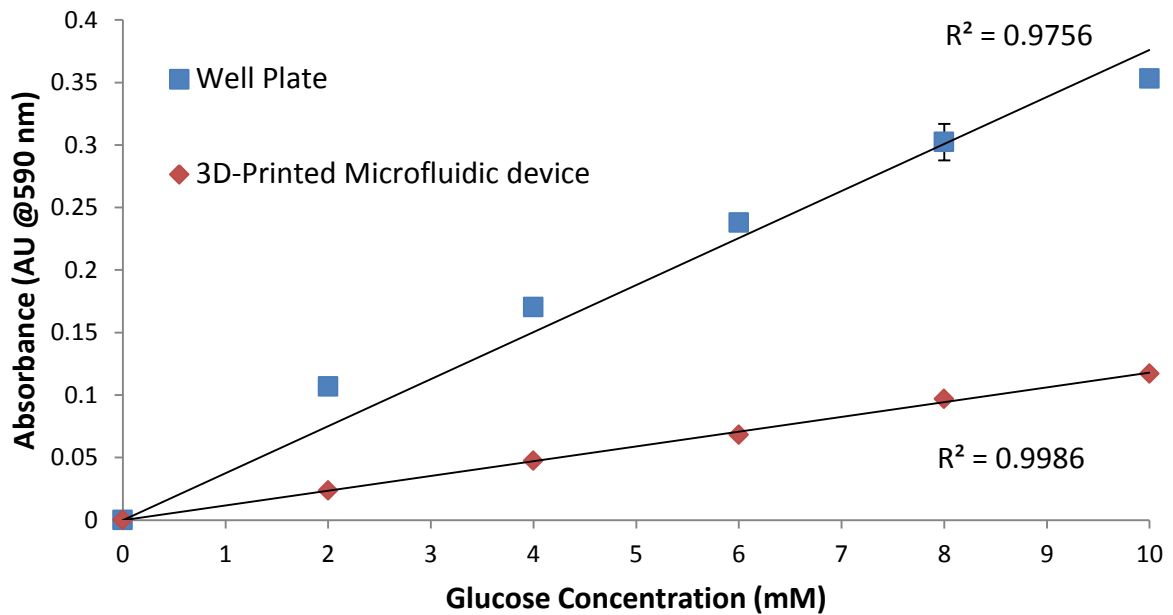


Figure 5.8: Absorbance comparison between 3D printed microfluidic device and well plate reader, n=3. Glucose (0-10 mM), CTA (20 mM), AAP (10 mM), GLOx (20 U/ml) and HRP (6 U/ml) in PBS solution. The assay was read after 2 minute incubation.

In Figure 5.8, the data produced shows a linear dilution curve for increasing glucose concentrations with an R^2 of 0.99. When compared to results produced with a commercial plate reader assay, the 3D-printed microfluidic device performs well. There is around a 2-3 times difference in absorbance, which is consistent with the native attenuation of the 3D-printed plastic and reduced sample pathlength in the device compared to the well plate, which reduces the sensitivity as discussed in section 5.3.2. However, neither the linearity nor the error of the assay were affected.

The LoD is the lowest analyte concentration likely to be distinguished from the limit of blank at a 99% confidence level, as defined by Quansys Biosciences (Utah, USA). The LoD can be calculated from the slope of the absorbance curve, however, due to the observed nonlinearity in the curve between 0-2 mM in the well plate, the repeatability will be calculated from a 2-10 mM range as this data is approximately linear. While this is not a true LoD, it gives a good estimate of the repeatability of the assay in the 2-10

mM range. It is assumed that the nonlinearity in the curve between 0-2 mM is a repeatable feature of the assay as pathlength increases due to the strong colour produced at low substrate concentrations. The repeatability was calculated for the glucose assay performed in PBS pH 7.4 for the plate reading and microfluidic device reading. The repeatability was calculated in Excel from the slope of the absorbance curve between 2-10 mM.

$$LoD = 3.3 \left(\frac{S_y}{S} \right) \quad (14)$$

The standard deviation of the response of the curve (S_y) for 2-10 mM was calculated using the '=STEYX' function in Excel. The slope of the calibration curve (S) for 2-10 mM was calculated using the '=SLOPE' function in Excel.

Repeatability of glucose assay in PBS pH 7.4 performed in a commercial plate reader: 0.59 mM.

Repeatability of glucose assay performed in PBS pH 7.4 and read using a low-cost FDM 3D-printed microfluidic cuvette device: 0.60 mM.

As can be seen, the assay repeatability is similar between the well plate and the 3D-printed cuvette device with a difference of < 0.1 mM. As the most clinically important quantification range for glucose is 2-10 mM this gives a good estimate for the precision and repeatability of the assay within this range. While not a true LoD, it is sufficient for this stage of assay development, however, a true LoD would need to be calculated following further assay optimisation.

The final stage of the glucose assay development was to test assay performance in whole blood samples. Glucose assay reagent solution was made by dissolving CTA (40 mM), AAP (20 mM), GIOx (20 U/ml) and HRP (6 U/ml) in 1 ml defibrinated whole horse blood. The reaction was started by adding glucose solution (0-10 mM). The assay was incubated for 2 minutes then centrifuged for 2 minutes at 6000 RPM and the liquid component isolated for analysis in the 500 μ m path length microfluidic cuvette device. The absorption spectrum recorded using the equipment described in section 5.2.3. Increasing colour generation in blood samples after

centrifugation as glucose concentration increases can be seen in Figure 5.9, and the absorbance at 590 nm in Figure 5.10.

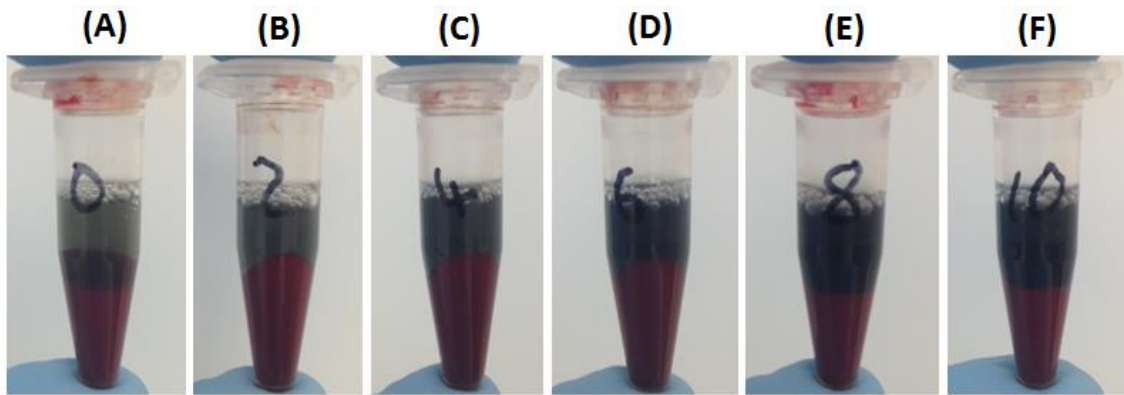


Figure 5.9: Glucose assay in whole blood samples, red cell mass is visible in the base of the tube. Glucose concentrations: (A) 0 mM; (B) 2 mM; (C) 4 mM; (D) 6 mM; (E) 8 mM; (F) 10 mM.

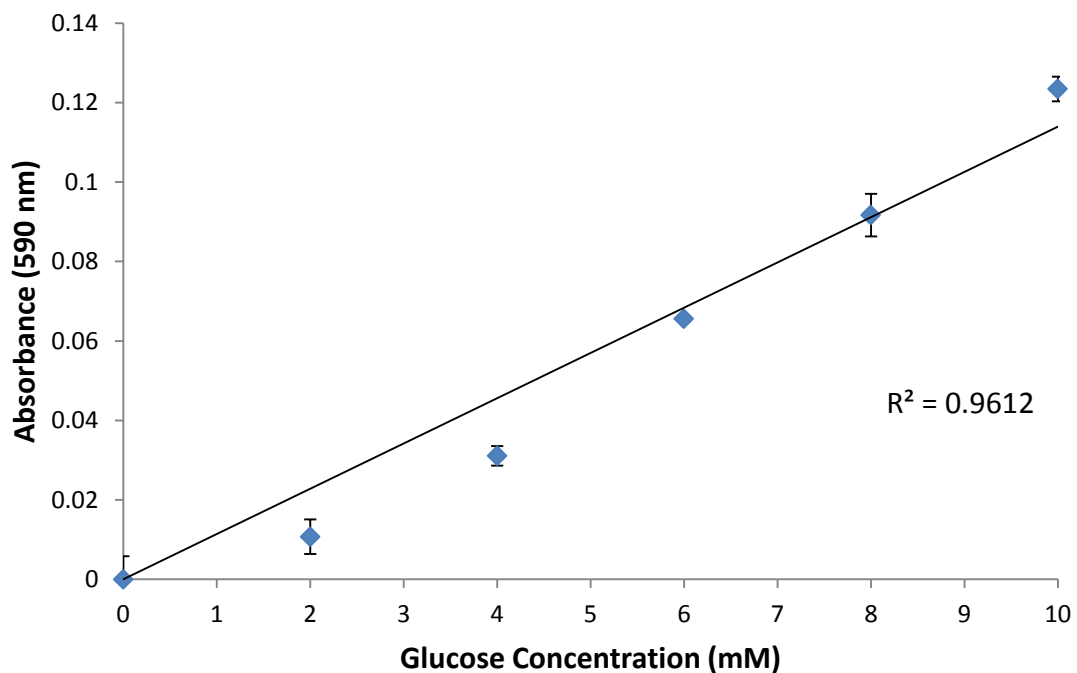


Figure 5.10: The glucose assay in whole blood read in a 500 μm path length microfluidic cuvette device, $n=3$. Glucose (0-10 mM), CTA (20 mM), AAP (10 mM), GLOx (20 U/ml) and HRP (6 U/ml) in defibrinated whole horse blood. The assay was read after 2 minute incubation.

The data shown in Figure 5.10 demonstrates that it is possible to measure glucose concentration in whole blood samples using a colourimetric assay in a 3D-printed microfluidic PLA device. The data produced shows a dilution curve for increasing glucose concentrations with an R-squared of 0.96. The glucose assay performed in whole blood 0-10 mM LoD = 2.07 mM and was calculated using Equation 14. The standard deviation of the response of the curve (S_y) was calculated using the '=STEYX' function in Excel. The slope of the calibration curve (S) was calculated using the '=SLOPE' function in Excel. The LOD of 2.07 mM is satisfactory for the requirements of this assay at this stage, since blood glucose levels <2 mM could generally be classed as 'LOW' when using a POC electrochemical sensor. By comparison, an Abcam enzymatic glucose assay kit (ab65333) (Abcam.com, 2017) for use with a well plate has an LoD of 1 μ M, has a 40 minute incubation time, and costs £285 for 100 tests, whereas the assay described in this project is a fraction of the cost and offers the same real world detection range required for a POC glucose assay within 5 minutes. It should be noted that it takes 1 hour to print a single device which is not commercially viable for mass production, however, the devices are highly customisable and low-cost.

- The price per 190 μ l assay: ~ 16.4 pence.
- The price per microfluidic device: ~7.66 pence (2 g) (Ultimaker PLA Translucent).
- Total cost per assay + disposable device: ~24 pence.
- Total cost for 100 tests: £24 (<10% cost of the Abcam test)
- (500 μ m path length microfluidic cuvettes cost 6 – 9 pence depending on filament used)

In comparison, Freestyle Optium blood glucose test strips cost £22.78 for 50 strips (at the time of writing) on Amazon.co.uk (Amazon.co.uk, 2017), however, it is stated that the test strips require a minimum of 0.6 μ l blood sample to operate and have a detection range of 1.1 mM to 27.8 mM. This costing comparison is applicable should the user be printing their own devices; commercial purchasing of 3D-printed devices would be more expensive due to extra costs such as employee wages, marketing etc.

5.3.2 Device Variability

To investigate the repeatability of the optical properties of the 3D printed devices, 3D-printed microfluidic cuvette devices, section 5.2.2, were manufactured from a selection of transparent PLA filaments: Ultimaker PLA Transparent, Ultimaker PLA Translucent, Innofil PLA Natural and InnoPET Natural. Three devices were produced from each filament and 5 spectral readings taken from each device, so the inter- and intra-filament variability could be observed. Devices were empty and repositioned between spectral measurements. The spectra were standardised and the difference was compared using the spectral analysis instrumentation described in section 5.2.3 and the resulting spectra are presented in Figure 5.11. In this data the spectra of a polymethylmethacrylate (PMMA) cuvette was standardised and used as 100% intensity in order to highlight the spectral difference from the commercial PMMA material and the 3D printed samples. All samples were printed at 10 mm/s with 0.06 mm layer height.

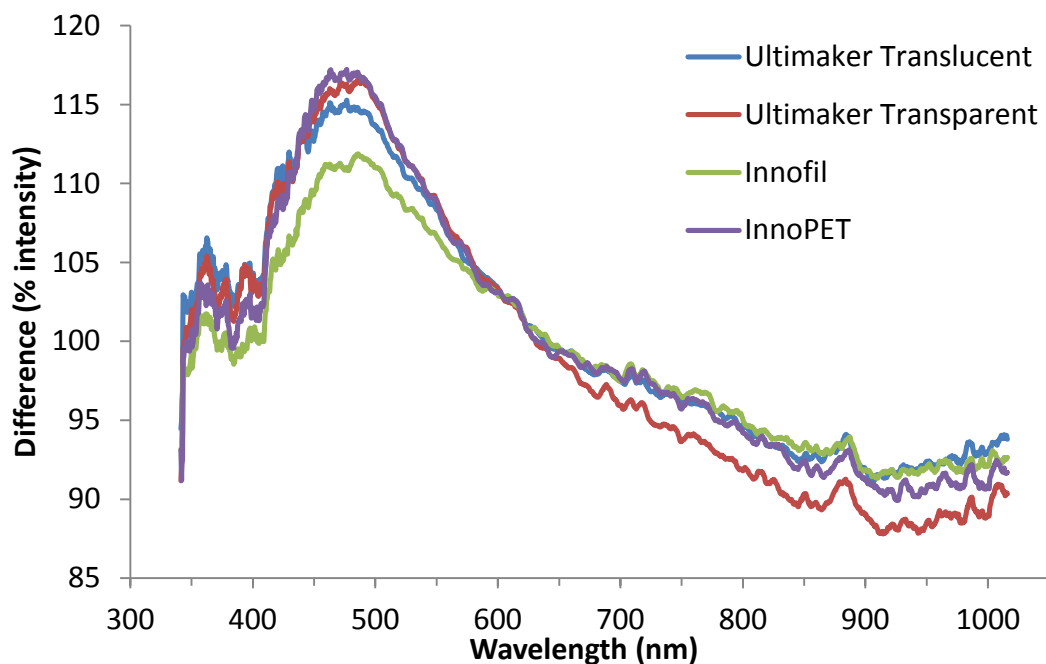


Figure 5.11: Difference as a percentage of intensity in the spectra of 3D printed cuvette devices compared to a PMMA cuvette.

All of the plastic filaments show around a 15% increase in the 390 to 700 nm region and approximately a 10% decrease from 700 to 1000 nm. The Innofil Natural and Ultimaker Translucent plastics have less absorbance in the 390 to 700 nm range and appear to have decreased in the 700 to 1000 nm wavelength range.

Coefficient of variation (CV) is a standardised measure of dispersion of a probability distribution; it is widely used to express precision and repeatability. At the 590 nm absorbance peak of the quinoneimine dye, the inter-filament CV was less than 1 % and there was a maximum CV of 2.6 % between 390–700 nm. The intra-filament CVs are shown in Table 5.1 where the transmission spectrum of each device was recorded a total of five times and averaged. Devices were empty and repositioned between measurements. CV values were not being compared to a PMMA cuvette.

Table 5.1: Intra-filament (%) CV

Filament type	CV between devices (n=3) (%)
Ultimaker translucent	4
Ultimaker transparent	7
Innofil	4
InnoPET	3

For a device to be used as an assay platform, reproducibility is imperative (a CV of < 5 % is generally seen as acceptable); any optical differences between 3D-printed devices could have an impact on the quantified data leading to inaccurate conclusions. While the spectral data showed good reproducibility between absorbance profiles of devices made from the same filament batch, the large differences observed between filament batches require that a filament specific calibration curve is used for each batch of filament to maximise the accuracy of quantitative data produced in each device.

5.3.3 Blood separation in 3D-Printed Device

The final principle required to be established, was whether centrifugation based whole blood separation could be performed in a low-cost FDM 3D-printed microfluidic device. Previous experimentation with liquids in 3D-printed devices (section 4.3.5) had mixed results regarding the water-tightness of printed channels. The first LOAD device to have its channels filled with red dye, section 4.3.5, showed dye permeation from the channels into the surrounding plastic, particularly during sample application when the sample was under pressure from the syringe. The microfluidic cuvettes, however, showed no evidence of fluid leakage into surrounding plastic. As a primary project aim was to perform whole blood separation in a 3D-printed microfluidic device utilizing centrifugal force, the unpredictable nature of the water-tight seal of 3D-printed devices was concerning. The evidence suggested fluid would not remain within a 3D-printed device when subjected to the extreme forces experienced during centrifugation, in addition, plastic samples had not been subjected to centrifugal force, so how they would behave was unknown; the devices themselves may not be able to withstand the force.

A microfluidic pellet device was designed to investigate whole blood separation within a 3D-printed microfluidic device. The pellets are described in section 5.2.4 and were printed at a rate of 10 mm/second with a layer height of 0.06 mm using PLA Transparent. 10 pellet devices were printed per batch. The pellets were filled with defibrinated whole horse blood, placed inside 1.5 ml Eppendorf tubes and centrifuged using a microcentrifuge at 6000 RPM for 2 minutes. The pellets were designed to be centrifuged inside 1.5 ml Eppendorf tubes for two reasons, (1) to contain any blood sample that leaked from the devices during centrifugation, and (2) to minimise the risk of injury should a device shatter. Examples from the first batch of pellets tested can be seen in Figure 5.12 and results in Table 5.2.

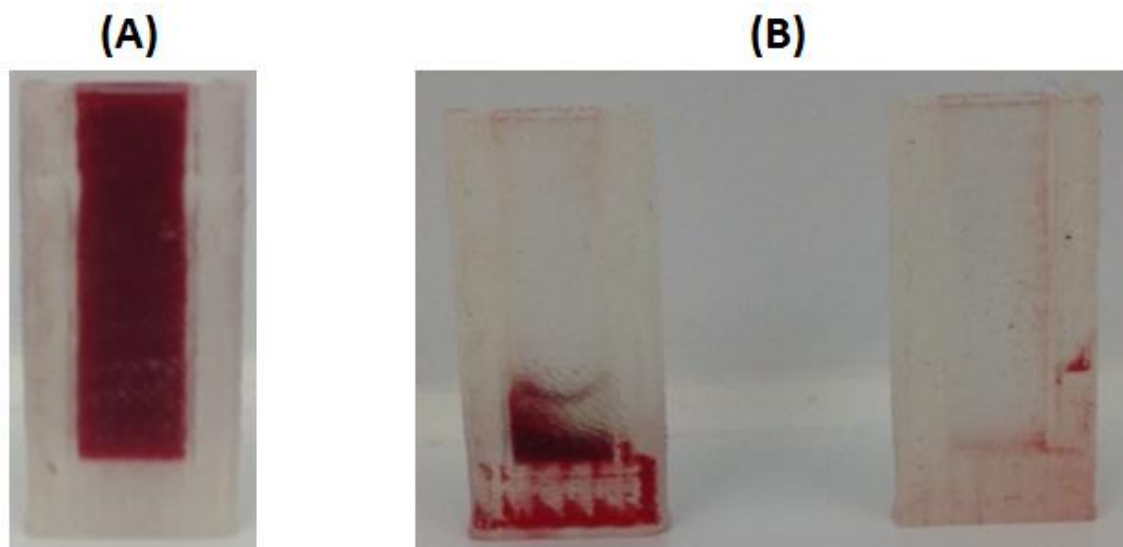


Figure 5.12: Batch 1 Pellet containing whole horse blood, (A) before centrifugation; (B) after centrifugation, (left) partial success with 25% of the blood sample remaining and separated, (right) 100% of blood sample leaked out of the pellet.

In every case the pellet remained structurally intact after centrifugation, with no evidence of compromise to the structural integrity even after prolonged (30 minute) centrifugation using a microcentrifuge at 6000 RPM.

Results were based on 25% thresholds of liquid remaining in the pellet channel following centrifugation. It should be noted that blood samples that collected in the bottom of the Eppendorf tube had undergone separation, indicating that sufficient time and force had been applied for successful plasma separation to occur in all cases. 7 pellets were unsuccessful, with 0% of the blood sample remaining in the pellet channel, having leaked through the base of the pellet and collected in the bottom of the Eppendorf tubes. The remaining 3 pellets had 25% of the blood sample remaining in pellet channel; despite the majority of blood leaking through the base of the pellets, there was clear evidence of blood separation having occurred within the three devices. This confirmed two important objectives for the project, firstly that low-cost FDM 3D-printed microfluidic devices can withstand the forces applied during centrifugation without any structural compromise, and secondly that it is possible to separate plasma

from whole blood in low-cost FDM 3D-printed microfluidic devices using centrifugation.

Due to the unpredictable results seen, testing continued. A second batch of pellets were printed under identical conditions to the first batch. Examples from the second batch of pellets tested can be seen in Figure 5.13 and results in Table 5.2.

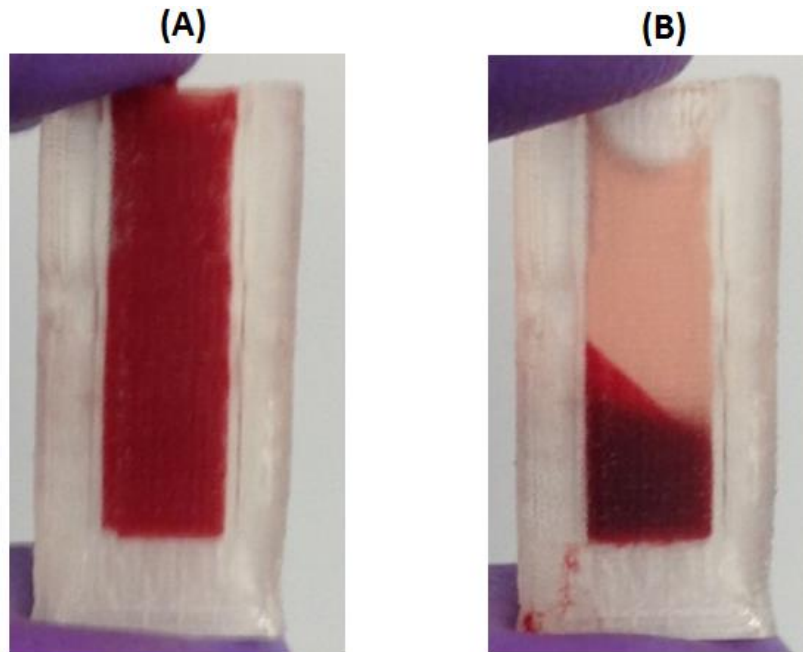


Figure 5.13: Batch 2 Pellet containing whole horse blood, (A) before centrifugation; (B) after centrifugation.

In contrast to the first batch of pellets tested, the 5 pellets had 50-100% of blood sample remained after centrifugation. Of the remaining 5 pellets, 3 had 25% of the blood sample remaining in pellet channel and 2 were unsuccessful, with 0% of the blood sample remaining in the pellet channel. In all cases, plasma had been separated from whole blood with no loss of structural integrity, further confirming and reinforcing the principles of whole blood separation in a 3D-printed device. It would appear that the water-tightness of 3D-printed devices was primarily based on the merging of the strands and layers forming the channel which is dependent on the accuracy of the 3D-printer. Variances in the accuracy of strand deposition during

printing, as seen in section 4.3.6, would result in inconsistencies in the integrity of the channel walls leading to weak points through which liquid can pass through when subjected to sufficient force. It is suspected that this is the reason for pellets printed under identical conditions within the same batch, displayed large variances in water-tightness. A better quality 3D-printer may demonstrate more reliable and reproducible water-tightness between batches of devices.

Table 5.2: Blood sample (%) remaining in 3D-printed PLA microfluidic pellet after centrifugation for 2 minutes at 6000 RPM.

Pellet	Blood sample (%) remaining: Batch 1	Blood sample (%) remaining: Batch 2
1	0	25
2	0	100
3	0	100
4	25	50
5	0	0
6	0	75
7	0	50
8	25	25
9	0	25
10	25	0

Following the observed variability in device water-tightness, post-print treatments were employed in an attempt to improve the water-seal of devices. First efforts utilised acetone liquid treatment to see if treating the surface of the channel would reduce imperfections and potentially seal any micro channels/cavities present in the channel walls. Pellets were filled with 100% acetone solution, incubated for 30 seconds, then the acetone liquid was emptied and the pellets flushed with dH₂O before being left to dry. All attempts were unsuccessful with no improvement observed in water-tightness following acetone liquid treatment; the observed water-tightness results were similar to those observed in batch 1.

Post-print heat treatment was employed to see if incubating the devices at an elevated temperature would improve layer and strand merging, increasing homogeneity and subsequently improving the water-tightness (3ders.org, 2017). 60 °C incubation temperature was chosen for the heat-treatment process as this is the glass transition temperature of PLA. Due to the improved properties observed that the heated build table (set to 60 °C) imparts on the surface and structure quality it is in direct contact with, it was anticipated that incubation at 60 °C may provide similar improvements throughout the entire device. 3D-printed pellets were filled with whole blood samples and centrifuged for 2 minutes. The remaining blood in the device was subsequently quantified. Pellets were flushed with dH₂O and allowed to dry before being incubated in an oven at 60°C for 2 hours before centrifugation testing again. It was decided to use a 2 hour incubation time as it has been recommended that heat-treatment performed at < 110 °C should have the incubation time increased from ≤ 60 minutes (Proto-Pasta.com, 2017).

Results were based on 25% thresholds of liquid remaining in the pellet channel following centrifugation. Examples from the batch of heat-treated pellets that were tested can be seen in Figure 5.14 and results in Table 5.3.

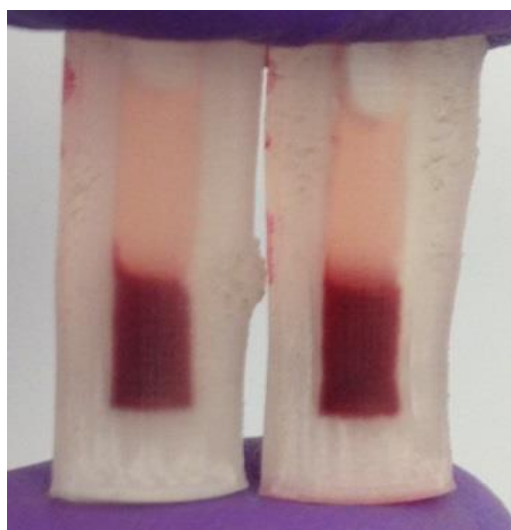


Figure 5.14: Heat-treated pellets containing whole horse blood after centrifugation. Warping to structure and clouding of the plastic is visible.

10 pellet devices were subjected to heat-treatment. 3 devices were rendered unusable by the process due to severe warping of the pellet devices; the 3 devices could not be put inside the Eppendorf tube and therefore were inadmissible. The 7 remaining samples also suffered warping, however, not to the same degree. All devices also showed signs of clouding in the plastic, with a decrease in optical transparency. However, blood samples could still be seen through the devices.

Table 5.3: Blood sample (%) remaining in 3D-printed PLA microfluidic pellet after centrifugation for 2 minutes at 6000 RPM following heat-treatment at 60 °C for 2 hours.

Pellet	Blood sample (%) remaining: Before treatment	Blood sample (%) remaining: After treatment
1	25	50
2	50	100
3	75	50
4	75	100
5	50	50
6	25	75
7	50	25
8	0	x
9	25	x
10	75	x

4 out of 7 pellet devices showed an increase in water-tightness, with up to 50% improvement observed in blood sample remaining after the second centrifugation process. 2 out of 7 pellet devices showed a decrease in water-tightness, with up to 25% reduction observed in blood sample remaining after the second centrifugation process. It is possible that the warping to the pellets increased the inter-layer weaknesses present rather than improving the layer merging. Across the 4 pellets that displayed increased water-tightness, a mean improvement of 37.5% was observed.

The use of heat-treatment on 3D-printed PLA pellets revealed 2 factors that must be considered should the treatment be utilised on devices, (1) heat-treatment of PLA devices can cause warping of the structure, which can be extreme in cases

rendering the device unusable; (2) heat-treatment causes visible clouding and subsequent loss of optical transparency in PLA devices. However, both of these factors were not unexpected as certain PLA filaments that are marketed as having 'improved high-temperature performance' following heat-treatment, are described as changing from translucent to opaque in colour and can suffer from deformation following heat-treatment (Proto-Pasta.com, 2017).

Preliminary data suggests that heat-treatment can be used to increase water-tightness in 3D-printed FDM PLA microfluidic devices but large statistical variation between devices means it is not possible to be unequivocal. The most influential factor in a devices water-tightness remains the print process and print quality. The use of heat-treatment to improve water-tightness in LOAD devices will be explored in future work.

5.3.4 Blood separation in a Low-Cost 3D-Printed FDM Microfluidic LOAD Device.

The work presented in this chapter has so far demonstrated that it is possible to perform and quantify blood based optical assays in a low-cost FDM 3D-printed microfluidic device (section 5.3.1) and that it is possible to perform whole blood separation via centrifugation in a low-cost FDM 3D-printed microfluidic device (section 5.3.3). This section will detail the changes in the designs of the LOAD made in order to perform whole blood separation using centrifugation within a low-cost FDM 3D-printed microfluidic LOAD device.

The first stage of development was to observe the existing state of water-tightness in initial LOAD platform design to establish if whole blood separation can be performed without need for changes to the design. A LOAD device (Figure 4.24) was printed from PLA Transparent at 10 mm/s with 0.06 mm layer height and shell thickness 0.41 mm, disc plates thickness were: plate 1 (top plate) 200 μm , plate 2 (channel plate) 400 μm , plate 3 (base plate) 600 μm . The channels were 1 mm wide

and 400 μm deep with $\sim 23 \mu\text{l}$ volumetric capacity. The channels were filled with whole horse blood and the disc placed on the optical drive centrifugation instrumentation as described in section 5.2.7. The disc was spun for ~ 5 seconds and the images shown in Figure 5.15. Assuming that channel formation is ideal (ideal cross section = 1 mm x 400 μm) and that the fill at time 0 is 100%, the volume is approximately 23 μl per channel, with approximately 184 μl in total across all 8 channels. The total percentage liquid loss across all channels was calculated using Equation 11.

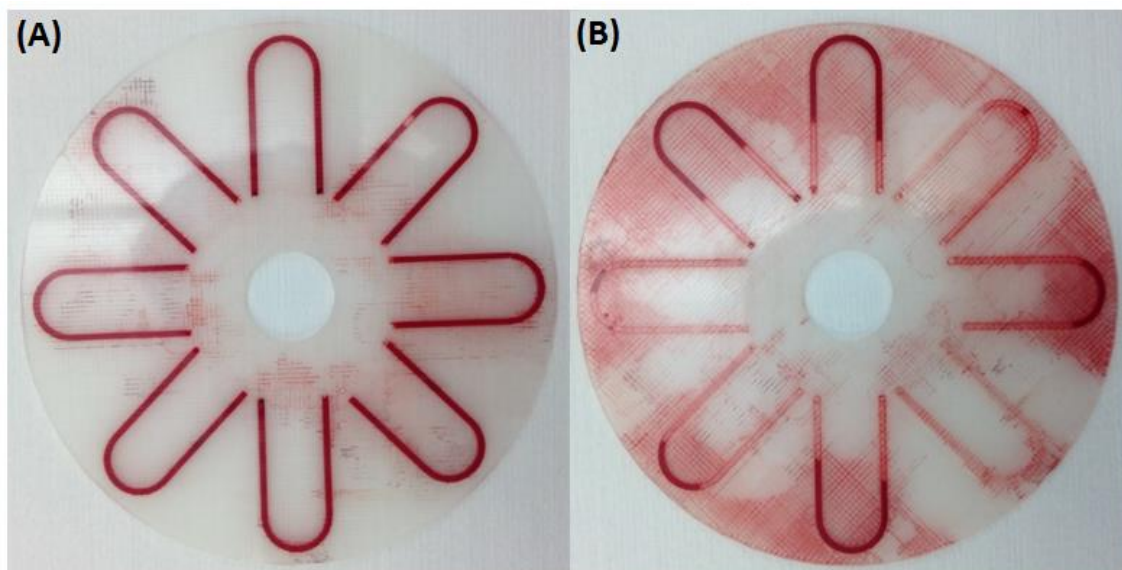


Figure 5.15: PLA LOAD microfluidic device with channels filled with whole horse blood, (A) before centrifugation; (B) after centrifugation for ~ 5 seconds.

The fluid loss in the channels occurred within 5 seconds, with approximate 70% of the total blood volume leaving the channels and permeating into the surrounding plastic; there was no evidence of blood separation occurring within the channels. This first centrifugation test involving a LOAD device illustrated how porous the devices were, as the blood flowed through pre-existing channels within the disc structure. Heat-treatment was then applied to a LOAD platform printed under identical conditions to investigate if channel water-tightness could be improved. The disc was

incubated at 60 °C for 2 hours, after which the device was allowed to cool naturally; Figure 5.16 displays a LOAD disc before and after the heat-treatment.

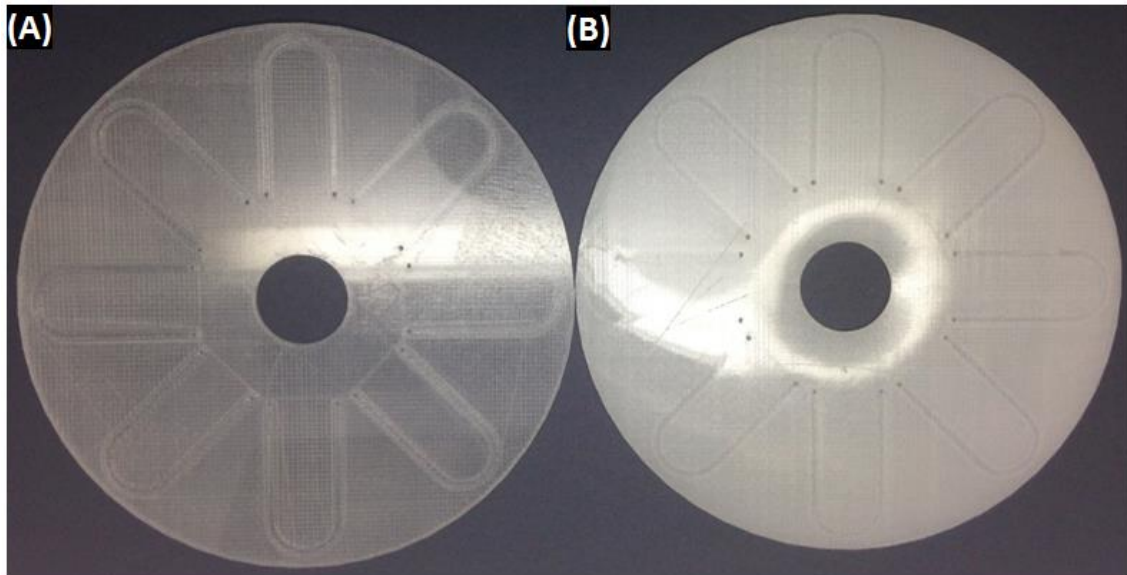


Figure 5.16: (A) PLA LOAD microfluidic device before heat-treatment; (B) PLA LOAD device after heat-treatment at 60 °C for 2 hours.

First observations gathered from the heat-treated disc was the difference in optical transparency; the heat-treated plastic became cloudy (Figure 5.16(B)), however, despite a decrease in optical transparency, blood was still visible in the channels. Warping was also observed, but not enough to affect device centrifugation capability. A time lapse experiment was performed to quantify the passive liquid loss over time for a heat-treated LOAD device under these conditions. The total percentage liquid loss across all channels was calculated using Equation 11.

- After 12 hours: liquid loss was calculated at approximately 55% across all channels.
- After 24 hours: liquid loss was calculated at approximately 73% across all channels.

This demonstrates no improvement in water-tightness over time compared to the previous time-lapse performed on an untreated disc in section 4.3.5. Another disc printed under identical conditions and subject to the same heat-treatment had its channels filled with whole horse blood and the disc was spun for approximately 5 seconds; the images are shown in Figure 5.17.

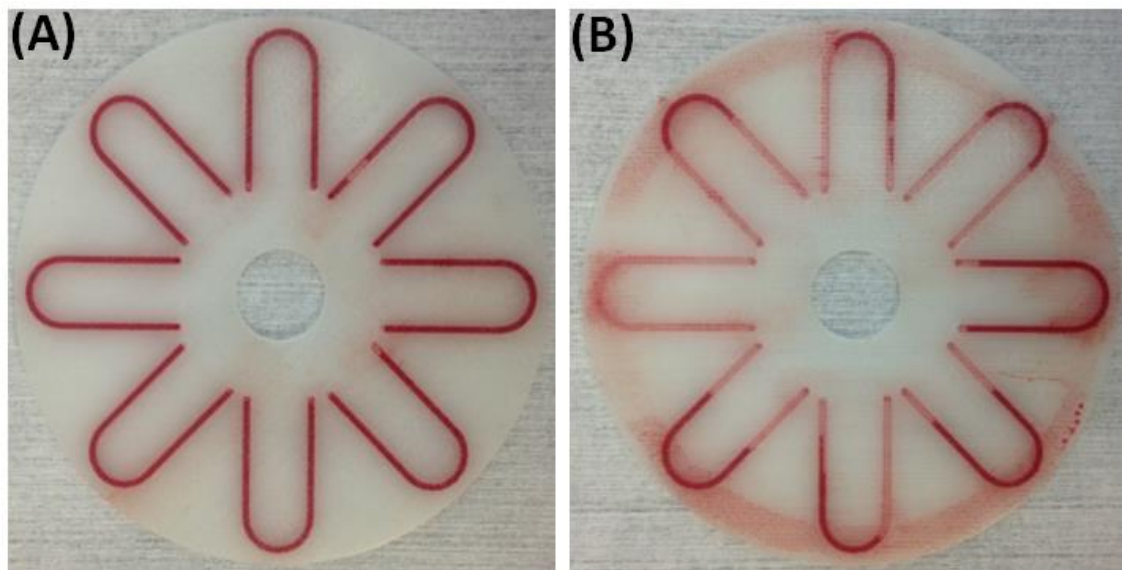


Figure 5.17: PLA LOAD microfluidic device containing whole blood following heat-treatment at 60 °C for 2 hours. (A) before centrifugation; (B) after ~ 5 seconds centrifugation.

After the first centrifugation of approximately 5 seconds, the fluid loss from the channels was approximately 55% of the total blood volume. Following a further 5 seconds centrifugation, fluidic loss was 100%. Despite an initial 15% improvement to water-tightness compared to the untreated device, (55% vs 70% fluid loss after approximately 5 seconds centrifugation), there was no evidence of blood separation occurring within the channels.

Upon inspection of the discs, it was suspected that the method of sample introduction using a syringe and hypodermic needle was applying leverage force to

plate 1 (top plate) of the disc, potentially causing delamination of the disc layers between plate 1 and plate 2, introducing additional weaknesses in the channel walls. Therefore, a new pore was designed with an approximate 17° pore angle vs the previous 90° angle (Figure 4.19) to allow easier insertion of the needle into the channel for sample introduction and to reduce this issue, potentially improving water-tightness. The new pore schematics can be seen in Figure 5.29 (P.203).

It was decided to subject a disc to a longer heat-treatment to investigate the effects of excess duration (> 24 hours) heat-treatment on the disks physical properties. A LOAD device was printed under the same conditions as before: from PLA Transparent at 10 mm/s with 0.06 mm layer height and shell thickness 0.41 mm. The disc's plates thicknesses were: plate 1 (top plate) 200 μm , plate 2 (channel plate) 400 μm , plate 3 (base plate) 600 μm . Channels were 1 mm wide and 400 μm deep with ~ 23 μl volumetric capacity. The device was incubated at 60 $^\circ\text{C}$ over a weekend for convenience. Images can be seen in Figure 5.18.

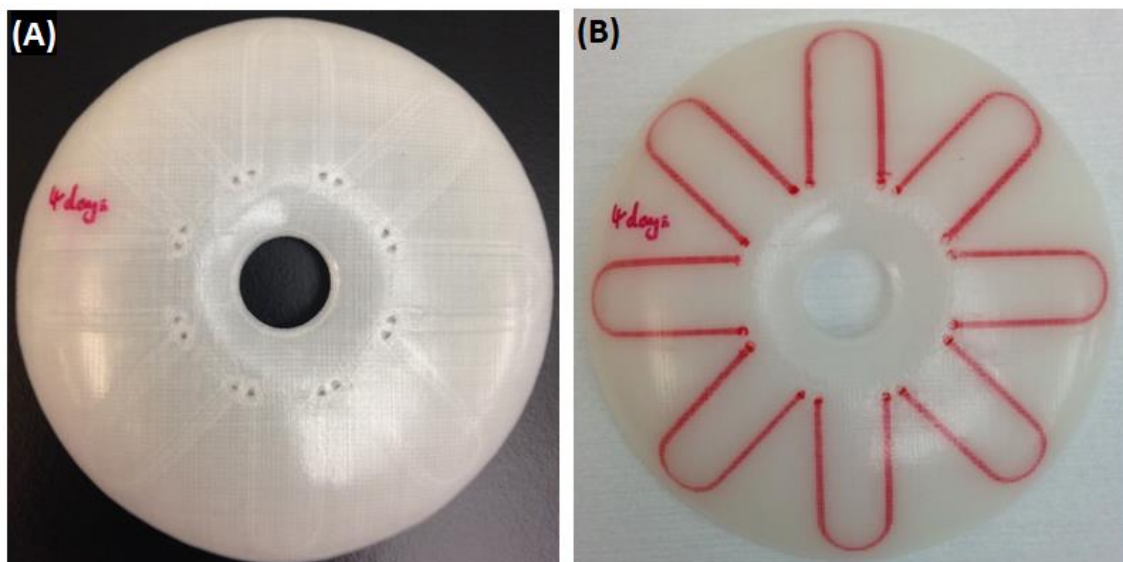


Figure 5.18: PLA LOAD microfluidic device after excess duration (>24 hours) heat-treatment at 60 $^\circ\text{C}$, (A) without red dye; (B) with red dye.

The disc after heat-treatment is shown in Figure 5.18(B). It was observed that the heat-treatment process caused the disc to warp so much so that centrifugation

experimentation could not be performed as the disc was not flat enough to come into contact with the optical drive spindle motor. The change in optical transparency was visually similar to that of the previous heat-treatment of 2 hours, with dye clearly visible within the channel; this implies that duration of heat-treatment above 2 hours does not increase clouding of the plastic, but further quantitative experimentation will need to be performed regarding heat-treatment and decreasing optical transparency of PLA. The quantification and description of PLA warping following heat-treatment would also be of value.

A time lapse experiment was performed to quantify the liquid loss over time for a heat-treated LOAD device under these conditions. The total percentage liquid loss across all channels was calculated using Equation 11.

- After 12 hours: liquid loss was calculated at approximately 45% across all channels.
- After 24 hours: liquid loss was calculated at approximately 67% across all channels.

An improvement in water-tightness of channels was observed following the excess duration (> 24 hours) heat-treatment. A summary of the passive fluid loss over time experiments is displayed in Table 5.4.

Table 5.4: Summary of passive fluid loss over time following heat-at 60 °C.

Heat treatment duration	Fluid loss after 12 hours	Fluid loss after 24 hours
none	48%	78%
2 hours	55%	73%
Excess (>24 hours)	45%	67%

Despite the improvement to passive fluid loss, the LOAD device could not be subjected to centrifugation testing due to the warping so the practical water-tightness could not be compared.

To prevent warping of LOAD devices induced by heat-treatment, subsequent LOAD devices would be covered with a sheet of tin foil and two 40g desiccant tins placed on top during heat-treatment. It had also been observed that disc diameter would shrink during heat-treatment on average 5.6%; the diameter of 10 discs was measured before and after being subjected to excess duration (> 24 hours) heat-treatment at 60 °C. Therefore 15 mm outer diameter washers would be placed into the spindle hole during heat-treatment to maintain spindle accessibility should the discs shrink; this prevented the requirement for physical enlargement of the spindle hole following excess duration (> 24 hours) heat-treatment.

So far, experimentation with heat-treatment alone had not been successful in creating a microfluidic LOAD device capable of performing centrifugation based whole blood separation. It was decided at this point that the fundamental disc parameters, specifically the 1.2 mm total disc thickness, be relaxed. It was believed that, despite appearances, the channels were not being adequately sealed above or below the channel. Therefore, additional layers were added to the CAD model to plate 1 (top plate) and plate 3 (base plate); the parameters of plate 2 (channel plate) remained the same.

Plate 1 and plate 3 were increased in thickness, in 100 µm increments, and tested with and without heat-treatment at 60 °C for 2 hours; LOAD device dimensions progressed up to: plate 1 (top plate) 800 µm and plate 3 (base plate) 800 µm. Plate 2 (channel plate) was not changed and remained 400 µm, with the channels remaining 1 mm wide and 400 µm deep with ~ 23 µl volumetric capacity. Total device thickness increased from 1.2 mm to 2 mm; the increase in device thickness increased print time from 5.5 hours to 9.3 hours and filament consumption from 9g to 15g compared to a 1.2 mm thick disc. All devices were capable of being spun using the ODD instrumentation, despite being up to 800 µm thicker than a regular optical disc. However, experiments failed to produce evidence of whole blood separation, with the fluid sample leaking into surrounding plastic in every device. Despite increasing the thickness of plate 1 by 100% (from 400 to 800 µm) and plate 3 by approximately 33.3% (from 600 to 800 µm), the blood samples continued to leak out of the channel and into

the surround plastic as soon as centrifugal force was applied. It was suspected that rather than the fluid leaking above and below the walls as was previously thought, the fluid was passing through the walls themselves via weak points that exist between the layers.

Samples printed for experiments have demonstrated varying levels of water-tightness; pellet devices (section 5.2.3) demonstrated superior water-tightness compared to LOAD devices when subjected to centrifugal force. It was suspected that the construction process, specifically the print orientation relative to the build table, had a large impact on the inherent water-tightness of a device. Pellet device channels were orientated orthogonal to the build table, whereas the LOAD device channels were parallel to the build table. The result of this was orthogonal channels did not have layers, and the subsequent interlayer weaknesses, located where fluid would be forced against it, whereas parallel channels did. Orthogonal channels had less inter-layer weak points relative to parallel channels, which must withstand and contain the fluid when centrifugal force was applied. This is illustrated in Figure 5.19.

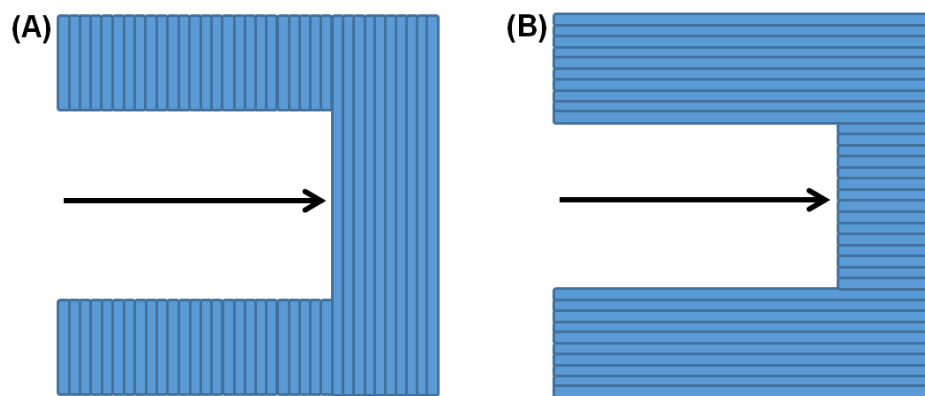


Figure 5.19: Illustration of channels printed (A) orthogonal to the build table; (B) parallel to the build table. The arrow indicates motion of fluid when centrifugal force is applied.

As the LOAD devices could not be printed in another orientation whilst maintaining channel structure, optical transparency, device quality and surface finish, it was decided that wall structure must be improved without changing the print orientation. It was suspected that increasing the shell thickness, a print parameter in

Cura that defines 'walls' within a print, would increase the number of PLA strands deposited to define the channels. When a CAD file is uploaded to the Cura software, the 'shell' or 'walls' are used to define the physical edges of the object relative to open space. The solid space within the shell is defined as 'fill'. When printing an object, shell strands are deposited first in the layer to construct the edges, and then fill strands are deposited to fill the solid space. Fill percentage can be adjusted depending on how solid the object is required. For a completely solid object, a fill percentage of 100% is used. Fill strands are deposited in a way that minimises the tool path of the nozzle, and as a result, the fill strand orientation in the X Y plane is independent of the shell strand orientation. This can result in weaknesses in the shell strand integrity if the fill strands are deposited in such a way that they interrupt the shell strands (due to inaccurate fill deposition by the printer). By increasing the shell thickness, the number of strands used to define the edges within a layer can be increased, which can increase the strength/integrity of the walls and reduce weakness introduced by the fill strands overlapping the wall strands. This is illustrated in Figure 5.20.

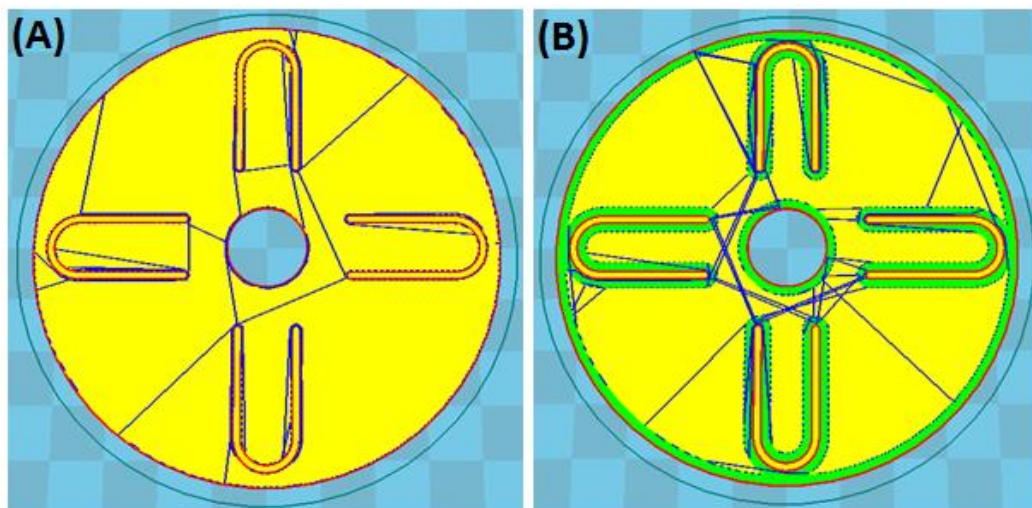


Figure 5.20: LOAD device as seen in Cura software. (A) 0.41 mm shell thickness; (B) 2 mm shell thickness.

In Figure 5.20, the red lines are the outer shell wall (bordering open space), the green lines are the inner shell wall, the yellow region is fill and blue lines are

movements the print head will make without extruding (not relevant to this discussion).

As can be seen in Figure 5.20, when the shell thickness is 0.41 mm there is a single strand defining the outer edges (red lines). Any inaccuracy when the fill strands (yellow region) are being deposited could compromise the integrity of the shell. When the shell thickness is 2 mm, the shell definition is reinforced with additional strands (green lines) that are deposited in line/parallel with the edges, reducing any impact on surface structure from inaccuracies when fill strands are being deposited.

Previously all prints had been performed using a shell thickness of 0.41 mm for print accuracy, as this was the closest value to the nozzle head extrusion diameter that could be successfully interpreted by the Cura software. The investigation proceeded by observing the effect of increased shell thickness on water-tightness; shell thickness specified was increased from 0.41 mm to 1 mm in the Cura software. Disc dimensions would remain: plate 1 800 μm , plate 2 400 μm , plate 3 800 μm , print speed 10 mm/s, layer height 0.06 mm. The increased shell thickness resulted in the need to remove four of the channels. 10 LOAD devices were printed, with a selection being subjected to excess duration (> 24 hours) heat-treatment at 60 °C then being allowed to cool naturally. Whole blood was introduced to the channels and devices were spun for approximately 5 seconds; images can be seen in Figure 5.21.

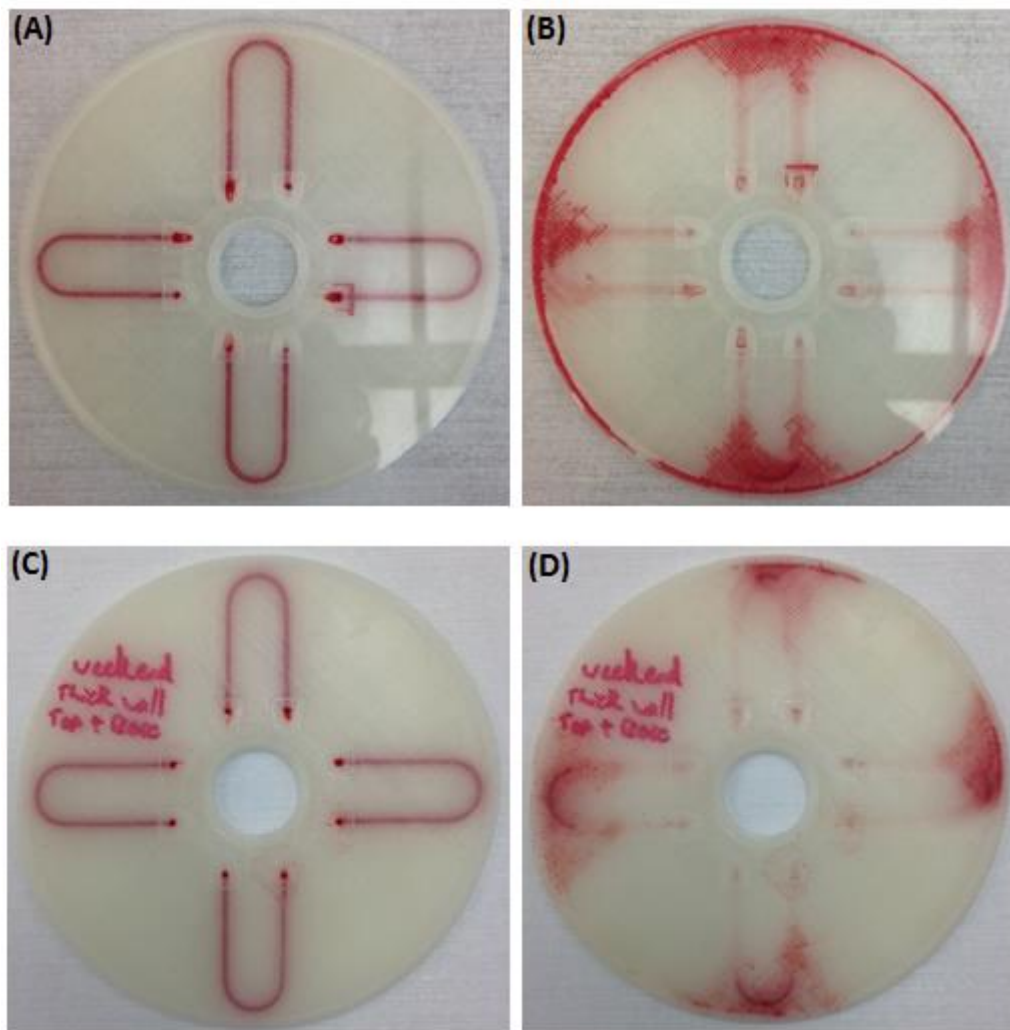


Figure 5.21: PLA LOAD device containing whole blood. (A) before centrifugation; (B) after ~ 5 second centrifugation; (C) after excess duration (> 24 hours) heat-treatment at 60 °C before centrifugation; (D) after excess duration (> 24 hours) heat-treatment at 60 °C after ~ 5 second centrifugation.

As can be seen in Figure 5.21, the increased wall thickness of 0.41 mm to 1 mm was not successful in sealing the channels; fluid continues to leak into surrounding plastic, therefore shell thickness was increased further. The shell thickness was increased from 1 mm to 2 mm.

It has been suggested that putting thermal stress relief holes through 3D-printed objects could promote even cooling throughout the parts and reduce warping due to thermal stress (Herrmann *et al.*, 2014). Due to the loss of 4 channels, free space became available in the model in which holes could be introduced to

explore this and potentially remove the requirement for weights being used to prevent warping during the heat-treatment process. The introduction of thermal stress relief holes did not reduce warping induced by the heat-treatments so the prints continued to be weighed down during heat-treatments. However, a positive consequence of this was a reduction in disc print time and filament consumption. The inclusion of holes decreased print time from 9.3 hours to 8.5 hours and filament consumption from 15g to 14g compared to a 2 mm thick disc without holes, however, this is still ~34% longer than a 1.2 mm thick disc with 8 channels.

10 devices were printed with the following dimensions: plate 1 800 μm , plate 2 400 μm , plate 3 800 μm , print speed 10 mm/s, layer height 0.06 mm, shell thickness 2 mm, channels remain 1 mm wide and 400 μm deep with $\sim 23 \mu\text{l}$ volumetric capacity. 3 devices were subjected to heat-treatment at 60 $^{\circ}\text{C}$ for 2 hours, and 3 were subjected to excess duration (> 24 hours) heat-treatment at 60 $^{\circ}\text{C}$. Devices were allowed to cool naturally, then whole blood was introduced to the channels and devices were centrifuged for ~ 5 seconds. Devices that were not subjected to heat-treatment and those subjected to 2 hour heat-treatment were unsuccessful in separating whole blood; as before, the blood leaked into the surrounding plastic. Devices subjected to excess duration (> 24 hours) heat-treatment can be seen in Figure 5.22.

The devices were centrifuged for ~ 5 seconds, and then the results observed. As seen in Figure 5.22(B), one channel lost 100% of sample into surrounding plastic, however the other channel showed no signs of sample loss and evidence of blood separation occurring. As can be seen in Figure 5.22(C), there is clear and significant separation of blood plasma from whole blood ($\sim 10 \mu\text{l}$ plasma from 23 μl of whole blood), with red cell solids collecting at the bottom of the channel and clear blood plasma towards the top half of the channel. The unsuccessful channel, Figure 5.22(D), has been included for a direct comparison of colour difference between the empty channel and successful plasma separation. It is unknown exactly why one channel failed and one was sealed, however, it was suspected that there was an inter-layer weakness that could not be rectified by heat-treatment. This again displays the variation

in strand deposition accuracy and the subsequent shell integrity that can occur within samples.

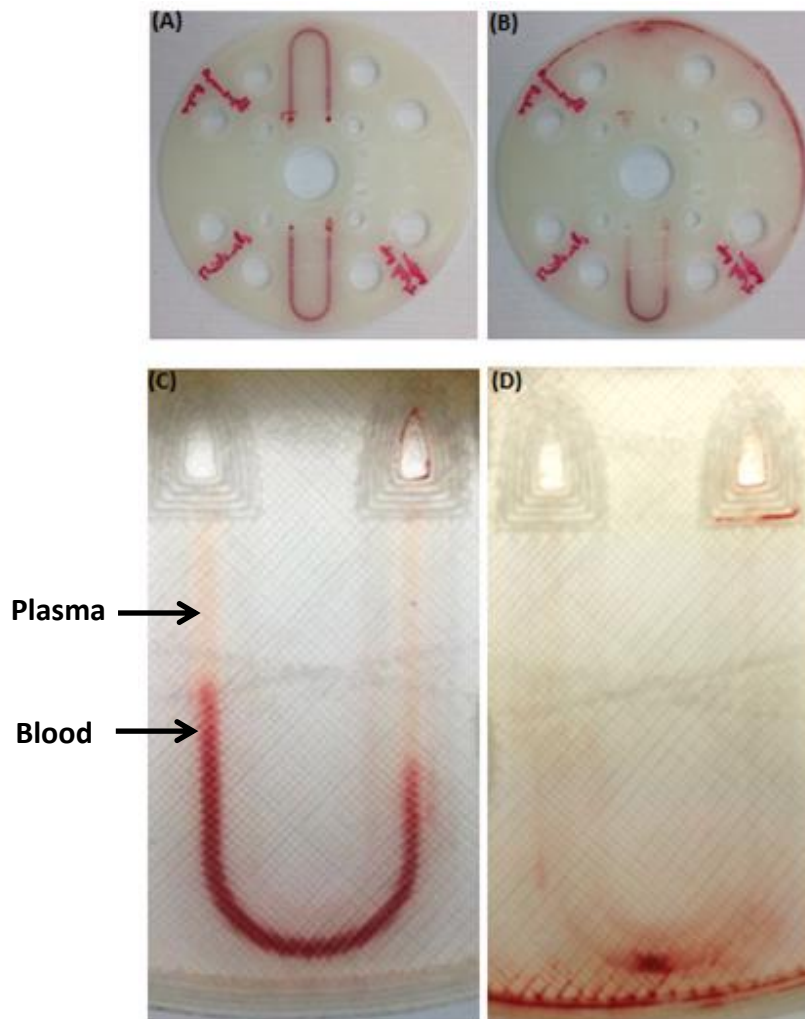


Figure 5.22: 2 mm shell thickness PLA LOAD device containing whole blood after excess duration (> 24 hours) heat-treatment at 60 °C, (A) before centrifugation; (B) after ~ 5 seconds centrifugation; (C) successful blood separation in microfluidic LOAD channel; (D) unsuccessful channel.

Following a further centrifugation period of ~ 10 seconds one of the channels showed no signs of fluid loss into surrounding plastic and a fluid decrease of < 5% after a total centrifugation period of ~ 20 seconds. As assay performance displays observable colour generation within 5 seconds, an incubation period of < 20 seconds is achievable with further enzyme optimisation; this would provide potential for a total

assay and centrifugation time of < 20 seconds. The combination of increased shell/wall thickness and heat-treatment resulted in the successful water-sealing of a low-cost 3D-printed FDM PLA microfluidic channel in a LOAD device, so that whole blood separation can be performed in ~ 23 μ l of whole blood and blood plasma can be viewed inside the channels; a key objective and obstacle in developing a 3D-printed POC LOAD device.

Further alterations to devices were performed in an attempt to improve the water-tightness across all channels. As it was observed that increasing shell thickness improved water-tightness by reinforcing the channel walls with additional strands, it was possible that increasing layer height, and subsequently decreasing the number of layers and inter-layer weak points/ imperfections in channel walls, would also improve the water-tightness. So far all LOAD devices have been printed with 0.06 mm layer height, as this demonstrated the best optical transparency in devices. However, as has been demonstrated, colour change can be seen in devices with relatively poor optical transparency. Therefore, layer heights of 0.1 mm and 0.2 mm were investigated in an attempt at reducing the number of layers used to construct the disc, therefore, reducing the number of potential inter-layer weak points; illustrated in Figure 5.23.

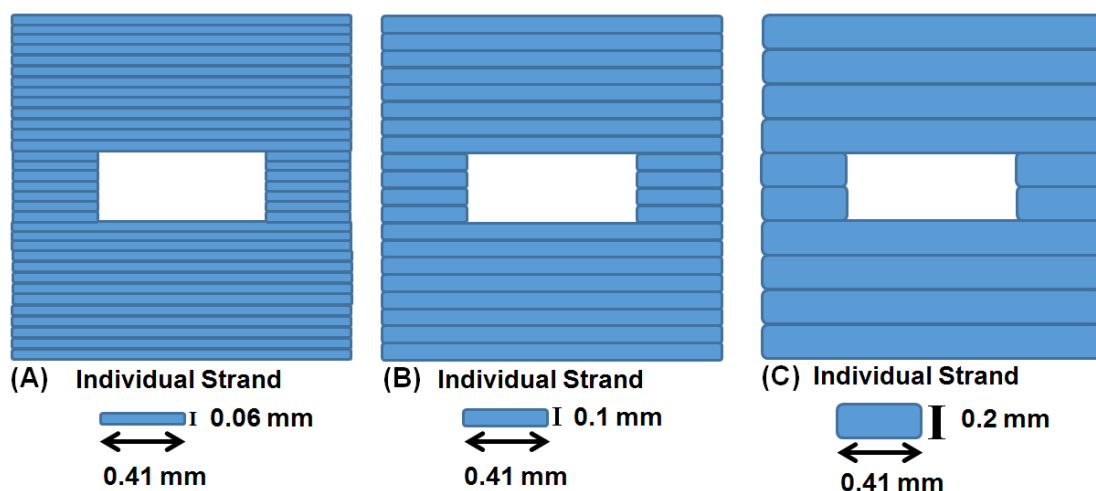


Figure 5.23: Illustration of channels printed with varying layer heights: (A) 0.06 mm; (B) 0.1 mm; (C) 0.2 mm.

10 devices were printed with the following dimensions: plate 1 800 μ m, plate 2 400 μ m, plate 3 800 μ m, print speed 10 mm/s, layer height 0.1 mm and 0.2 mm, shell

thickness 2 mm, channels were 1 mm wide and 400 μm deep with $\sim 23 \mu\text{l}$ volumetric capacity. 4 devices were subjected to heat-treatment at 60 $^{\circ}\text{C}$ for 2 hours. Devices were allowed to cool naturally, then whole blood was introduced to the channels and devices were centrifuged for ~ 5 seconds. Devices with 0.2 mm layer height, both untreated and heat-treated, were unable to separate whole blood; as before, the blood leaked into the surrounding plastic. It is suspected that the poor layer homogeneity and strand merging that introduced poor optical transparency in previous experiments, was responsible for weaknesses in the channel walls.

Untreated devices printed with 0.1 mm layer height were capable of separating whole blood, as can be seen in Figure 5.24, however, $\sim 30\%$ fluid was lost during the ~ 5 second centrifugation, which is inferior to the previous successful result of $< 5\%$ fluid loss after ~ 20 seconds centrifugation and significantly less plasma was separated ($\sim 3 \mu\text{l}$ plasma from $\sim 23 \mu\text{l}$ whole blood). Despite this, this demonstrates that low-cost FDM 3D-printed microfluidic LOAD devices are capable of being used for the centrifugation of $\sim 23 \mu\text{l}$ whole blood without any post-print treatments being applied. The potential exists for optimisation to further improve the water-tightness of the LOAD channels to improve fluid retention and plasma yield, and to negate the requirement for any post-print treatments.

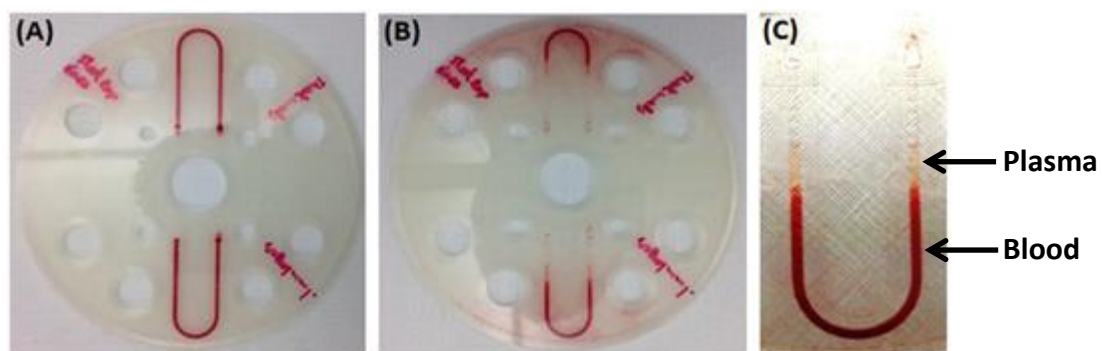


Figure 5.24: 0.1 mm layer height PLA LOAD device containing whole blood, (A) before centrifugation; (B) after ~ 5 seconds centrifugation; (C) blood separation in microfluidic LOAD channel.

Devices printed with 0.1 mm layer height that were subjected to heat-treatment of 60 °C for 2 hours were also capable of separating whole blood, as can be seen in Figure 5.25, however, ~85% fluid was lost during the ~ 5 second centrifugation which is inferior to the untreated device results (Figure 5.24) of ~ 30% fluid loss after ~5 seconds centrifugation and only ~1.5 µl plasma was produced from ~23 µl whole blood.

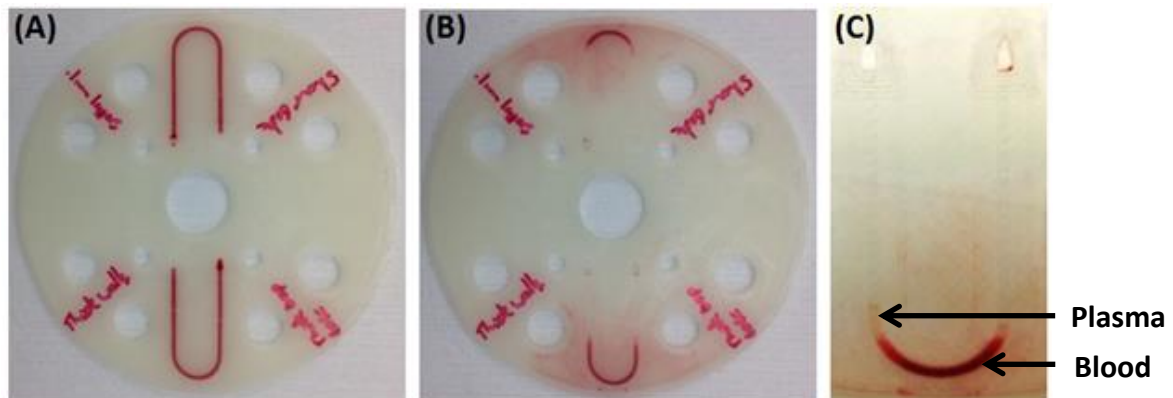


Figure 5.25: 0.1 mm layer height PLA LOAD device containing whole blood after 60 °C heat-treatment for 2 hours, (A) before centrifugation; (B) after ~ 5 seconds centrifugation; (C) blood separation in microfluidic LOAD channel.

The results presented in this section have demonstrated that it is possible to centrifuge whole blood and to produce plasma within a 3D-printed microfluidic LOAD device. Post-print excess duration (>24 hours) heat-treatment at 60 °C was used in combination with print and device optimisation to create a water-tight channel in a device that could withstand ~20 seconds of centrifugation, which was sufficient time to produce ~10 µl plasma from ~23 µl whole blood.

It was suspected that the inconsistency of the effectiveness of heat-treatment on water-tightness could be attributed to the inaccuracy and inconsistency of the 3D-printer strand deposition, as varying degrees of channel water-tightness were observed between channels on the same device. This reemphasises the importance of printer quality and the role it plays determining whether a device will be viable. It was

suspected that post-print treatments could be used to improve the water-tightness of channels, but the channels must already have acceptable channel wall integrity and therefore a high degree of water-tightness. Further experimentation and optimisation improving water-tightness is necessary to produce consistent results. It is likely that a 3D-printer with improved accuracy of strand deposition would have better print consistency and therefore more consistent water-tightness across devices for optimisation to be truly effective.

5.3.5 Performing the Glucose Assay in Whole Blood and Centrifugation in a Low-Cost FDM 3D-Printed Microfluidic LOAD Device.

The final stage of LOAD device development was to perform the glucose assay in whole blood and separate quinoneimine dye coloured plasma within a LOAD device.

The 3 LOAD devices in which plasma separation was performed, described in section 5.3.4, were used to perform the assay experimentation. Only 2 channels were utilized during the whole blood centrifugation experiments, leaving 2 channels per device available for assay testing. As every channel on each device had different properties, it was uncertain whether the remaining channels would be capable of separating whole blood and producing coloured plasma, however, as the other channels on each device demonstrated some degree of capability it was anticipated that at least 1 of the remaining channels would be viable. Assay experimentation was performed within 2 hours of the initial centrifugation experiments.

Glucose assay reagent solution was made by dissolving CTA (20 mM), AAP (10 mM), GLOx (20 U/ml) and HRP (6 U/ml) in defibrinated whole horse blood. The reaction was started by adding glucose solution (10 mM). The assay was applied to the LOAD channels, incubated for 2-minutes, and then centrifuged using the ODD for ~5 seconds.

The first LOAD device tested using the assay in whole blood was the only device to separate whole blood without having being subjected to heat-treatment (Figure 5.23). To recap: the LOAD device was printed with the following dimensions: plate 1

800 μm , plate 2 400 μm , plate 3 800 μm , print speed 10 mm/s, layer height 0.1 mm, shell thickness 2 mm, channels 1 mm wide and 400 μm deep with $\sim 23 \mu\text{l}$ volumetric capacity. The disc was not subjected to heat-treatment before testing. The assay-blood sample was prepared, applied to the disc and centrifuged as described above and in section 5.2.7. The results can be seen in Figure 5.26.

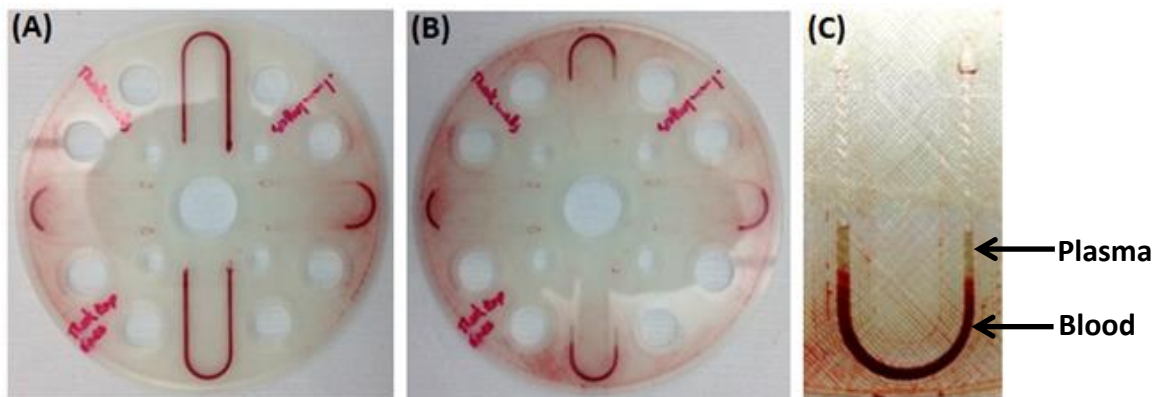


Figure 5.26: 0.1 mm layer height PLA LOAD device containing whole blood, (A) before centrifugation; (B) after ~ 10 seconds centrifugation; (C) blood separation and colour generation in microfluidic LOAD channel.

It can be seen from Figure 5.25(C) that, despite $\sim 10.4 \mu\text{l}$ fluid loss during centrifugation ($\sim 45\%$), the whole blood was successfully separated and $\sim 3.2 \mu\text{l}$ of coloured plasma is clearly visible in the channel. While the channel water-tightness was inferior to the whole blood separation previously performed in this device ($\sim 30\%$ fluid loss), plasma generation performance remained the same.

The second LOAD device to be tested using the assay in whole blood had 0.1 mm layer height wand was subjected to heat-treatment (Figure 5.24). To recap: the LOAD device was printed with the following dimensions: plate 1 800 μm , plate 2 400 μm , plate 3 800 μm , print speed 10 mm/s, layer height 0.1 mm, shell thickness 2 mm, channels 1 mm wide and 400 μm deep with $\sim 23 \mu\text{l}$ volumetric capacity. The disc was subjected to heat-treatment at 60 $^{\circ}\text{C}$ for 2 hours, and was allowed to cool naturally before testing with whole blood. The assay-blood sample was prepared, introduced to

the channels and centrifuged as described above and in section 5.2.6. The results can be seen in Figure 5.27.

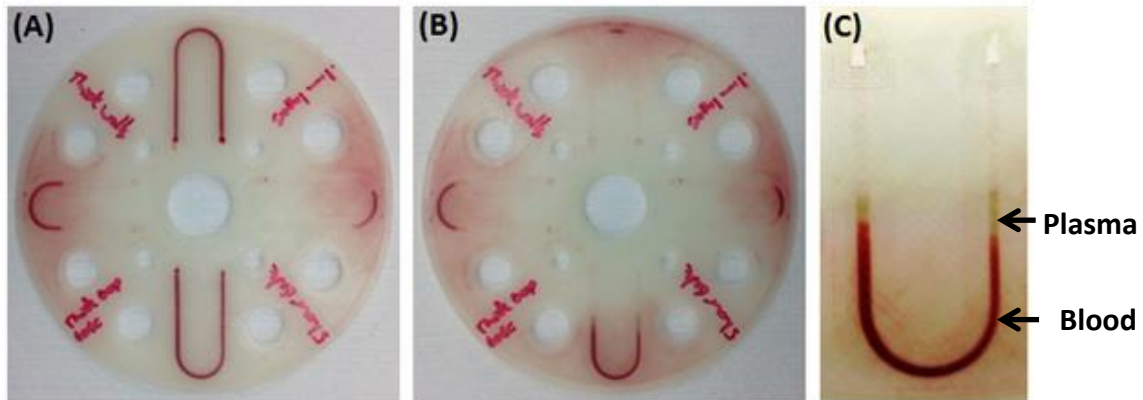


Figure 5.27: 0.1 mm layer height PLA LOAD device containing whole blood after 60 °C heat-treatment for 2 hours, (A) before centrifugation; (B) after ~ 5 seconds centrifugation; (C) blood separation and colour generation in microfluidic LOAD channel.

As can be seen in Figure 5.27(C), the channel had superior water-tightness ($\sim 8 \mu\text{l}$, $\sim 35\%$ fluid loss) and plasma production ($\sim 2.4 \mu\text{l}$) compared with the initial blood separation performed in this device ($\sim 85\%$ fluid loss and $\sim 1.5 \mu\text{l}$ plasma produced). Despite the low volume of plasma produced in the channel, the remaining plasma is visibly coloured by the glucose assay reaction.

The third and final LOAD device to be tested using the assay in whole blood was the first and most successful device in which whole blood separation was demonstrated (Figure 5.22). To recap: the LOAD device was printed with the following dimensions: plate 1 800 μm , plate 2 400 μm , plate 3 800 μm , print speed 10 mm/s, layer height 0.06 mm, shell thickness 2 mm, channels 1 mm wide and 400 μm deep with $\sim 23 \mu\text{l}$ volumetric capacity. The disc was subjected to excess duration (>24 hours) heat-treatment at 60 °C, and was allowed to cool naturally before testing with whole

blood. The assay-blood sample was prepared, applied to the disc and centrifuged as described above and in section 5.2.6. The results can be seen in Figure 5.28.

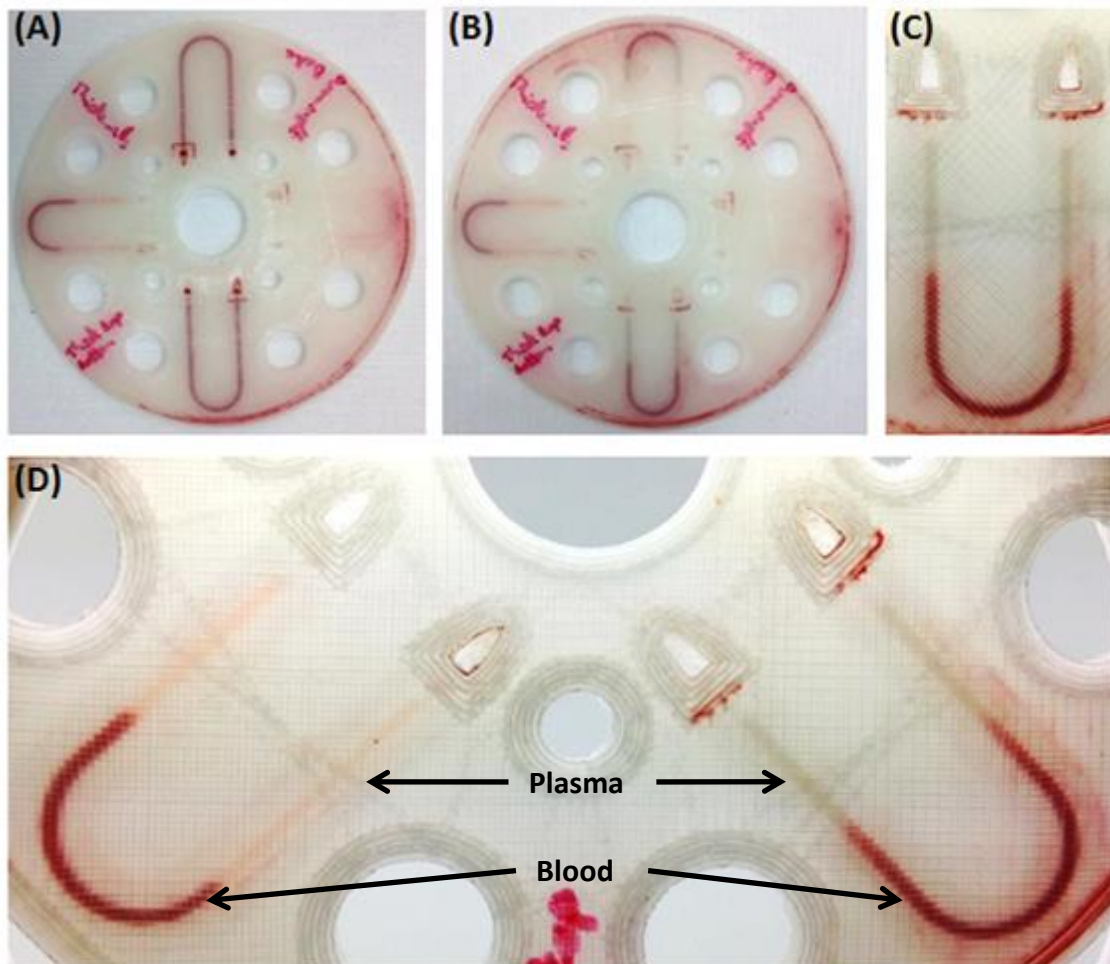


Figure 5.28: 0.06 mm layer height PLA LOAD device containing whole blood after excess duration (>24 hours) heat-treatment at 60 °C, (A) before centrifugation; (B) after ~ 5 seconds centrifugation; (C) blood separation and colour generation in microfluidic LOAD channel; (D) comparison of whole blood separation without assay reagents (left) and with assay reagents (right).

Following the assay-blood centrifugation, it is clear that this device contains channels of superior water-tightness when compared to the others tested. After ~ 10 second centrifugation the fluid loss from the channel was ~3.6 μl (~15%) and with ~8.8 μl of coloured plasma remaining in the channel as can be seen in Figure 5.28(C). Figure

5.28(D) shows two successful channels on the same device displaying the distinct colour difference between the basic unreacted plasma (left) and the plasma containing quinoneimine dye from the glucose assay that was performed in the whole blood sample (right).

The final specifications for the LOAD device developed are as follows, the most successful options are underlined, schematics can be seen in Figure 5.29:

- 90 mm diameter with 15 mm diameter spindle hole at the centre, 2 mm total thickness,
- Plate 1 (top plate) 800 μm thickness,
- Plate 2 (channel plate) 400 μm thickness,
- Plate 3 (base plate) 800 μm thickness,
- 4 U-bend channels with 1 mm width and 400 μm depth with approximately 23 μl volumetric capacity positioned in plate 2. Pores have $\sim 17^\circ$ angle for sample introduction.
- Print speed: 10 mm/s, layer height 0.06 mm or 0.1 mm, shell thickness 2 mm.
- Heat-treatment: None / 60 $^\circ\text{C}$ for 2 hours / 60 $^\circ\text{C}$ for excess duration (>24 hours).
- Print time per device: 8.5 hours (0.06 mm layer height); 5 hours (0.1 mm layer height).
- Extrusion temperature 200 $^\circ\text{C}$
- Cost per device using Ultimaker PLA Transparent: 57 pence, $\sim 14\text{g}$ filament.
- Cost per device: 43-71 pence depending on filament used.

The final assay specifications for glucose or cholesterol quantification range of 0-10 mM are:

- 20 mM chromotropic acid (CTA),
- 10 mM 4-aminoantipyrine (AAP),
- 6 U/ml horseradish peroxidase (HRP),
- 20 U/ml glucose oxidase (GLOx) or cholesterol oxidase (ChOx),

- Glucose assay price per 23 μl channel: \sim 2 pence,
- Cholesterol assay price per 23 μl channel: \sim 58 pence,

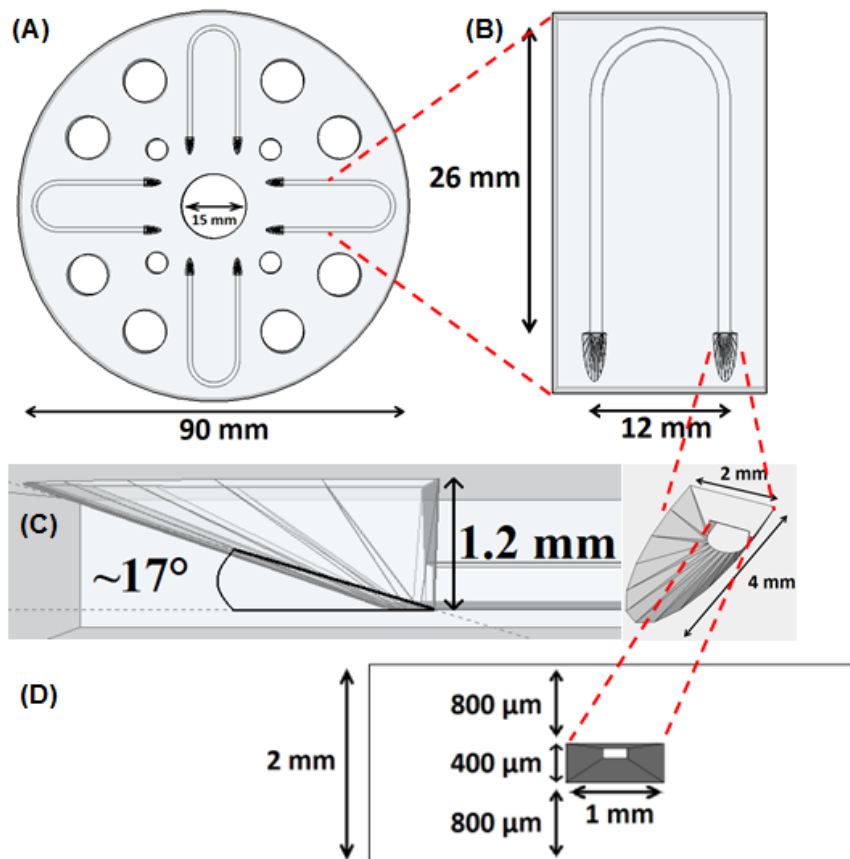


Figure 5.29: Schematics of final LOAD design, channel capacity \sim 23 μl . (A) Device specifications and channel layout; (B) channel specifications; (C) pore specifications; (E) cross-sectional specifications.

It has been demonstrated that whole blood optical assays and centrifugation based whole-blood separation can be performed within a low-cost 3D-printed FDM microfluidic LOAD device. All successful devices were capable of being spun using an unmodified optical disc drive and coloured blood plasma produced and clearly visible within the channels \leq 10 seconds centrifugation time.

5.4 Conclusions

A colourimetric glucose assay capable of distinguishing between a range of glucose concentrations (0-10 mM) in whole blood has been used to demonstrate the capability and functionality of FDM 3D-printed microfluidic devices. The glucose assay was performed in an FDM 3D-printed microfluidic cuvette device with 500 μm sample path length. Absorbance data was gathered during testing that shows that it is possible to quantify colourimetric assay data in a low-cost FDM 3D-printed device.

Each device cost ~ 7.6 pence (2g filament), which is comparable to purchasing standard disposable PMMA cuvettes which cost approximately 7 pence each (Sigma-Aldrich, 2016b), resulting in an economical device that can be custom designed and built to the users' requirements without having to wait for purchasing or delivery. This provides the potential for the user to print their own highly customisable devices in the laboratory.

The cuvette devices demonstrated water-tightness, with no sample leakage. The use of an enzymatic cascade demonstrated that a multistage assay process can be performed within the device as a single user step. It has been previously thought that the poor optical transparency of low-cost FDM 3D-printed polymers is a fundamental obstacle that considerably limits their potential to fabricate optically interrogated devices (Willis *et al.*, 2012). Furthermore, the variability and error in low-cost FDM printers was thought to limit their use in fabricating microfluidic structures, however, it has been demonstrated that accurate quantification of absorbance data can be performed in devices printed using a low-cost FDM 3D-printer. Further investigation is required into secondary adsorption phenomena that may influence the analytical spectroscopy and reproducibility of data involving 3D-printed PLA devices however the use of PLA in biochemical devices is already established (Pioggia *et al.*, 2007; Kadimisetty *et al.*, 2016).

Microfluidic cuvette devices with a channel width of 100 μm were also manufactured which are 66% narrower than the minimum channel width possible using the closest comparable commercial device currently on the market, the Dolomite Fluidic Factory

(Dolomite, Royston, UK). The Fluidic Factory FDM 3D-printer has a minimum channel width limitation of 300 μm , costs £14,000 and requires print material only available from their website for £350 per 60 m reel. The price per metre for the Dolomite cyclic olefin copolymer is approximately £5.83 compared to the Ultimaker PLA Transparent price per metre of approximately 33 pence. The Dolomite Fluidic Factory is unable to print the LOAD microfluidic devices developed and demonstrated in this project due to the limited print volume of 80mm x 50mm x 25mm. However if it could, the price per 500 μm microfluidic cuvette would be £1.34 and per LOAD device it would be £10.08; this is compared to 7.6 pence and 57 pence respectively for the same devices printed using the Ultimaker 2+ and Ultimaker PLA Transparent filament. This demonstrates the significant potential reduction in manufacturing costs possible when low-cost (< £2000) FDM 3D-printing technology and low-cost (< £50 per reel) print filament is optimised for the production of microfluidic devices; this is the difference between producing low-cost disposable devices that are suitable for a point-of-care setting and expensive devices that would need to be cleaned and reused to maintain financial viability.

Whole blood separation was performed in 3D-printed microfluidic pellets with a volumetric capacity of $\sim 112 \mu\text{l}$ to demonstrate the capability of low-cost FDM devices in performing centrifugation using significantly less volume of blood than traditional methods that typically require $>1 \text{ ml}$. The optimised pellet devices displayed sufficient water-tightness to withstand the centrifugal forces required to separate whole blood, a significant obstacle in FDM 3D-printed devices.

The progression of investigation culminated in the design and manufacture of a low-cost FDM 3D-printed microfluidic lab-on-a-disc device that was capable of performing centrifugation based whole blood separation within 10 seconds and viewing optical quantitative assays within. Despite the LOAD devices being thicker than anticipated, at 2 mm vs 1.2 mm of a normal optical disc, this was not shown to be an issue as all discs were capable of being spun using the unmodified optical disc drive. In addition, discs can be designed so that region around the central spindle hole is 1.2 mm thick should it be required for spindles with locking clips. Further optimisation is

required to reliably and consistently produce LOAD devices with sufficient water-tightness for centrifugation purposes. Due to difficulties in water-sealing the LOAD devices and inconsistent load performance at this stage, time constraints meant that quantification of glucose in whole blood using a LOAD device was not performed. However, the accurate quantification of absorbance within a FDM 3D-printed microfluidic device has already been demonstrated using the cuvette devices, which have a similar sample path length (500 μm) to that of the LOAD devices (400 μm). Further investigation will be necessary into secondary adsorption phenomena that may influence the analytical spectroscopy and reproducibility of data involving 3D-printed PLA devices.

Chapter 6: General Conclusions and Future Work

6.1 General Conclusions

Health care establishments globally are overworked, underfunded and understaffed. With an increasing aging population and the exponential increase in people developing cardiovascular disease and diabetes, the dependence and pressure on healthcare services could potentially rise to unsustainable and dangerous levels. A consequence of this is the increasing reliance on point-of-care (POC) diagnostic and quantitative devices as an attempt at relieving the burden being placed on healthcare professionals and pathology departments in hospitals.

Whilst many industrial microfluidics are produced using injection moulding, this is a costly production method for research labs (Fiorini and Chiu, 2005) as each design change can cost as much as £2750 to have the moulds made. The use of low-cost FDM 3D-printing in device fabrication would allow researchers to prototype various microfluidic systems quickly and cheaply, both reducing the cost and time for development of a microfluidic platform. 3D-printing also allows for structures and shapes that are not possible in injection moulding and could open up new three dimensional designs in microfluidics.

The aim of this project was to investigate the use of 3D-printing in the development and manufacture of a low-cost lab-on-a-disc (LOAD) device with multiple imbedded microfluidic channels. The device needed to have sufficient optical transparency that optical assays can be performed within. The existence of multiple separate channels would mean the quantification of multiple analytes could be performed simultaneously on a single device, reducing operator workload, providing a panel of diagnostic and quantitative data and mitigating previous concerns regarding accuracy of POC testing. The device was intended to be capable of separating plasma from whole blood via centrifugation ≤ 2 minutes and to be used with an unmodified optical disc drive (ODD). It was hoped, that if successful, the combination of low-cost (< £2000) fused deposition modelling (FDM) 3D-printing technology with a microfluidic LOAD could provide POC functionality, portability and affordability with the diagnostic capability of laboratory tests.

Three fundamental principles had to be demonstrated to establish the feasibility of using low-cost FDM 3D-printing technology as a means of developing and manufacturing microfluidic LOAD assay devices for use with whole blood samples.

1. Imbedded microfluidic channels can be formed using a low-cost FDM 3D-printer.
2. Quantitative whole blood optical assays can be performed in a low-cost FDM 3D-printed microfluidic device.
3. Separation of plasma from whole blood via centrifugation can be performed in a low-cost FDM 3D-printed microfluidic device.

The work performed over the course of this thesis demonstrated all three of the principles and culminated in the development of a LOAD device with imbedded microfluidic channels and centrifugation based plasma separation from whole blood utilising an unmodified optical disc drive (ODD). Improvements made to the optical transparency of 3D-printed devices provide the potential of performing quantitative colourimetric whole blood assays within. The development process of the LOAD device involved many minor but cumulative and necessary changes; all iterations were manufactured and physically examined, which would not have been possible if being developed using traditional manufacturing techniques.

This demonstrates that despite more expensive 3D-printing technology existing, low-cost consumer grade FDM 3D-printing technology and print materials have the potential for developing and manufacturing low-cost POC diagnostic devices that are highly customisable and capable of performing multiple whole blood centrifugations and quantitative assays simultaneously using existing unmodified ODDs as reader devices. It should be noted that the more expensive 3D-printing technologies have higher resolution and better accuracy, which can improve the optical properties and performance of the devices. However, these systems can cost as much as £150,000 which is beyond the budget of many research laboratories and render the cost per consumable device prohibitive in many applications.

6.2 Development of an Optical Cholesterol and Glucose Assay

The experiments presented demonstrate a quantification method for cholesterol in whole blood and glucose in whole blood. It was shown that cholesterol oxidase or glucose oxidase, horseradish peroxidase, chromotropic acid and 4-aminoantipyrine when mixed together produce an enzymatic cascade and optical reaction that can distinguish between a range of analyte concentrations in various solution mediums including whole blood. Testing showed that the absorbance curves can be shifted up or down according to incubation time, enzyme concentration and to a lesser extent chromotropic acid concentration. This allows the assay to be calibrated to the requirements of the optical device recording absorbance and the assay platform and allow accurate quantification of cholesterol and glucose by increasing or decreasing colour intensity. The final assay reagent concentrations were as follows: chromotropic acid (20 mM), 4-aminoantipyrine (10 mM), horseradish peroxidase (6 U/ml), cholesterol oxidase or glucose oxidase (20 U/ml). The current study has been attempting to quantify free cholesterol in whole blood. The reaction can be expanded to quantify total cholesterol in blood through the addition of cholesterol esterase into the enzyme mixture. However, this has yet to be implemented at this stage. Cholesterol and glucose colourimetric assays have been developed in this work successfully that produce distinct absorbance curves in the 650 nm region, the wavelength of a DVD optical drive laser, therefore a standard unmodified DVD ODD laser diode has the capability of quantifying absorbance changes in these assays.

6.3 LOAD Device Design, Manufacture and Optimisation

It has been previously thought that the poor optical transparency of low-cost FDM 3D-printed polymers is a fundamental obstacle that considerably limits their potential to fabricate optically interrogated devices (Willis *et al.*, 2012). Furthermore, the variability and error in low cost (< £2000) FDM printers was thought to limit their use in fabricating microfluidic structures. In this work it has been demonstrated that

through printer calibration and print optimisation, it is possible to improve optical transparency of FDM 3D-printed devices such that colourimetric optical assays can be viewed within. In addition, visible imbedded microfluidic channels with a volumetric capacity of approximately 23 μl have been successfully manufactured in a LOAD device as a single manufacturing step without the need for any post-print treatment techniques. The LOAD devices developed at this stage of the project would be suitable vessels for performing multiple parallel colourimetric assays simultaneously for optical quantification, despite not being suitable for centrifugation purposes at the time. When acetone vapour treatment (Naga *et al.*, 2013) was used, it was possible to improve the transparency of plastic samples by up to a further 30%. While not applicable to microfluidics this highlights that for some applications it is possible to further improve sensitivity and surface quality of devices manufactured using low-cost 3D-printers with simple post-processing techniques. Acetone liquid treatment displayed significant potential for reducing the surface roughness of microfluidic channels by up to 32%, which provides a low-cost method of further improving inaccessible microfluidic surfaces. In this work, a key fundamental principle was demonstrated, that imbedded microfluidic channels can be formed using a low-cost FDM 3D-printer.

6.4 The Performance of a Whole Blood Colourimetric Assay in a Low-Cost FDM 3D-Printed LOAD Microfluidic Device

Microfluidic cuvette devices with channels ranging from 100 - 500 μm wide were designed and manufactured in this work. Each device cost approximately 7.6 pence (2 g filament) rivalling commercially available PMMA cuvettes which cost approximately 7 pence each. The optimised colourimetric whole blood glucose assay was performed in a 500 μm path length microfluidic cuvette and was capable of distinguishing between a range of glucose concentrations (0-10 mM) which has been used to demonstrate the capability and functionality of the printed devices. The absorbance data gathered during testing shows that it is possible to quantify

colourimetric assay data in a low-cost FDM 3D-printed microfluidic device. The use of an enzymatic cascade demonstrates how a multistage assay process can be performed within the device as a single user step. The microfluidic cuvette devices were produced in a single manufacturing step and required no post-print treatment techniques for the generation of calibration curves. This demonstrates the second key fundamental principle required as set out in the aims and objectives for the project.

Whole blood centrifugation was performed in 3D-printed pellet devices to investigate and demonstrate if plasma can be separated from whole blood via centrifugation using a FDM 3D-printed device. Clear plasma was separated from whole blood in 3D-printed pellet devices which demonstrated the third and final key fundamental principle.

The final stage of the project attempted to combine the whole blood colourimetric assays previously developed, with a FDM 3D-printed microfluidic LOAD device in order to demonstrate the three key principles in a single FDM 3D-printed microfluidic POC device. The aim was to investigate the performance of whole blood separation in a LOAD device and produce coloured plasma from which absorbance data could potentially be gathered. Through further print and design optimisation, the centrifugation based separation of coloured plasma from the whole blood glucose assay was performed in a LOAD device using an unmodified ODD. LOAD devices were designed and produced in a single manufacturing step and untreated devices displayed evidence of successful coloured plasma generation following centrifugation; however, the devices subjected to post-print heat-treatment demonstrated superior evidence compared to the untreated devices. Each load device contained 4 embedded microfluidic channels with a volumetric capacity of approximately 23 μl and cost pence 57 pence each (14 g filament). Due to time constraints, the generation of a calibration curve in a LOAD device was not possible; however, the fundamental principle has already been demonstrated in the microfluidic cuvette devices. This demonstrates that it is possible to use low-cost readily available FDM 3D-printing technology and print materials to design, develop and manufacture viable POC LOAD device capable of utilising existing unmodified ODDs to perform centrifugation based whole blood separation within 10 seconds and quantitative assays.

6.5 Limitations

The primary advantages and disadvantages of the low-cost FDM 3D-printing technology and 3D-printed devices are summarised below.

Advantages

- Low relative upfront costs, < £1500 for the 3D-printer.
- Low relative print material and maintenance costs, £29.99 per 90 metre filament reel, freely accessible software and no subscription fees.
- Device flexibility and freedom of design. Devices can be designed to the users' specifications at little to no additional cost. For example parameters such as sample size can be adjusted by altering channel specifications and the low-cost per device renders trial-and-error viable with low financial restrictions.
- Whole blood separation using centrifugation. There is no risk of interaction with membranes or requirement of coagulation factors as blood separation is performed via centrifugation.
- Small sample size ~23 μ l.
- Ability to perform multiple different assays on a single device simultaneously provides the flexibility of POC testing with the capability of laboratory testing.
- Low cost of devices renders them disposable.
- Ability to improve device properties further using low-cost post-print treatment techniques.
- LOAD devices can be centrifuged using an unmodified ODD, with the potential for assay quantification using existing 650 nm DVD laser diodes present in DVD drives should device development continue, providing cheap diagnostic reader devices from existing technology.

Disadvantages

- Requirement for substantial calibration and optimisation of the 3D-printer and print parameters.
- Inherent inaccuracy, inconsistency and relative low-quality of devices produced using low-cost 3D-printer technology.

It should be noted that all disadvantages witnessed could potentially be overcome with higher quality 3D-printers with improved strand deposition accuracy and consistency, however, this can substantially increase costs, both upfront and running which will impact price per device. But over time such improvements often trickle down into lower cost kits.

6.6 Proposed Future Work

The overall results achieved in this project include the development and demonstration of a low cost FDM 3D printed microfluidic LOAD device that is highly customisable, capable of performing whole blood centrifugation and optical assays with a sample volume of approximately 23 μl . In addition to this, a colourimetric whole blood cholesterol assay, and colourimetric whole blood glucose assay were optimised for use in a low cost FDM 3D printed microfluidic cuvette device. The assays produce absorbance in the 650 nm region and have the potential of being quantified by an unmodified ODD; a DVD ODD utilises a 650 nm laser diode. The assay involves a single aqueous reagent, requires no sample pre-treatment, is reproducible, simple, specific, and uses no corrosive reagents. Due to the multifaceted nature of the project, and the requirement of first overcoming and demonstrating previously unachievable and undocumented fundamental principles, there are areas which due to time constraints were not fully developed and suggestions for possible future work for both the assay and device development.

1. Colourimetric Assay Development

- Implement cholesterol esterase into cholesterol assay for the quantification of total cholesterol in samples.
- Investigate assay reaction < 2 minutes incubation and optimise assay for time-to-result ≤ 10 seconds by increasing enzyme concentration.
- Investigate long term stability of assay reagents in solution and as solid mixture.
- Progress to human blood samples.
- Investigation of matrix effect and potential interactions with assay.

2. Low-Cost FDM 3D-Printed Microfluidic LOAD Device Development

- Water-tight and perform blood separation in 1.2 mm thick LOAD device to ensure device dimensions are compatible with all ODDs.
- Reduce dimensions of microfluidic channels, and therefore sample volume, to volumetric capacity of <15 μl to rival existing POC devices.
- Further explore heat-treatment. Avenues of investigation include: a range of temperatures, duration vs optical transparency, warping of devices, quantification of changes to water-tightness in printed devices, method of heating and their effects (e.g. direct contact, baking, etc.).
- Investigate alternative liquid-solvent treatments suitable for the internals of microfluidic channels.
- Investigate additional post-print finishing techniques for improving transparency and build quality suitable for application within sealed microfluidic channels.
- Use computational fluid modelling to aid in channel design optimisation for sample flow and reagent mixing in microfluidic channels.
- Perform accurate measurement of microfluidic channels to gauge deviation from the 'ideal' model.

- Investigate other low-cost 3D-printing technology for device manufacture and compare advantages and disadvantages of devices produced to FDM technology.

3. Performing The Colourimetric Assays In 3D-Printed Microfluidic Devices

- Generate a calibration curve for the whole blood glucose assay performed in the LOAD device.
- Investigate the performance of the assay during centrifugation in load device. The effect of the centrifugation process on the assay performance will determine how the LOAD device usage protocol is developed.
- Investigate the performance of assay reagent and sample mixing within the LOAD microfluidic channels; the assay reagents should be deposited in the channels either in liquid or solid form, then the blood sample is applied and the assay performed.
- Investigate deposition of dry assay reagents into channels, potentially through developing liquid reagent mix which is introduced to channels, then the solution allowed to evaporate, leaving a dry reagent mix in the channels to then be dissolved by the sample.
- Perform a cross-reactivity study of the assay reagents with print materials and investigate secondary adsorption phenomena.

4. Progress Towards the use of an Optical Disc Drive as a Reader Device

- Investigate and develop software necessary for directly controlling spindle motor for centrifuging whole blood in the LOAD device.
- Investigate implementation of reflective surface into LOAD device as ODDs utilise reflection not transmission.

6.7 Final Conclusions

As discussed in section 2.1, the global healthcare systems are already stretched beyond capacity so the development of affordable multi-analyte diagnostic development technology is of utmost importance. The capability of developing and manufacturing POC diagnostic devices tailored to specific requirements for a fraction of current costs will provide establishments, especially those with restricted resources, essential diagnostic data cheaply and quickly that would otherwise be unavailable. This may significantly improve prognostic and therapeutic patient outcomes and reduce financial strain on healthcare services. In addition, low-cost POC devices that are capable of quantifying multiple biomarkers in biological fluids have the potential of combining existing home testing devices into a single platform, reducing costs to the customer as well as reducing waste from used devices.

The overall outputs achieved from this study include the development of two highly customisable low-cost FDM 3D-printed microfluidic devices; a microfluidic cuvette which has been used to quantify glucose concentration and a LOAD device with multiple microfluidic channels (~23 μ l) capable of performing centrifugation based whole blood separation and generation of coloured plasma that has the potential for analyte quantification. In addition to this, two whole blood optical assays suitable for use within low-cost 3D-printed devices were developed and optimised that demonstrate the quantitative potential of assays read in microfluidic FDM 3D-printed devices. All device development and manufacture was performed using an Ultimaker 2+ FDM 3D-Printer costing ~£1600 at the time of writing; with the closest commercial competitor capable of producing similar products being the Dolomite Fluidic Factory which costs £14,000 at the time of writing. It is hoped that the results produced in this work will, as a consequence, aid in reducing the price of high-end 3D-printing technology to more affordable levels rendering it accessible to a much larger proportion of research and development groups who currently cannot afford it. This will drive diagnostic device research forward to the benefit of all.

LIST OF PUBLICATIONS

Peer-Reviewed Journal Papers

A M Tohill, M Partridge, S W James and R P Tatam. (2017) 'Fabrication and optimisation of a fused filament 3D-printed microfluidic platform', *Micromechanics and Microengineering*, 27, 035018 (8pp)

Conference Paper

A M Tohill, M Partridge, S W James and R P Tatam. (2016) Optical detection of glucose using 3D-printed microfluidic platform. Biosensors 2016 Congress, Gothenburg Sweden.

Awards

A M Tohill, M Partridge, S W James and R P Tatam. (2016) Optical detection of glucose using 3D-printed microfluidic platform. Biosensors 2016 Congress, Gothenburg Sweden. Biosensors 2016 Congress Gothenburg, Sweden. Best Paper Winner (1st out of ~900)

News Article

Beau Jackson. (2017) Cranfield University makes biological microfluidics research possible at home. 3D-Printing Industry. Available at: <https://3dprintingindustry.com/news/cranfield-university-makes-biological-microfluidics-research-possible-home-104514/>

REFERENCES

3ders.org (2017) *A few ways to strengthen 3D printed parts*. Available at: <http://www.3ders.org/articles/20141010-a-few-ways-to-strengthen-3d-printed-parts.html> (Accessed: 5 March 2017).

Abaxis.com (2014) *Piccolo Xpress*. Available at: <https://www.abaxis.com/medical/piccolo-xpress> (Accessed: 23 January 2015).

Abcam.com (2017) *Glucose Assay Kit (ab65333)*. Available at: <http://www.abcam.com/glucose-assay-kit-ab65333.html> (Accessed: 21 February 2017).

Amazon.co.uk (2017) *Freestyle Optium Glucose Test Strips*. Available at: https://www.amazon.co.uk/d/Glucose-Kits/Optium-Freestyle-Test-Strips/B0034LSAHW/ref=sr_1_1_a_it?ie=UTF8&qid=1491250968&sr=8-1&keywords=freestyle+optium+test+strips (Accessed: 17 February 2017).

American Diabetes Association (2010) 'Standards of Medical Care in Diabetes—2010', *Diabetes Care*, 33(1), pp. 11–61.

American Heart Association (2014) *Good vs. Bad Cholesterol*. Available at: http://www.heart.org/HEARTORG/Conditions/Cholesterol/AboutCholesterol/Good-vs-Bad-Cholesterol_UCM_305561_Article.jsp (Accessed: 12 February 2014).

Ansari, M.I.H., Hassan, S., Qurashi, A. and Ahmad, F. (2016) 'Micro fluidic-integrated DNA nanobiosensors', *Biosensors and Bioelectronics*, 85, pp. 247–260.

Arnandis-Chover, T., Morais, S., González-Martínez, M.Á., Puchades, R. and Maquieira, Á. (2014) 'High density MicroArrays on Blu-ray discs for massive screening', *Biosensors and Bioelectronics*, 51, pp. 109–114.

Aronoff, S.L., Berkowitz, K. and Shreiner, B. (2004) 'Glucose Metabolism and Regulation : Beyond Insulin and Glucagon', *Diabetes Spectrum*, 17, pp. 183–190.

Asiello, P.J. and Baeumner, A.J. (2011) 'Miniaturized isothermal nucleic acid amplification , a review', *Lab on a chip*, , pp. 1420–1430.

Assadollahi, S., Reininger, C., Palkovits, R., Pointl, P. and Schalkhammer, T. (2009) 'From Lateral Flow Devices to a Novel Nano-Color Microfluidic Assay', *Sensors*, , pp. 6084–6100.

Au, A.K., Lee, W. and Folch, A. (2014) 'Mail-Order Microfluidics: Evaluation of Stereolithography for the Production of Microfluidic Devices', *Lab Chip*, 14(7), pp. 1294–1301.

Ausgamestore.com (2008) *PS3 Game Disc Reading Error Blu Ray Drive Repair Service In Melbourne Victoria*. Available at: <http://www.ausgamestore.com/ps3/ps3-blu-ray-drive.html> (Accessed: 11 February 2017).

Ballyns, J.J., Cohen, D.L., Malone, E., Maher, S.A., Potter, H.G., Wright, T., Lipson, H. and Bonassar, L.J. (2009) 'An optical method for evaluation of geometric fidelity for anatomically shaped tissue-engineered constructs', *Tissue Engineering Part C: Methods*, 16(4) Mary Ann Liebert, Inc. 140 Huguenot Street, 3rd Floor New Rochelle, NY 10801 USA, pp. 693–703.

Bankar, S.B., Bule, M. V, Singhal, R.S. and Ananthanarayan, L. (2009) 'Glucose oxidase — An overview', *Biotechnology Advances*, 27(4), pp. 489–501.

Bartholomeusz, D.A., Boutté, R.W. and Andrade, J.D. (2005) 'Xurography: rapid prototyping of microstructures using a cutting plotter', *Journal of Microelectromechanical Systems*, 14(6), pp. 1364–1374.

Becker, H. and Locascio, L.E. (2002) 'Polymer microfluidic devices', *Talanta*, 56, pp. 267–287.

Behrman, E.J. and Gopalan, V. (2005) 'Cholesterol and plants', *Journal of chemical education*, 82(12) ACS Publications, p. 1791.

Benchoff, B. (2013) *GIVING 3D PRINTED PARTS A SHINY SMOOTH FINISH*. Available at: <http://hackaday.com/2013/02/26/giving-3d-printed-parts-a-shiny-smooth-finish/> (Accessed: 16 August 2015).

Berer, T., Leiss-holzinger, E., Bauer-marschallinger, J., Buchsbaum, A., Berer, T., Leiss-holzinger, E., Hochreiner, A. and Bauer-marschallinger, J. (2015) 'Multimodal

noncontact photoacoustic and optical coherence tomography imaging using wavelength-division multiplexing wavelength-division multiplexing', *Biomedical Optics*, 20, p. 046013 1-6.

Berry, S. (2004) 'Lipid Analysis: Isolation, separation, identification and structural analysis of lipids', *Nutrition Bulletin*, 29(1) Wiley Online Library, pp. 72–73.

Birtwell, S. and Morgan, H. (2009) 'Microparticle encoding technologies for high-throughput multiplexed suspension assays', *Integrative Biology*, 1(5)

Bissonnette, L. and Bergeron, M.G. (2010) 'Diagnosing infections - current and anticipated technologies for point-of-care diagnostics and home-based testing', *European Society of Clinical Microbiology and Infectious Diseases*, 16, pp. 1044–1053.

Blockscientificstore.com (2017) *ABBOTT I-STAT 1*. Available at: <http://www.blockscientificstore.com/Abbott-i-STAT-1-p/abbott-i-stat-1.htm> (Accessed: 15 February 2017).

Bosco, F.G., Bache, M., Yang, J., Chen, C.H., Hwu, E., Lin, Q. and Boisen, A. (2013) 'Micromechanical PDGF recognition via lab-on-a-disc aptasensor arrays', *Sensors & Actuators: A. Physical*, 195 Elsevier B.V., pp. 154–159.

Boutati, E.I. and Raptis, S.A. (2009) 'Self-Monitoring of Blood Glucose as Part of the Integral Care of Type 2 Diabetes', *Diabetes Care*, 32(2), pp. 205–210.

bpac.org (2013) *Interpreting urine dipstick tests in adults: a reference guide for primary care*. Available at: <http://www.bpac.org.nz/BT/2013/June/urine-tests.aspx> (Accessed: 14 February 2017).

Brahim, S., Narinesingh, D. and Guiseppi-Elie, A. (2001) 'Amperometric determination of cholesterol in serum using a biosensor of cholesterol oxidase contained within a polypyrrole–hydrogel membrane', *Analytica Chimica Acta*, 448(1), pp. 27–36.

Bruchet, A., Taniga, V., Descroix, S., Malaquin, L., Goutelard, F. and Mariet, C. (2013) 'Centrifugal microfluidic platform for radiochemistry: Potentialities for the chemical analysis of nuclear spent fuels', *Talanta*, 116, pp. 488–494.

Burger, R., Kirby, D., Glynn, M., Nwankire, C., O'Sullivan, M., Siegrist, J., Kinahan, D.,

Aguirre, G., Kijanka, G. and Gorkin III, R.A. (2012) 'Centrifugal microfluidics for cell analysis', *Current opinion in chemical biology*, 16(3), pp. 409–414.

Calctool.org (2008) *Centrifugal Force*. Available at: <http://www.calctool.org/CALC/phys/newtonian/centrifugal> (Accessed: 7 October 2013).

Capewell, S., Allender, S., Critchley, J., Lloyd-Williams, F., O'Flaherty, M., Rayner, M., Scarborough, P. and Coalition, V. (2008) *Modelling the UK burden of cardiovascular disease to 2020* JOUR. London: British Heart Foundation.

Di Carlo, D., Edd, J.F., Irimia, D., Tompkins, R.G. and Toner, M. (2008) 'Equilibrium separation and filtration of particles using differential inertial focusing', *Analytical Chemistry*, 80(6), pp. 2204–2211.

Chambers, J.P., Arulanandam, B.P., Matta, L.L., Weis, A. and Valdes, J.J. (2008) 'Biosensor Recognition Elements', *Current Issues Molecular Biology*, 10, pp. 1–12.

Chen, B., Zhou, X., Li, C., Wang, Q., Liu, D. and Lin, B. (2011) 'Rapid screening of phenylketonuria using a CD microfluidic device', *Journal of Chromatography A*, 1218(14), pp. 1907–1912.

Chen, C., Wang, Y., Lockwood, S.Y. and Spence, D.M. (2014) '3D-printed fluidic devices enable quantitative evaluation of blood components in modified storage solutions for use in transfusion medicine.', *The Analyst*, 139(13), pp. 3219–26.

Chen, H., Li, X., Wang, L. and Li, P.C.H. (2010) 'A rotating microfluidic array chip for staining assays', *Talanta*, 81(4), pp. 1203–1208.

Chen, Q.L., Cheung, K.L., Kong, S.K., Zhou, J.Q., Kwan, Y.W., Wong, C.K. and Ho, H.P. (2012) 'An integrated lab-on-a-disc for automated cell-based allergen screening bioassays', *Talanta*, 97, pp. 48–54.

Chilson, L. (2013) *The Difference Between ABS and PLA for 3D Printing*. Available at: <http://www.protoparadigm.com/news-updates/the-difference-between-abs-and-pla-for-3d-printing/> (Accessed: 12 February 2014).

Chin, C.D., Linder, V. and Sia, S.K. (2012) 'Commercialization of microfluidic point-of-

care diagnostic devices', *Lab Chip*, 12, pp. 2118–2134.

Cho, Y.-K., Lee, J.-G., Park, J.-M., Lee, B.-S., Lee, Y. and Ko, C. (2007) 'One-step pathogen specific DNA extraction from whole blood on a centrifugal microfluidic device', *Lab on a Chip*, 7(5), pp. 565–573.

Clarke, S.F. and Foster, J.R. (2012) 'A history of blood glucose meters and their role in self-monitoring of diabetes mellitus ABSTRACT', 69(2), pp. 83–93.

Cochrane, N. (2002) *Life in the fast lane can be a disc-shattering experience*. Available at: <http://www.theage.com.au/articles/2002/12/09/1039379779472.html> (Accessed: 20 November 2014).

Cohen, D.L., Malone, E., Lipson, H.O.D. and Bonassar, L.J. (2006) 'Direct Freeform Fabrication of Seeded Hydrogels in Arbitrary Geometries', *Tissue engineering*, 12(5), pp. 1325–1335.

Custompart.net (2008) *Stereolithography*.

Davis, R.H. and Acrivos, A. (1985) 'Sedimentation of noncolloidal particles at low Reynolds numbers', *Annual Review of Fluid Mechanics*, 17(1) Annual Reviews 4139 El Camino Way, PO Box 10139, Palo Alto, CA 94303-0139, USA, pp. 91–118.

Diabetes.co.uk (2017) *Diabetes and Hypoglycemia*. Available at: <http://www.diabetes.co.uk/Diabetes-and-Hypoglycaemia.html> (Accessed: 25 March 2017).

Diabetes UK (2015) *Monitoring Your Diabetes: Testing*. Available at: <https://www.diabetes.org.uk/Guide-to-diabetes/Monitoring/Testing/#glucose> (Accessed: 20 January 2016).

Dolomite (2016) *Fluidic Factory Innovative Technology*. Available at: http://www.dolomite-microfluidics.com/webshop/fluidic_factory_innovative_technology (Accessed: 2 December 2016).

Douketis, J.D. (2001) 'Patient Self-Monitoring of Oral Anticoagulant Therapy Potential Benefits and Implications for Clinical Practice', *American Journal of Cardiovascular*

Drugs, 1(4), pp. 245–251.

Drexler, W. and Fujimoto, J.G. (2015) 'Theory of Optical Coherence Tomography', in *Optical Coherence Tomography, Technology and Applications: Second Edition.*, pp. 65–95.

Ebay.com (2014) *How to Clean a CD ROM*. Available at: <http://www.ebay.com/gds/How-to-Clean-a-CD-ROM-/10000000178705948/g.html> (Accessed: 16 January 2015).

English, A. (2012) *3D Printer Filament Buyer's Guide*. Available at: <http://www.protoparadigm.com/news-updates/3d-printer-filament-buyers-guide/> (Accessed: 12 September 2014).

Erkal, J.L., Selimovic, A., Gross, B.C., Lockwood, S.Y., Walton, E.L., McNamara, S., Martin, R.S. and Spence, D.M. (2014) '3D printed microfluidic devices with integrated versatile and reusable electrodes', *Lab Chip*, 14(12), pp. 2023–2032.

Ferraris, R. (2001) 'Dietary and developmental regulation of intestinal sugar transport', *Biochemical Journal*, 360, pp. 265–276.

Fiorini, G.S. and Chiu, D.T. (2005) 'Disposable microfluidic devices: Fabrication, function, and application', *BioTechniques*, 38(3), pp. 429–446.

Focke, M., Stumpf, F., Roth, G., Zengerle, R. and von Stetten, F. (2010) 'Centrifugal microfluidic system for primary amplification and secondary real-time PCR', *Lab on a Chip*, 10(23), pp. 3210–3212.

Food and Agriculture Organization (2003) 'Chapter 3: Calculation of the Energy Content of Foods – Energy Conversion Factors', in *FAO Food and Nutrition Paper 77. Food energy – methods of analysis and conversion factors.*, pp. 18–37.

Fox, M. (2001) *Optical Properties of Solids*. 1st edn. Oxford University Press.

Freeman, M. and Junge, C. (2005) *Understanding Cholesterol: The Good, the Bad, and the Necessary*. Available at: http://www.health.harvard.edu/newsweek/Understanding_Cholesterol.htm (Accessed: 13 February 2014).

Gabbrielli, R., Turner, I.G. and Bowen, C.R. (2008) 'Development of modelling methods for materials to be used as bone substitutes', *Key Engineering Materials*, 361, pp. 903–906.

Girotti, A.W. (2002) *Cholesterol Oxidation: Mechanisms and Signature Products* Society of Free Radical Biology and Medicine

Goode, J., Dillon, G. and Millner, P.A. (2016) 'The development and optimisation of nanobody based electrochemical immunosensors for IgG', *Sensors & Actuators: B. Chemical*, 234 Elsevier B.V., pp. 478–484.

Grand View Research (2016) *Glucose Biosensor Market To Reach \$31.0 Billion By 2022*. Available at: <https://www.grandviewresearch.com/press-release/global-glucose-biosensor-market> (Accessed: 18 October 2016).

Grieser, F. (2016) *PLA vs ABS: Filaments for 3D Printing Explained & Compared*. Available at: <https://all3dp.com/pla-abs-3d-printer-filaments-compared/> (Accessed: 19 April 2016).

Gross, B.C., Erkal, J.L., Lockwood, S.Y., Chen, C. and Spence, D.M. (2014) 'Evaluation of 3D printing and its potential impact on biotechnology and the chemical sciences', *Analytical Chemistry*, 86(7), pp. 3240–3253.

Gubala, V., Harris, L.F., Ricco, A.J., Tan, M.X. and Williams, D.E. (2012) 'Point of care diagnostics: Status and future', *Analytical Chemistry*, 84(2), pp. 487–515.

Gubala, V., Nooney, R., Hearty, S., McDonnell, B., Heydon, K., Kennedy, R.O., Maccraith, D. and Williams, D.E. (2011) 'Kinetics of immunoassays with particles as labels : effect of antibody coupling using dendrimers as linkers', *Analyst*, , pp. 2533–2541.

Guilbault, G. and Lubrano, G. (1973) 'An Enzyme Electrode For The Amperometric Determination Of Glucose', *Analytica Chimica Acta*, 64, pp. 439–455.

Hanukoglu, I. (1992) 'Steroidogenic enzymes: structure, function, and role in regulation of steroid hormone biosynthesis', *The Journal of steroid biochemistry and molecular biology*, 43(8), pp. 779–804.

Harvard School of Public Health (2016) *Carbohydrates and Blood Sugar*. Available at: <https://www.hsph.harvard.edu/nutritionsource/carbohydrates/carbohydrates-and-blood-sugar/> (Accessed: 10 January 2017).

Heller, A. and Feldman, B. (2008) 'Electrochemical Glucose Sensors and Their Applications in Diabetes Management', *Chemical Reviews*, , pp. 2482–2505.

Heller, A. and Feldman, B.E.N. (2010) 'Electrochemistry in Diabetes Management', *Accounts of Chemical Research*, 43(7), pp. 963–973.

Herrmann, K., Gärtner, C., Güllmar, D., Krämer, M. and Reichenbach, J.R. (2014) 'Medical Engineering & Physics 3D printing of MRI compatible components : Why every MRI research group should have a low-budget 3D printer', *Medical Engineering and Physics*, 36(10) Institute of Physics and Engineering in Medicine, pp. 1373–1380.

Higson, S. (2004) *Analytical Chemistry* BOOK. UK: Oxford Univeristy Press.

Hiratsuka, A., Fujisawa, K. and Muguruma, H. (2008) 'Amperometric Biosensor Based on Glucose Dehydrogenase and Plasma-polymerized Thin Films', *Analytical Sciences*, 24(April), pp. 483–486.

Hnilička, B., Voda, A. and Schröder, H.-J. (2005) 'Modelling the characteristics of a photodetector in a DVD player', *Sensors and actuators A: Physical*, 120(2), pp. 494–506.

Ho, C.M.B., Ng, S.H., Li, K.H.H. and Yoon, Y. (2015) '3D Printed Microfluidics for Biological Applications', *Lab On A Chip*, 15(18) Royal Society of Chemistry, pp. 3627–3637.

Hobson, T. and Le, L. (2012) 'Surface geometry , miniaturization and metrology', *Phil. Trans. R. Soc. A*, 370, pp. 4042–4065.

Hormone.org (2017) *What Does Insulin Do?., Hormones and Health- What Do Hormones Do?*

Hussain, M.M. (2000) 'A proposed model for the assembly of chylomicrons Review article', *Atherosclerosis*, 148(February), pp. 1–15.

Hutmacher, D.W., Sittinger, M. and Risbud, M. V (2004) 'Scaffold-based tissue engineering: rationale for computer-aided design and solid free-form fabrication systems', *Trends in biotechnology*, 22(7), pp. 354–362.

hyperphysics (2016) *Glucose*. Available at: <http://hyperphysics.phy-astr.gsu.edu/hbase/Organic/sugar.html> (Accessed: 29 January 2017).

IASA Technical Committee (2009) *Guidelines on the Production and Preservation of Digital Audio Objects (web edition)*. Second. Bradley, K. (ed.).

Javitt, N.B. (1994) 'Bile acid synthesis from cholesterol: regulatory and auxiliary pathways', *FASEB journal : official publication of the Federation of American Societies for Experimental Biology*, 8(15) Division of Hepatic Diseases, New York University Medical Center, New York 10016., pp. 1308–1311.

Jonsson, C., Aronsson, M., Rundstrom, G., Pettersson, C., Mendel-Hartvig, I., Bakker, J., Martinsson, E., Liedberg, B., MacCraith, B., Ohmana, O. and Melin, J. (2008) 'Silane – dextran chemistry on lateral flow polymer chips for immunoassays', *Lab on a chip*, 8, pp. 1191–1197.

Kadimisetty, K., Mosa, I.M., Malla, S., Satterwhite-warden, J.E., Kuhns, T.M., Faria, R.C., Lee, N.H. and Rusling, J.F. (2016) '3D-printed supercapacitor-powered electrochemiluminescent protein immunoarray', *Biosensors and Bioelectronics*, 77, pp. 188–193.

Kantaros, A. and Karalekas, D. (2013) 'Fiber Bragg grating based investigation of residual strains in ABS parts fabricated by fused deposition modeling process', *Materials & Design*, 50, pp. 44–50.

Kazarine, A., Kong, M.C.R., Templeton, E.J. and Salin, E.D. (2012) 'Automated liquid–liquid extraction by pneumatic recirculation on a centrifugal microfluidic platform', *Analytical Chemistry*, 84(16) ACS Publications, pp. 6939–6943.

Kim, T., Hwang, H., Gorkin, R., Madou, M. and Cho, Y. (2013) 'Geometry effects on blood separation rate on a rotating disc', *Sensors and Actuators B: Chemical*, 178, pp. 648–655.

Kinahan, D.J., Kearney, S.M., Glynn, M.T. and Ducreé, J. (2014) 'Spira mirabilis enhanced whole blood processing in a lab-on-a-disk', *Sensors and Actuators, A: Physical*, 215, pp. 71–76.

Koczula, K.M. and Gallotta, A. (2016) 'Lateral flow assays', *Essays in Biochemistry*, 60(June), pp. 111–120.

Lange, S.A., Roth, G., Wittemann, S., Lacoste, T., Vetter, A., Grässle, J., Kopta, S., Kolleck, M., Breitingner, B., Wick, M., Hörber, J.K.H., Dübel, S. and Bernard, A. (2006) 'Measuring biomolecular binding events with a compact disc player device', *Angewandte Chemie - International Edition*, 45(2), pp. 270–273.

Laurence, C.O., Moss, J.R., Briggs, N.E., Beilby, J.J. and Management, T. (2010) 'The cost-effectiveness of point of care testing in a general practice setting : results from a randomised controlled trial', *BMC Health Services Research*, 10, pp. 165–176.

Lee, B.S., Lee, J.-N., Park, J.-M., Lee, J.-G., Kim, S., Cho, Y.-K. and Ko, C. (2009) 'A fully automated immunoassay from whole blood on a disc', *Lab on a Chip*, 9(11), pp. 1548–1555.

Lee, B.S., Lee, Y.U., Kim, H.-S., Kim, T.-H., Park, J., Lee, J.-G., Kim, J., Kim, H., Lee, W.G. and Cho, Y.-K. (2011) 'Fully integrated lab-on-a-disc for simultaneous analysis of biochemistry and immunoassay from whole blood', *Lab on a chip*, 11(1), pp. 70–78.

Lee, T.M. (2008) 'Over-the-Counter Biosensors: Past, Present, and Future', *Sensors*, 8, pp. 5535–5559.

Leedsth.nhs.uk (2014) *Introduction to Point of Care*. Available at: <http://www.pathology.leedsth.nhs.uk/pathology/Departments/BloodSciences/ClinicalBiochemistry/PointofCareTesting.aspx> (Accessed: 6 March 2017).

Li, Y., Ou, L.M.L. and Yu, H.Z. (2008) 'Digitized molecular diagnostics: Reading disk-based bioassays with standard computer drives', *Analytical Chemistry*, 80(21), pp. 8216–8223.

Lien, K. and Lee, G. (2010) 'Miniaturization of molecular biological techniques for gene assay', *The Royal Society of Chemistry*, 135, pp. 1499–1518.

Von Lode, P. (2005) 'Point-of-care immunotesting: Approaching the analytical performance of central laboratory methods', *Clinical Biochemistry*, 38(7), pp. 591–606.

Lolekha, P.H. and Jantaveesirirat, Y. (1992) 'Streptomyces: a superior source for cholesterol oxidase used in serum cholesterol assay', *Journal of clinical laboratory analysis*, 6(6) Wiley Online Library, pp. 405–409.

Lolekha, P.H., Srisawasdi, P., Jearanaikoon, P., Wetprasit, N., Sriwanthana, B. and Kroll, M.H. (2004) 'Performance of four sources of cholesterol oxidase for serum cholesterol determination by the enzymatic endpoint method', *Clinica chimica acta*, 339(1), pp. 135–145.

Lutz, S., Weber, P., Focke, M., Faltin, B., Hoffmann, J., Müller, C., Mark, D., Roth, G., Munday, P. and Armes, N. (2010) 'Microfluidic lab-on-a-foil for nucleic acid analysis based on isothermal recombinase polymerase amplification (RPA)', *Lab on a Chip*, 10(7), pp. 887–893.

Madou, M., Zoval, J., Jia, G., Kido, H., Kim, J. and Kim, N. (2006) 'Lab on a CD', *Annual Review of Biomedical Engineering*, 8, pp. 601–628.

Makeitfrom.com (2017) *Compare ABS to PLA*. Available at: <http://www.makeitfrom.com> (Accessed: 3 February 2017).

MakerBot.com (2016) *MakerBot.com*. Available at: <http://www.makerbot.com/> (Accessed: 6 June 2016).

MakerGeeks.com (2014) *PLA vs ABS - The tale of two Thermoplastics*.

Mankovich, N.J., Samson, D., Pratt, W., Lew, D. and Beumer 3rd, J. (1994) 'Surgical planning using three-dimensional imaging and computer modeling', *Otolaryngologic clinics of North America*, 27(5), pp. 875–889.

Mark, D., Haeberle, S., Roth, G., von Stetten, F. and Zengerle, R. (2010) 'Microfluidic lab-on-a-chip platforms: requirements, characteristics and applications.', *Chemical Society reviews*, 39(3), pp. 1153–82.

Mark, D., von Stetten, F. and Zengerle, R. (2012) 'Microfluidic Apps for off-the-shelf instruments.', *Lab Chip*, 12(14), pp. 2464–8.

Markets and Markets (2015) *Microfluidics Market worth \$7.5 Billion by 2020., Microfluidics Market by Material (Polymer, Glass, Silicon) Application (Pharmaceutical (Genomics, Proteomics, Capillary Electrophoresis) Diagnostic (POC, Clinical, Environmental, Industrial) Drug Delivery (Inhaler, Micropump)) - Global Forecast to 2020* Available at: <http://www.marketsandmarkets.com/PressReleases/microfluidics.asp> (Accessed: 13 January 2016).

Matthews, D.R. and Neil, H.A.W. (2008) '10-Year Follow-up of Intensive Glucose Control in Type 2 Diabetes', *The New England Journal of Medicine*, (359), pp. 1577–89.

Meagher, R.J., Hatch, A. V, Renzi, R.F. and Singh, A.K. (2008) 'An integrated microfluidic platform for sensitive and rapid detection of biological toxins', *Lab on a chip*, 8(12)

Mehta, S. (2013) *Biosynthesis and Regulation of Cholesterol (With Animation)*.

Melchels, F.P.W., Feijen, J. and Grijpma, D.W. (2010) 'A review on stereolithography and its applications in biomedical engineering', *Biomaterials*, 31(24), pp. 6121–6130.

Mellon, D., Pring, A. and Verne, J. (2013) *Deaths from cardiovascular diseases: Implications for end of life care in England*. London: National End of Life Care Intelligence.

Mendis, S., Puska, P. and Norrving, B. (eds.) (2011) *Global Atlas on cardiovascular disease prevention and control*. Geneva: World Health Organization.

Mensink, R.P. and Katan, M.B. (1992) 'Effect of dietary fatty acids on serum lipids and lipoproteins. A meta-analysis of 27 trials', *Arteriosclerosis and Thrombosis : A Journal of Vascular Biology / American Heart Association*, 12(8) Department of Human Biology, Limburg University, Maastricht, The Netherlands., pp. 911–919.

Mirasoli, M., Guardigli, M., Michelini, E. and Roda, A. (2014) 'Recent advancements in chemical luminescence-based lab-on-chip and microfluidic platforms for bioanalysis', *Journal of pharmaceutical and biomedical analysis*, 87, pp. 36–52.

Miserere, S., Mottet, G., Taniga, V., Descroix, S., Viovy, J.-L. and Malaquin, L. (2012) 'Fabrication of thermoplastics chips through lamination based techniques.', *Lab on a*

chip, 12(10), pp. 1849–56.

Moen, S.T., Hatcher, C.L. and Singh, A.K. (2016) 'A Centrifugal Microfluidic Platform That Separates Whole Blood Samples into Multiple Removable Fractions Due to Several Discrete but Continuous Density Gradient Sections', *PloS one*, 11(4), pp. 1–11.

Morais, S., Tamarit-López, J., Carrascosa, J., Puchades, R. and Maquieira, Á. (2008) 'Analytical prospect of compact disk technology in immunosensing', *Analytical and bioanalytical chemistry*, 391(8), pp. 2837–2844.

Moschou, E.A., Nicholson, A.D., Jia, G., Zoval, J. V, Madou, M.J., Bachas, L.G. and Daunert, S. (2006) 'Integration of microcolumns and microfluidic fractionators on multitasking centrifugal microfluidic platforms for the analysis of biomolecules', *Analytical and bioanalytical chemistry*, 385(3), pp. 596–605.

Naga, N., Yoshida, Y., Noguchi, K. and Murase, S. (2013) 'Crystallization of Amorphous Poly (Lactic Acid) Induced by Vapor of Acetone to Form High Crystallinity and Transparency Specimen', 2013(May), pp. 29–33.

Nakashima, Y., Hata, S. and Yasuda, T. (2010) 'Blood plasma separation and extraction from a minute amount of blood using dielectrophoretic and capillary forces', *Sensors and Actuators B: Chemical*, 145(1), pp. 561–569.

Newegg.com (2014) *ASUS G72Gx G74SX G72 G73 G74 CD DVD Burner Writer Blu-ray BD-ROM Player Drive*. Available at: <https://www.newegg.com/Product/Product.aspx?Item=9SIA7252VJ3914> (Accessed: 13 January 2015).

Newman, J.D. and Setford, S.J. (2006) 'Enzymatic Biosensors', *Molecular Biotechnology*, 32, pp. 249–268.

NHS UK (2013) *Diagnosing High Cholesterol - Getting a Cholesterol Test*. Available at: <http://www.nhs.uk/Conditions/Cholesterol/Pages/Diagnosis.aspx> (Accessed: 13 November 2013).

NICE (2012) *Services for the prevention of cardiovascular disease*. Available at: <https://www.nice.org.uk/guidance/cmg45/chapter/1-Commissioning-services-for-the->

prevention-of-cardiovascular-disease (Accessed: 25 November 2015).

NICE (2014) *Lipid modification: cardiovascular risk assessment and the modification of blood lipids for the primary and secondary prevention of cardiovascular disease*.

Nicell, J. a and Wright, H. (1997) 'A model of peroxidase activity with inhibition by hydrogen peroxide', *Enzyme and Microbial Technology*, 22(97), pp. 302–310.

Nie, Z., Deiss, F., Liu, X., Akbulut, O. and Whitesides, G.M. (2010) 'Integration of paper-based microfluidic devices with commercial electrochemical readers.', *Lab on a chip*, 10(22), pp. 3163–9.

Nobelprize.org (2014) *The Nobel Prize in Physiology or Medicine 1985*. Available at: http://www.nobelprize.org/nobel_prizes/medicine/laureates/1985/ (Accessed: 7 May 2014).

Nunes, P.S., Ohlsson, P.D., Ordeig, O. and Kutter, J.P. (2010) 'Cyclic olefin polymers: emerging materials for lab-on-a-chip applications', *Microfluidics and nanofluidics*, 9(2–3), pp. 145–161.

Nwankire, C.E., Donohoe, G.G., Zhang, X., Siegrist, J., Somers, M., Kurzbuch, D., Monaghan, R., Kitsara, M., Burger, R. and Hearty, S. (2013) 'At-line bioprocess monitoring by immunoassay with rotationally controlled serial siphoning and integrated supercritical angle fluorescence optics', *Analytica Chimica Acta*, 781, pp. 54–62.

Pawlina, W. and Ross, M.H. (2007) *Histology: a text and atlas: with correlated cell and molecular biology* BOOK. 5th edn. Lippincott Williams & Wilkins.

Petersson, F., Nilsson, A., Holm, C., Jönsson, H. and Laurell, T. (2005) 'Continuous separation of lipid particles from erythrocytes by means of laminar flow and acoustic standing wave forces', *Lab on a Chip*, 5(1), pp. 20–22.

Pham, D.T. and Gault, R.S. (1998) 'A comparison of rapid prototyping technologies', *International Journal of Machine Tools and Manufacture*, 38(10–11), pp. 1257–1287.

Photometrics Inc. (2016) *Surface Roughness*. Available at: <http://photometrics.net/surface-roughness/> (Accessed: 15 October 2016).

Pioggia, G., Francesco, F. Di, Marchetti, A., Ferro, M. and Ahluwalia, A. (2007) 'A composite sensor array impedentiometric electronic tongue Part I . Characterization', *Biosensors and Bioelectronics*, 22, pp. 2618–2623.

Plessis, M., Ubbink, J.B. and Vermaak, W.J.H. (2000) 'Analytical Quality of Near-Patient Blood Cholesterol and Glucose Determinations', *Clinical Chemistry*, 46, pp. 1085–1090.

Potyrailo, R.A., Morris, W.G., Leach, A.M., Sivavec, T.M., Wisnudel, M.B. and Boyette, S. (2006) 'Analog signal acquisition from computer optical disk drives for quantitative chemical sensing', *Analytical Chemistry*, 78(16), pp. 5893–5899.

Price, C.P. (2001) 'Point of care testing Clinical review Point of care testing', *BMJ Clinical Research*, 322(November), pp. 1284–1288.

Proto-Pasta.com (2017) *High Performance HTPLA - Aromatic Coffee*. Available at: <https://www.proto-pasta.com/products/aromatic-coffee-high-temp-pla> (Accessed: 12 March 2017).

Qureshi, A., Gurbuz, Y. and Niazi, J.H. (2012) 'Biosensors for cardiac biomarkers detection: A review', *Sensors and Actuators B: Chemical*, 171, pp. 62–76.

Rees, P. (2003) *Mythbusters - Exploding CDs?* Discovery Channel, United States

RepRage.com (2015) *3D Printer PLA moisture problems and storage solutions*. Available at: <https://reprage.com/post/3D-Printer-PLA-moisture-problems-and-storage-solutions> (Accessed: 23 February 2017).

RepRap.org (2014) *Fused Filament Fabrication*.

Riegger, L., Grumann, M., Steigert, J., Lutz, S., Steinert, C.P., Mueller, C., Viertel, J., Prucker, O., Rühle, J., Zengerle, R. and Ducreé, J. (2007) 'Single-step centrifugal hematocrit determination on a 10- μ s processing device', *Biomedical Microdevices*, 9(6), pp. 795–799.

Rivet, C., Lee, H., Hirsch, A., Hamilton, S. and Lu, H. (2011) 'Microfluidics for medical diagnostics and biosensors', *Chemical Engineering Science*, 66(7), pp. 1490–1507.

Ryan, F., O'Shea, S. and Byrne, S. (2010) 'The "carry-over" effects of patient self-

testing: Positive effects on usual care management by an anticoagulation management service', *Thrombosis Research*, 126(5), pp. e345–e348.

Saher, G., Brügger, B., Lappe-Siefke, C., Möbius, W., Tozawa, R., Wehr, M.C., Wieland, F., Ishibashi, S. and Nave, K.-A. (2005) 'High cholesterol level is essential for myelin membrane growth', *Nature neuroscience*, 8(4) Nature Publishing Group, pp. 468–475.

Scarborough, P., Wickramasinghe, K., Bhatnagar, P. and Rayner, M. (2011) *Trends in coronary heart disease, 1961-2011* BOOK. Weissberg, P. (ed.) London: British Heart Foundation.

Schaefermeier, P.K., Szymanski, D., Weiss, F., Fu, P., Lueth, T., Schmitz, C., Meiser, B.M., Reichart, B. and Sodian, R. (2009) 'Design and fabrication of three-dimensional scaffolds for tissue engineering of human heart valves', *European surgical research. Europäische chirurgische Forschung. Recherches chirurgicales europeennes*, 42(1) S. Karger AG, Basel, pp. 49–53.

Schaff, U.Y. and Sommer, G.J. (2011) 'Whole blood immunoassay based on centrifugal bead sedimentation', *Clinical Chemistry*, 57(5) Am Assoc Clin Chem, pp. 753–761.

Schudel, B.R., Tanyeri, M., Mukherjee, A., Schroeder, M. and Kenis, P.J.A. (2011) 'Multiplexed detection of nucleic acids in a combinatorial screening chip', *Lab on a chip*, 11, pp. 1916–1923.

Sharpless, G. (2003) 'CD and DVD Disc Manufacturing', Jul

Siegrist, J., Gorkin, R., Bastien, M. and Stewart, G. (2010) 'Validation of a centrifugal microfluidic sample lysis and homogenization platform for nucleic acid extraction with clinical samples', *Lab Chip*, , pp. 363–371.

Sigma-Aldrich (2017) *D-(+)-Glucose ≥99.5% (GC)*. Available at: <http://www.sigmaaldrich.com/catalog/product/sigma/g8270?lang=en®ion=GB> (Accessed: 4 February 2017).

Sigma-Aldrich (2016a) *BRAND standard disposable cuvettes PMMA*. Available at: <http://www.sigmaaldrich.com/catalog/product/sigma/z330388?lang=en®ion=GB> (Accessed: 11 October 2016).

Sigma-Aldrich (2013) *Assay Procedure for Cholesterol Oxidase*. Available at: <http://www.sigmaaldrich.com/technical-documents/protocols/biology/assay-procedure-for-cholesterol-oxidase.html> (Accessed: 26 February 2014).

Sigma-Aldrich (2014a) *Peroxidase from horseradish Type VI, essentially salt-free, lyophilized powder, ≥ 250 units/mg solid (using pyrogallol)*. Available at: <http://www.sigmaaldrich.com/catalog/product/sigma/p8375?lang=en®ion=GB> (Accessed: 14 November 2014).

Sigma-Aldrich (2014b) *Cholesterol Oxidase from Streptomyces sp. lyophilized powder, ≥ 20 units/mg protein*. Available at: <http://www.sigmaaldrich.com/catalog/product/sigma/c8649?lang=en®ion=GB> (Accessed: 12 November 2014).

Sigma-Aldrich (2015) *Glucose Oxidase from Aspergillus niger Type VII, lyophilized powder, $\geq 100,000$ units/g solid (without added oxygen)*. Available at: <http://www.sigmaaldrich.com/catalog/product/sigma/g2133?lang=en®ion=GB> (Accessed: 12 May 2015).

Sigma-Aldrich (2014c) *Cholesterol Quantification Kit*. Available at: <http://www.sigmaaldrich.com/catalog/product/sigma/mak043?lang=en®ion=GB> (Accessed: 22 May 2014).

Sigma-Aldrich (2016b) *Sigma-Aldrich.com*. Available at: www.sigmaaldrich.com (Accessed: 6 June 2016).

Simplify3D (2016) *Print Quality Troubleshooting Guide*. Available at: <https://www.simplify3d.com/support/print-quality-troubleshooting/> (Accessed: 31 May 2016).

Singh, S., Chaubey, A. and Malhotra, B.D. (2004) 'Amperometric cholesterol biosensor based on immobilized cholesterol esterase and cholesterol oxidase on conducting polypyrrole films', *Analytica Chimica Acta*, 502(2), pp. 229–234.

Singh, S., Solanki, P.R., Pandey, M.K. and Malhotra, B.D. (2006) 'Cholesterol biosensor based on cholesterol esterase, cholesterol oxidase and peroxidase immobilized onto

- conducting polyaniline films', *Sensors and Actuators B: Chemical*, 115(1), pp. 534–541.
- Skeie, S., Kristensen, G.B.B., Carlsen, S. and Sandberg, S. (2009) 'Self-Monitoring of Blood Glucose in Type 1 Diabetes Patients with Insufficient Metabolic Control: Focused Self-Monitoring of Blood Glucose Intervention Can Lower Glycated Hemoglobin A1C', *Diabetes Science and Technology*, 3(1), pp. 83–88.
- Sodian, R., Loebe, M., Hein, A., Martin, D.P., Hoerstrup, S.P., Potapov, E. V, Hausmann, H., Lueth, T. and Hetzer, R. (2002) 'Application of stereolithography for scaffold fabrication for tissue engineered heart valves.', *American Society for Artificial Internal Organs Journal*, 48(1), pp. 12–16.
- Soper, S.A., Brown, K., Ellington, A., Frazier, B., Garcia-Manero, G., Gau, V., Gutman, S.I., Hayes, D.F., Korte, B., Landers, J.L., Larson, D., Ligler, F., Majumdar, A., Mascini, M., Nolte, D., Rosenzweig, Z., Wang, J. and Wilson, D. (2006) 'Point-of-care biosensor systems for cancer diagnostics/prognostics', *Biosensors and Bioelectronics*, 21(10), pp. 1932–1942.
- Støvring, H., Andersen, M., Beck-nielsen, H., Green, A. and Vach, W. (2003) 'Rising prevalence of diabetes : evidence from a Danish pharmaco- epidemiological database .', *The Lancet*, 362, pp. 537–538.
- Study.com (2014) *What Is an Optical Drive? - Definition, Types & Function*. Available at: <http://study.com/academy/lesson/what-is-an-optical-drive-definition-types-function.html> (Accessed: 16 January 2015).
- Takayasu, M., Kolland, D.R. and Minervini, J. V. (2000) 'Continuous Magnetic Separation of Blood Components from Whole Blood', *IEEE Transactions on Magnetics*, 10(1), pp. 927–930.
- Tang, W.H.W. et al. (2007) 'National Academy of Clinical Biochemistry Laboratory Medicine Practice Guidelines: Clinical Utilization of Cardiac Biomarker Testing in Heart Failure', *Circulation*, 116(5), pp. 99–109.
- Tcsbiosciences.co.uk (2015) *Donor Animal Blood*. Available at: https://www.tcsbiosciences.co.uk/animal_blood_products.php?genre=clinical

(Accessed: 26 April 2015).

Temani, M., Baccar, Z.M. and Mansour, H. Ben (2014) 'Activity of cholesterol oxidase immobilized on Layered Double Hydroxide nanomaterials for biosensor application: Acacia salicina scavenging power of hypercholesterolemia therapy', *Microelectronic Engineering*, 126(0), pp. 165–168.

Thelibraryofmanufacturing.com (2014) *The Library of Manufacturing*. Available at: <http://www.thelibraryofmanufacturing.com/> (Accessed: 27 January 2015).

Thingiverse.com (2016) *Thingiverse*. Available at: <http://www.thingiverse.com/> (Accessed: 6 June 2016).

Thorlabs Inc. (2007) *Spectral Radar OCT Operating Manual*. Rev C. Thorlabs Inc.

Thorlabs Inc. (2016) *Roughness Tutorial., Super Polished Mirror Blanks* Available at: https://www.thorlabs.com/newgrouppage9_pf.cfm?objectgroup_id=7028 (Accessed: 26 October 2016).

Toner, M. and Irimia, D. (2005) 'Blood-on-a-chip', *Annual Review of Biomedical Engineering*, 7 BioMEMS Resource Center, Center for Engineering in Medicine and Surgical Services, Massachusetts General Hospital, Shriners Hospital for Children, Boston, MA 02114, USA. mtoner@hms.harvard.edu, pp. 77–103.

Townsend, N., Wickramasinghe, K., Bhatnagar, P., Smolina, K., Nichols, M., Leal, J., Luengo-Fernandez, R., Rayner, M., Heart, B. and Health, F. (2012) *Coronary Heart Disease Statistics 2012 Edition*. 2012th edn. weissberg, P. (ed.) London: British Heart Foundation.

Tsierkezos, N.G. and Ritter, U. (2014) 'Non-enzymatic analysis of cholesterol in acetonitrile solutions', *Physics and Chemistry of Liquids*, (ahead-of-print) Taylor & Francis, pp. 1–7.

Tunis, S.L. and Minshall, M.E. (2010) 'Self-monitoring of blood glucose (SMBG) for type 2 diabetes patients treated with oral anti-diabetes drugs and with a recent history of monitoring: cost-effectiveness in the US', *Current Medical Research and Opinion*, 26(1) Taylor & Francis, pp. 151–162.

Turner, A.P.F. (2000) 'Biosensors--sense and sensitivity', *Science Magazine*, 290, pp. 1315–1317.

Ultimaker.com (2016a) *Vapor treating: How to smooth PLA or ABS prints*. Available at: <https://ultimaker.com/en/resources/17897-vapor-treating-how-to-smooth-pla-or-abs-prints> (Accessed: 17 October 2016).

Ultimaker.com (2016b) *Calibration*. Available at: <https://ultimaker.com/en/resources/18769-calibration> (Accessed: 25 May 2016).

VanDelinder, V. and Groisman, A. (2006) 'Separation of plasma from whole human blood in a continuous cross-flow in a molded microfluidic device', *Analytical Chemistry*, 78(11), pp. 3765–3771.

Velleman.eu (2016) *velleman.eu*. Available at: <https://www.velleman.eu/home/> (Accessed: 6 June 2016).

Venge, P., Ohberg, C., Flodin, M. and Lindahl, B. (2010) 'Early and late outcome prediction of death in the emergency room setting by point-of-care and laboratory assays of cardiac troponin I', *American Heart Journal*, 160, pp. 835–841.

VWR.com (2017) *Varioskan Flash Spectral Scanning Multimode Readers*, Thermo Scientific. Available at: <https://us.vwr.com/store/product/4784681/varioskan-flash-spectral-scanning-multimode-readers-thermo-scientific> (Accessed: 23 January 2017).

Wang, J. (2008) 'Electrochemical Glucose Biosensors', *Chemical Reviews*, 108, pp. 814–825.

Wang, J., Ahmad, H., Ma, C., Shi, Q., Vermesh, O. and Heath, J. (2010) 'A self-powered, one-step chip for rapid, quantitative and multiplexed detection of proteins from pinpricks of whole blood', *Lab on a chip*, 10, pp. 3157–3162.

Wang, T.-M., Xi, J.-T. and Jin, Y. (2007) 'A model research for prototype warp deformation in the FDM process', *The International Journal of Advanced Manufacturing Technology*, 33(11–12) Springer, pp. 1087–1096.

Warnick, G.R. (1986) 'Enzymatic methods for quantification of lipoprotein lipids', *Methods in enzymology*, 129 UNITED STATES, pp. 101–123.

Weber, M., Rau, M., Madlener, K., Elsaesser, A., Bankovic, D., Mitrovic, V. and Hamm, C. (2005) 'Diagnostic utility of new immunoassays for the cardiac markers cTnI, myoglobin and CK-MB mass', *Clinical biochemistry*, 38(11), pp. 1027–1030.

Weibel, M. and Brights, H. (1971) 'The Glucose Oxidase Mechanism', *The Journal of Biological Chemistry*, 246(9), pp. 2734–2744.

Wendel, B., Rietzel, D., Kühnlein, F., Feulner, R., Hülder, G. and Schmachtenberg, E. (2008) 'Additive processing of polymers', *Macromolecular materials and engineering*, 293(10), pp. 799–809.

Whitesides, G.M. (2006) 'The origins and the future of microfluidics.', *Nature*, 442(7101), pp. 368–73.

Van Wie, B.J. and Hustvedt, E.L. (1988) 'Particle interaction effects on blood cell sedimentation and separations', *Biorheology*, 25(4) Chemical Engineering Department, Washington State University, Pullman 99164-2710., pp. 651–662.

Wild, S., Roglic, G., Green, A., Sicree, R. and Hilary, K. (2004) 'Global Prevalence of Diabetes: Estimates for the year 2000 and projection for 2030', *Diabetes Care*, 27(5), pp. 1047–1053.

Willis, K.D.D., Brockmeyer, E., Hudson, S.E. and Poupyrev, I. (2012) 'Printed Optics : 3D Printing of Embedded Optical Elements for Interactive Devices', *UIST '12*, , pp. 589–598.

Wilson, P.W.F. (2016) 'Changing Cholesterol Levels and Coronary Heart Disease Risk', *Circulation*, 133, pp. 239–241.

Wong, R.C., Ngo, T.T. and Lenhoff, H.M. (1981) 'Formation of blue chromophore from oxidative coupling of aminoantipyrine with chromotropic acid in the presence of peroxide and horseradish peroxidase', *International Journal of Biochemistry*, 13(2), pp. 159–163.

Woodford, C. (2016) *CD and DVD players*. Available at: <http://www.explainthatstuff.com/cdplayers.html> (Accessed: 13 October 2016).

World Health Organisation (2016) *Diabetes Fact Sheet November 2016.*, *Diabetes Fact*

Sheet Available at: <http://www.who.int/mediacentre/factsheets/fs312/en/> (Accessed: 14 November 2016).

World Health Organisation (2015) *WHO Model List of Essential Medicines*.

Yoo, E.-H. and Lee, S.-Y. (2010) 'Glucose Biosensors: An Overview of Use in Clinical Practice', *Sensors*, 10, pp. 4558–4576.

Yu, H.Z., Li, Y. and Ou, L.M.L. (2013) 'Reading disc-based bioassays with standard computer drives', *Accounts of Chemical Research*, 46(2), pp. 258–268.

Yuan, Y. and Lee, T.R. (2013) 'Contact Angle and Wetting Properties', in Bracco, G. and Holst, B. (eds.) *Surface Science Techniques*. , pp. 3–29.

Zhang, C., Anzalone, N.C., Faria, R.P. and Pearce, J.M. (2013) 'Open-source 3D-printable optics equipment', *PloS one*, 8(3), p. e59840.

ZYGO (2016) *Surface Measurement: Essential for Technology*. Available at: <http://www.zygo.com/?/met/profilers/surfaceroughnessmeasurement.htm> (Accessed: 21 October 2016).

PEER-REVIEWED JOURNAL PAPER

OPEN ACCESS
IOP Publishing

Journal of Micromechanics and Microengineering

J. Micromech. Microeng. 27 (2017) 035018 (8pp)

doi:10.1088/1361-6439/aa5ae3

Fabrication and optimisation of a fused filament 3D-printed microfluidic platform

A M Tothill, M Partridge, S W James¹ and R P Tatam

Centre for Engineering Photonics, Cranfield University, Cranfield, Bedfordshire, MK43 0AL, United Kingdom

E-mail: s.w.james@cranfield.ac.uk

Received 11 October 2016, revised 5 January 2017

Accepted for publication 20 January 2017

Published 15 February 2017



Abstract

A 3D-printed microfluidic device was designed and manufactured using a low cost (\$2000) consumer grade fusion deposition modelling (FDM) 3D printer. FDM printers are not typically used, or are capable, of producing the fine detailed structures required for microfluidic fabrication. However, in this work, the optical transparency of the device was improved through manufacture optimisation to such a point that optical colorimetric assays can be performed in a 50 μ l device. A colorimetric enzymatic cascade assay was optimised using glucose oxidase and horseradish peroxidase for the oxidative coupling of aminoantipyrine and chromotropic acid to produce a blue quinoneimine dye with a broad absorbance peaking at 590nm for the quantification of glucose in solution. For comparison the assay was run in standard 96 well plates with a commercial plate reader. The results show the accurate and reproducible quantification of 0–10mM glucose solution using a 3D-printed microfluidic optical device with performance comparable to that of a plate reader assay.

Keywords: 3D-printing, microfluidics, devices, glucose, enzymatic

(Some figures may appear in colour only in the online journal)

1. Introduction

The increasing burden being placed on health care services by an aging population, obesity epidemic and diabetes epidemic [1] is creating a necessity for point-of-care testing for serious pathologies such as cardiovascular disease and diabetes [2]. New developments in economical analytical screening tools such as lab-on-a-chip [3], lab-on-a-disc [4] and microfluidic analysis systems [5] focus on miniaturisation and disposability to improve performance, speed, and portability.

The advance of solid freeform fabrication techniques, such as 3D-printing, has significantly improved the ability to prepare solid structures with precise geometries [6], including internal cavities, facilitating the rapid production of analytical platforms and the ability to alter or redesign any aspect without

significantly inflating costs. The rapid advancement of low-end 3D printing technology is due largely to the development of free and open source software and hardware development [7]. In addition, there is a large library of freely available CAD models, which provides shortcuts to product development.

The ability to manufacture detailed and complex prototypes in a fast and efficient way has caused rapid prototyping technology to become a fundamental tool for many areas of research and development. Fused deposition modelling (FDM) based 3D printers are readily available for purchase either as self-assembly kits or as pre-assembled units. While the use of 3D-printing to produce cost-effective tools for biomedical applications has significant potential [8, 9], to date its use in the optical and biosensors field is limited.

Traditionally, glass and silicon have been used in the fabrication of microfluidic devices due to their well-established properties and manufacturing techniques, such as photolithography and micromachining [10]. However, more recently, the use of relatively inexpensive large scale techniques such as injection molding and hot embossing has led to an increase in the use of polymers for economical microfluidic device

¹ Author to whom any correspondence should be addressed.



Original content from this work may be used under the terms of the Creative Commons Attribution 3.0 licence. Any further distribution of this work must maintain attribution to the author(s) and the title of the work, journal citation and DOI.

manufacturing [11]. As well as being low-cost and disposable, polymers are highly adaptable for diagnostic purposes [12]. This has resulted in materials such as polymethylmethacrylate (PMMA) and polydimethylsiloxane (PDMS) becoming highly desirable for microfluidic device prototyping [10], and for the manufacture of disposable lab equipment such as the PMMA cuvettes used in this work. While polylactic acid (PLA) is not yet commonly used as a microfluidic platform, devices have been developed [13], and PLA's biochemical properties and suitability for surface chemistry are understood [14, 15].

3D-printed optical assay platforms can suffer from the poor optical characteristics [16] of the available polymers such as PLA and acrylonitrile butadiene styrene (ABS), particularly their poor optical transparency, which is a fundamental obstacle that must be overcome for the technology to progress. In addition, FDM suffers from a large inhomogeneity between the layers and strands of plastic, which causes the formation of air pockets between strands. The distribution of small air pockets throughout the model causes scattering and attenuation of transmitted light. Other 3D printing techniques such as stereolithography and inkjet printing have higher resolution, which greatly reduces the formation of these gaps.

Chen *et al* used FDM of a proprietary acrylate-based polymer material, Vero Clear, to produce plates for use with a standard plate reader for the quantitative analysis of red blood cells for transfusion medicine. Whilst capable of printing the plates, the Objet Connex 350 Multi-material 3D printer that was used to print the devices costs over \$200000 and the devices required post-print finishing including cleaning and polishing using sand paper and water to achieve acceptable physical properties and the levels of optical transparency required for use with a standard plate reader [17]; these finishing techniques would be unsuitable for use in sealed microfluidic channels. In addition, the material used is not readily available for public use.

Dolomite FDM printers have been able to produce reliable channels of dimensions down to 300 μm using PLA plastic [18]. While the Dolomite printers are an order of magnitude cheaper than the most expensive printers, they currently cost $\sim\text{£}13000$ for the printer and $\sim\text{£}350$ for the materials, which is still expensive when compared to consumer grade FDM printer prices ($\sim\text{£}1000$ and $\text{£}15$).

Erkal *et al* also used an Objet Connex 350 Multi-material 3D printer to produce 0.5 mm² microfluidic channels for use with electrodes for the detection of dopamine. Post-print techniques including sonication and scraping were required to properly form channels of the desired specification [19].

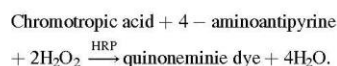
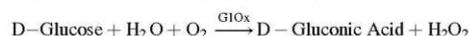
The requirement for post-print finishing techniques such as the physical removal of material and polishing to improve 3D-printed objects limits greatly the potential for the 3D printing of optical microfluidic devices, especially for the fabrication of inaccessible microfluidic channels. This emphasises the need for the development of accessible and affordable prototyping technology.

Here we demonstrate a low cost disposable microfluidic optical device designed and manufactured using single step 3D-printing technology; the device is based on a cuvette, with a path length of 500 μm and a capacity of 50 μl . Optimisation of the optical transparency of the 3D-printed plastic was also

investigated using various techniques during and after manufacture. The device was used to perform an enzymatic cascade reaction for the optical quantification of glucose.

While numerous analytical procedures involving chemical and enzymatic techniques have been used within glucose assays, enzymatic methods have been the most popular due to their increased specificity and selectivity. Enzymatic methods use glucose oxidase (GLOx) to oxidize glucose to produce D-gluconic acid and hydrogen peroxide (H_2O_2); the H_2O_2 is then quantified. Wong *et al* discovered that horseradish peroxidase (HRP) catalyses the oxidative coupling of chromotropic acid (CTA) and aminoantipyrine (AAP) with hydrogen peroxide to produce a blue quinoneimine dye with high absorbance in a spectral region centred on 590 nm [20].

In this work, a glucose assay utilizing an enzymatic cascade of glucose oxidase, HRP, CTA and 4-AAP was used for the production of a blue quinoneimine dye.



The absorbance could be measured and compared against a calibration curve giving an accurate concentration of glucose in solution. The method involves a single aqueous reagent, requires no sample pre-treatment, is reproducible, simple, specific, and uses no corrosive reagents.

The platform has been designed and manufactured using standard, readily available 3D-printing software and hardware, capable of providing results in less than 5 min, which can be read using spectrometers and photometric equipment.

2. Methods

Phosphate buffered saline (PBS, 10 mM phosphate buffer, 2.7 mM potassium chloride and 137 mM sodium chloride, pH 7.4) tablets, CTA disodium salt dihydrate (CTA), 4-AAP, isopropyl alcohol, HRP Type II essentially salt-free, lyophilized powder, 150–250 units mg^{-1} solid (using pyrogallol) (HRP), D-glucose, glucose oxidase from *Aspergillus niger* lyophilized, powder, and ~ 200 units mg^{-1} protein (GLOx), were purchased from Sigma-Aldrich (Poole, UK). Ultrapure water ($18 \text{ M}\Omega \text{ cm}^{-1}$) was produced using a Milli-Q water system (Millipore Corp., Tokyo, Japan). The concentration of glucose in samples was tested and quantified independently using an Optium Exceed Blood Glucose Monitoring System (Abbott, UK).

2.1. Glucose assay optimisation

The glucose assay consists of using an enzymatic cascade to produce a blue dye with an absorbance correlating to glucose concentration. The reagents which combine to produce the dye are CTA and 4-AAP. According to the reaction proposed by Wong *et al*, H_2O_2 reacts with CTA and AAP in the presence of HRP [20] with a molar ratio of CTA:AAP for maximum

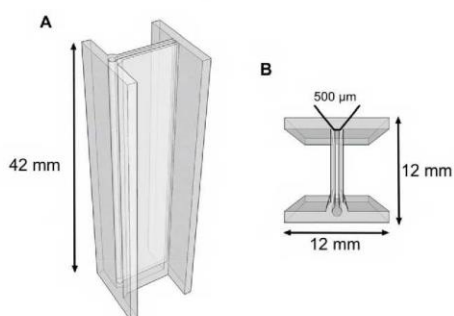


Figure 1. Schematic of the microfluidic device [22].

colour produced being 5:1. It is necessary that the concentrations of CTA and AAP are sufficient to quantify accurately the substrate within the required detection range (0–10 mM). It was determined that a concentration ratio of 2:1 CTA:AAP was required for a substrate detection range of 0–10 mM glucose.

It should be noted, that although a 1:1 CTA:AAP ratio should be sufficient, the concentration of CTA must be in excess of that of AAP to prevent AAP dimerization. In the CTA/AAP reaction, CTA is oxidised by HRP producing CTA radicals. The CTA radicals then react with AAP to produce AAP radicals and CTA. The AAP radicals then react with CTA radicals in solution and H_2O_2 to produce blue quinonimine dye. By increasing the AAP in the reagent mixture, the probability of direct oxidation of AAP by oxidised HRP is increased, which then increases the concentration of aminyl radicals and subsequently the probability of their dimerization [21]. The result of this is a decreased concentration of blue quinonimine dye and an increased concentration of AAP dimers. By maintaining a high concentration of CTA with respect to AAP, the blue dye reaction pathway is enhanced.

Glucose assay reagent solution was made by dissolving CTA, 4-AAP, glucose oxidase (0–50 units ml^{-1}) and HRP (0–10 units ml^{-1}) in the PBS solution. The reaction was started by adding the glucose solution (up to a final concentration range of 0–10 mM). The assay was read after 2 min incubation and the absorption spectrum recorded.

Serial dilution matrices were performed for CTA (0–80 mM) and 4-AAP (0–80 mM) using 6 U ml^{-1} HRP and 10 U ml^{-1} glucose oxidase (GLOx). The reaction was started by adding 0–10 mM glucose solution. Concentration curves were produced (see the supplementary data) to determine the optimum concentration values for enzyme and reagents.

Glucose oxidase and HRP concentrations were determined using a fixed time method as this is more applicable in most clinical assays. Serial dilutions were performed of GLOx (0–50 U ml^{-1}) and HRP (0–10 U ml^{-1}) using CTA 20 mM and AAP 10 mM. The reactions were started by adding a 10 mM glucose solution. The assay was incubated for 2 min and the absorbance was then measured. Samples were allowed to incubate for a further 3 min and the absorbance was measured again.

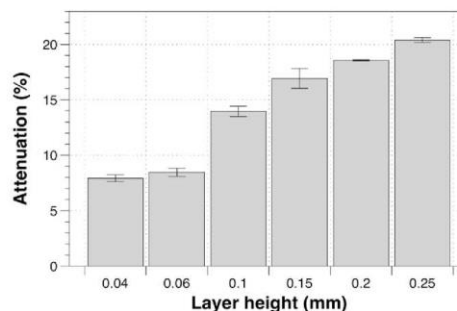


Figure 2. Attenuation at 633 nm in 400 μm thick plastic samples of Ultimaker PLA translucent made with six different layer heights, $n = 3$, error bars are the standard deviation of the repeats [23].

A Varioskan Flash spectral scanning multimode reader (ThermoScientific LTD, UK) was used in conjunction with the PC software package SkanIt to determine the absorbance values of the assays. Assay optimisation was carried out in Nunc-Immuno MaxiSorp flat bottom 96 well plates (Sigma-Aldrich, UK).

2.2. Fabrication of 3D-printed microfluidic device and 3D printed samples

The primary stages involved in making a 3D printed product are the creation of a CAD file, conversion and preparation of the file using a slicer program, uploading the file to the printer and finally the physical creation of the object. All 3D printed models were fabricated using an Ultimaker 2 + 3D printer using a 0.4 mm nozzle size. The accuracy of the printer in the X, Y and Z dimensions is 12.5, 12.5 and 5 μm respectively. The nozzle size of 0.4 mm limits the positioning of features close to each other but still allows for the design and construction of features (such as channels) of dimensions down to approximately 20 μm . However, while it is possible to create channels with this resolution, currently their formation is not reliable, and working at this scale would require improvements to the consistency of the plastic extrusion.

A number of different batches and makes of transparent filaments were used. The filaments tested include: Ultimaker PLA Translucent, Ultimaker PLA Transparent, Innofil PLA Natural and InnoPET Natural.

For this work, two different 3D models were designed. The first was a square of Ultimaker PLA Translucent plastic 20 mm² with 400 μm thickness and path length. The second was a 12 × 12 × 42 mm cuvette which has an internal microfluidic cavity with a thickness of 500 μm , this design is shown in figure 1. The circular tube to one side is included to allow for the total filling of the cavity. Multiple cuvettes were made from the variety of plastic filaments mentioned previously.

When printed, the measured thickness of the cavity was 480 μm . This was measured using an Olympus light microscope (model) in three locations along the length of the cavity. The measurement had an error of $\pm 10 \mu m$.

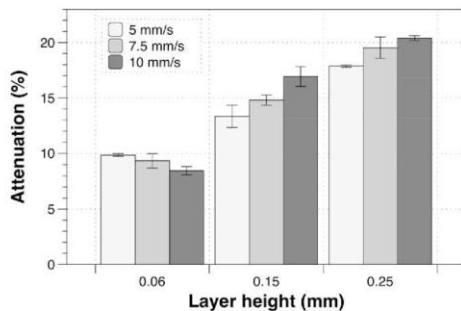


Figure 3. Attenuation in Ultimaker PLA translucent plastic samples made with three different layer heights at three different speeds, $n = 3$, error bars are the standard deviation of the repeats [24].

Both models were designed using the 3D-modelling CAD software Sketchup 2015 Pro (Trimble Navigation Ltd, USA). The device file was converted to an STL file and processed using the slicer program Cura (Ultimaker Ltd, Netherlands). Cura was also used to calibrate and optimise the print parameters by adjusting layer height and print speed.

2.3. Glucose assay in 3D-printed microfluidic device

Glucose assay reagent solution was made by dissolving CTA (up to a final concentration of 20mM), 4-AAP (up to a final concentration of 10mM), glucose oxidase (20 units ml^{-1}) and HRP (6 units ml^{-1}) in a PBS solution. The reaction was started by adding glucose solution (up to a final concentration of 0–10mM). The assay was read after a 2min incubation and the absorption spectrum recorded. The assay was performed in a microfluidic device and the absorbance spectra assessed using the equipment described in section 2.5.

2.4. Instrumentation used to measure attenuation

Instrumentation was assembled to quantify the optical attenuation of the 3D-printed plastic samples. Plastic samples were mounted at a fixed distance in front of a Newport 1825-C Optical Power Meter (Newport, USA). The sample was then illuminated with a helium–neon laser (Uniphase, UK), operating at 633nm and with an output power of 0.8 mW and fitted with a beam expander to create a beam waist of 20mm. The attenuation of the sample was recorded as the difference between the transmitted power with and without the sample under test.

2.5. Spectral analysis instrumentation

The absorbance of the substrate assay reaction in the 3D-printed microfluidic devices was quantified by analysing the transmission spectrum of the assay using a fibre coupled tungsten halogen light source (Ocean Optics ecoVis, Ocean Optics, USA) and a CCD spectrometer Ocean Optics ADC1000-USB spectrometer (Ocean Optics, USA). The light

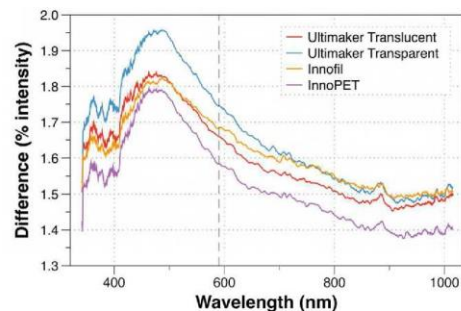


Figure 4. Difference as a percentage of intensity in the spectra of 3D printed cuvette devices compared to a PMMA cuvette [25].

source has an integrated cuvette holder which was adapted to hold the microfluidic devices. The light source and the spectrophotometer were connected using a short length (10cm) of multimode optical fibre.

3. Results and discussion

The investigation of the use of 3D printed plastics for microfluidic devices had two key aims. Firstly, the optimisation of the 3D printing methodology to produce plastic samples of sufficient optical quality to allow the optical interrogation of internal cavities. Secondly, the demonstration of filling and reading a biological assay within a 3D printed microfluidic device.

Optimisation of the 3D printing methodology focussed on both the printing layer height and the speed of the plastic deposition. Once optimised the device repeatability was also demonstrated.

Prior to running a colorimetric glucose assay the microfluidic device, an optimisation process was undertaken to first develop a reliable glucose assay protocol and then produce a dilution curve by running the assay in a commercial well plate which was subsequently read with a commercial plate reader system.

3.1. The effect of print speed and layer height on optical transparency

As previously discussed, many factors can influence a 3D-printed object; it can take several print attempts and varying conditions to produce an object with the desired properties. The FDM printer used here deposits layers of polymer on top of each other to build up the object. The influence of these layers' height on the attenuation of the transmitted light was investigated by characterising 3D-printed solid plastic samples as described in 2.4. These samples were fabricated at 10mm s^{-1} with varying layer heights of the plastic. The total thickness of the object was unchanged; only the height of the layers (and therefore the number of layers) was altered.

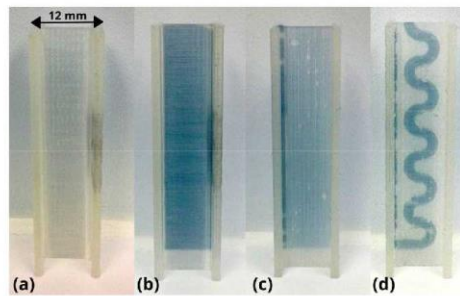


Figure 5. Microfluidic cuvette before (a) and after (b) quinoneimine dye reaction. Also shown are a microfluidic cuvette prepared with a 100 μm thick chamber (c) and an S-shaped channel (d).

As demonstrated in figure 2, an increase in the layer height increases the attenuation of the transmitted light. However, at 0.04 and 0.06 mm layer heights the difference between the attenuation measurements was less than the experimental error.

As layers are deposited, air can be trapped between the layers, reducing homogeneity. Such air pockets and the corresponding reduction in the merging of the polymer layers is thought to be responsible for the clouding observed in the printed samples and the measured reduction in optical transparency. Where homogeneity between layers was improved, it was observed by eye that the optical transparency increased, even if intermittently and not through the entire object. It could be expected that increasing layer height would increase the optical transparency, as there are fewer layers and therefore less potential for air gaps, however it is proposed that as the layer height increases the circular nature of the FDM extruded plastic, causing the air pockets to become larger, decreasing optical transparency.

A proposed solution to the formation of air gaps was to vary the print speed to allow the plastic time to flow into the gaps. However, as shown in figure 3, the variation of the print speed had a mixed impact on the attenuation caused by the Ultimaker PLA Translucent plastic samples. For 0.06 mm layer height, the increased speeds appeared to reduce the attenuation slightly. Whereas layer heights of 0.15 and 0.25 mm showed a slight increase in attenuation with speed. In all cases the change is small and is less than 10% of the overall attenuation.

Further experiments at a wider range of speeds were attempted but this increased the failure rate of the prints. It has been documented that at higher print speeds the chance of print failure increases. This is due to the increased risk of the print not sticking to the bed, overheating, layer shifting and misalignment, grinding of the filament leading to interruption of the feed, and increased vibrations impacting the quality of fine details. This results in either incomplete, inadequate quality or aborted prints.

3.2. Device variability

To investigate the repeatability of the optical properties of the 3D printed devices, microfluidic devices were manufactured from a selection of transparent PLA filaments as described in

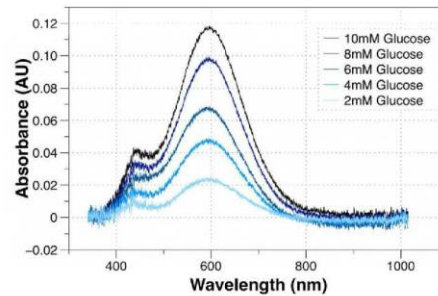


Figure 6. Change in the absorbance spectra with glucose concentration [27].

Table 1. Summary table showing intra filament % coefficient of variance (CV).

Filament type	CV between devices ($n = 3$) (%)
Ultimaker translucent	4
Ultimaker transparent	7
Innofil	4
InnoPET	3

section 2.2. Three devices were produced from each filament so that the inter and intra-filament variability could be observed. The difference in the spectra of multiple devices ($n = 3$) made from the same filament were compared using the equipment described in section 2.5 and the resulting average spectra are presented in figure 4. Each device was read a total of five times. In this data the spectra of a PMMA cuvette was used as the reference in order to highlight the spectral differences between the commercial PMMA material and the 3D printed samples.

The spectra shown all have a similar form. All of the plastic filaments show around a 15% increase in the 390 to 700 nm region and around a 10% decrease in from 700 to 1000 nm. The Innofil Natural and Ultimaker Translucent plastics have less absorbance in the 390 to 700 nm range and appear to have decreased absorbance in the 700 to 1000 nm range.

At the 590 nm absorbance peak of the quinoneimine dye the inter-filament coefficient of variance (CV) was less than 1% and there was a maximum CV of 2.6% between 390–700 nm. The intra-filament CVs are shown in table 1, where the transmission spectrum of each device was recorded a total of five times and averaged.

For a device to be used as an assay platform, reproducibility is imperative; any optical differences between 3D-printed devices could have an impact on the quantified data leading to inaccurate conclusions. While the spectral data showed good reproducibility between absorbance profiles of devices made from the same filament batch, the large differences observed between filament batches require that a filament specific calibration curve is used for each batch of filament to maximise the accuracy of quantitative data produced in each device.

Using an optical coherence tomography (OCT) instrument (Spectral Radar OCT, Thorlabs, Germany), the characteristics of three channels of depth 400 μm and width 1000 μm were

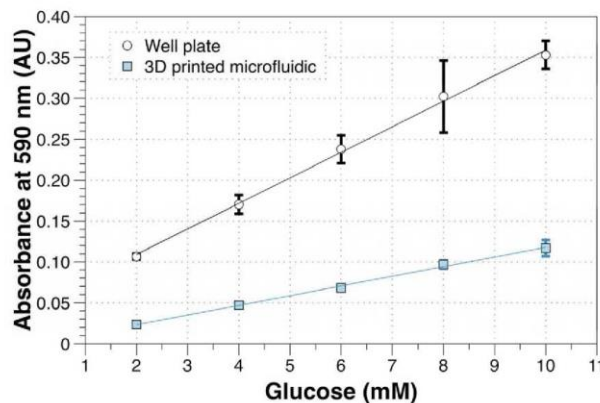


Figure 7. Absorbance at 590 nm comparison between 3D printed microfluidic and well plate reader. Error bars on all points represent three standard deviation of three repeats [28].

investigated. OCT is a low coherence interferometry technique that can be used to measure the optical thickness of layers within semi-transparent materials with a resolution on the micron scale [26]. From the OCT images it was possible to assess the surface roughness of the internal channels. Each channel was assessed at four locations, revealing a surface roughness of $135 \mu\text{m}$ with an average standard deviation of $53 \mu\text{m}$. It is thought that one of the largest contributing factors in the roughness is the nozzle size of the plastic extruder (in this case $400 \mu\text{m}$). The features most predominant in the OCT images were $400 \mu\text{m}$ wide plastic strands sitting slightly above the line of the adjacent strands. Future work will explore the improvement of surface roughness using smaller nozzles, of diameter down to $125 \mu\text{m}$, which are also supported by the Ultimaker FDM printer.

3.3. Glucose assay optimisation

Optimisation experiments for the glucose assay were performed in 96 well plates using the chemical and enzyme concentrations and equipment described in section 2.1.

Glucose oxidase and HRP concentrations were determined using a fixed time method as this is more applicable in most clinical assays. In all cases, blue quinoneimine dye was produced and visible immediately with the colour intensity increasing as GIOx or HRP concentration increased. In the absence of GIOx or HRP no blue dye was produced. As 1 U corresponds to the amount of enzyme which oxidizes $1 \mu\text{mol}$ D-glucose to D-gluconolactone and H_2O_2 per minute at pH 7.0 and 25°C , 20 U ml^{-1} GIOx should ensure a fast reaction rate ($<2 \text{ min}$) with tolerances for pH and temperature fluctuations [26]. It was determined that enzyme concentrations of GIOx 20 U ml^{-1} and HRP 6 U ml^{-1} would be sufficient for an assay capable of quantifying accurately a biologically relevant glucose range of 0–10 mM with a reaction time of 2 min (data not shown). Reaction rates can be increased by increasing enzyme concentrations accordingly.

3.4. Glucose assay performed in 3D-printed microfluidic device

The microfluidic devices manufactured for use with the glucose assay were printed at a rate of 10 mm s^{-1} with a layer height of 0.06 mm using Ultimaker Translucent. The glucose assay was performed in the 3D-printed device as described in section 2.3. Samples were prepared using the chemical and enzyme concentrations described in section 2.2. The reaction was started by adding glucose solution of the desired concentration. Figure 5 shows a photograph the microfluidic channel before and after the quinoneimine dye reaction. Additionally, figure 5 shows a microfluidic cuvette manufactured with a $100 \mu\text{m}$ thick fluid cavity and a cuvette with a $500 \mu\text{m}$ thick S-shaped channel. These are included to show the range of designs possible using of 3D printing.

The absorbance spectra of the $500 \mu\text{m}$ thick single chamber microfluidic (figure 5(b)) cuvette were recorded using the methodology described in section 2.5. The resulting spectra are shown in figure 6.

As the glucose concentration increases, the quinoneimine dye concentration also increases, resulting in an increase in absorbance centred around 590 nm. The spectra produced illustrate the range over which absorbance can be quantified, providing flexibility in the wavelength, which may be used for quantitative purposes. In this work, the absorbance of quinoneimine dye was quantified at 590 nm. The approximate peak absorbance of the quinoneimine dye, for the full range of glucose concentrations are shown in figure 7, alongside the data from previous plate reader based experiments.

The data shown in figure 7 demonstrates that it is possible to measure glucose concentration using a colourimetric assay in a 3D-printed PLA device. The data produced shows a linear dilution curve for increasing glucose concentrations with an R -squared of 0.99. When compared to results produced with a commercial plate reader assay, the 3D-printed microfluidic device performs well. There is around a 20–30% difference in attenuation, which is consistent with the native attenuation of

the 3D-printed plastic, which reduces the sensitivity as shown in figure 3. The limits of detection of the well plate and the printed microfluidic devices were determined to be 0.12 and 0.03 mM, respectively. The lower limit of detection for the 3D printed microfluidics is due to the lower error between reps compared to the well plate.

4. Conclusions

A colorimetric glucose assay capable of distinguishing between a range of glucose concentrations (0–10 mM) in PBS pH 7.4 solution has been used to demonstrate the capability and functionality of the printed devices. The glucose assay was performed in a 3D-printed microfluidic device and absorbance data was gathered during testing that shows that it is possible to quantify colorimetric assay data in a 3D-printed device. The use of an enzymatic cascade demonstrates how a multistage assay process can be performed within the device as a single user step.

It has previously been thought that the poor optical transparency of 3D-printed polymers is a fundamental obstacle that considerably limits their potential to fabricate optically interrogated devices [16]. Furthermore, the variability and error in low cost FDM printers was thought to limit their use in fabricating microfluidic structures. When acetone vapour treatment [29] was used, it was possible to improve the transparency of plastic samples by a further 30%. While not applicable to microfluidics this highlights that for some applications it is possible to further improve the sensitivity and surface quality of devices manufactured using cheap 3D-printers with simple post-processing techniques.

Additionally, more expensive 3D-printing techniques have higher resolution and better accuracy, which can also improve the optical properties of the plastic. However, these systems can cost as much as \$200,000, which is beyond the budget of many research laboratories and would make the cost of individual sample holders prohibitive in many applications.

The microfluidic device demonstrated in this paper was manufactured using an Ultimaker 2 + FDM printer costing \$2000, using filament purchased from the Ultimaker website for \$30–\$50 per 750 gram reel. Each device cost 3–10¢ depending on the filament used, when compared to purchasing standard disposable PMMA cuvettes which cost approximately 7¢ each, resulting in an economical device that can be custom designed and built to the users' requirements without having to wait for purchasing or delivery. Further investigation is to be performed into secondary adsorption phenomena that may influence the analytical spectroscopy and reproducibility of data involving 3D-printed PLA devices however the use of PLA in biochemical devices is already established [14,15].

Whilst many industrial microfluidic devices are produced using injection molding, this is a very costly production method for research labs [30] as each design change can cost as much as \$3000 to have the molds made. The use of 3D-printing in device fabrication would allow researchers to prototype various microfluidic systems quickly and cheaply,

both reducing the cost and time for development of a microfluidic platform. 3D printing also allows for structures and shapes that are not possible in injection molding and could open up new 3D designs in microfluidics. This includes the inclusion of electrodes and other devices into the 3D printed structure. This is something we have already begun exploring with simple electrode systems and fibre optic sensors.

In future work we will look at complex microfluidic structures as well as the flow dynamics of 3D-printed surfaces. It is also envisaged that this will expand into testing the suitability of this approach for blood and urine analysis and further develop in to complex 3D-printed devices such as lab-on-a-disc assay platforms providing mobile diagnostic information efficiently and cheaply for personal health monitoring.

Acknowledgments

The authors acknowledge funding from the Engineering and Physical Sciences Research Council (EPSRC) UK, via grants EP/N002520 and EP/H02252X. The underlying data can be found on the Cranfield Online Research Data repository using the links provided in the reference list.

References

- [1] NICE 2010 *Cardiovascular Disease Prevention* (PH25) (available at <https://www.nice.org.uk/guidance/ph25>) (accessed 07/02/2017)
- [2] Tang W H W, Francis G S, Morrow D A, Newby L K, Cannon C P, Jesse R L, Storrow A B, Christenson R and HNACB Committee 2008 National academy of clinical biochemistry laboratory medicine practice guidelines: clinical utilization of cardiac biomarker testing in heart failure *Clin. Biochem.* **41** 210–21
- [3] Mirasoli M, Guardigli M, Michelini E and Roda A 2014 Recent advancements in chemical luminescence-based lab-on-chip and microfluidic platforms for bioanalysis *J. Pharm. Biomed. Anal.* **87** 36–52
- [4] Arandis-Chover T, Morais S, González-Martínez M Á, Puchades R and Maquieira A 2014 High density microarrays on Blu-ray discs for massive screening *Biosens. Bioelectron.* **51** 109–14
- [5] Livak-Dahl E, Sinn I and Burns M 2011 Microfluidic chemical analysis systems *Annu. Rev. Chem. Biomol. Eng.* **2** 325–53
- [6] Huttmacher D W, Sittinger M and Risbud M V 2004 Scaffold-based tissue engineering: rationale for computer-aided design and solid free-form fabrication systems *Trends Biotechnol.* **22** 354–62
- [7] Zhang C, Anzalone N C, Faria R P and Pearce J M 2013 Open-source 3D-printable optics equipment *PLoS ONE* **8** e59840
- [8] Cohen D L, Malone E, Lipson H and Bonassar L J 2006 Direct freeform fabrication of seeded hydrogels in arbitrary geometries *Tissue Eng.* **12** 1325–35
- [9] Ballyns J J, Cohen D L, Malone E, Maher S A, Potter H G, Wright T, Lipson H and Bonassar L J 2010 An optical method for evaluation of geometric fidelity for anatomically shaped tissue-engineered constructs *Tissue Eng. Part C Methods* **16** 693–703
- [10] Ansari M I H, Hassan S, Qurashi A and Khanday F A 2016 Microfluidic-integrated DNA nanobiosensors *Biosens. Bioelectron.* **85** 247–60

- [11] Becker H and Locascio L E 2002 Polymer microfluidic devices *Talanta* **56** 267–87
- [12] Siegrist J, Gorkin R, Bastien M, Stewart G, Peytavi R, Kido H, Bergeron M and Madou M 2010 Validation of a centrifugal microfluidic sample lysis and homogenization platform for nucleic acid extraction with clinical samples *Lab. Chip* **10** 363–71
- [13] Zhao Y, Leung L, Naguib H and You L 2009 Microfluidics chamber system for bone cell mechanotransduction study and bone tissue engineering application *55th Annual Meeting of the Orthopaedic Research Society*
- [14] Pioggia G, Di Francesco F, Marchetti A, Ferro M and Ahluwalia A 2007 A composite sensor array impedentiometric electronic tongue Part I. Characterization *Biosens. Bioelectron.* **22** 2618–23
- [15] Kadimisetty K, Mosa I M, Malla S, Satterwhite-Warden J E, Kuhns T M, Faria R C, Lee N H and Rusling J F 2016 3D-printed supercapacitor-powered electrochemiluminescent protein immunoarray *Biosens. Bioelectron.* **77** 188–93
- [16] Willis K, Brockmeyer E, Hudson S and Poupayev I 2012 *Printed Optics: 3D Printing of Embedded Optical Elements for Interactive Devices* (New York: ACM)
- [17] Chen C, Wang Y, Lockwood S Y and Spence D M 2014 3D-printed fluidic devices enable quantitative evaluation of blood components in modified storage solutions for use in transfusion medicine *Analyst* **139** 3219–26
- [18] Bhattacharjee N, Urrios A, Kang S and Folch A 2016 The upcoming 3D-printing revolution in microfluidics *Lab Chip* **16** 1720–42
- [19] Erkal J L, Selimovic A, Gross B C, Lockwood S Y, Walton E L, McNamara S, Martin R S and Spence D M 2014 3D printed microfluidic devices with integrated versatile and reusable electrodes *Lab. Chip* **14** 2023–32
- [20] Wong R C, Ngo T T and Lenhoff H M 1981 Formation of blue chromophore from oxidative coupling of aminoantipyrine with chromotropic-acid in the presence of peroxide and horseradish-peroxidase *Int. J. Biochem.* **13** 159–63
- [21] Nicell J A and Wright H 1997 A model of peroxidase activity with inhibition by hydrogen peroxide *Enzyme Microb. Technol.* **21** 302–10
- [22] Tohill A 2016 *BIOS2016 P2.006 Microfluidic Device (500 µm)* (online) (www.thingiverse.com/thing:1558265) (Accessed: 12th May 2016)
- [23] Tohill A 2016 3D printed plastic attenuation with layer height (figshare) Retrieved: 06 49, 6 October 2016 (GMT) (doi: 10.17862/cranfield.rd.3443639.v1)
- [24] Tohill A 2016 3D printed plastic attenuation with print speed (figshare) Retrieved: 06 49, 6 October 2016 (GMT) (doi: 10.17862/cranfield.rd.3363049.v1)
- [25] Tohill A 2016 Percentage intensity difference of transparent 3D plastics (figshare) Retrieved: 06 49, 6 October 2016 (GMT) (doi: 10.17862/cranfield.rd.3443645.v1)
- [26] Wilson R and Turner A P F 1992 Glucose oxidase: an ideal enzyme *Biosens. Bioelectron.* **7** 165–85
- [27] Tohill A 2016 Absorbance spectra of microfluidic cuvette glucose sensor (figshare) Retrieved: 06 49, 6 October 2016 (GMT) (doi: 10.17862/cranfield.rd.3443648.v1)
- [28] Tohill A 2016 Absorbance of 3D printed microfluidic biosensor at 590nm (figshare) Retrieved: 06 49, 6 October 2016 (GMT) (doi: 10.17862/cranfield.rd.3443651.v1)
- [29] Naga N, Yoshida Y, Noguchi K and Murase S 2013 Crystallization of amorphous poly(lactic acid) induced by vapor of acetone to form high crystallinity and transparency specimen *Open J. Polym. Chem.* **2013** 29–33
- [30] Fiorini G S and Chiu D T 2005 Disposable microfluidic devices: fabrication, function, and application *BioTechniques* **38** 429–46

CONFERENCE PAPER/AWARD

Overall Poster Prize Winner (1st out of ~900)

Optical Detection of Glucose Using 3D-Printed Microfluidic Platform

A. M. Tothill*, M. Partridge, S. W. James and R. P. Tatam

Engineering Photonics, Cranfield University, Cranfield, Bedfordshire MK43 0AL, England, UK.

Cranfield
UNIVERSITY



Introduction

An aging population in combination with an obesity and diabetes epidemic is placing huge burden on health care services and increasing the need for point-of-care testing for serious pathologies. The advance of solid freeform fabrication techniques such as 3D-printing has significantly improved the ability to prepare solid structures with precise geometries; this provides a means for rapid device development for point-of-care devices. However, 3D-printed optical assay platforms can suffer from the poor optical properties and performance of polymers available.

- To develop a cheap disposable 3D-printed microfluidic optical device.
- Improve optical transparency of the devices such that optical colourimetric assays can be performed within.
- Produce calibration curve of colourimetric glucose assay performed within device.

Methodology

A Microfluidic device was designed using CAD software and fabricated using an Ultimaker 2+ 3D-printer. Optical transparency was improved using optimisation techniques of the printer and print conditions. Further optical improvement has been achieved with solvent vapour treatment. A colourimetric glucose assay was performed within the device and the absorbance determined via a spectrometer.

The glucose assay utilized an enzymatic cascade of glucose oxidase and horseradish-peroxidase was used for the oxidative coupling of 4-aminoantipyrine and chromotropic acid to produce a blue quinoneimine dye. The assay was performed in a the 3D-printed prototype, the absorbance was quantified and a glucose concentration curve was successfully produced.

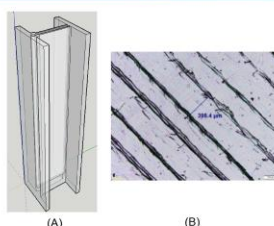


Figure 1: (A) CAD design of microfluidic device. Channel diameter 500 µm. (B) Image of plastic sample.

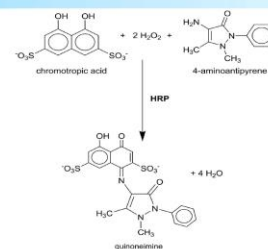


Figure 2: Proposed mechanism for peroxidase-catalysed formation of a quinoneimine dye.

Results

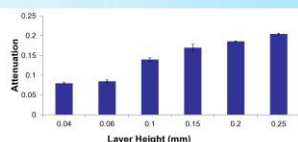


Figure 3: The effect of print resolution/layer height on optical transparency.

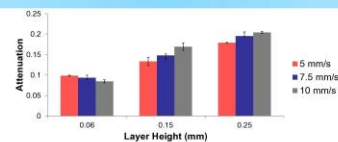


Figure 4: The effect of print speed on optical transparency.

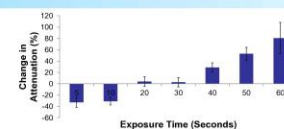


Figure 5: The effect of acetone vapour treatment on improving optical transparency.

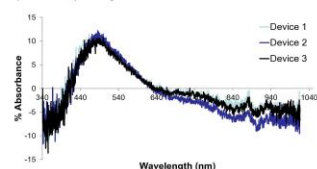


Figure 6: Variability of printed devices.

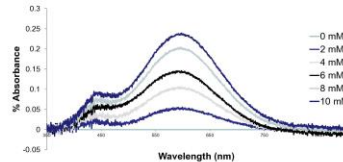


Figure 7: Absorbance spectra of quinoneimine dye produced by assay in 3D-printed device.

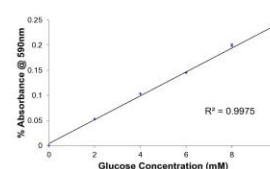


Figure 8: Quinoneimine dye absorbance at 590 nm. CV 2.4%.

Conclusions

The current work demonstrated that with proper optimisation of equipment and operating parameters, it is possible to produce microfluidic devices suitable for point-of-care testing using a 3D-printer. The optical transparency of the devices was improved using various techniques during and after manufacture to such a point that optical colourimetric assays can be performed in the device. The data gathered shows that excellent assay reproducibility is possible in the 3D-printed device. Future work focuses on blood and urine analysis and complex 3D-printed devices such as lab-on-a-disc assay platforms, providing mobile diagnostic information efficiently and cheaply for personal health monitoring.

www.cranfield.ac.uk

Cranfield University, Cranfield, Bedfordshire MK43 0AL, England, UK.
Corresponding author: a.m.tothill@cranfield.ac.uk.



Microfluidic Device
Download Link



Poster/Data
Download Link